Plasma Physics Reports, Vol. 26, No. 4, 2000, pp. 283–291. Translated from Fizika Plazmy, Vol. 26, No. 4, 2000, pp. 309–317.

PLASMA DYNAMICS

Formation of Electrode Sheaths during the Acceleration of a Magnetized Plasma

S. F. Garanin

All-Russia Research Institute of Experimental Physics, Russian Federal Nuclear Center, Sarov, Nizhni Novgorod oblast, 607190 Russia

Received April 14, 1999; in final form, July 27, 1999

Abstract—A study is made of the motion of a plasma with a frozen-in magnetic field along the electrode surfaces in the direction transverse to the magnetic field. A one-dimensional problem of an electrode sheath is formulated in which all of the quantities depend only on the coordinate orthogonal to the electrode surface. Viscous plasma heating, plasma cooling via heat conduction, and other kinetic effects are taken into consideration. Account is also taken of the effect of plasma acceleration and of the related current that is transverse to the electrode surfaces and, due to the Hall effect, carries the magnetic flux away from the cathode and toward the anode. Solving the one-dimensional problem with a constant electric current and constant magnetic field shows that, in a sheath that forms near the cathode, the solution becomes self-similar, the plasma mass grows linearly, and the electron magnetization parameter remains unchanged. It is found that the anode sheath cannot be described in the magnetohydrodynamic approximation, according to which the plasma density in the sheath rapidly vanishes, while the current through the sheath remains constant. This difficulty can be overcome by incorporating some of the nonhydrodynamic effects (primarily, electron dispersion), thereby making the problem physically correct. Solving the problem numerically shows that a decrease in the plasma density in the anode sheath due to the Hall effect gives rise to additional significant plasma acceleration. © *2000 MAIK "Nauka/Interperiodica"*.

1. INTRODUCTION

A magnetohydrodynamic (MHD) approach is widely used to describe the operation of many plasma devices such as plasma accelerators, dense plasma focus discharge devices, and liners. The applicability condition for the validity of the MHD description is governed by the value of the parameter $\xi \equiv \frac{c}{\omega_{pi}L}$, where L is the characteristic spatial scale of the plasma flow. For $\xi \ll 1$, the flow can be described by the ideal MHD equations into which the electrodes bounding the plasma region are introduced via the boundary conditions (in the case of a magnetic field parallel to the electrode surfaces, they reduce to the ideal slippage condition). Near the electrodes, the plasma (which is assumed to be cold, $\beta \equiv \frac{8\pi p}{B^2} \ll 1$) flows along the electrode surfaces and is either accelerated or decelerated under the action of the Lorentz force $[\mathbf{jB}]/c$. The sheaths that form near the electrodes are characterized by viscous plasma heating and plasma cooling via heat conduction. In the electrode sheaths, the Hall effect can play an important role, because it forces the current to carry the magnetic flux away from the cathode (thereby causing plasma compression near the cathode) and toward the anode (thereby causing plasma rarefaction near the anode).

Interest in studying electrode sheaths in magnetohydrodynamics (see [1–3] and the literature cited therein) stems from the following three reasons. First, for diagnostic purposes, it is important to know how much the plasma parameters in the electrode sheaths differ from those far from the electrodes. Second, the sheath thicknesses and the plasma mass in the sheaths can be large enough to affect the operation of many plasma devices, as is the case, e.g., with the MAGO chamber [4, 5]. Finally, investigating electrode sheaths is of interest from a methodological standpoint, because the MHD approach is insufficient to describe them (especially, the anode sheath). Below, we will show that, in the MHD approximation, the density of the plasma accelerated near the anode rapidly vanishes, thereby giving rise to a vacuum sheath similar to that formed by a shock wave front near the anode [3]. However, in the case of a shock wave, the time scales were assumed to be long enough so that a steady-state two-dimensional structure with a current-free vacuum region forms. In contrast, in the case in which we are interested here (when a bulk plasma flow is treated and the time scales are not too long), the current, which is governed by MHD effects, should flow in a vacuum (in the MHD approximation) region. Hence, the MHD approach fails to describe regions near the anode, thereby necessitating the incorporation of nonhydrodynamic effects.

Here, we further develop the approach that was applied earlier in [6], where the plasma was assumed to be accelerated over long distances and no account was taken of such important phenomena as plasma turbulence in a boundary sheath [7] and anomalous plasma

1063-780X/00/2604-0283$20.00 © 2000 MAIK "Nauka/Interperiodica"

resistivity due to the onset of a lower hybrid drift instability. Here, we take these phenomena into account and assume that the plasma is accelerated over shorter distances. We also consider the motion of a low-density plasma along the electrode surfaces, in which case the plasma can be heated to high temperatures, thus making it possible to explain neutron generation in the nozzle of the MAGO chamber when the neutron energy distribution is highly anisotropic [8].

2. ONE-DIMENSIONAL PROBLEM

We assume that the electrode sheath thicknesses are small in comparison with the characteristic spatial scales of the complete MHD problem. Under this assumption, we can describe unsteady electrode sheaths in a one-dimensional approximation in which all of the quantities depend only on the coordinate perpendicular to the electrode surfaces and on time. We assume that, far from the electrodes, the plasma is homogeneous with density n_0, temperature T_0, and constant current density **j** perpendicular to the electrode surfaces, the magnetic field $\mathbf{B}_0$ being parallel to them. The Lorentz force [**jB**]/*c* acts to accelerate the plasma in the direction parallel to the electrode surfaces both near the electrodes and far from them.

Let the coordinate normal to the electrode surfaces be *x* and let the magnetic field be directed along the *z*-axis, in which case the electric field will be directed along the *y*-axis and the plasma will be accelerated in the same direction. The electrode sheaths are assumed to be sufficiently thin so that the total pressure has enough time to be equalized in the *x* direction; i.e.,

$$p + \frac{B^2}{8\pi} = P_0, \tag{1}$$

where the total pressure P_0 depends only on time (in fact, we are solving problems in which P_0 is constant and the density n_0, temperature T_0, and magnetic field B_0 experience slight time variations due to Joule heat release and thermal expansion). Along with relationship (1), the dynamics of the electrode sheaths is described by the following MHD equations: the equation of motion in the *y*-direction in terms of the plasma velocity v,

$$\rho\frac{dv}{dt} = \frac{jB}{c} - \frac{\partial\pi_{xy}}{\partial x}, \tag{2}$$

where the *xy*-element of the viscous stress tensor π_{xy} is

$$\pi_{xy} = -\eta\frac{\partial v}{\partial x}; \tag{3}$$

the equation for the magnetic field,

$$\rho\frac{d(B/\rho)}{dt} = -c\frac{\partial E}{\partial x}, \tag{4}$$

where the electric field is represented in Lagrangian form,

$$E = -RjB - \frac{c}{4\pi\sigma}\frac{\partial B}{\partial x} - N\frac{\partial T}{\partial x}; \tag{5}$$

and the heat-conduction equations for plasma ions and electrons,

$$\frac{3}{2}n\frac{dT_i}{dt} - T_i\frac{dn}{dt} = -\frac{\partial q_i}{\partial x} + \eta\left(\frac{\partial v}{\partial x}\right)^2 + Q_i \tag{6}$$

$$\begin{aligned}\frac{3}{2}n\frac{dT_e}{dt} - T_e\frac{dn}{dt} &= -\frac{\partial q_e}{\partial x} + \frac{j^2}{\sigma} - \frac{j}{en}\frac{\partial(nT_e)}{\partial x}\\ &- \alpha j\frac{\partial T_e}{\partial x} + \frac{c}{4\pi}\frac{\partial B}{\partial x}\left(\frac{c}{4\pi\sigma}\frac{\partial B}{\partial x} + N\frac{\partial T_e}{\partial x}\right) - Q_i,\end{aligned} \tag{7}$$

where

$$q_i = -\kappa_i\frac{\partial T_i}{\partial x}, \tag{8}$$

$$q_e = -\kappa_e\frac{\partial T_e}{\partial x} + \frac{c}{4\pi}NT_eB\frac{\partial B}{\partial x} - \left(\alpha + \frac{5}{2e}\right)jT_e. \tag{9}$$

Here, η is the plasma viscosity; σ is the plasma conductivity; κ_i is the ion thermal conductivity; κ_e is the electron thermal conductivity; and *R*, *N*, and α describe the Hall and Nernst effects and the heat carried by the current, respectively. All of these coefficients depend on the extent to which the plasma is magnetized. The term Q_i accounts for the energy exchange between electrons and ions. The formulas for all of these quantities are presented in [9].

The physical processes incorporated into equations (2)–(9) occur on different spatial and temporal scales and may play different roles in different stages of the evolution of a plasma flow near an electrode. If the plasma flows along the electrode surface at a constant velocity (the transverse current density *j* is equal to zero), then the structure of the electrode sheath will be primarily governed by viscosity and ion heat conduction, in which case the classical viscosity coefficient and classical ion thermal conductivity are of the same order of magnitude [9]. If the plasma velocity is initially coordinate-independent, then, with allowance for only these two effects, the characteristic plasma temperature in the electrode sheath will be determined by the squared plasma velocity and the sheath will become thicker according to the self-similar diffusion law $\sim\sqrt{t}$.

If the plasma is accelerated along the electrode surfaces (the current transverse to the electrodes is nonzero), then, due to the Hall effect, the current will carry the magnetic flux away from the cathode and toward the anode. If the magnetic diffusion caused by the finite plasma resistivity is not taken into account, then the zones in which the Hall effect enhances or reduces the magnetic flux will be infinitely thin, in which case the plasma density distributions at the electrode surfaces

will be described by delta-functions. However, in reality, the magnetic diffusion smears out these zones. Although the Hall effect and classical magnetic diffusion occur on spatial scales shorter than those characteristic of the plasma viscosity, they are very important near the electrodes and also on short time scales (see below). Magnetic diffusion should be analyzed with allowance for the electron heat conduction, which is of the same order of magnitude in a magnetized plasma and smears out the Joule heating region, thereby preventing the formation of an infinitely thin current skin layer.

However, as will be shown below, the plasma density falls off to zero near the anode due to the Hall effect even with allowance for magnetic diffusion. Consequently, our problem is clearly beyond the range of validity of the MHD approximation. To overcome this difficulty, we take into account electron inertia.

For some experimental applications, it is of interest to know the characteristic value of the electric field perpendicular to the metal surfaces of the electrodes. Without allowance for the collision terms, which are small in the case of a magnetized plasma, the equation of motion for the electron fluid yields

$$E_x = -\frac{1}{en}\frac{\partial}{\partial x}\left(\frac{B^2}{8\pi} + nT_e\right).$$

However, the equilibrium condition (1), which can be rewritten as

$$\frac{\partial}{\partial x}\left(\frac{B^2}{8\pi} + nT_e\right) = -\frac{\partial}{\partial x}(nT_i),$$

gives

$$E_x = \frac{1}{en}\frac{\partial}{\partial x}(nT_i).$$

Consequently, it is an easy matter to find E_x from the known profiles of the plasma density and ion temperature.

Note that, in a magnetized plasma $[\omega\tau)_i \gg 1]$, the spatial scales characteristic of heat conduction and plasma viscosity (in our problem, they are described by small thermal conductivity and a small viscosity coefficient) become, at a certain stage, shorter than the ion Larmor radius. Consequently, the MHD approximation and the relevant kinetic coefficients, strictly speaking, fail to describe the problem at hand. In order to make the MHD approach adequate for qualitatively describing the resulting kinetic problem, we supplement the coefficients η and κ_i in equations (3) and (8) in the case $(\omega\tau)_i > 1$ by the additional terms

$$\eta_{an} = \frac{nT_i}{8\omega_i}\frac{x}{r_{Li}}\left(1 - \frac{x}{r_{Li}}\right),$$
$$\kappa_{ian} = \frac{nT_i}{4M_i\omega_i}\frac{x}{r_{Li}}\left(1 - \frac{x}{r_{Li}}\right) \quad (10)$$

(M_i is the mass of an ion), which are nonzero over distances x from the electrode surfaces shorter than the ion Larmor radius r_{Li}. Introducing these terms, we incorporate the kinetic ion fluxes that carry the momentum and heat from the wall plasma toward the wall.

Possible high current velocities u in the electrode sheaths at $T_e \le T_i$ can give rise to a lower hybrid drift instability and, accordingly, to anomalous resistance. For a magnetized plasma, we model the anomalous resistance in accordance with [10], i.e., by setting

$$\frac{1}{\sigma_{an}} = \begin{cases} 4\pi\sqrt{\frac{\pi}{2}}\frac{M_i u^2}{T_i}\frac{mc}{eB}\sqrt{\frac{m}{M_i}} & \text{for } \frac{M_i u^2}{T_i} < 3 \\ 12\pi\sqrt{\frac{\pi}{2}}\frac{mc}{eB}\sqrt{\frac{m}{M_i}} & \text{for } \frac{M_i u^2}{T_i} > 3 \end{cases} \quad (11)$$

and by introducing the relevant anomalous contribution to the electron thermal conductivity,

$$(\kappa_e)_{an} = 1.5n\beta_e\frac{c^2}{4\pi\sigma_{an}}.$$

In the electrode sheaths, the possible onset of an MHD instability (due to large velocity gradients [11]) and, accordingly, a turbulent boundary sheath [7] can give rise to two-dimensional structures (according to [11], in the case of subsonic motion, the onset of an instability with a wave vector parallel to the magnetic field is hindered). To describe these phenomena in an averaged fashion in the one-dimensional approximation used here, we introduce the turbulent diffusion coefficient equal to

$$0.1x\delta v, \quad (12)$$

where δv is the characteristic variation of the plasma velocity at the distance x from the wall. We also take into account the related contributions to the viscosity and magnetic diffusion coefficients and to the electron and ion thermal conductivities. Below, we will show that, in reality, turbulent diffusion plays a relatively minor role until, at a certain time, it starts to develop and affect the structures of the electrode sheaths.

The initial conditions for a deuterium plasma were chosen to be as follows: a constant (in space) temperature $T_i = T_e = T_0 = 2$ eV, zero velocity $v = 0$, constant magnetic field $B = B_0 = 10^5$ G, and densities $n = n_0 = 6 \times 10^{17}$ cm^{-3} (to describe the main plasma flow through the nozzle of the MAGO plasma chamber [4, 5]) and $n = n_0 = 1.5 \times 10^{16}$ cm^{-3} (to describe the residual plasma flow through the nozzle). During the evolution of the electrode sheaths, the solutions fairly rapidly "forget" the quite arbitrary small initial temperature $T_0 = 2$ eV. We will show that the solutions become self-similar and describe the sheath plasmas with much higher temperatures. Because of the Joule heating, the plasma temperature far from the electrodes also increases, regardless of the initial temperature level. As the

plasma temperature in the electrode sheaths increases, the heat fluxes to the electrode surfaces become substantially more intense in comparison with the heat flux driven by a self-similar cooling wave corresponding to the initial plasma temperature.

The boundary conditions for equations (2) and (3) are

$$v(x = 0) = 0, \quad \frac{\partial v}{\partial x}(x = \infty) = 0.$$

At the boundary $x = 0$, the electric field was specified to correspond to a magnetic diffusion into the copper wall:

$$E = -\frac{B}{c}\sqrt{\frac{\chi_{Cu}}{\pi t}}, \tag{13}$$

where χ_{Cu} is the magnetic diffusion coefficient for copper. At $x = \infty$, the gradients were assumed to be zero and the electric field in (5) was described as

$$E_H = -jBR. \tag{14}$$

The temperatures T_i and T_e at the boundary $x = 0$ were set to be

$$T_i = T_e = 0,$$

and, at $x = \infty$, we put

$$\frac{\partial T_i}{\partial x} = \frac{\partial T_e}{\partial x} = 0,$$

in which case the electron heat flux is equal to

$$q_e = -\alpha T_e j.$$

Equations (1)–(14) for the anode and cathode differ in the sign of j: the plus and minus signs refer to the anode and cathode, respectively. In our one-dimensional problems, we chose the current magnitude j to be $j = cB/4\pi L$ with $L = 5$ cm; this gives $j = \pm 16$ kA/cm^2, which approximately corresponds to the parameters of the MAGO chamber.

3. CATHODE SHEATH

The mass of the plasma in the cathode sheath (from which the magnetic flux is carried away by the current) is determined by the relationship

$$\int n dx = \frac{|j|t}{e}. \tag{15}$$

On short time scales on which the plasma viscosity and viscous plasma heating are both unimportant, the plasma mass will be accumulated in a sheath whose thickness is governed by magnetic diffusion and electron heat conduction. For this to occur, the rates of magnetic diffusion and electron heat conduction should be of the same order of magnitude. For a low-β plasma, this means that

$$\chi = \frac{c^2}{4\pi\sigma}\beta \sim \frac{\kappa_e}{n}$$

or

$$(\omega\tau)_e \sim 1.$$

Since, in this case, the thickness x of the cathode sheath is equal to

$$x \sim \sqrt{\chi t},$$

the main plasma parameters of the sheath can be described by the following self-similar functions:

$$T \sim \frac{(j\sqrt{4\pi})^{1/2}\lambda^{1/2}e^{5/4}m^{1/4}c^{1/4}}{(B_0/\sqrt{4\pi})^{1/4}}t^{1/4},$$
$$n \sim \frac{(j\sqrt{4\pi})^{3/4}(B_0/\sqrt{4\pi})^{5/8}}{\lambda^{1/4}e^{9/8}c^{5/8}m^{1/8}}t^{3/8}, \tag{16}$$
$$x \sim \frac{(j\sqrt{4\pi})^{1/4}\lambda^{1/4}e^{1/8}c^{5/8}m^{1/8}}{(B_0/\sqrt{4\pi})^{5/8}}t^{5/8},$$

where λ is the Coulomb logarithm and m is the mass of an electron.

The results of solving our one-dimensional problem numerically for $n_0 = 6 \times 10^{17}$ cm^{-3} justify these self-similar dependences. For example, by the time $t = 0.1$ μs (when viscous plasma heating is still insignificant), formulas (16) give the following characteristic parameter values: $T = 4$ eV, $n = 9 \times 10^{17}$ cm^{-3}, and $x = 0.04$ cm. The relevant profiles shown in Fig. 1a, which were computed from a one-dimensional model, agree with these estimates. By this time, the electron and ion temperatures are essentially the same and, according to (2), the plasma velocity far from the cathode,

$$v = \frac{jB_0}{cn_0M_i}t, \tag{17}$$

is equal to $v_\infty = 0.8 \times 10^7$ cm/s. A decrease in the plasma velocity in the cathode sheath is governed by the elevated (near the cathode) plasma density and the turbulent viscosity coefficient (12). Since the temperature at the cathode surface is assumed to be zero (i.e., the magnetic diffusion coefficient is infinitely large), the thermal pressure and parameter β at the metal surface are both finite [12]. This means that the plasma density at the cathode surface is infinitely high.

During the next stage, turbulent diffusion starts to dominate over magnetic diffusion and the mass of the plasma involved in turbulent mixing starts to exceed the mass of the plasma in the sheath from which the magnetic flux has been carried away by the current. A comparison of relationship (15) with the turbulent diffusion coefficient (12) taken with the characteristic plasma

velocity (17) shows that this stage begins at the time $t \sim 0.1\omega_i^{-1}$. The viscous plasma heating becomes important, but we can assume that $\beta \ll 1$. The electron and ion temperatures start to differ from one another; the ion temperature is governed exclusively by viscous heating due to the friction between the plasma flowing with the velocity (17) and the cathode surface:

$$T_i \sim \frac{j^2 B_0^2}{M_i c^2 n_0^2} t^2. \quad (18)$$

The characteristic thickness of the electrode sheath becomes on the order of $0.1vt$, where the velocity v is determined by (17), and increases with the square of time. According to (15), the characteristic increase in the plasma density decreases in inverse proportion to t. The characteristic electron temperature is governed by the electron–ion heat exchange and increases at a lower rate in comparison with the characteristic ion temperature.

For this stage of the evolution of the cathode sheath, the profiles of the quantities computed at the time t = 0.5 μs in the one-dimensional approximation are shown in Fig. 1b. At this time, the plasma velocity far from the cathode is equal to $v_\infty = 4 \times 10^7$ cm/s and the maximum β is as high as 0.46.

In order to characterize plasma deposition onto the cathode surface (this process may be of interest for many MHD problems, because it illustrates the influence of the cathode sheath on the MHD flow), Fig. 2 demonstrates how the bulk plasma mass decreases with time due to plasma deposition onto the cathode. According to (15), the mass of the plasma deposited onto the cathode $[n_0 \Delta x]$ increases approximately linearly with time until such effects as viscous plasma heating and an increase in β come into play and start to expel the plasma from the cathode sheath.

In the case of acceleration of a low-density (n_0 = 1.5×10^{16} cm^{-3}) plasma, the thickness of the cathode sheath increases much more rapidly. An important role in the formation of the sheath is played by anomalous ion viscosity and anomalous ion heat conductivity (on a spatial scale of approximately the ion Larmor radius near the cathode surface) described by coefficients (10), anomalous electron resistivity described by (11), and anomalous electron heat conductivity. For a low-density plasma, the profiles of the quantities computed at the time t = 55 ns are shown in Fig. 3, the plasma velocity far from the cathode being $v_\infty = 1.75 \times 10^8$ cm/s. We can see that, for such plasma flow velocities, the ions in the cathode sheath are heated to temperatures of about several kiloelectronvolts, the electrons are heated to fractions of a kiloelectronvolt, and the sheath is as thick as several millimeters.

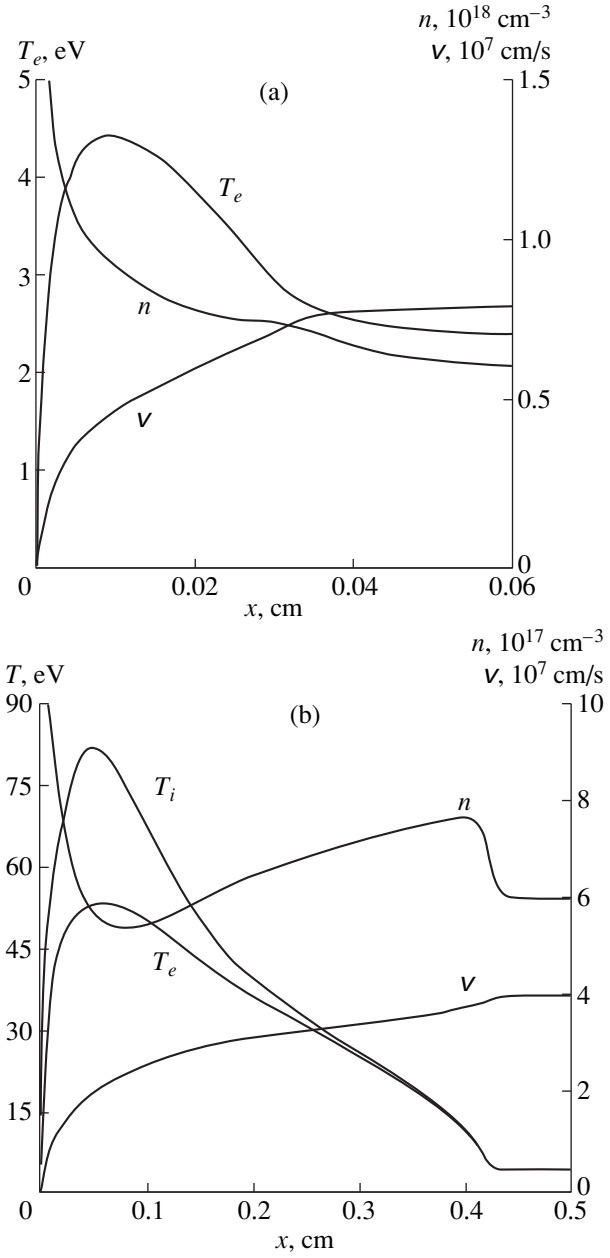

Fig. 1. Profiles of the plasma temperature, plasma density, and plasma velocity near the cathode for $n_0 = 6 \times 10^{17}$ cm^{-3}, T_0 = 2 eV, $B_0 = 10^5$ G, and j = –16 kA/cm^2 at the times t = (a) 0.1 and (b) 0.5 μs.

4. ANODE SHEATH

In the initial stage of the evolution of the anode sheath, in the MHD approximation, the magnetic flux is carried toward the anode, thereby expelling the plasma from the anode sheath. As in the cathode sheath, the time evolution of the main plasma parameters on short time scales in the anode sheath is described by the self-similar formulas (16) but with $|t_0 - t|$ (where t_0 is a certain time) in place of t. In other words, in the MHD

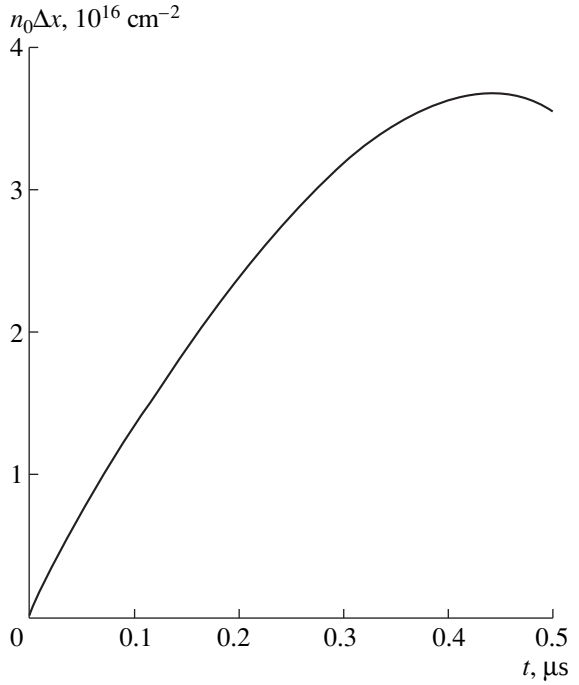

Fig. 2. Decrease in the bulk plasma mass, $n_0\Delta x$, due to the deposition of a plasma onto the cathode surface as a function of time.

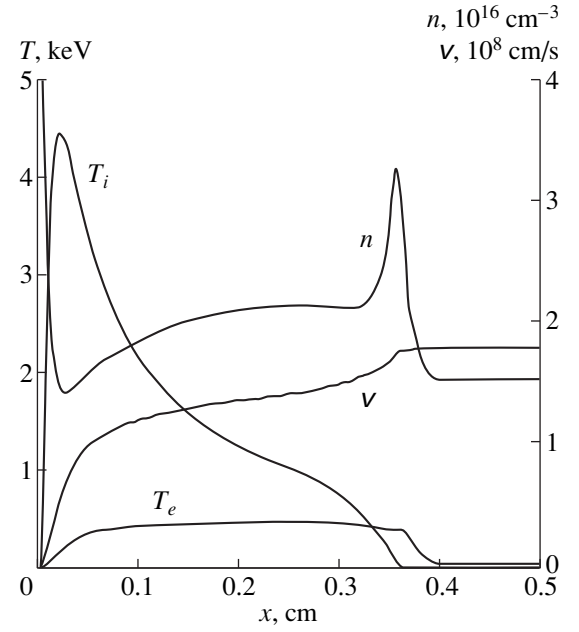

Fig. 3. Profiles of the plasma temperature, plasma density, and plasma velocity near the cathode for $n_0 = 1.5 \times 10^{16}$ cm^{-3}, $T_0 = 2$ eV, $B_0 = 10^5$ G, and $j = -16$ kA/cm^2 at the time $t = 55$ ns.

approximation, the plasma density in the anode sheath will fall off to zero over a finite time interval. However, according to the conditions assumed, the current continues to flow through the sheath. This contradiction can only be resolved by introducing additional kinetic effects and by treating the problem on short spatial scales, over which the MHD approximation, strictly speaking, fails. In our study, we supplement the MHD model with electron inertia, thus treating spatial scales of about $\sim c/\omega_{pe}$. Using as earlier the MHD approach, we qualitatively incorporate the terms associated with electron inertia into Ohm's law and consider time scales long enough for the electrons to be described in the quasisteady approximation; i.e., we neglect the time derivative $\partial \mathbf{v}_e/\partial t$ and keep only the spatial derivative $v_{ex}\partial \mathbf{v}_e/\partial x$. As a result, the electric field in (5) will contain the additional term

$$E_{me} = \frac{mc}{4\pi e^3}\frac{j}{n}\frac{\partial}{\partial x}\left(\frac{1}{n}\frac{\partial B}{\partial x}\right), \tag{19}$$

the corresponding contribution to the equation for the electron temperature being

$$-\frac{c}{4\pi}\frac{\partial B}{\partial x}E_{me}.$$

Incorporating the additional term into Ohm's law makes it possible to compensate for the first (Hall) term in equation (5) even in the case of a plasma with a very low density (the Hall term is proportional to $\sim 1/n$, because, for a magnetized plasma, we have $R = 1/nec$). Solving the problem as formulated leads to the following situation. According to relationships (16) taken with $|t_0 - t|$ in place of t, the vacuum sheath should form near the anode by the time t_0. However, in our approach, after that time, this sheath will be filled with a plasma of finite density decreasing exponentially from the hydrodynamic boundary. The plasma sheath will become wider as the current carries the magnetic flux from infinity toward the anode.

Let us turn to an isothermal plasma (T = const) and consider how the electron inertia described by the additional term (19) affects the plasma distribution, leading to the formation of a plasma (rather than vacuum) sheath near the anode. Near the boundary of the vacuum (in the hydrodynamic approximation) sheath, the plasma distribution is determined by the equations

$$E \simeq \text{const} = -RjB - \frac{c}{4\pi\sigma}\frac{\partial B}{\partial x} + \frac{mc}{4\pi e^3}\frac{j}{n}\frac{\partial}{\partial x}\left(\frac{1}{n}\frac{\partial B}{\partial x}\right)$$

$$= -\frac{jB}{nec} - \frac{c}{4\pi\sigma}\frac{\partial B}{\partial x} + \frac{mc}{4\pi e^3}\frac{j}{n}\frac{\partial}{\partial x}\left(\frac{1}{n}\frac{\partial B}{\partial x}\right),$$

$$nT + \frac{B^2}{8\pi} = \text{const}.$$

We assume $nT \ll B^2/8\pi$ and take into account that, in the case of an isothermal plasma, the classical conductivity, which is proportional to the temperature, is constant. Without allowance for electron inertia, these equations imply that, near the boundary of the vacuum sheath, the plasma density behaves as n =

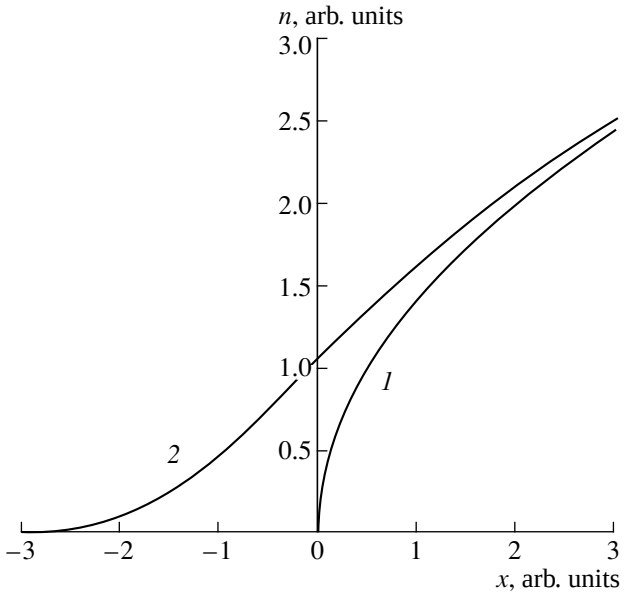

Fig. 4. Density profiles of an isothermal plasma near the hydrodynamic boundary with a vacuum (*1*) without and (*2*) with allowance for electron inertia.

$\sqrt{2j\sigma B^2 x/c^2 eT}$. However, taking into account electron inertia results in the characteristic density $\sim(mj^2\sigma^2B^2/c^2e^4T)^{1/4}$ varying on the spatial scale $\sqrt{mc^2T/e^2B^2}$, in which case the plasma density profile, shown in Fig. 4, decreases toward the anode surface according to the exponential law $\sim\exp(-e^2B^2x^2/2mc^2T)$.

The current near the anode may strongly accelerate the plasma in the low-density sheath and, in a real two-dimensional problem, may give rise to the inflow of a higher density plasma into the anode sheath from regions with different *y*-coordinates where the current density *j* is lower and the vacuum sheath is smaller or is completely absent. In order to describe this effect qualitatively, we incorporate the additional electric field component

$$E' = -\frac{4\pi}{c^2} j\int (v - v_\infty)\left(1 - \frac{\rho}{\rho_\infty}\right)dx$$

(where v_∞ and ρ_∞ are the plasma velocity and plasma density far from the anode) into the electric field (13) at the anode surface.

One-dimensional simulations of the evolution of the anode sheath were carried out with allowance for the contribution of E' to the boundary condition at the anode surface and for the electron inertia described by (19). To simplify numerical solution, we increased the coefficient in (19) by a factor of 100 so that the characteristic spatial scales would not to be too short.

Figure 5a shows profiles of the electron and ion temperatures; plasma density; and plasma velocity at the time $t = 60$ ns, when the self-similar solutions (16) pass over to solutions describing a linearly expanding low-density region where electron inertia plays a significant role. At this time, the plasma velocity is maximum [$v_{max} = 6.1 \times 10^6$ cm/s] at the distance $x = 9.5 \times 10^{-3}$ cm from the anode surface, the plasma velocity far from the anode being $v_\infty = 4.8 \times 10^6$ cm/s. By this time, the impact of the additional field E' on the processes near the anode can still be neglected: this field is 0.01% of the Hall electric field E_H (14), which delivers the magnetic flux from infinity toward the anode surface. The electric field (13) corresponding to the loss of the magnetic flux in the anode material is, at this time, 14% of E_H.

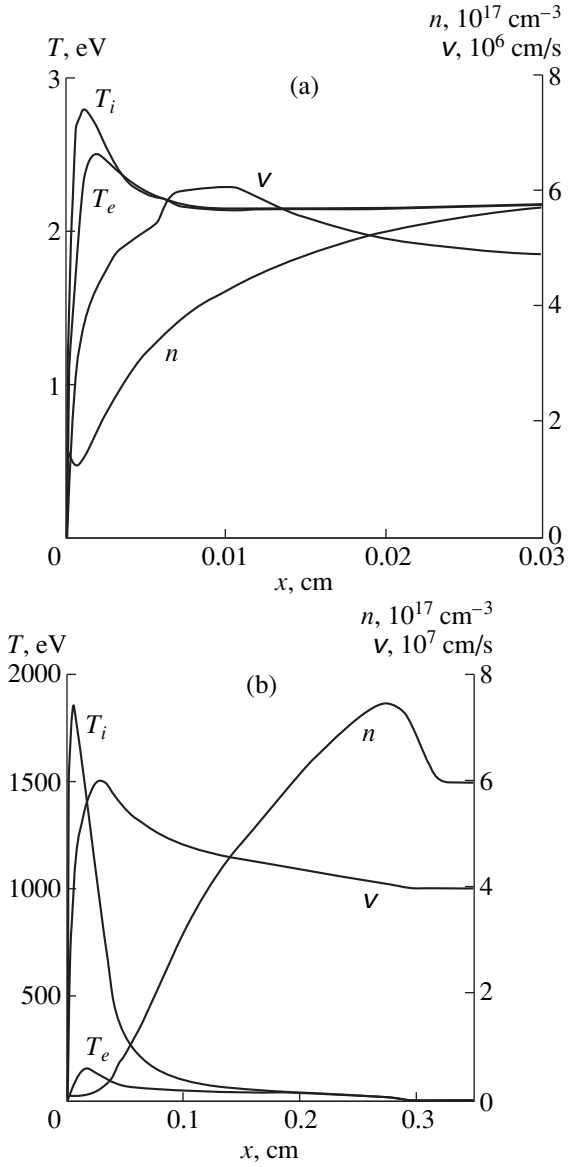

Fig. 5. Profiles of the plasma temperature, plasma density, and plasma velocity near the anode for $n_0 = 6 \times 10^{17}$ cm^{-3}, $T_0 = 2$ eV, $B_0 = 10^5$ G, and $j = 16$ kA/cm^2 at the times $t =$ (a) 60 ns and (b) 0.5 μs.

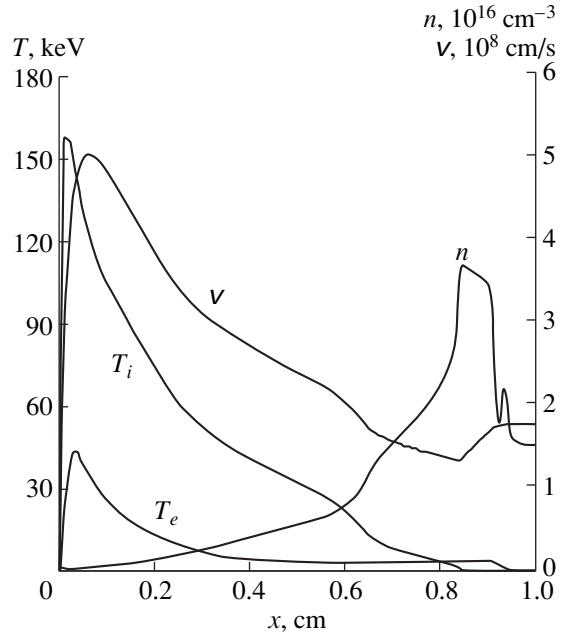

Fig. 6. Profiles of the plasma temperature, plasma density, and plasma velocity near the anode for $n_0 = 1.5 \times 10^{16}$ cm^{-3}, T_0 = 2 eV, $B_0 = 10^5$ G, and j = 16 kA/cm^2 at the time t = 55 ns.

Later, the plasma density in the anode sheath continues to decrease and the transport of the magnetic flux due to hydrodynamic motion driven by the electric field E' is still unimportant. The decrease in the plasma density significantly increases the plasma velocity and ion temperature due to the friction between the plasma and the anode surface (see Fig. 5b, which corresponds to the time t = 0.5 μs). At this time, the field E' is 58% of E_H and electric field (13), associated with the magnetic field diffusion into the copper wall, falls to 4.7% of E_H. By this time, the Hall electric field accelerates the plasma electrons, thereby heating them significantly (to fractions of a kiloelectronvolt). The plasma velocity at the anode surface [$v_{\max} = 6 \times 10^7$ cm/s] is higher than that far from the anode [$v_\infty = 4 \times 10^7$ cm/s].

Figure 6 shows the profiles that are characteristic of the anode sheath for the case of acceleration of a low-density plasma at the same time t = 55 ns as that in Fig. 3 for the cathode sheath. We can see that the plasma velocity near the anode is extremely high—$v_{\max} = 5.1 \times 10^8$ cm/s (it is much higher than that far from the anode—and the electron and ion temperatures are also high, $T_{i\max}$ = 160 keV and $T_{e\max}$ = 48 keV. According to Fig. 6, DD fusion neutrons can be produced in the plasma sheath near the anode. If we set the area of the anode in the region of the nozzle of the MAGO chamber to be S = 170 cm^2 [4] and estimate the characteristic time during which a low-density plasma flows through the nozzle as ~3×10^{-7} s (the estimate is obtained from the time over which the current at the entrance to the chamber rapidly ramps down [5]), then, for the temperature and density profiles shown in Fig. 6 and under the assumption that the plasma ions obey the Maxwellian distribution, we obtain a neutron yield of about ~1.6×10^9. This yield will agree with that measured experimentally in the "nose" region of a neutron pulse (5.5×10^9 neutrons, which is about 6% of the total number of neutrons in the pulse [8]) if we take into account the fact that, in comparison with the Maxwellian spectrum, the ion spectrum should be enriched with a larger number of high-energy ions produced when a high-speed ion flow is scattered by the anode surface. The characteristic velocity $v = 2.2 \times 10^8$ cm/s and characteristic temperature T_i = 27 keV of the neutron-producing plasma also agree with those measured in the nose region of a neutron pulse from the spectrum of emitted fusion neutrons [8].

A comparison between Figs. 3 and 6 shows that low-density plasmas in cathode and anode sheaths are heated very differently. For example, the neutron yield from the cathode sheath (Fig. 3) should be about two orders of magnitude lower than that from the anode sheath; the ion temperature $T_i \sim 4$ keV and flow velocity $v = 7 \times 10^7$ cm/s of the neutron-producing plasma in the cathode sheath should accordingly be lower than those in the anode sheath. Presumably, such differences in the structure of the cathode and anode sheaths may explain why the MAGO chamber operates in a different mode and why the neutron yield becomes significantly lower when the polarity of the electrodes is changed to the reverse one [4].

5. CONCLUSION

A numerical solution of the one-dimensional problem describing the evolution of the cathode sheath in the case of acceleration of a magnetized plasma by a current of constant density shows that, during a short initial stage (until the plasma velocity is low and viscous plasma heating is insignificant), a high-density plasma sheath is formed near the cathode in which the plasma mass increases linearly with time and the electron magnetization parameter is $(\omega\tau)_e \sim 1$. As the plasma velocity further increases and plasma turbulence develops, from the time $t \sim 0.1\,\omega_i^{-1}$, viscous plasma heating becomes important, the ion temperature grows with the square of time, and the characteristic spatial scale also increases with the square of time and becomes as long as about 4% of the entire path of the plasma along the cathode surface.

An analysis of the same problem but for the plasma near the anode shows that the MHD approach is insufficient to describe the anode sheath: in the MHD approximation, the plasma density in the sheath rapidly vanishes, while the current density, according to the conditions assumed, remains constant. We have overcome this difficulty by going beyond the scope of the

MHD approach, i.e., by introducing electron dispersion, in which case the plasma density in the anode sheath remains small but finite. A low-density plasma in the anode sheath can be accelerated by the Lorentz force to velocities much higher than the plasma velocities far from the anode and can be heated to high temperatures due to the friction on the anode surface. As in the case of a cathode sheath, the characteristic ion temperature in the anode sheath on long time scales is proportional to the squared plasma velocity and the characteristic spatial scale is governed by the zone of turbulent mixing. Plasma heating in the anode sheath can initiate fusion reactions; this circumstance may explain the generation of DD neutrons with an anisotropic energy distribution in experiments with the MAGO chamber.

ACKNOWLEDGMENTS

I am grateful to V.B. Yakubov for fruitful discussions.

REFERENCES

1. K. V. Brushlinskiĭ and A. I. Morozov, in *Reviews of Plasma Physics*, Ed. by M. A. Leontovich (Consultants Bureau, New York, 1980; Atomizdat, Moscow, 1974), Vol. 8.
2. L. M. Alekseeva, Pis'ma Zh. Tekh. Fiz. **15** (10), 1 (1989) [Sov. Tech. Phys. Lett. **15**, 371 (1989)].
3. S. F. Garanin and V. I. Mamyshev, Fiz. Plazmy **16**, 1218 (1990) [Sov. J. Plasma Phys. **16**, 706 (1990)].
4. A. M. Buĭko, G. I. Volkov, S. F. Garanin, *et al.*, Dokl. Akad. Nauk **344**, 323 (1995) [Phys. Doklady **40**, 459 (1995)].
5. S. F. Garanin, IEEE Trans. Plasma Sci. **26**, 1230 (1998).
6. S. F. Garanin, *Proceedings of 23rd International Conference on Phenomena in Ionized Gases, Toulouse, 1997*, Vol. 4, p. 158.
7. L. D. Landau and E. M. Lifshitz, *Fluid Mechanics* (Pergamon, Oxford, 1987; Nauka, Moscow, 1986).
8. O. M. Burenkov, S. F. Garanin, A. N. Demin, *et al.*, Fiz. Plazmy **23**, 203 (1997) [Plasma Phys. Rep. **23**, 165 (1997)].
9. S. I. Braginskii, in *Reviews of Plasma Physics*, Ed. by M. A. Leontovich (Consultants Bureau, New York, 1965; Gosatomizdat, Moscow, 1963), Vol. 1.
10. R. C. Davidson and N. T. Gladd, Phys. Fluids **18**, 1327 (1975).
11. S. F. Garanin and S. D. Kuznetsov, Fiz. Plazmy **22**, 743 (1996) [Plasma Phys. Rep. **22**, 647 (1996)].
12. G. E. Vekshteĭn, in *Reviews of Plasma Physics*, Ed. by B. B. Kadomtsev (Consultants Bureau, New York, 1990; Énergoatomizdat, Moscow, 1987), Vol. 15.

Translated by G. V. Shepekina

Plasma Physics Reports, Vol. 26, No. 4, 2000, pp. 292–297. Translated from Fizika Plazmy, Vol. 26, No. 4, 2000, pp. 318–323.

PLASMA DYNAMICS

Generation of Vortex Electric Fields in the Pinch Constriction

V. I. Afonin

Russian Federal Nuclear Center, All-Russia Research Institute of Technical Physics, Snezhinsk, Chelyabinsk oblast, 456770 Russia

Received December 28, 1998; in final form, May 22, 1999

Abstract—A study is made of physical effects that accompany the convergence of the pinch constriction and are caused by vortex electric fields generated in the constriction cavity. © *2000 MAIK "Nauka/Interperiodica".*

A fast Z-pinch produced in the electric explosion of a thin wire by a powerful current pulse has been actively investigated for more than twenty years [1, 2]. Interest in these investigations is related, in particular, to the generation of high-temperature dense plasma objects (hot plasma points) during the pinching of the plasma column. These hot points are the sources of intense soft X radiation. At present, it is commonly accepted that the generation of hot plasma points (HPPs) in fast pinches is related to MHD instabilities [2]. According to this concept, HPPs are constrictions of the plasma column. The formation and further evolution of these constrictions are accompanied by a number of physical effects. Zhdanov and Trubnikov [3] pointed to the possibility of the generation of a powerful vortex electric field during the breaking of a constriction, which is accompanied by the generation of hard X radiation and superthermal ions. Below, we will show that this field can be generated during the convergence of the pinch constriction. The vortex electric field leads to the emergence of a plasma jet that can shunt the constriction; this explains the experimentally observed effect of redistribution of the current, which begins to flow mainly at the periphery of the plasma column [4].

Let us consider the processes occurring during the convergence of the constriction of the pinch current-carrying shell (corona). As in [5], we will assume that, when a thin wire placed in the interelectrode gap of a high-current accelerator explodes under the action of the electric current, a plasma is produced that consists of a core and a current-carrying shell (corona). The plasma pressure in the corona is balanced by the pressure of the magnetic field produced by the current flowing through the corona, and the radiative cooling of the shell is balanced by Joule heating. As an example, in Table 1, we present the estimates [5] for the characteristic parameters of the corona of a pinch produced in the electric explosion of a 20-μm-diameter aluminum wire: the average ion charge Z, the ion density N, the corona thickness δ_1, the outer corona radius R, the plasma temperature T, the electric field E_1, and the quasi-equilibrium current J.

For simplicity, we will assume the constriction to be a hollow cylinder with the outer radius b [cm], thickness δ [cm], ion density n [cm^{-3}], and height h [cm]; this cylinder moves toward the pinch axis with the velocity $db/dt = -U$. (Note that, according to analytical solutions [3], such a plasma configuration can form as a result of the evolution of a local constriction in an incompressible pinch.) We will assume that the plasma–vacuum interface coincides with the outer boundary of the current shell, including the constriction.

We write the longitudinal component of Ohm's law in the form $E = j/\sigma + UH/c$ [6], where j is the current density in the constriction, H is the azimuthal magnetic field produced by the current, σ is the plasma electric conductivity, and c is the speed of light; the thermoelectric force and electron pressure are neglected. From this expression, it is seen that, when the constriction converges toward the axis, an electric field parallel to the field $E_0 = j/\sigma$ is generated in it. Representing the azimuthal field H as a field produced by the longitudinal current J(A) flowing through the constriction, we rewrite Ohm's law in units adopted here as E[V/cm] = $E_0 + 2 \times 10^{-9}UJ/b$, where $E_0 = J/2\pi b\delta\sigma$, $\sigma(\mathrm{s}^{-1}) = 20b_1(Z)T^{3/2}/Z$ is the electric conductivity of an unmagnetized plasma, T [eV] is the plasma temperature, and Z is the average ion charge (from [6], we can approximately take $b_1(Z) = 1.5$ for all Z). Assuming the current J in the constriction to be equal to the quasi-equilibrium current (i.e., $J = 2\pi R\delta_1\sigma_1 E_1$), we can write the final expression for the field E [V/cm] in the constriction in the laboratory frame as

$$E = (R\delta_1\sigma_1/b\delta\sigma)E_1 + 2 \times 10^{-9}UJ/b, \qquad (1)$$

where R, δ_1, and σ_1 are the radius, thickness, and conductivity of the current shell, respectively, and E_1 is the electric field in the accelerator diode.

1063-780X/00/2604-0292$20.00 © 2000 MAIK "Nauka/Interperiodica"

For estimates we will use the average velocity $U = (1/p)\int_0^p v(t)\,dt$ of the constriction moving from the radius R to radius $b = R - Ut_1$ under the action of the magnetic-field pressure produced by the current J. The mass of the constriction is $M = 2\pi b\delta n m_i = 2\pi R\delta_1 N m_i$. Here, $p = t_1$ and m_i is the ion mass. In the simplest case, neglecting the plasma raking, we can write the equation of motion in the form $dv(t)/dt = 10^{-2}J^2/Mb$. Using the relationship $b(t) = R - Ut$, integrating the equation of motion, and averaging the resulting expression for $v(t)$ over time t, we obtain $U = (10^{-2}J^2R/MU^2t)[(R - b)/R + (b/R)\ln(b/R)]$. It follows from here that

$$U = 0.1(J/M^{0.5})[1 + b/(R - b)\ln(b/R)]^{0.5}. \qquad (1')$$

Then, we find the vortex field E in the constriction cavity (i.e., in the region $b \le r \le R$) in the laboratory frame. We will use Faraday's law taking the integration contour L in the form of a rectangle lying in the plane passing through the longitudinal axis of the system. One of the rectangle's sides is a segment of the outer generatrix of the pinch (lying at the radius R), another passes through the constriction at the radius b and moves toward the axis with the velocity U, and the other two are the radial segments passing along the boundary between the constriction and the unperturbed region of the corona. The change in the magnetic field flux Φ through the membrane S bounded by the given contour can be written in the form

$$d\Phi/dt = \int_S \{\partial\mathbf{H}/\partial t - \mathrm{rot}(\mathbf{U}\times\mathbf{H})\}d\mathbf{S} = -Uh[H(R) - H(b)],$$

where the surface element $d\mathbf{S}$ is oriented perpendicularly to the magnetic field; since $\partial H/\partial t = 0$, we have $dS = hdr$. The circulation of the electric field vector around the closed contour L is

$$\oint_L \mathbf{E}d\mathbf{L} = \int_0^h E(R, t)dh + \int_0^h E(b)dh + 2\int_b^R E(r)dr,$$

where $E(R, t)$ and $E(b)$ are the values of the electric field at the radii R and b. In the units adopted, Faraday's law takes the form

$$E(R, t) = -(2/h)\int_b^R E(r)dr - 2\times 10^{-9}J(U/b) - 2\times 10^{-9}UJ(1/b - 1/R), \qquad (2)$$

where $b = b(t)$ and $E(r)$ is the radial field component. Differentiating (2) and using the expression $E(r = b) = 2\times 10^{-9}UJ/b$, we obtain

$$dE/dt = -4\times 10^{-9}J(U^2/b^2)(1 + b/h). \qquad (3)$$

Table 1

T, eV	35	40	50	65	80	100
z	7	7	8	8	9	10
δ_1, μm	210	50	80	32	22	13
R, μm	1800	1400	850	450	280	130
$N\times 10^{-18}$, cm^{-3}	4.74	3	8.44	29	82	1.37
E_1, kV/cm	5.5	27	26.2	101	210	250
J, kA	123	130	144	176	210	250

Integrating (3) over time and taking into account that $E(R) = -2\times 10^{-9}UJ/R$ at $b(0) = R$, we rewrite the expression for the field E in a more convenient form:

$$E(R, t) = -2\times 10^{-9}(UJ/b)[2 - b/R + (2b/h)\ln(R/b)]. \qquad (4)$$

It is well known [7] that, in a slowly varying electric field directed perpendicularly to the magnetic field, there exists an inertial drift of charged particles with the velocity $\mathbf{V} = (mc^2/zeH^2)d\mathbf{E}(R, t)/dt$, where $E(R, t)$ is expressed in electrostatic units and m and e are the mass and charge of the particle, respectively. Using equation (3) and substituting the necessary constants and the expression for H, we can find the ion velocity, which turns out to be much higher than the electron velocity. In the units adopted, this velocity can be written as

$$V = -10^{-3}(AR^2U^2/Jb^2z)(1 + b/h), \qquad (5)$$

where A is the atomic mass of the element. It follows from here that the distance over which the ions are displaced is

$$\Delta z = -10^{-3}(AR^2U/zJb)[1 - 0.5b/R + (b/h)\ln(R/b)]. \qquad (6)$$

It is easily seen that, if the condition $2 - b/R + 2(b/h)\ln(R/b) > 0$ is satisfied, then the generated field is negative, $E < 0$, which leads to the ion drift from the cathode to the anode. The drift of ions with respect to electrons results in the occurrence of a space charge and electric field; under the action of this field, the plasma electrons also start moving. In fact, in the uniform plasma layer, the displacement of ions results in the appearance of a charge on the layer boundary. Equations (4) and (6) give the relation between the displacement Δz and the field E:

$$\Delta z = 2.5\times 10^5(AR^2/zJ^2)E(R, t).$$

If the field in the plasma is E_p, then the polarization is $P \approx NZe\Delta z = 2.5\times 10^5(AR^2/ZJ^2)E_p$. The field created by the surface charge P is opposite in direction to the external field and is equal to $\delta E[\mathrm{V/cm}] = 1.2\times 10^3\pi P$. By adding this field to the external vortex field, we find the field in the plasma: $E_p = E/\varepsilon$, where $\varepsilon = 1 + 0.144\pi N(AR^2/J^2) \gg 1$ is the plasma permittivity. Since $E_p \ll E$, the main drift of the charged particles in the direction perpendicular to both the magnetic field and the radial component of the vortex electric field is suppressed. (Note that the radial component of the vortex electric field also increases with time, so that an addi-

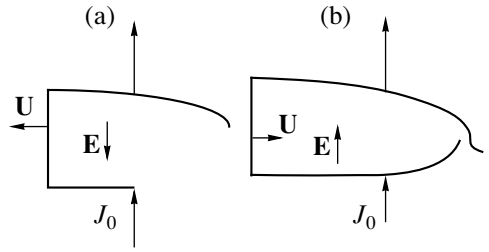

Fig. 1. Expected shape of the constriction cavity (a) in the case when it converges and (b) in the case when it expands.

tional drift of the jet can also occur in the radial direction.) Thus, the emergence of the vortex electric field that increases with time finally results in the emergence of an annular quasineutral plasma jet propagating with an ion drift velocity above the constriction, which is accompanied by a charge separation in the narrow region near the jet front. At the same time, the negative electric charge is produced at the anode side of the constriction. The jet can reach the opposite end of the cavity and shunt the constriction, which reaches the radius b_2 by time t_2. By using equations (1) and (6), we can easily find the constriction radius b_2 and, consequently, the characteristic time t_2 required for the constriction cavity to be closed at the radius R

$$(h/R)^2(x-1) = 10^{-8}(A^2/Mz^2)[x-0.5+(R/h)\ln x]^2(x-1-\ln x),$$

where $x = R/b_2$.

When the constriction is shunted by the jet, the current through the constriction decreases. This can be interpreted as the switching of the constriction current to the pinch periphery, which was observed experimentally in [4]. At the same time, the thermal energy contained in the constriction is rapidly lost via radiation and the constriction converges by inertia to the pinch axis. An additional burst of X radiation from the constriction can occur in the final stage of convergence due to deceleration of the constriction on the dense plasma core or on the pinch axis, when the plasma kinetic energy $MU^2/2$ is converted into thermal energy with the temperature $T[\text{eV}] = 3.5 \times 10^{-13}AU^2/Z_1$, where Z_1 is the average ion charge.

Table 2

T, eV	35	40	50	65	80	100
h, mm	3.6	2.8	3.4	1.8	0.56	0.26
U, km/s	51	136	106	157	156	158
b_2, μm	146	286	52	39	32	26
E_2, MV/cm	0.18	0.26	1.19	3.4	4.32	7.42
E_c, MV/cm	1.06	0.6	1.59	4.18	10.5	40.3
Σ, MeV	0.20	0.26	6.4	10.2	0.97	0.08
Σ_e, MeV	0.06	0.07	0.4	0.61	0.24	0.1

In addition, when the constriction is shunted by the jet, the ions reach the maximum velocity V_2 corresponding to the energy $\Sigma[\text{MeV}] = 5.2 \times 10^{-19}AV_2^2$ by time t_2 and then are decelerated in the pinch corona and on the anode, thus ionizing and exciting the plasma ions and the atoms of the anode material. When the constriction is shunted, the polarization field in the jet vanishes (i.e., $\delta E = 0$), so that the electric field in the constriction becomes equal to the external vortex field $E(R, t_2)$. It is well known that, in a highly ionized plasma, the electron mean free path rapidly increases with increasing the electron energy. In a sufficiently high electric field E, such that $E \geq E_c \approx 0.8\pi ZNe^3\Lambda/T = 0.2e\Lambda/R_d^2$ (where Λ is the Coulomb logarithm and $R_d = 500(T/ZN)^{0.5}$ is the Debye radius), the energy that the electrons gain between collisions is comparable or greater than the thermal energy and the electrons pass over to the runaway regime [7]. However, in lower fields, a partial runaway regime is also possible for the electrons whose transport collision frequency is lower than that of the bulk plasma electrons. At $E < E_c$, the bulk electrons move in the electric field **E** with a quasi-steady drift velocity, whereas the electrons from the tail of the distribution function pass over to the runaway regime. According to [7], for the given field **E**, the velocity v at which the electrons moving along the electric field start passing over to the runaway regime is determined by the inequality $m_e v^2/T > 15E_c/E$. Thus, when the jet shunts the constriction and the current begins to flow through the jet, the polarization field vanishes and the electrons can accelerate in the field $E_2 = E(R, t_2)$ over the constriction length h; the subsequent deceleration of electrons on the accelerator cathode can cause X radiation with the photon energy $\Sigma_e \sim E_2 h$.

We estimate the effects above with the use of the data from Table 1. Based on the considerations above, we will assume that the plasma jet with the ion density N propagates at the radius R with a velocity equal to the ion drift velocity V from the pinch corona with temperature T and thickness δ into the constriction cavity of length h. Table 2 presents the estimates made for the velocity and radius of the constriction, the particle energy, and the electric field. (It can be easily shown that the drift motion of the plasma particles in the jet can pass over to the runaway regime at $b \ll b_2$, i.e., at the radii at which the model allowing for the constriction breaking and the emergence of the displacement currents, whose vortex fields accelerate the electrons [3], is more appropriate.)

From calculations, it follows that the motion of the constriction is accompanied by the appearance of fairly strong vortex fields, in which both the ions and electrons can gain energy substantially exceeding the thermal energy.

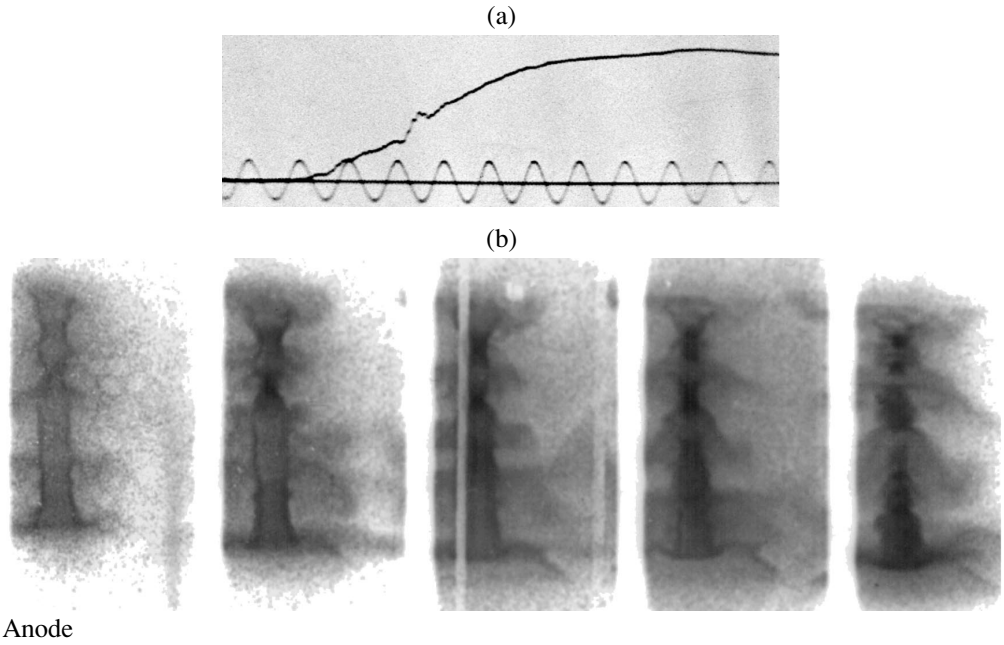

Fig. 2. Electric explosion of a 8-mm-long, 40-μm-diameter aluminum wire. (a) The current oscillogram: the maximum current is 190 kA, the current rise time is 150 ns, and the period of the reference signal is 40 ns. (b) Subsequent photodetector images: the diameter of the aperture of the SKhR4 pin-hole camera is 100 μm, the frame exposure time is 12 ns, and the interval between frames is 10 ns; the first frame starts 75 ns after the beginning of the load current pulse.

Note that the estimates presented relate, first, to a quasi-equilibrium plasma corona and, second, to a jet drifting only in the axial direction. The actual processes are much more complicated. It may be expected that, with allowance for the corona motion, a jet drifting in both the radial and axial directions cannot shunt the constriction. In this case, it will take the form of a radial plasma protuberance emerging from one of the ends of the constriction cavity and bent toward the other end (Fig. 1a).

When the constriction plasma is reflected from the pinch axis and moves outward, the directions of both the vortex field and jet propagation change. At the lower boundary of the constriction cavity, a second jet emerges, which propagates in both the radial and axial directions toward the cathode (Fig. 1b). When the first and second jets meet, the constriction can be shunted so that the current begins to flow through the jets. Note that, in this concept, the pinch consists of a set of successive constrictions and jets.

The above considerations can be illustrated by the results of experiments. Wire-explosion experiments were performed in the SIGNAL high-current generator with an inductive storage and plasma opening switch [8]. The generator produced a current pulse with an amplitude up to 200 kA and a ~100-ns rise time in the load. The shape of the current pulse was measured by a Rogowski coil, and the voltage was measured by a resistive divider; 8-mm-long 20- to 50-μm-diameter aluminum wires were used as loads.

The multiframe imaging of the Z-pinch plasma column in 0.1- to 10-keV X radiation was carried out with an SKhR4 frame photorecorder producing five frames with an exposure time from 3 to 12 ns; the interval between frames was 3–15 ns.

From the qualitative considerations, it may be expected that, in the case of a converging constriction, the jets deflect toward the anode. Such jet dynamics was recorded experimentally (Figs. 2, 3). When one or more constrictions change the direction of motion, a characteristic bending of the jets toward the cathode can occur, which is clearly seen in the last two frames in Fig. 2. The structure of two jets shunting the constriction is clearly seen in the first upper and lower frames in Fig. 3b.

In conclusion, we make some general remarks. First, in obtaining estimates, we implied that the MHD approximation is applicable. It is well known [9] that the applicability conditions of the hydrodynamic approximation for both of the plasma components can be written in the form (here, the corona thickness δ and the time τ are chosen as the characteristic space and time scales of variations in the plasma parameters)

$$\delta \gg l_i, l_e, \quad \tau \gg \tau_e, \tau_i,$$

where $l_i = 2.97 \times 10^{12} T_i^2 / Z^4 N(\Lambda/10)$ and $l_e = 2.06 \times 10^{12} T_e^2 / Z^2 N(\Lambda/10)$ are the mean free paths (in cm) and $\tau_i = 2.12 \times 10^6 A^{1/2} T_i^{3/2} / Z^4 N(\Lambda/10)$ and $\tau_e = 3.5 \times 10^4 T_e^{3/2} / Z^2 N(\Lambda/10)$ are the mean free times (in s) for

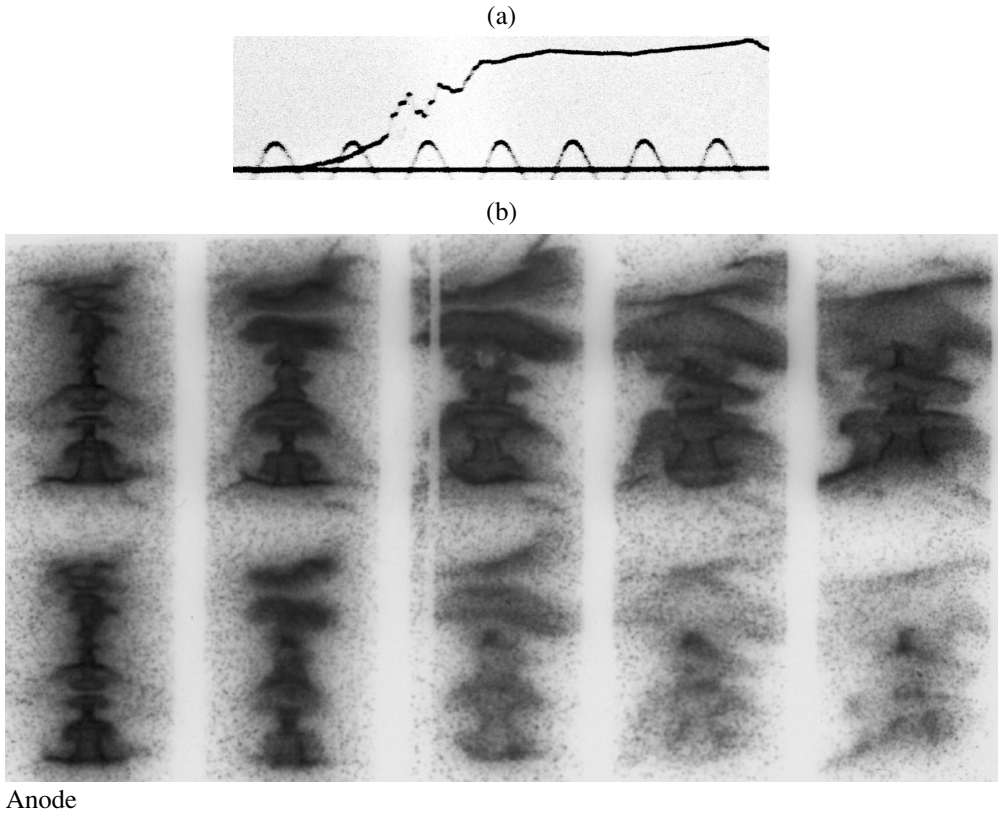

Fig. 3. Electric explosion of a 8-mm-long 20-μm-diameter aluminum wire. (a) The current oscillogram: the maximum current is 150 kA, the current rise time is 80 ns, and the period of the reference signal is 40 ns. (b) Subsequent photodetector images: the diameter of the aperture of the SKhR4 pin-hole chamber is 30 μm for the upper row and 10 μm for the lower row, the frame exposure time is 7 ns, and the interval between frames is 10 ns; the first frame starts 80 ns after the beginning of the load current pulse.

ions and electrons, respectively [6]. It is seen that, for the corona plasma whose parameters are presented in Table 1, at $\Lambda = 10$ and equal ion T_i and electron T_e temperatures ($T_i = T_e = T$), we have $l_e \sim 10^{-5}$–10^{-6} cm, $l_i \sim 10^{-6}$–10^{-7} cm, $\tau_e \sim 10^{-14}$–10^{-15} s, and $\tau_i \sim 10^{-13}$–10^{-14} s, so that the hydrodynamic approximation is applicable in the plasma corona. In addition, the displacement current in the plasma corona can be neglected compared to the conduction current if the characteristic time τ of the change in the plasma parameters is sufficiently large: $\tau \gg \tau_{ei} = 10^{-9}$–$10^{-10}$ s, where $\tau_{ei} = 3.15 \times 10^7 AT^{3/2}/NZ^2$ is the characteristic electron mean free time in terms of electron–ion collisions [10]. According to [9], the nonhydrodynamic stage of the evolution of the Z-pinch constriction is realized only in the second implosion of the plasma column; however, the study of this problem is beyond the scope of this paper.

Second, we used the important assumptions that the plasma consists of two components and that the space charge can occur in the plasma, which finally results in the generation of jets. Obviously, this effect is absent in the one-fluid two-temperature MHD approximation, assuming that the plasma is quasineutral [9]. For the same reason, this effect is also absent in the model in which only the electron plasma component is taken into account [9]. Thus, the above effects can occur only in a two-fluid MHD model incorporating Poisson's equation for the electric potential produced by the space charge.

Finally, it should be noted that the adopted model of a constriction that converges at a constant velocity meets difficulties associated with the nonphysical initial conditions, e.g., the instant onset of the plasma velocity and vortex electric field at the edge of the constriction (at $b = R$) and the presence of ions with $V \neq 0$ at $b = R$. Although these assumptions are not crucial, they do not allow us to accurately investigate the problems related to constriction stability. Moreover, a scenario of the physical processes occurring even in the presence of only one constriction is very idealized. Nevertheless, the model of the generation of the vortex electric field allows a satisfactory qualitative interpretation of the experimental data.

REFERENCES

1. K. N. Koshelev, Yu. V. Sidel'nikov, V. V. Vikhrev, and V. V. Ivanov, in *Spectroscopy of Multicharged Ions in a Hot Plasma*, Ed. by U. N. Safronova (Nauka, Moscow, 1991), p. 163.

2. V. V. Yan'kov, Fiz. Plazmy **17**, 521 (1991) [Sov. J. Plasma Phys. **17**, 305 (1991)].
3. S. K. Zhdanov and B. A. Trubnikov, Fiz. Plazmy **12**, 851 (1986) [Sov. J. Plasma Phys. **12**, 490 (1986)].
4. G. S. Sarkisov, B. Etlisher, V. V. Yan'kov, *et al.*, Zh. Éksp. Teor. Fiz. **108**, 1355 (1995) [Phys. JETP **81**, 743 (1995)].
5. V. I. Afonin, Fiz. Plazmy **25**, 678 (1999) [Plasma Phys. Rep. **25**, 620 (1999)].
6. V. N. Derzhiev, A. G. Zhidkov, and S. I. Yakovlenko, *Ion Radiation in a Nonequilibrium Dense Plasma* (Énergoatomizdat, Moscow, 1986).
7. V. E. Golant, A. P. Zhilinskii, and I. E. Sakharov, *Fundamentals of Plasma Physics* (Atomizdat, Moscow, 1977; Wiley, New York, 1980).
8. V. I. Afonin, V. M. Murugov, S. V. Ponomarev, and A. V. Senik, Fiz. Plazmy **23**, 1008 (1997) [Plasma Phys. Rep. **23**, 930 (1997)].
9. V. S. Imshennik and N. A. Bobrova, *Dynamics of Collisional Plasmas* (Énergoatomizdat, Moscow, 1997).
10. Ya. B. Zel'dovich and Yu. P. Raizer, *Elements of Gas Dynamics and the Classical Theory of Shock Waves* (Nauka, Moscow, 1966; Academic, New York, 1968).

Translated by A. D. Smirnova[†]

[†] Now deceased.

Plasma Physics Reports, Vol. 26, No. 4, 2000, pp. 298–302. Translated from Fizika Plazmy, Vol. 26, No. 4, 2000, pp. 324–328.

PLASMA DYNAMICS

Cumulative Gas-Compression Configuration Intermediate between Spherical and Cylindrical

V. I. Tarzhanov

Russian Federal Nuclear Center, All-Russia Research Institute of Technical Physics, Snezhinsk, Chelyabinsk oblast, 454070 Russia

Received June 2, 1999

Abstract—A two-dimensional axisymmetric configuration of a cumulative gas compression that can be applied to inertial microfusion is proposed. Both adiabatic gas compression and compression with energy losses are considered. The limiting gas temperature that can be attained during shock stopping of the cavity wall is estimated. It is pointed out that the energy losses during the compression cannot be ignored when considering the cumulative effects occurring in microscopic regions of a gas target of any configuration under the action of a loading pulse of any shape. © *2000 MAIK "Nauka/Interperiodica".*

1. INTRODUCTION

The spherical and cylindrical configurations of a cumulative gas compression are well known [1]. A plasma generator with the phase acceleration of a gas in a cusp configuration is described in [2]. Conical and biconical configurations were studied in [3]. In this paper, a two-dimensional axisymmetric configuration of cumulative gas compression is suggested. This configuration can be applied to inertial microfusion.

2. CONFIGURATION OF A GAS COMPRESSION

The gas cavity (Fig. 1) is spindle-shaped. The width (maximum diameter) of the cavity is $2h_0$, and the generatrix radius is R. Each point of the cavity wall moves toward the symmetry axis with the velocity W. The cumulative effect occurs due to the collapse of the cavity wall on the axis accompanied by a decrease in the angles β in the vertexes of the cavity as the wall approaches the axis.

The phase velocity v_x of the cavity vertexes can be written in the form

$$v_x = W(R-h)/\sqrt{h(2R-h)},$$

where h is the running value of the half-width of the cavity. For $h \ll R$, we have $v_x = W\sqrt{R/2h}$. It is seen that $v_x \longrightarrow \infty$ as $h \longrightarrow 0$.

The cavity volume Ω is

$$\Omega = 2\pi\int_0^A r^2 dx = 2\pi R^3\sqrt{\left(2-\frac{h}{R}\right)\frac{h}{R}}\left\{\frac{2}{3}+\frac{1}{3}\left(1-\frac{h}{R}\right)^2\right.$$

$$\left.-\left(1-\frac{h}{R}\right)\left(\frac{h}{R}\left(2-\frac{h}{R}\right)\right)^{-1/2}\arcsin\sqrt{\frac{h}{R}\left(2-\frac{h}{R}\right)}\right\}.$$

For $h \ll R$, we obtain

$$\Omega = \frac{16}{15}\pi h^3\sqrt{\frac{2R}{h}}. \quad (1)$$

The area of the cavity surface is

$$S = 4\pi R\int_0^A\left(1-\frac{R-h}{\sqrt{R^2-x^2}}\right)dx$$

$$= 4\pi R^2\left[\sqrt{\frac{h}{R}\left(2-\frac{h}{R}\right)}-\left(1-\frac{h}{R}\right)\arcsin\sqrt{\frac{h}{R}\left(2-\frac{h}{R}\right)}\right].$$

For $h \ll R$, we obtain

$$S = \frac{8\sqrt{2}}{3}\pi R^2\left(\frac{h}{R}\right)^{3/2}. \quad (2)$$

3. ADIABATIC GAS COMPRESSION

For an ideal gas, the equation of state is $p = \rho RT$ and the isentropic equation is $p = C\rho^\gamma$. Thus, the pressure p, temperature T, and mass density ρ during adiabatic compression in the proposed cavity are $p = p_0(h_0/h)^{2.5\gamma}$, $T = T_0(h_0/h)2.5^{(\gamma-1)}$, and $\rho = \rho_0(h_0/h)^{2.5}$. Here, the zero

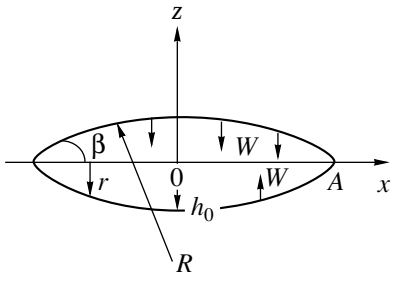

Fig. 1. Configuration of the cavity.

1063-780X/00/2604-0298$20.00 © 2000 MAIK "Nauka/Interperiodica"

index stands for the initial values of the parameters and γ is the Poisson index. In dimensionless form, these expressions take the form $\bar{p} = \bar{h}^{-2.5\gamma}$, $\bar{T} = \bar{h}^{-2.5(\gamma-1)}$, and $\bar{\rho} = \bar{h}^{-2.5}$.

The factor 2.5 in the exponent is intermediate between analogous factors in the spherical and cylindrical configurations (3 and 2, respectively). This indicates that, as the characteristic size of the cavity decreases, the gas parameters increase at an intermediate rate.

At high rates of energy deposition, the process of gas compression begins with the appearance of a shock wave when the cavity wall starts to move [4]. Hence, the model of adiabatic compression should be used starting from a somewhat later instant, e.g., after the first passage of the shock wave through the gas. The parameters characterizing the state of the gas at this instant can be adopted as initial values for the adiabatic compression.

The asymptotic solutions for converging shock waves were constructed in [5]. The values of the exponent α in the radial dependence of the pressure variations at the wave front $p \sim r^{-\alpha}$ for the sphere and cylinder were found to be 0.90 and 0.45, respectively. For the configuration under study, we have $\alpha = 0.675$, which is the average between these numbers.

In view of (1) and (2), the mean increase in the gas temperature in the cavity due to the wave convergence is written in the form

$$\frac{T}{T_f} = \frac{1}{\Omega_0}\int_0^{h_0}\left(\frac{h_0}{h}\right)^{0.675} S dh = 1.37$$

(for the sphere and cylinder, this quantity is equal to 1.43 and 1.3, respectively). Here, T_f is the temperature behind the front of the shock wave entering the cavity.

Thus, for $W = 13$ km/s (which is typical of explosion facilities [6]), $T_0 = 293$ K, $\gamma = 5/3$, and $\rho_0 = 3 \times 10^{-4}$ and 3×10^{-2} g/cm^3, the mean temperature in deuterium at the instant when the shock wave arrives at the cavity axis is 1.7 eV. An increase in the temperature behind the reflected wave can be estimated by the formulas for a plane wave [7], which yield the value 3 eV. The threefold increase in W (to values typical of ICF) results in an increase in the gas temperature by one order of magnitude after the passage of the shock wave.

Figure 2 shows the deuterium temperature during adiabatic compression as a function of the running cavity parameter h for $h_0 = 0.1$ cm and $T_0 = 3$ eV. It is seen that a temperature of 0.3 keV (at which easily detected neutron fluxes are produced) can be achieved for $h \sim 3 \times 10^{-3}$ cm and an ignition temperature of 10 keV [8] can be reached for $h \sim 8 \times 10^{-4}$ cm.

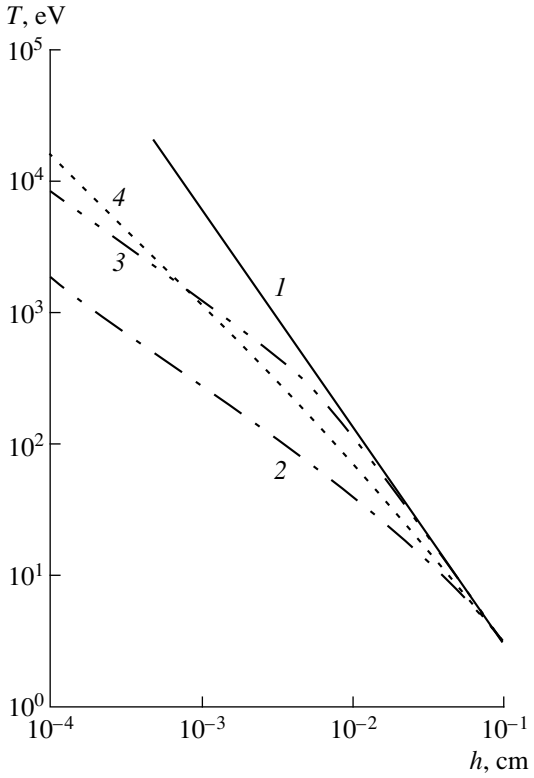

Fig. 2. Deuterium temperature during compression as a function of the running cavity parameter h for $W = 13$ km/s and $T_0 = 3$ eV: (*1*) adiabatic compression ($\rho_0 = 0.0003$ and 0.03 g/cm^3), (*2*, *3*) compression with energy losses ($\rho_0 = 0.0003$ and 0.03 g/cm^3, respectively), and (*4*) compression with allowance for energy losses and acceleration of the cavity wall during its convergence toward the axis ($\rho_0 = 0.0003$ g/cm^3).

4. SHOCKLESS COMPRESSION WITH ENERGY LOSSES

The energy losses during gas compression can be estimated using the approaches developed in [9–13].

If the cavity volume Ω changes by $d\Omega$ in a time dt, the change in the internal gas energy dE, which is written in the form

$$dE = \frac{3}{2} nk\Omega dT,$$

is a sum of two components: dE_1 and dE_2. The dE_1 component is the increase in the energy due to compression,

$$dE_1 = -pd\Omega = -nkTd\Omega,$$

and dE_2 is the radiative energy loss from the area S of the cavity surface,

$$dE_2 = -S\sigma T^4 dt.$$

Table 1. Comparison of the characteristic times of plasma cooling due to radiative loss and heat conduction

T, eV	10		100		300	
L, cm	0.1	0.01	0.1	0.01	0.1	0.01
τ_{rad}, s	7.6×10^{-7}	7.6×10^{-8}	7.6×10^{-10}	7.6×10^{-11}	2.8×10^{-11}	2.8×10^{-12}
τ_c, s	2×10^{-3}	2×10^{-5}	6×10^{-6}	6×10^{-8}	4×10^{-7}	4×10^{-9}

Taking into account the change in the particle density $n(t) = n_0\Omega_0/\Omega(t) = n_0(h_0/h)^{5/2}$ and that, by definition, $W = -dh/dt$, we obtain the expression

$$\frac{dT}{dh} = \frac{5}{3}\left[-\frac{T}{h} + \frac{\sigma T^4 h^{3/2}}{W(h)kn_0h_0^{5/2}}\right]. \quad (3)$$

The solution to equation (3) expressed through the dimensionless quantities $\bar{T} = T/T_0$ and $\bar{h} = h/h_0$ can be written as

$$\bar{T} = \bar{h}^{-5/3}\left\{1 + \frac{30}{31}\frac{\sigma T_0^3}{kn_0W}[\bar{h}^{-5/2} - 1]\right\}^{-\frac{1}{3}}. \quad (4)$$

For $h \ll h_0$, the solution to (3) takes the form

$$T \approx \left(\frac{k}{\sigma}\right)^{1/3} n_0^{1/3} W^{1/3}\left(\frac{h_0}{h}\right)^{5/6}. \quad (5)$$

Note that we assumed the Stefan–Boltzmann cooling to be the main energy-loss mechanism. The reason for this assumption is seen, first, from a comparison of the characteristic plasma-cooling times corresponding to this mechanism and the cooling due to thermal conduction in the cavities of lengths $L = 0.1$ and 0.01 cm. These times,

$$\tau_{rad} = \frac{nkL}{2\sigma T^3}, \quad \tau_c = 6.3\times10^{-21}\frac{nL^2}{T^{5/2}},$$

where T is in eV, are presented in Table 1 for $n = 10^{22}$ cm^{-3} and three temperature values. Second, the Stefan–Boltzmann cooling becomes stronger than the cooling due to emission from the gas volume if the deuterium contains high-Z impurities [4] that are inevitably present in experiments. Note that, in a pure deuterium plasma, the mean free path l_{eff} for the Wien wavelength $\lambda_{max} = 2.6\times10^{-5}/T$ of free-free radiation is equal to

$$l_{eff} = 4.5\times10^{38}\frac{T^{7/2}}{Z^2n_in_e}$$

(here, T is in eV and λ and l are in cm) and exceeds the cavity size of interest (0.1–0.01 cm) (see Table 2).

Table 2. Mean free paths of free–free radiation (in cm)

n, cm^{-3} \ T, eV	10	100	300
10^{20}	140	4.5×10^5	2.1×10^7
10^{22}	0.014	45	2.1×10^3

Returning to formulas (4) and (5), we see that, for $h \longrightarrow 0$, we have $T \longrightarrow \infty$ independently of the values of n_0 and W. The $T(h)$ dependences calculated according to (4) for two values of the initial gas mass density, $T_0 = 3$ eV, and $W(h) = \text{const} = 13$ km/s are shown in Fig. 2. It is seen that the deviation of these curves from the adiabatic-compression curve begins from temperatures of ~10 and 100 eV for $\rho_0 = 0.0003$ and 0.03 g/cm^3, respectively.

5. THE EFFECT OF THE CONVERGENCE OF THE CAVITY WALL TOWARD THE AXIS

The convergence of the cavity wall toward the axis is taken into account in (3) via the function $W(h)$.

The convergence law for an incompressible inviscid cylindrical shell is [1]

$$W^2(r_1) = \text{const}\, r_1^{-2}\ln^{-1}\left(\frac{r_2}{r_1}\right), \quad (6)$$

where r_2 and r_1 are the outer and inner shell radii. For $r_1 \longrightarrow 0$, we have $W = \text{const}/r_1$.

Figure 2 presents an example of calculations by (6) for a copper wall for $\rho_0 = 0.0003$ g/cm^3, $W_0 = 13$ km/s, $r_2/r_1 = 2$, $T_0 = 1$ eV, and $h_0 = 0.1$ cm. It is seen that the accelerated motion of the cavity wall appreciably decreases the role of energy losses.

It was shown in [1] that the role that the viscosity of the cavity wall material plays in the reduction of a cumulative effect can be decreased to a negligible level by choosing a sufficiently thick shell and increasing its energy. From a comparison of the laws of motion of the walls of spherical bubbles in incompressible and compressible liquids ($W \sim 1/r^{1.5}$ and $\sim 1/r^{0.411}$, respectively), it follows that the compressibility of the wall material can substantially decrease the wall acceleration (down to $W(h) = \text{const}$). Hence, the actual curve $T(h)$ lies between curves *2* and *4* (Fig. 2) corresponding to $W(h) = \text{const}$ and W given by (6).

6. ESTIMATE OF THE LIMITING GAS TEMPERATURE DURING THE SHOCK DECELERATION OF THE CAVITY WALL

The limiting gas temperature in the cavity is achieved when the cavity wall is decelerated by the gas pressure. In some compression regimes $h(t)$, the model of shock deceleration of the wall is realized [1, 10] when the wall is stopped by the shock wave propagating away from the center of the cavity. In this case, the mass velocity both in the gas and in the wall material is zero and the pressure in the gas is equal to that in the wall material behind the wave front and is determined by the velocity that the wall had before it stopped.

Assuming that the shock adiabat of the wall material has the form

$$p_* = \rho_*\left(c_* + \chi_*\frac{W}{2}\right)\frac{W}{2},$$

where p_* and ρ_* are the pressure and mass density of the wall material and c_* and χ_* are the parameters of its D, u-relation, and taking into account (4) and the equation of state $p = nkT$, we obtain the following set of equations for determining $T_{\max}$ and $h_{\min}$:

$$T_{\max} = T_0\rho_* p_0^{-1}\left(\frac{h_0}{h_{\min}}\right)^{-5/2}\left(c_* + \chi\frac{W}{2}\right)\frac{W}{2},$$

$$T_{\max} = T_0\left(\frac{h_0}{h_{\min}}\right)^{5/3}\left\{1 + \frac{30}{31}\frac{\sigma T_0^3}{kn_0 W}\left[\left(\frac{h_0}{h_{\min}}\right)^{5/2} - 1\right]\right\}^{-1/3}.$$

For $h \ll h_0$, the quantity $T_{\max}$ can be written in the explicit form

$$T_{\max} = \left(\frac{\rho_*}{4\sigma}\right)^{1/4}(2c_* + \chi W)^{1/4}W^{1/2}. \qquad (7)$$

The values of $T_{\max}$ calculated by (7) for an iron cavity wall (with the D, u-relation taken from [14]) are presented in Table 3.

These estimates demonstrate that, as in the case of a spherical configuration, a special law of motion of the cavity wall should be chosen to provide cool gas compression [1, 4, 8, 11, 15].

7. THE ROLE OF THE NONUNIFORMITY OF GAS HEATING

If the gas energy losses during the compression are ignored, then we can expect that, during the first passage of the shock wave in the cavity, the temperature will be higher near the axis and especially high near the cavity center because of the convergence of the shock wave and its reflection from the axis. Qualitatively, the temperature distribution will remain the same in the main (quasi-isentropic) phase of the compression by a sequence of shock waves during the second, third, and subsequent loading pulses.

Table 3. Limiting gas temperature

W, km/s	5	10	25	85	100
$T_{\max}$, eV	30	46	84	200	225

However, the picture changes radically if we take into account the radiative loss during gas compression. Table 1 indicates that, in the axial region, whose volume is one order of magnitude smaller than the entire cavity volume and has a ten times higher temperature, the Stefan–Boltzmann cooling rate is four orders of magnitude higher. This means that the radiative heat conduction equalizes the temperature throughout the cavity (the higher the temperature, the more rapidly the equalization proceeds). Thus, we can assume that the gas temperature and, consequently, the other thermodynamic parameters in the cavity are uniform. The reason for this is that the speed of light is much higher than the substance velocity [9]. Hence, the energy losses during the compression cannot be ignored when considering the cumulative effects occurring in the microscopic regions of the gas target of any configuration under the action of loading pulses of any shape.

8. POTENTIAL ADVANTAGES OF THE CONFIGURATION

In conclusion, we list the following potential advantages of the configuration proposed.

(i) The shape of the cavity makes it possible to use a simpler system for focusing laser radiation in ICF devices.

(ii) The cavity can be open in its vertexes up to the start of the wall; during this time, the cavity is accessible for gas heating, magnetization, increasing the pressure, etc.

(iii) Instabilities are more efficiently suppressed in the configuration proposed.

REFERENCES

1. E. I. Zababakhin and I. E. Zababakhin, *Unlimited Cumulative Phenomena* (Nauka, Moscow, 1988).
2. A. E. Voĭtenko, Dokl. Akad. Nauk **158**, 1278 (1964).
3. S. Kaliski, J. Tech. Phys. (Warsaw) **19** (4) (1978).
4. K. A. Brueckner, in *Proceedings of 4th European Conference on Controlled Fusion and Plasma Physics, 1973*, Vol. 2, p. 259.
5. Yu. S. Vakhrameev, Fiz. Plazmy **16**, 1036 (1990) [Sov. J. Plasma Phys. **16**, 602 (1990)].
6. S. Kaliski, J. Tech. Phys. (Warsaw) **19** (24), 143 (1978).
7. *Physics of Explosions*, Ed. by K. P. Stanyukovich (Nauka, Moscow, 1975).

8. V. A. Shcherbakov, Vopr. At. Nauki Tekh., Ser.: Teor. Prikl. Fiz. **1**, 7 (1991).
9. Ya. B. Zel'dovich and Yu. P. Raizer, *Elements of Gas Dynamics and the Classical Theory of Shock Waves* (Nauka, Moscow, 1966; Academic, New York, 1968).
10. E. I. Zababakhin and V. A. Simonenko, Prikl. Mat. Mekh. **42**, 573 (1978).
11. H. Alstrom and L. Steinhauer, in *Proceedings of 7th International Conference on Quantum Electronics, Montreal, 1972*.
12. V. V. Babikov and V. I. Kogan, in *Plasma Physics and Thermonuclear Research*, Ed. by M. A. Leontovich (USSR Academy of Sciences, Moscow, 1958; Pergamon, Oxford, 1959).
13. A. E. Voĭtenko, Dissertation (Novosibirsk, 1972).
14. L. V. Al'tshuler, A. A. Bakanova, and R. F. Trunin, Zh. Éksp. Teor. Fiz. **42** (1962).
15. J. Nuckolls, L. Wood, A. Thiessen, and G. Zimmerman, in *Proceedings of 7th International Conference on Quantum Electronics, Montreal, 1972*.

Translated by N. F. Larionova

Plasma Physics Reports, Vol. 26, No. 4, 2000, pp. 303–307. Translated from Fizika Plazmy, Vol. 26, No. 4, 2000, pp. 329–333.

PLASMA OSCILLATIONS AND WAVES

Emission Spectra of a Cherenkov Plasma Relativistic Maser

P. S. Strelkov and D. K. Ul'yanov

Institute of General Physics, Russian Academy of Sciences, ul. Vavilova 38, Moscow, 117942 Russia

Received June 24, 1999

Abstract—The spectra of a plasma relativistic maser are measured. It is shown that the microwave frequency can be varied from 4 to 28 GHz by varying the plasma density from 4×10^{12} to 7×10^{13} cm^{-3} at a power of 30–50 MW. The relative width of the emission spectrum is within 50–80% for low plasma densities and 15–30% for high densities. Experimental results are compared with calculations. © *2000 MAIK "Nauka/Interperiodica".*

A Cherenkov plasma relativistic maser (PRM) is based on the Cherenkov mechanism for the excitation of a slow eigenmode of a plasma waveguide by a high-current relativistic electron beam (REB). The phase velocity of the excited wave is approximately equal to the electron velocity, and the frequency range of the generated microwaves is determined by the plasma density and the diameter of a metal waveguide surrounding the plasma.

The first experimental study of a PRM [1] showed that, as the plasma density increases eightfold, the microwave emission frequency nearly doubles. In [2], attempts were made to measure the shape of the PRM spectrum; finally, in [3], absolute measurements of the PRM spectrum (in units of MW/GHz) were carried out with the help of a specially designed calorimetric spectrometer. By this time, both the linear and nonlinear theories of the Cherenkov PRM were well developed [4]. The problem of an amplifier was solved in the following way. A noisy signal in a wide frequency band was taken as an input signal, and the longitudinal profile of the emission power along the plasma waveguide was calculated. The length at which the microwave power reached its maximum was determined. The emission spectrum and the efficiency of the amplifier were studied. The bandwidth of the input signal was chosen as follows: it was increased from one calculation to another until the output emission spectrum became narrower than the input-signal spectrum. In calculations, the plasma, REB, and waveguide diameters coincided with those of the existing experimental devices. The REB and the plasma were assumed to be in a homogeneous, infinitely strong longitudinal external magnetic field; i.e., it was assumed that $\Omega_e \gg \omega_p$, where Ω_e is the electron cyclotron frequency and ω_p is the plasma frequency.

It is known that the onset of a beam–plasma instability in a bounded plasma occurs if the plasma density exceeds the threshold value [5]. In the linear stage of the instability, the amplitude E of the electric field oscillations at the frequency f increases along the beam (along the z-axis) according to the law $E = E_0 e^{\delta k z}$, where E_0 is the electric field amplitude at the amplifier input and δk is the spatial growth rate. Figure 1 shows the calculated frequency dependence of the spatial growth rate δk for different values of the plasma density.[1] It is seen that, according to linear theory, the mean emission frequency increases with increasing the plasma density; the frequency band in which the amplification occurs can be very broad. In contrast, in the nonlinear stage of amplification, the emission spectrum is markedly narrower. In Fig. 1, the spectrum width is represented by line segments *b–f* showing the frequency ranges in which the spectral density of emission power dP/df exceeds a level of 0.3 of its maximum value.

A comparison of the experimental spectra of a PRM with the calculated spectrum of a microwave amplifier showed that they differed markedly [3]. According to calculations, the amplifier spectrum had one maximum; however, in the experiment with an oscillator, two maximums were observed. One of these maxima was observed at low frequencies. The mean frequency of this spectral component was lower than the calculated value of the mean amplifier frequency. The high-frequency component of the oscillator emission was observed near the relativistic electron cyclotron frequency Ω_e/γ, where γ is the relativistic factor. The energies of these two spectral components differed insignificantly (by no more than a factor of 2). As the plasma density n_p increased from 1.5×10^{13} to 3.8×10^{13} cm^{-3}, the mean frequency of the low-frequency spectral component increased from 5 to 12 GHz, whereas the mean frequency of the high-frequency spectral component remained almost unchanged and was equal to 26–28 GHz ($\Omega_e/2\pi\gamma = 24$ GHz). According to calculations, the mean amplifier frequency should vary from 10 to 22 GHz and the 26-GHz component should be absent for $n_p = 1.5 \times 10^{13}$ cm^{-3}. There was a significant discrepancy in the spectral width Δf; e.g., the calculation

[1] Figure 1 and the calculated curve in Fig. 5 were presented by the authors of [4].

1063-780X/00/2604-0303$20.00 © 2000 MAIK "Nauka/Interperiodica"

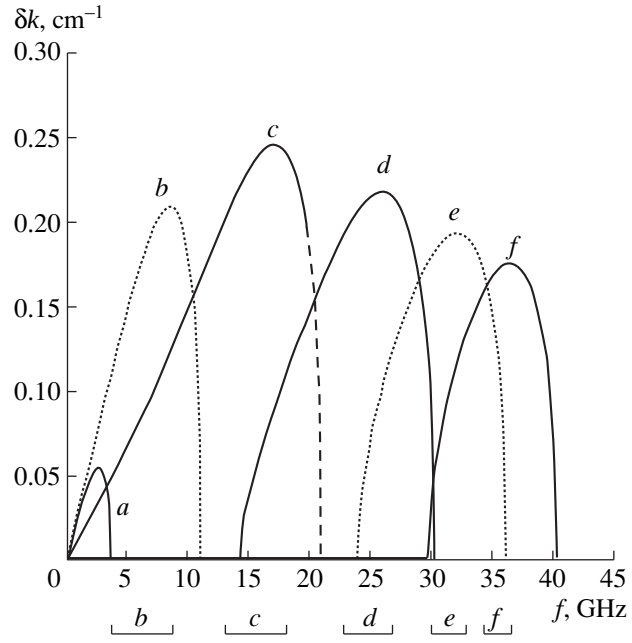

Fig. 1. Dependence of the spatial growth rate δk on the frequency f for plasma densities of (*a*) 0.3, (*b*) 0.8, (*c*) 2.3, (*d*) 4.4, (*e*) 6.0, and (*f*) 7.0×10^{13} cm^{-3}. The curves represent the results of calculation by linear theory, and the horizontal line segments on bottom show the results of calculations of the spectrum width by nonlinear theory.

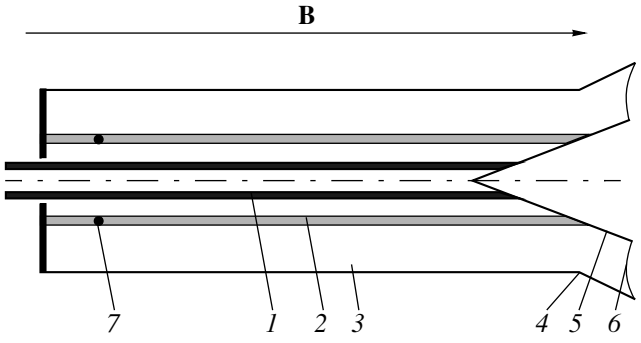

Fig. 2. Schematic of the PRM: (*1*) REB, (*2*) plasma, (*3*) metal waveguide, (*4*) coaxial conical emitting horn, (*5*) collector, (*6*) dielectric window, and (*7*) hot ring cathode of the plasma source.

yielded $\Delta f/f \approx 0.3$, whereas the experimental value was $\Delta f/f \sim 1$.

As was mentioned above, the amplifier was calculated assuming the external magnetic field to be infinitely strong. In the experiment, we had $\Omega_e = (1.4–0.85)\omega_p$. Nevertheless, the generation of gyrotron emission at the frequency Ω_e/γ by an electron beam in which electrons entering the waveguide only had the longitudinal velocity component was an unexpected result.

All these discrepancies were discussed in [3], in which it was noted that "the main discrepancies—a wide experimental spectrum and the presence of a low-frequency emission simultaneously with a high-frequency emission—require further theoretical and experimental investigations."

In [3], we compared the spectra of the microwave oscillator with the calculated spectra of an amplifier. The subsequent theoretical study was aimed at the development of numerical methods for calculating the microwave oscillator. The beam instability is convective in nature; for this reason, generation can occur in a plasma waveguide of a limited length L if the reflection coefficient κ of the wave reflecting from the end of the plasma waveguide is high enough to satisfy the condition $\kappa e^{\delta kL} > 1$. On the other hand, if $\kappa = 1$ in the generation frequency range, then no emission leaves the microwave oscillator. Therefore, there exists an optimum κ value for which the oscillator emission power is maximum. In the linear stage of the instability, a high-current REB generates a broad frequency spectrum (Fig. 1). If the reflection coefficient κ in the generation frequency range depends substantially on the frequency, then the spectrum of the microwave oscillator can differ markedly from that of the microwave amplifier. In the papers on the plasma microwave oscillator [6, 7], an approximate formula is used to describe the dependence of κ on the frequency and the dimensions of a device. Thus, the development of the numerical model of the microwave oscillator is still far from completion even for $\Omega_e \gg \omega_p$.

This paper is devoted to the experimental study of a PRM in which, as compared to [3], we changed the geometry of the transition of a plasma waveguide to a coaxial emitting horn in order for the coefficient κ to be independent of the frequency. As a result, the measured PRM spectrum became close to the calculated spectrum of the microwave amplifier [4].

Figure 2 shows the schematic of the experiment. The Terek-2 accelerator produces a high-current REB with an electron energy of 500 keV, a beam current of 2 or 3 kA, and a current-pulse duration of 30 ns. An annular electron beam (*1*) with a mean radius of r_b = 6 mm and thickness of Δr_b = 1 mm passes inside a hollow plasma column (*2*) with a mean radius of r_p = 9 mm and thickness of Δr_p = 1 mm. A coaxial plasma waveguide consisting of a hollow plasma and a metal waveguide (*3*) with a radius of R = 18 mm ends in a conical horn with metal outer (*4*) and inner (*5*) cones. Microwaves are generated in the plasma waveguide, enter the metal coaxial horn, and then are output into free space through a dielectric window (*6*).

The REB and the plasma are in a homogeneous longitudinal quasistatic magnetic field (B = 1.3–2.2 T and the current pulse duration is 5.5 ms). As in the previous experiments [3, 8], the plasma is created in a discharge with a hot ring cathode (Fig. 2, position *7*). The plasma source has the following parameters: the cathode volt-

age is 500 V, the discharge current is up to 90 A, the working gas is xenon, and the gas pressure is 4.5×10^{-4} torr. At first, the voltage is applied to the plasma-source cathode and the plasma is created over 30 μs. Then, the REB is injected into the plasma. The discharge current is controlled by changing the cathode temperature, which allows us to change the plasma density from shot to shot.

To solve the main problem of this study (to carry out measurements of the PRM spectrum), we used a calorimetric spectrometer described in [3]. The total energy of the radiation flux from the PRM was measured in eight frequency bands: 5.1–9.3, 9.3–12.1, 12.1–15.3, 15.3–19.5, 19.5–24.1, 24.1–28.9, 28.9–32.4, and 32.4–38.8 GHz. The energy spectrum was measured in units of J/GHz. The measurements of the microwave-pulse shape allowed us to calculate the power spectrum in units of MW/GHz. Typical values of the spectral power density were 2–4 MW/GHz to within a measurement accuracy of ±0.25 MW/GHz.

Figure 3 shows the dependence of the total emission energy on the plasma density for several values of the plasma-waveguide length L = 10, 12.5, 15, and 20 cm. The total REB energy per one pulse is ≈ 30 J (at an electron energy of 500 keV, a current of 2 kA, and pulse duration of 30 ns). Hence, it follows from Fig. 3 that the PRM energy efficiency is ≈3%. The microwave-pulse duration is 20 ns; therefore, the emission power attains ~50 MW and the power efficiency is ≈5%. For L = 20 cm (curve *1*), emission arises when the plasma density exceeds a threshold level of 2.5×10^{12} cm^{-3}. This value is close to the calculated value of the plasma density at which, under our conditions, the spatial growth rate is $\delta k > 0$. Since for low plasma densities the maximum value of the spatial growth rate $\delta k_{\max}$ increases with increasing the plasma density (Fig. 1), a PRM with L = 15 cm operates at a higher plasma density, $n_p = 4 \times 10^{12}$ cm^{-3} (Fig. 3), according to the formula $\kappa e^{\delta kL} > 1$. The fact that the threshold plasma density increases as the plasma-waveguide length further decreases (L = 12.5, 10 cm) cannot be explained by this simple model because the value of $\delta k_{\max}$ for $n_p = 5$–6×10^{13} cm^{-3} (Fig. 1, curves *e*, *f*) is lower than the maximum value, which is attained at $n_p = 2 \times 10^{13}$ cm^{-3} (Fig. 1, curves *c*, *d*).

Figure 4 shows the PRM spectra for the length of the plasma waveguide L = 20 cm and different plasma densities. The total microwave-pulse energy expressed in J is shown in each of the six plots. It is evident that the mean emission frequency increases from 4 to 28 GHz as the plasma density varies from 4×10^{12} to 7×10^{13} cm^{-3}. The accuracy of the measurements of the spectral width is rather low. It follows from the measurements that the spectral width exceeds the width of the spectrometer bands; i.e., $\Delta f > 3$ GHz. This can be inferred from the fact that the microwave frequency is a continuous function of the plasma density and, for any value of the plasma density, the measured spectrum

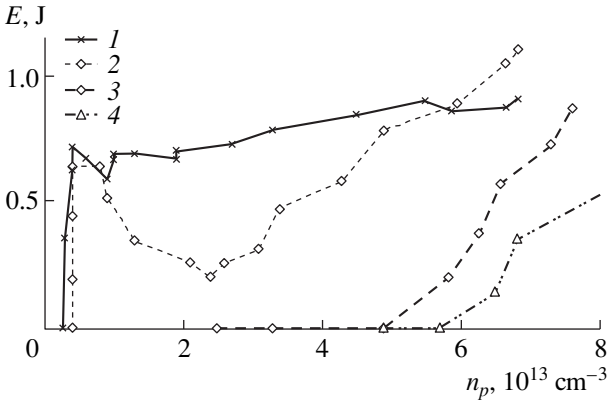

Fig. 3. Microwave-pulse energy as a function of the plasma density for different values of the interaction length: (*1*) 20, (*2*) 15, (*3*) 12.5, and (*4*) 10 cm at B = 2.2 T, r_p = 0.9 cm, r_b = 0.6 cm, and $p = 4.5 \times 10^{-4}$ torr; the working gas is xenon.

never falls into one spectrometer band. The maximum spectral width is determined by the boundaries shown in Fig. 4; i.e., this width comprises two or three spectrometer bands. In Fig. 5, the calculated dependence of the mean emission frequency of the microwave amplifier on the plasma density (assuming $B \longrightarrow \infty$) is compared with the experimental dependences for PRM for two values of the magnetic field: B = 1.3 and 2.2 T. The shaded area is the domain in which the calculation gives $dP/df > 0.3\ (dP/df)_{\max}$. It is seen that, for low plasma densities (low emission frequencies), the experimental results agree with the calculations. For higher plasma densities, there is a discrepancy between the experiment and calculation. For example, the experiment shows that, for $n_p = 6 \times 10^{13}$ cm^{-3} and $\Omega_e = 0.5\omega_p$, the emission frequency f is equal to 21 GHz and, as the electron cyclotron frequency increases to $\Omega_e = 0.9\omega_p$, the emission frequency increases to f = 27 GHz. The calculation for $n_p = 6 \times 10^{13}$ cm^{-3} and $\Omega_e \gg \omega_p$ yields the frequency f = 32 GHz. Hence, the discrepancy between the calculation and experiment can be attributed to the fact that, in the experiment, the condition $\Omega_e \gg \omega_p$ is not satisfied at high plasma densities.

The maximum widths of the experimental spectra are shown in Fig. 5 by vertical line segments. As was mentioned above, the spectral width is measured rather roughly. Nevertheless, we can conclude that, for low plasma densities, the experimental spectral width is approximately equal to the calculated value; for high plasma densities, the experimental spectral width exceeds the calculated values.

The coincidence of the experimental results with the calculated dependence of the emission frequency on the plasma density $f(n_p)$ is the most reliable argument in favor that the generated mode is the azimuthally symmetric lowest radial mode of the slow plasma wave. In our previous papers, we suggested that the generated mode was precisely this mode, but the dependence $f(n_p)$

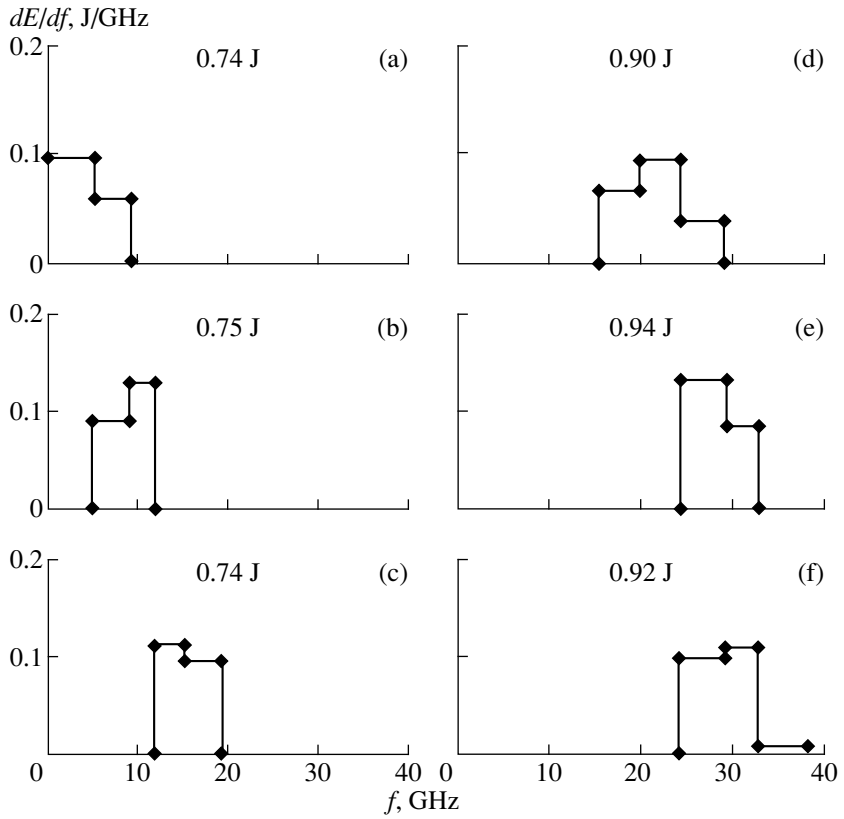

Fig. 4. Spectra of the plasma microwave oscillator for plasma densities of (a) 0.4, (b) 0.8, (c) 2.3, (d) 4.4, (e) 6.0, and (f) 7.0×10^{13} cm^{-3} at $B = 2.2$ T, $L = 20$ cm, $r_p = 0.9$ cm, $r_b = 0.6$ cm, and $p = 4.5 \times 10^{-4}$ torr.

did not confirm this suggestion. Our suggestion was based on the fact that emission was observed in the frequency range $\omega < \omega_p$ and the threshold value of the plasma density (for long plasma waveguides) coincided with the calculated one.

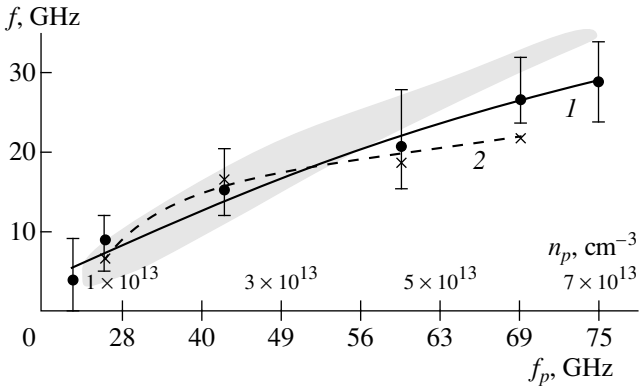

Fig. 5. Mean emission frequency as a function of the plasma frequency $f_p = \omega_p/2\pi$. Experimental curves *1* and *2* correspond to $B = 1.3$ and 2.2 T, respectively. The shaded domain shows the results of calculations by nonlinear theory. The vertical line segments indicate the maximum measured spectral width.

It is seen from Fig. 3 (curve *1*) that the measured emission power remains almost constant as the plasma density varies. This is due to the fact that the maximum value of the spatial growth rate δk remains at nearly the same level for different values of the plasma density (Fig. 1). Furthermore, this means that the coefficient of reflection from the transition of the plasma waveguide to the vacuum coaxial waveguide remains nearly constant when the plasma density and the generation frequency change simultaneously.

As is known, filling a waveguide with a plasma makes it possible to transport currents exceeding the limiting vacuum current [9]. Therefore, it is interesting to examine how the microwave power depends on the current. All of the above results were obtained at a current of 2 kA, whereas the limiting vacuum current was equal to 3.5 kA. The increase in the beam current to 3 kA did not lead to an increase in the microwave power. This agrees with the theoretical prediction [10] that the amplifier efficiency decreases as the beam current approaches the limiting vacuum current.

Thus, it is experimentally shown that, in a Cherenkov PRM, the azimuthally symmetric lowest radial mode of a slow plasma wave can be generated over a wide range of plasma densities. For the first time, a sevenfold frequency change (from 4 to 28 GHz) was

obtained at a power of 30–50 MW by changing only the plasma density. From a practical standpoint, it is important that such a frequency change can be performed during a time of about 30 μs, which is determined by the rate of the plasma density variation.

Further progress in PRM studies requires the development of a numerical model for a plasma microwave oscillator, which will make it possible to increase the PRM efficiency to 15–20%, as is predicted by the calculations of the amplifier. These calculations show that the width of the emission spectrum can be varied by changing the gap between the beam and the hollow plasma. However, to date, we have failed to implement such control of the spectral width at a constant microwave-oscillator power. These two problems form the basis for future PRM studies.

ACKNOWLEDGMENTS

We thank A.A. Rukhadze, M.A. Krasil'nikov, M.V. Kuzelev, and O.T. Loza for fruitful discussions. This work was performed with the Plasma Relativistic Maser device (registration no. 01-04) under the financial support of the Ministry of Science and Technology of the Russian Federation and the Russian Foundation for Basic Research (project no. 97-02-16948 and the grant "Controlled Fusion and Plasma Processes").

REFERENCES

1. M. V. Kuzelev, F. Kh. Mukhametzyanov, M. S. Rabinovich, *et al.*, Zh. Éksp. Teor. Fiz. **83**, 1358 (1982) [Sov. Phys. JETP **56**, 780 (1982)].
2. A. A. Rukhadze, P. S. Strelkov, and A. G. Shkvarunets, Fiz. Plazmy **20**, 686 (1994) [Plasma Phys. Rep. **20**, 617 (1994)].
3. M. V. Kuzelev, O. T. Loza, A. V. Ponomarev, *et al.*, Zh. Éksp. Teor. Fiz. **109**, 2048 (1996) [JETP **82**, 1102 (1996)].
4. M. Biro, M. A. Krasil'nikov, M. V. Kuzelev, and A. A. Rukhadze, Usp. Fiz. Nauk **167**, 1025 (1997) [Phys. Uspekhi **40**, 159 (1997)].
5. L. S. Bogdankevich, M. D. Raizer, A. A. Rukhadze, and P. S. Strelkov, Zh. Éksp. Teor. Fiz. **58**, 1219 (1970) [Sov. Phys. JETP **31**, 655 (1970)].
6. M. A. Krasil'nikov, M. V. Kuzelev, and A. A. Rukhadze, Zh. Éksp. Teor. Fiz. **108**, 521 (1995) [JETP **81**, 280 (1995)].
7. M. Biro, M. A. Krasil'nikov, M. V. Kuzelev, and A. A. Rukhadze, Zh. Éksp. Teor. Fiz. **111**, 1258 (1997) [JETP **84**, 694 (1997)].
8. O. T. Loza, A. V. Ponomarev, P. S. Strelkov, *et al.*, Fiz. Plazmy **23**, 222 (1997) [Plasma Phys. Rep. **23**, 201 (1997)].
9. V. I. Krementsov, P. S. Strelkov, and A. G. Shkvarunets, Fiz. Plazmy **2**, 936 (1976) [Sov. J. Plasma Phys. **2**, 519 (1976)].
10. M. V. Kuzelev, A. A. Rukhadze, and D. S. Fillipychev, Fiz. Plazmy **8**, 537 (1982) [Sov. J. Plasma Phys. **8**, 302 (1982)].

Translated by N. F. Larionova

Plasma Physics Reports, Vol. 26, No. 4, 2000, pp. 308–313. Translated from Fizika Plazmy, Vol. 26, No. 4, 2000, pp. 334–339.

NONLINEAR PHENOMENA

Helical Waves in the Vortex Electron Anisotropic Hydrodynamic Model

V. A. Terekhin*, V. T. Tikhonchuk, and E. V. Uvarov***

**Russian Federal Nuclear Center, All-Russia Research Institute of Experimental Physics, Sarov, Nizhni Novgorod oblast, 607200 Russia*

***Lebedev Institute of Physics, Russian Academy of Sciences, Leninskiĭ pr. 53, Moscow, 117924 Russia*

Received November 25, 1998; in final form, April 2, 1999

Abstract—Solutions to the vortex electron anisotropic hydrodynamic equations are investigated that describe nonlinear helical waves in an anisotropic magnetized plasma. The possibility of constructing such solutions is provided by the symmetry properties of the equations. An optimum family of one-dimensional subgroups of a symmetry group consistent with the equations is constructed that makes it possible to derive other, essentially different solutions. *© 2000 MAIK "Nauka/Interperiodica".*

1. INTRODUCTION

In order to describe the dynamics of electron flows in a plasma with an anisotropic electron energy distribution, Bychenkov *et al.* [1] developed the vortex electron anisotropic hydrodynamic (VEAH) model—a quasi-hydrodynamic model that is based on equations for the moments of the distribution function and describes the dynamic properties of an anisotropic collisionless plasma via the equations for the magnetic field vector **B** and the electron pressure tensor $\hat{P}$. The VEAH model, being much simpler than the kinetic model, provides an efficient tool for describing the phenomena in an anisotropic plasma analytically.

The most detailed study of VEAH equations has been carried out in the one-dimensional approximation in planar geometry, in which case the magnetic field has a single nonzero component and the pressure tensor is characterized by three nonzero elements. Bychenkov *et al.* [2] compared the results obtained from the hydrodynamic and kinetic models by simulating, as an example, the relaxation of the Weibel instability [3] and found that they are in qualitative agreement. Here, we study one-dimensional VEAH equations for a magnetized plasma in the case in which a nonequilibrium magnetic field has two nonzero components and all of the six independent elements of the pressure tensor should be taken into account. Our purpose here is to search for analytic solutions to these equations. We obtain an analytic solution that, on the one hand, can serve to test the algorithms for solving VEAH equations numerically and, on the other hand, describes the possible state of an anisotropic plasma. This solution refers to waves with a helical polarization of the perturbed magnetic field and makes it possible to trace the evolution of these waves in the VEAH model.

2. BASIC EQUATIONS

We assume that the nonequilibrium magnetic field $\mathbf{B} = (0, B_y, B_z)$ and the pressure tensor elements P_{ij} depend only on the x-coordinate and time t. In this case, the VEAH equations for an anisotropic plasma in a uniform magnetic field $\mathbf{B}_0 = (B_0, 0, 0)$ can be written as

$$\frac{\partial}{\partial t}\left(B_y - \frac{\partial^2 B_y}{\partial x^2}\right) = -B_0\frac{\partial^2 B_z}{\partial x^2} + \frac{\partial^2 P_{xz}}{\partial x^2},$$

$$\frac{\partial}{\partial t}\left(B_z - \frac{\partial^2 B_z}{\partial x^2}\right) = B_0\frac{\partial^2 B_y}{\partial x^2} - \frac{\partial^2 P_{xy}}{\partial x^2},$$

$$\frac{\partial P_{xx}}{\partial t} = -2B_y P_{xz} + 2B_z P_{xy},$$

$$\frac{\partial P_{yy}}{\partial t} = -2P_{xy}\left(B_z - \frac{\partial^2 B_z}{\partial x^2}\right) + 2B_0 P_{yz},$$

$$\frac{\partial P_{zz}}{\partial t} = 2P_{xz}\left(B_y - \frac{\partial^2 B_y}{\partial x^2}\right) - 2B_0 P_{yz}, \qquad (1)$$

$$\frac{\partial P_{xy}}{\partial t} = -P_{xx}\left(B_z - \frac{\partial^2 B_z}{\partial x^2}\right) + B_z P_{yy} - B_y P_{yz} + B_0 P_{xz},$$

$$\frac{\partial P_{xy}}{\partial t} = P_{xx}\left(B_y - \frac{\partial^2 B_y}{\partial x^2}\right) - B_y P_{zz} + B_z P_{yz} - B_0 P_{xy},$$

$$\frac{\partial P_{yz}}{\partial t} = P_{xy}\left(B_y - \frac{\partial^2 B_y}{\partial x^2}\right)$$

1063-780X/00/2604-0308$20.00

$$- P_{xz}\left(B_z - \frac{\partial^2 B_z}{\partial x^2}\right) + B_0(P_{zz} - P_{yy}).$$

Equations (1) are written in dimensionless variables: the magnetic field, pressure tensor elements, coordinate, and time are expressed, respectively, in units of $\sqrt{4\pi P_*}$, P_*, c/ω_p, and $c/\omega_p\sqrt{P_*/m_e n_e}$, where ω_p is the plasma frequency, m_e is the electron mass, n_e is the electron density, and P_* is an arbitrary normalizing pressure. Note that, in these variables, the quantity B_0 acquires the meaning of the plasma parameter β—the ratio of the magnetic pressure to the thermal plasma pressure.

Equations (1) have the energy integral

$$\int dx\left[B_y^2 + B_z^2 + \left(\frac{\partial B_y}{\partial x}\right)^2 + \left(\frac{\partial B_z}{\partial x}\right)^2 + P_{xx} + P_{yy} + P_{zz}\right] = \text{const} \tag{2}$$

and a first integral that coincides with the determinant of the pressure tensor:

$$P_{xx}P_{yy}P_{zz} + 2P_{xy}P_{xz}P_{yz} - P_{xy}^2 P_{zz} - P_{xz}^2 P_{yy} - P_{yz}^2 P_{xx} = C(x). \tag{3}$$

The presence of the first integral implies that the product of the diagonal elements of the pressure tensor, $P_1P_2P_3 = C(x)$, is time-independent and, consequently, remains unchanged at each spatial point, thereby limiting the fraction of the electron thermal energy that can be converted into magnetic-field energy.

We consider small perturbations $\propto \exp(i\omega t - ikx)$ of the initial plasma state, which is characterized by the electron pressure tensor

$$P_{ij0} = \begin{pmatrix} P_\parallel & 0 & 0 \\ 0 & P_\perp & 0 \\ 0 & 0 & P_\perp \end{pmatrix}. \tag{4}$$

The spectrum of these perturbations, which are transverse right-polarized waves, can be evaluated from equations (1):

$$\omega(k) = B_0\frac{1+2k^2}{2(1+k^2)} \pm \sqrt{\frac{B_0^2}{4(1+k^2)^2} + k^2P_\parallel - \frac{k^2P_\perp}{1+k^2}}. \tag{5}$$

Relationship (5) describes two oscillation branches: the plus sign corresponds to the stable cyclotron mode and the minus sign refers to the helicons [4]. For $P_\perp > P_\parallel$ and under the condition $B_0 < 2(1 + k^2)\gamma_W(k)$, where $\gamma_W(k) = k\sqrt{P_\perp/(1+k^2) - P_\parallel}$ is the growth rate of the Weibel instability [3], the helicon mode is unstable with the growth rate

$$\gamma_s(k) = \sqrt{\gamma_W^2(k) - \frac{B_0^2}{4(1+k^2)^2}}.$$

Helicons are waves with a special helical polarization. Below, we will treat equations (1) in order to derive nonlinear solutions that possess helical symmetry and make it possible to follow the nonlinear evolution of helical waves in the VEAH model.

3. VEAH SOLUTIONS HAVING HELICAL SYMMETRY

To search for the desired class of solutions, we start by noting that equations (1) possess helical symmetry. This means that, if the functions $\mathbf{B}(x, t)$ and $P_{ij}(x, t)$ are solutions to the basic equations (1), then the functions

$$\mathbf{B}'(x', t) = \mathbf{A}(\theta)\mathbf{B}(x, t), \qquad P'_{ij}(x', t) = A_i^m(\theta)A_j^n(\theta)P_{mn}(x, t) \tag{6}$$

will also satisfy these equations. In (6), the matrix $\mathbf{A}(\theta)$ describes the operation of rotating by an angle of θ about the x-axis,

$$\mathbf{A}(\theta) = \begin{pmatrix} 1 & 0 & 0 \\ 0 & \cos\theta & -\sin\theta \\ 0 & \sin\theta & \cos\theta \end{pmatrix},$$

and the coordinate is transformed as $x = x' + \theta/k$, where the nonzero quantity k specifies the spatial scale of the transformation. We can readily see that transformations (6) do not change the functions of the form

$$\mathbf{B}(x, t) = \tilde{\mathbf{A}}(kx)\mathbf{b}(t), \qquad P_{ij}(x, t) = \tilde{A}_i^m(kx)\tilde{A}_j^n(kx)R_{mn}(t), \tag{7}$$

where $\tilde{\mathbf{A}}(kx)$ is the matrix inverse to $\mathbf{A}(kx) = \mathbf{A}(\theta)|_{\theta = kx}$. Substituting formulas (7) into the basic equations, we obtain the set of ordinary differential equations

$$\begin{aligned} \dot{b}_y &= B_0\frac{k^2}{1+k^2}b_z - \frac{k^2}{1+k^2}R_{xz}, \\ \dot{R}_{xy} &= b_z[S - D - (1+k^2)R_{xx}] - b_yR_{yz} + B_0R_{xz}, \\ \dot{b}_z &= -B_0\frac{k^2}{1+k^2}b_y + \frac{k^2}{1+k^2}R_{xy}, \\ \dot{R}_{xz} &= -b_y[S + D - (1+k^2)R_{xx}] + b_zR_{yz} - B_0R_{xy}, \\ \dot{R}_{xx} &= 2(b_zR_{xy} - b_yR_{xz}), \\ \dot{S} &= (1+k^2)(b_yR_{xz} - b_zR_{xy}), \end{aligned} \tag{8}$$

$$\dot{D} = (1+k^2)(b_y R_{xz} + b_z R_{xy}) - 2B_0 R_{yz},$$

$$\dot{R}_{yz} = (1+k^2)(b_y R_{xy} - b_z R_{xz}) + 2B_0 D,$$

where $S = (R_{yy} + R_{zz})/2 = (P_{yy} + P_{zz})/2$ and $D = (R_{zz} - R_{yy})/2$. In accordance with (4), we will solve these equations with the initial conditions $R_{xy}(0) = R_{xz}(0) = R_{yz}(0) = D(0) = 0$, $R_{xx}(0) = P_\parallel$, and $S(0) = P_\perp$. We also assume that the amplitude of the seed magnetic perturbation is small: $b(0) = \sqrt{b_y^2 + b_z^2}\Big|_{t=0} = \varepsilon$.

From equations (8) with the initial conditions adopted, we can find the integrals that relate the thermal energy of the electrons moving parallel and perpendicular to the *x*-axis to the magnetic field magnitude:

$$R_{xx} = P_\parallel + \frac{1+k^2}{k^2}(b^2 - \varepsilon^2),$$
$$S = P_\perp - \frac{(1+k^2)^2}{2k^2}(b^2 - \varepsilon^2). \tag{9}$$

We can see that, as the magnetic field increases, the transverse pressure of the electrons falls off, while their longitudinal pressure rises. Note that expressions (9) are hydrodynamic analogues of the approximate conservation laws obtained by Davidson and Hammer [5] using a kinetic approach.

We change the variables according to the prescription

$$X = D\cos 2\varphi + R_{yz}\sin 2\varphi - \frac{(1+k^2)^2}{2k^2}b^2$$
$$= P_{z'z'} - P_\perp - \frac{(1+k^2)^2}{2k^2}\varepsilon^2,$$
$$Y = D\sin 2\varphi - R_{yz}\cos 2\varphi = -P_{y'z'},$$
$$b_y = b\sin\varphi, \quad b_z = b\cos\varphi,$$

which corresponds to the transformation to the coordinate system *x*, *y*', *z*' with the *z*'-axis directed along the vector **B** of a nonequilibrium magnetic field at each spatial point. The magnetic field components are related to the variables *b* and φ as

$$B_y(x,t) = b(t)\sin[kx + \varphi(t)],$$
$$B_z(x,t) = b(t)\cos[kx + \varphi(t)],$$

so that the solution under consideration describes nonlinear helical waves whose amplitude depends solely on time. The variable φ is the time-dependent part of the angle through which the vector of a nonequilibrium magnetic field rotates. The quantities *b*, *X*, *Y*, and $\Omega = \dot{\varphi}$ satisfy the ordinary differential equations

$$\ddot{b} = \left[\frac{k^2(B_0^2 + P_\perp)}{1+k^2} - k^2 P_\parallel - 2(1+k^2)\left(b^2 - \frac{3}{4}\varepsilon^2\right)\right.$$
$$\left. - \frac{k^2}{1+k^2}X + \Omega^2 - B_0\frac{1+2k^2}{1+k^2}\Omega\right]b,$$
$$\dot{X} = 2(B_0 - \Omega)Y, \quad \dot{Y} = -B_0\frac{1+k^2}{k^2}b^2 - 2(B_0 - \Omega)X, \tag{10}$$
$$\dot{\Omega} = \frac{k^2}{1+k^2}Y + \left(B_0\frac{1+2k^2}{1+k^2} - 2\Omega\right)\frac{\dot{b}}{b}.$$

Since the variable φ drops out of the equations, its initial value will not affect the evolution of the desired solution. We will solve equations (10) with the initial conditions $b(0) = \varepsilon$, $\dot{b}(0) = 0$, $2X(0) = -\varepsilon^2(1+k^2)^2/k^2$, $Y(0) = 0$, and $\Omega(0) = B_0 k^2(1+k^2)$, which correspond to the assumption that, at the initial instant, the helical magnetic field configuration was created in a plasma by the relevant current system.

We will investigate the solutions to equations (10) by assigning the values from the instability domain to the wave vector *k* and the external magnetic field B_0, because, in the stability region, there are only small oscillations that can be described in terms of linear theory. Specifically, we will treat $B_0 = 0.1$ (the magnetic pressure is much lower than the thermal plasma pressure) and $B_0 = 1$ and set $k = 1$ in both cases so that the growth rate will be close to its maximum value. The solutions to equations (10) for these cases are shown in the figure. In the initial stage, the magnetic field amplitude grows exponentially at a rate close to that predicted by linear theory, the instantaneous frequency Ω also being close to $\mathrm{Re}[\omega(k)]$. The plots of the electron pressure components in the (*x*, *y*', *z*') coordinate system show that the mechanisms for the growth of the magnetic field and electric current $j_{z'} = kb$ in the two cases under analysis are essentially different. For $B_0 = 0.1$, the thermal energy of the electrons moving across a nonequilibrium magnetic field is converted into the energy of the magnetic field and current, in which case, according to (9), a decrease in the $P_{y'y'}$ element is accompanied by an increase in the P_{xx} element because of the electron gyration in a nonequilibrium magnetic field. For $B_0 = 1$, the overall picture of electron flows in the exponential growth stage of the magnetic field is more complicated: the $P_{y'y'}$ and $P_{z'z'}$ elements fall off by approximately equal amounts. We have also found that, in the cases under discussion, the instability saturates in different ways. In the case of a weak external magnetic field, in the saturation stage, two peaks appear in the profile of the magnetic field amplitude and the instantaneous frequency changes sign; i.e., the magnetic field

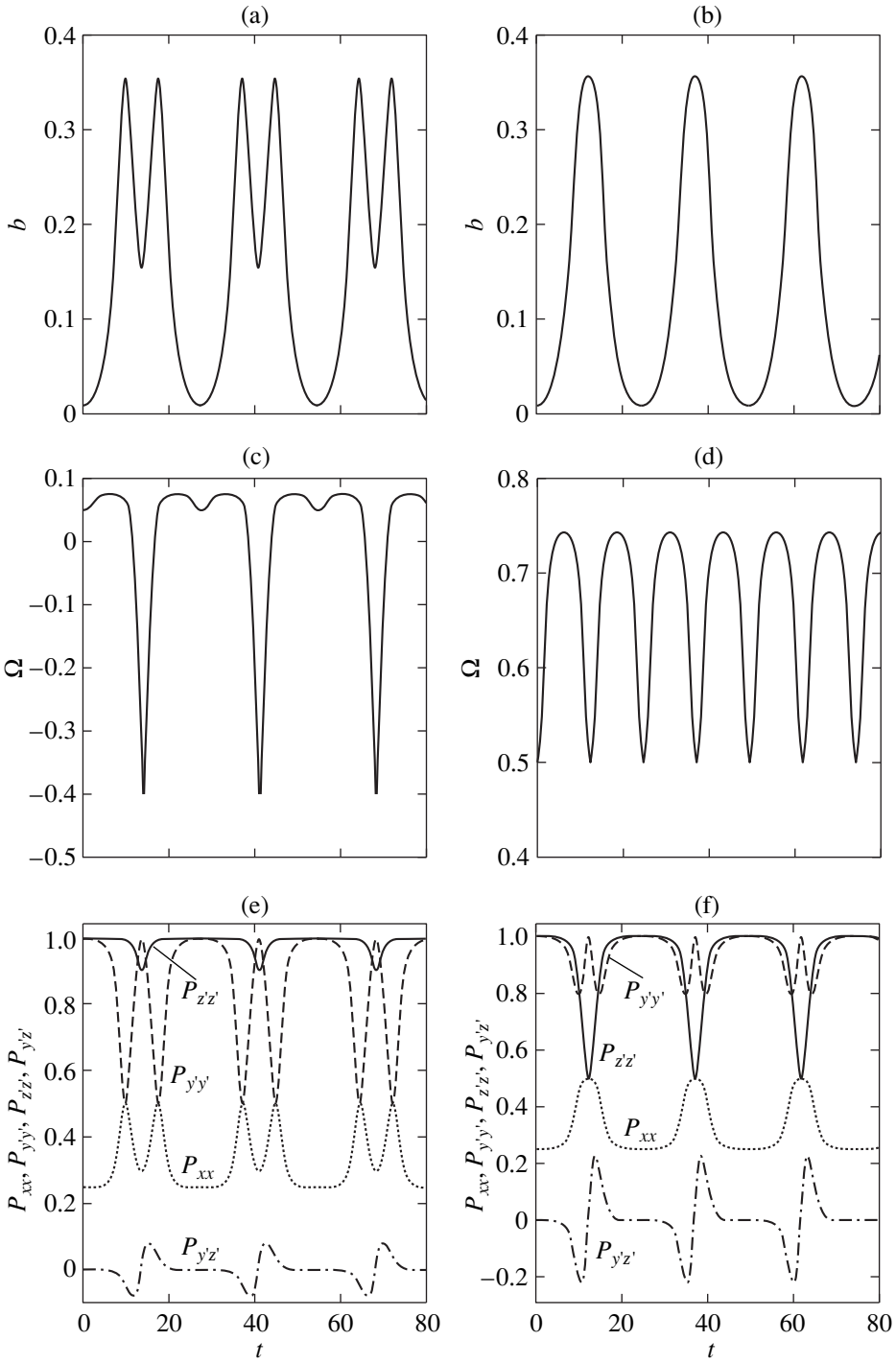

Time evolutions of the magnetic field amplitude b, instantaneous frequency Ω, and electron pressure elements $P_{z'z'}$ (solid curve), $P_{y'y'}$ (dashed curve), P_{xx} (dotted curve), and $P_{y'z'}$ (dashed-and-dotted curve) in the (x, y', z') coordinate system for (a, c, e) $k = 1$ and $B_0 = 0.1$ and (b, d, f) $k = 1$ and $B_0 = 1$.

vector starts to rotate in the opposite direction. On the other hand, in both cases, the magnetic field saturates nearly at the same level $b_{max} \approx 0.35$. The cases have another common feature: in the saturation stage, the electron thermal energy is redistributed in the ($y'z'$) plane so that the $P_{y'y'}$ element falls off and the $P_{z'z'}$ element rises. Then, the magnetic field amplitude and the pressure tensor elements evolve to their initial values and the process repeats over and over again.

In the absence of a constant magnetic field, we must set $\Omega(0) = 0$, in which case we can show that the electron pressure along the nonequilibrium magnetic field

remains constant and is equal to $P_{z'z'} = P_\perp$, while the pressure across the field changes according to the law $P_{y'y'} = P_\perp - (b^2 - \varepsilon^2)(1 + k^2)/k^2$. Equations (10) reduce to the following equation describing the magnetic field evolution in a standing wave [6]:

$$\ddot{b} = \left[\frac{k^2 P_\perp}{1 + k^2} - k^2 P_\parallel + 2(1 + k^2)(\varepsilon^2 - b^2)\right] b. \quad (11)$$

This equation can be solved exactly. The first integral of (11),

$$(\dot{b})^2 = (1 + k^2)(b^2 - \varepsilon^2)\left(\frac{k^2 P_\perp}{(1 + k^2)^2} - \frac{k^2 P_\parallel}{1 + k^2} + \varepsilon^2 - b^2\right),$$

implies that the magnetic field is a bounded function, which varies in the range

$$\varepsilon^2 \le b^2 \le b_{\max}^2 = \varepsilon^2 + \frac{k^2 P_\perp}{(1 + k^2)^2} - \frac{k^2 P_\parallel}{1 + k^2},$$

$$\text{when } \frac{k^2 P_\perp}{1 + k^2} > k^2 P_\parallel$$

(i.e., when the condition corresponding to the onset of the Weibel instability holds); otherwise, it varies in the range $b^2 < \varepsilon^2$. Integrating equation (11) again, we obtain the following relationship, which implicitly contains information about the magnetic field evolution in terms of an elliptic integral:

$$t = \frac{1}{\sqrt{1 + k^2}} \int_\varepsilon^b \frac{dy}{\sqrt{(y^2 - \varepsilon^2)(b_{\max}^2 - y^2)}}. \quad (12)$$

This formula describes two types of solutions to equation (10). The first type refers to the conditions for the onset of the Weibel instability and describes periodic oscillations of the magnetic field during which the magnetic field direction remains unchanged at each spatial point, the oscillation period being

$$T = \frac{2}{\sqrt{1 + k^2}} \int_\varepsilon^{b_{\max}} \frac{dy}{\sqrt{(y^2 - \varepsilon^2)(b_{\max}^2 - y^2)}}.$$

The solutions of the second type describe oscillations about the steady state $b = 0$ during which the magnetic field periodically reverses direction.

4. CONCLUSION

We have obtained a solution to the VEAH equations that describes the nonlinear evolution of waves with helical polarization in an anisotropic magnetized plasma. The characteristic feature of these waves is that the amplitude of their magnetic field varies periodically with time. This corresponds to periodic energy exchange between the thermal electrons and the magnetic field. Such waves evolve from a seed magnetic field perturbation that depends on the coordinate in a heliconlike fashion in a plasma that is isotropic in the plane orthogonal to the axis along which the plasma is inhomogeneous. The solution obtained can be used to test the algorithms for solving VEAH equations numerically. We have also classified one-dimensional subgroups of the symmetry group consistent with the VEAH equations that make it possible to derive some other types of solutions.

ACKNOWLEDGMENTS

This work was supported in part by the International Science and Technology Center, project no. 310.

APPENDIX

Symmetry Group for the VEAH Equations

We can show that the solution obtained above can also be derived as a solution that is invariant under the group of point transformations admitted by the VEAH equations. However, this solution is not the only invariant solution. The method for constructing the complete family of invariant solutions of a given range 1 for the sets of differential equations of the form (1) is well known and can be found in the literature (see, e.g., [7, 8]). Here, we describe only the most important aspects.

Group G of the point transformations consistent with equations (1) is generated by translations along the t- and x-axes,

$$t \mapsto t + t_0, \quad (13)$$

$$x \mapsto x + x_0 \quad (14)$$

and by rotations around the x-axis,

$$\mathbf{B} \mapsto \mathbf{A}(\theta)\mathbf{B}, \quad P_{ij} \mapsto A_i^m(\theta) A_j^n(\theta) P_{mn}, \quad (15)$$

where $\mathbf{A}(\theta)$ is the matrix of rotations and t_0, x_0, and θ are arbitrary real quantities. Also, equations (1) admit a discrete transformation $(t, \mathbf{B}) \mapsto (-t, -\mathbf{B})$, which corresponds to time inversion. The infinitesimal operators of transformations (13)–(15),

$$X_1 = \frac{\partial}{\partial t}, \quad X_2 = \frac{\partial}{\partial x},$$

$$X_3 = B_z \frac{\partial}{\partial B_y} - B_y \frac{\partial}{\partial B_z} + 2P_{yz} \frac{\partial}{\partial P_{yy}} - 2P_{yz} \frac{\partial}{\partial P_{zz}} \quad (16)$$

$$+ P_{xz} \frac{\partial}{\partial P_{xy}} - P_{xy} \frac{\partial}{\partial P_{xz}} + (P_{zz} - P_{yy}) \frac{\partial}{\partial P_{yz}}$$

constitute the basis of the three-dimensional Lie algebra L_3. The most complete (optimum) family of dissimilar one-dimensional subalgebras in basis (16) is com-

posed of these operators and their linear combinations,

$$X_1, X_2, X_3, \quad X_1 + \alpha_1 X_2, \quad X_1 + \alpha_2 X_3,$$
$$X_2 + \alpha_3 X_3, \quad X_1 + \alpha_4 X_2 + \alpha_5 X_3,$$

where α_i are arbitrary nonzero constants. Each of these subgroups, except for the one related to the operator X_3, provides the possibility of reducing equations (1) to a set of ordinary differential equations via the standard procedure. The solution obtained above corresponds to the subgroup related to the operator $X_2 + kX_3$. Unfortunately, in most of the remaining cases, the set of ordinary differential equations is very involved and difficult to analyze.

REFERENCES

1. V. Yu. Bychenkov, V. P. Silin, and V. T. Tikhonchuk, Fiz. Plazmy **15**, 706 (1989) [Sov. J. Plasma Phys. **15**, 407 (1989)].
2. V. Yu. Bychenkov, V. N. Novikov, and V. P. Silin, Fiz. Plazmy **17**, 830 (1991) [Sov. J. Plasma Phys. **17**, 485 (1991)].
3. E. W. Weibel, Phys. Rev. Lett. **2**, 83 (1959).
4. A. F. Alexandrov, L. S. Bogdankevich, and A. A. Rukhadze, *Principles of Plasma Electrodynamics* (Vysshaya Shkola, Moscow, 1978; Springer-Verlag, Berlin, 1984).
5. R. C. Davidson and D. A. Hammer, Phys. Fluids **14**, 1452 (1971).
6. V. A. Terekhin, V. T. Tikhonchuk, and E. V. Uvarov, Phys. Lett. A **254**, 210 (1999).
7. L. V. Ovsyannikov, *Group Analysis of Differential Equations* (Nauka, Moscow, 1968; Academic, New York, 1982).
8. N. Kh. Ibragimov, *Transformation Groups Applied to Mathematical Physics* (Nauka, Moscow, 1983; Riedel, Dordrecht, 1985).

Translated by O. E. Khadin

Plasma Physics Reports, Vol. 26, No. 4, 2000, pp. 314–319. Translated from Fizika Plazmy, Vol. 26, No. 4, 2000, pp. 340–345.

PLASMA INSTABILITIES

Parametric Decay Instability of an Inhomogeneous Plasma in a Frequency-Modulated Pump Wave

V. I. Arkhipenko*, V. N. Budnikov, E. Z. Gusakov**, A. K. Kapanik*, V. A. Pisarev*, and L. V. Simonchik***

**Institute of Molecular and Atomic Physics, National Academy of Sciences of Belarus, pr. F. Skoriny 70, Minsk, 220072 Belarus*

***Ioffe Institute for Physics and Technology, Russian Academy of Sciences, Politekhnicheskaya ul. 26, St. Petersburg, 194021 Russia*

Received April 20, 1999; in final form, July 2, 1999

Abstract—It is found experimentally that the broadening of the pump-wave spectrum affects the parametric instability in an inhomogeneous plasma more weakly than is predicted by theory. The suppression of the absolute instability is only observed for a pump-wave spectrum width of $2\pi\Delta f > 100\gamma$, which is much greater than the instability growth rate γ. © *2000 MAIK "Nauka/Interperiodica".*

1. INTRODUCTION

According to widespread opinion based on the theoretical results obtained for a homogeneous plasma [1, 2], stochastic phase modulation of a pump wave is an efficient method for controlling parametric decay instabilities in a plasma. The theory predicts that the parametric decay instability is suppressed when the width of the pump wave spectrum exceeds the instability growth rate. Such a suppression was observed in experiments [3, 4] in which stochastic and sinusoidal phase modulation of the pump wave was used and the plasma was uniform. Here, we present experimental results from studies of the influence of stochastic and sinusoidal phase modulation of the pump wave on the absolute parametric instability associated with stimulated backward scattering (SBS) in an inhomogeneous plasma. It is shown that the above prediction is not universally valid and, presumably, is only applicable to homogeneous plasmas.

2. SCHEME OF THE EXPERIMENT

Experiments were carried out in the Granit device [5]. The plasma was produced through electron-cyclotron breakdown in a 100-cm-long quartz balloon 2 cm in diameter filled with argon at a pressure of 2×10^{-2} torr. The balloon was in a 3-kG homogeneous magnetic field. The plasma was inhomogeneous both across and along the magnetic field, $n_e = n_e(r, z)$. The maximum electron density in the breakdown region was $n_e = 10^{12}$ cm^{-3}, and the electron temperature in the discharge was $T_e \approx 2$ eV. A pump wave—the Trivelpiece–Gould (TG) mode at a frequency of $f_0 = 2480$ MHz—was excited in the plasma with the help of a waveguide. The scheme of the excitation and propagation of the TG mode is shown in Fig. 1. The central part of the plasma column with the electron density $n_e(r, z) > n_c$ is a plasma waveguide for the TG mode. As the TG mode propagates through this waveguide toward the lower density, its amplitude and wavenumber grow [5]. This growth becomes particularly rapid near the point on the discharge axis where $n_e(0, z) = n_c$ (i.e., $2\pi f_0 = \omega_p = (4\pi n_e e^2/m_e)^{1/2}$). In the vicinity of this point, which is a focuslike attractor of ray trajectories for the TG mode, the oblique Langmuir wave linearly transforms into a "warm" plasma wave.

In this region, where the electric field of the wave is maximum, the onset of the SBS parametric instability, $l_0 \longrightarrow l_0' + s$, can occur. This instability was observed previously in experiments with a monochromatic pump wave [6]. It was found that, at low pumping powers [$P_0 < 20$ mW], the onset of the convective decay insta-

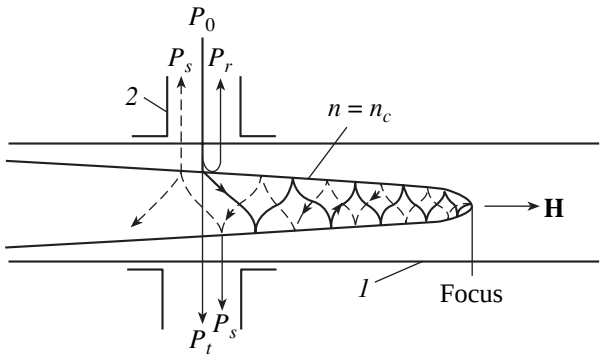

Fig. 1. Schematic diagram of the wave propagation: (*1*) quartz balloon; (*2*) waveguide; and P_0, P_r, P_t, and P_s are the incident, reflected, transmitted, and scattered waves, respectively.

1063-780X/00/2604-0314$20.00 © 2000 MAIK "Nauka/Interperiodica"

bility is accompanied by the generation of a reflected fundamental TG mode l_0' and an ion-acoustic wave propagating along the magnetic field toward the lower density. In this case, a red satellite arises in the spectrum of the scattered signal; this satellite is shifted from the pumping frequency by 3 MHz (Fig. 2a). At low pumping powers, $P_0 < P_{th} = 20$ mW, the satellite amplitude increases exponentially with the pumping power, $\ln[A_s(P_0)] \sim P_0$ [6], which corresponds to the convective instability.

When the pumping power exceeds the threshold value, $P_0 > P_{th} = 20$ mW, the dependence of the satellite amplitude on the pumping power $A_s(P_0)$ becomes stronger (Fig. 3, curve $\Delta f = 0$). In this case, the level of the scattered signal increases by more than four orders of magnitude if the pumping power varies by several percent. This was interpreted in [7] as the onset of the absolute parametric instability $l_0 \longrightarrow l_0' + s$. As the pumping power increases, the instability growth rate increases in the interval $\gamma \sim 1\text{–}2 \times 10^6$ s^{-1}. The portion of the curve describing the exponential dependence $A_{ps}(P_0)$ for low pumping powers in Fig. 3 is absent because the sensitivity of the diagnostic equipment in this experiment was somewhat lower than that used in measurements of a similar dependence $A_s(P_0)$ in [6]. At a power of $P_0 \sim 40$ mW, which is twice as high as the threshold power for the absolute instability, we observed a strong, almost complete parametric reflection of the pump wave. In this case, the scattered-signal spectrum had the shape shown in Fig. 2a.

According to [7], the mechanism responsible for the onset of the absolute instability is associated with the intricate spatial structure of the pump wave, in which a small fraction of the first radial mode $P_1 \leq 0.1P_0$ is present. In the presence of the first radial mode of the pump wave, the second region of the resonant three-wave interaction arises and the feedback loop is formed. According to [7, 8], the instability growth rate and the structure of the spectrum are determined by the time during which the ion-acoustic wave propagates through the feedback loop.

3. EXPERIMENTAL RESULTS

In this experiment, we studied the influence of a stochastic and harmonic frequency modulation of the pump wave on the absolute parametric SBS instability, $l_0 \longrightarrow l_0' + s$.

The frequency modulation of pump microwaves was performed with a specially designed generator whose output signal had the form

$$U(t) = U_m \cos 2\pi[f_0 \pm \Delta f(U_c)]t.$$

Here, $\Delta f(U_c)$ is the frequency deviation under the action of the controlling voltage U_c. The generator had the following parameters: the mean frequency was $f_0 \approx$

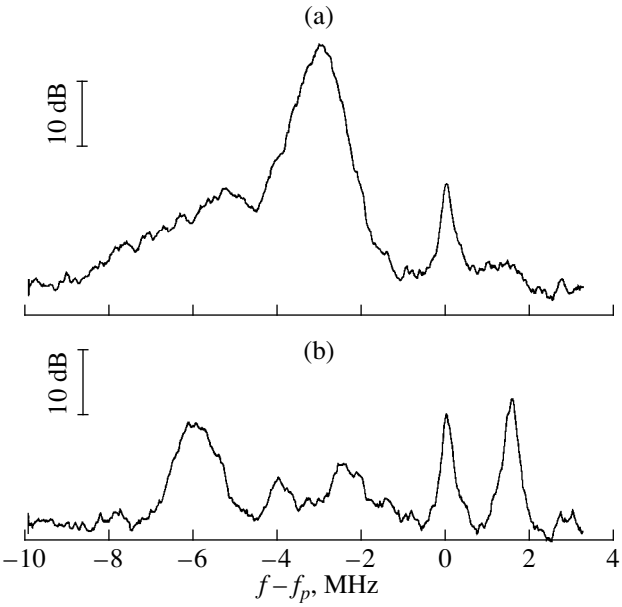

Fig. 2. Spectrum of the scattered signal in the cases of (a) a monochromatic pump wave and (b) harmonic modulation of the pumping frequency.

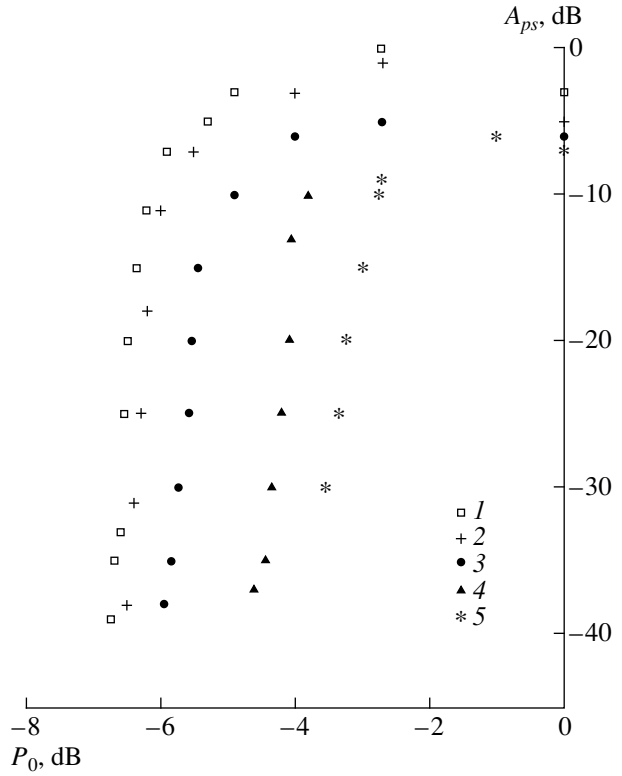

Fig. 3. Amplitude of the scattered signal as a function of the pumping power for different values of the frequency deviation: (*1*) 0, (*2*) 20, (*3*) 40, (*4*) 100, and (*5*) 150 MHz; $\Delta f = 0$ corresponds to monochromatic pumping, and $P_0 = 0$ dB corresponds to 100 mW.

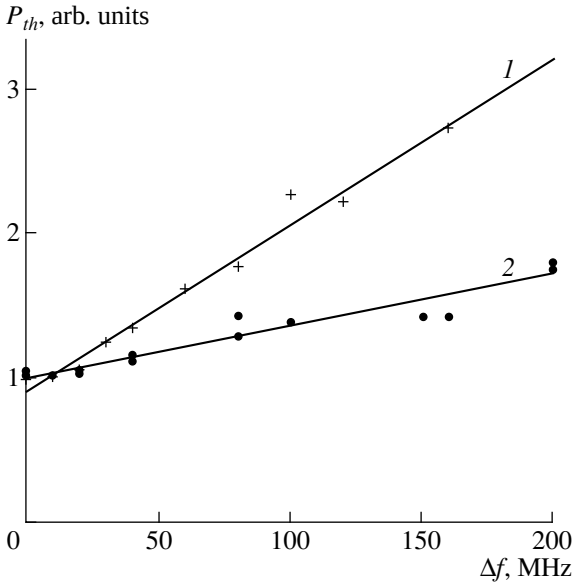

Fig. 4. The threshold power of the absolute instability as a function of the frequency deviation for (*1*) harmonic modulation (f_m = 1.8 MHz) and (*2*) stochastic modulation.

2.7 GHz, the maximum frequency deviation was $\Delta f_{\max} \sim \pm 500$ MHz when U_c varied from 3 to 20 V, and the transmission frequency band of the control signals was 0–50 MHz. This allowed us to control the generator frequency sufficiently rapidly using various laws for the frequency change. For the harmonic frequency modulation $\Delta f(U_c)$, the controlling sinusoidal voltage U_c at the frequency f_m was fed from a G4-102 RF generator. For the stochastic frequency modulation of the generator signals, the controlling voltage U_c was formed from the photocurrent of a photomultiplier operating in the photon-counting mode when its photocathode was illuminated by a filament lamp. In this case, the spectrum of the photocurrent in the multiplier working frequency band well approximates the white-noise spectrum. Thus, the control-signal spectrum formed in our experiment with the help of an FEU-140 photomultiplier and measured by an S4-25 spectrum analyzer in the frequency band up to 50 MHz was almost uniform.

In the general case, the spectrum of frequency-modulated oscillations is the Fourier transform of a signal and, depending on the modulation law, has a rather complicated form. Since the analytical representation of the spectral function of a frequency-modulated signal is a complicated problem (especially in the case of stochastic frequency modulation), the spectrum of this signal was measured in the experiment with the help of an SK4-62 spectrum analyzer. To attain the required width and homogeneity of the power density in the spectrum of the frequency-modulated pump wave, we varied the modulation depth of the pumping generator and the operating conditions of the photomultiplier. In the experiment, the instantaneous values of the pumping frequency were within the range $f_0 - \Delta f/2 < f < f_0 + \Delta f/2$ and the frequency deviation Δf was up to 200 MHz.

The modulation of the pumping frequency caused a substantial broadening of its spectrum, thus impeding direct observation of the satellite arising in the scattering spectrum in the presence of instability. Therefore, when studying the ion-acoustic wave generated due to the instability, we used the enhanced-scattering technique [6]. To do this, the probing low-power ($P_p <$ 5 mW) TG mode was excited at a frequency f_p = 2350 MHz with the same waveguide that was used to excite the pump wave (Fig. 1). The probing-wave frequency was chosen to be lower than the minimum frequency of the modulated pump wave: $f_p < f_0 - \Delta f/2$. This allowed us to obtain information about the amplitude of decay waves by analyzing the scattering spectra. The scattering of the probing wave by the decay ion-acoustic wave occurred outside the instability region at a distance of $\Delta z \approx 2a(f_0 - f_p)/f_0 \approx 0.52$ cm from the focus for the central frequency f_0 of the pump wave on the lower-density side, where $a = \left(\frac{1}{n_c}\frac{\partial n_e}{\partial z}\right)^{-1}_{n_e(0,z)=n_c}$ = 5 cm is the constant of the exponential law describing the decrease in the plasma density. This allowed us to obtain information about the decay-wave amplitude from analysis of the scattering spectra of the probing wave. In the experiment, we studied the dependence of the scattered-signal amplitude on the pumping power $A_{ps}(P_0)$ and on the character of the frequency modulation.

The influence of the stochastic modulation of the pump wave on the development of the parametric instability is demonstrated in Fig. 3. The figure shows the dependences of the amplitude of the signal of the scattered probing wave on the pumping power $A_{ps}(P_0)$ obtained for various widths of the pump-wave spectrum. It is seen that the suppression of the SBS instability occurs when the pumping-frequency deviation is $\Delta f >$ 40 MHz, which is 20 times higher than the instability growth rate $\gamma \sim (1–2) \times 10^6$ s^{-1}. The corresponding spatial broadening of the decay region, $\Delta z = (2\Delta f/f_0)\, a \approx 0.2$ cm, is comparable with the size of the feedback loop giving rise to the instability [7]. For smaller deviations, $\Delta f <$ 40 MHz, the effect of the stochastic modulation of the pump wave on the instability is less pronounced.

The suppression effect is most pronounced near the instability threshold. Figure 4 (closed circles) shows that, when the pump-wave spectrum width increases to 200 MHz, the threshold power P_{th} for the excitation of the absolute instability increases by a factor of ~1.8. However, far from the threshold, for P_0 = 0 dB (Fig. 3), which corresponds to a pumping power of ~100 mW, the effect of the stochastic frequency modulation of the pump wave is much less. Thus, for Δf = 150 MHz, the instability is only slightly suppressed; i.e., the scattered-wave amplitude decreases twofold.

An unexpectedly weak effect of the stochastic frequency modulation on the absolute SBS instability, $l_0 \longrightarrow l_0' + s$, was observed in the coherent instability regime [8] in which the temporal and spatial coherence of the interacting waves plays a decisive role. In this case, the scattered-signal spectrum, unlike the spectrum with a half-width of ~1 MHz shown in Fig. 2a, consisted of two or three narrow lines that had half-widths less than 100 kHz and corresponded to the instability eigenmodes. Strong suppression was observed only for $\Delta f \sim 120$ MHz; in this case, the fine spectral structure took place even for such a high value of the frequency deviation.

In the experiment, the influence of the harmonic frequency modulation of the pump wave on the parametric SBS instability was also studied over a wide range of the modulation frequency from 0.1 to 10 MHz. It turned out that the suppression effect is more pronounced for the harmonic modulation as compared with the stochastic frequency modulation and depends not only on the width of the pump-wave spectrum but also on the modulation frequency f_m. Figure 2b shows the satellite spectrum for modulated pumping with a spectral width of $\Delta f = 60$ MHz at $f_m = 1.8$ MHz. It is seen that the most pronounced decrease in the scattered-signal amplitude (by more than two orders of magnitude) occurs at the frequency $f - f_p = -3$ MHz, corresponding to the maximum of the satellite of the monochromatic pump wave (Fig. 2a). At the same time, new spectral components appear both in the Stocks, $f - f_p = -6$ MHz, and anti-Stocks, $f - f_p = +1.5$ MHz, spectral regions. The spectrum (Fig. 2b) is similar to the spectrum observed in the case of the absolute parametric instability associated with stimulated forward scattering (SFS) in earlier experiments in the same device [9]. The mechanism of the SFS instability is associated with the presence of two closely spaced plasma regions in which the three-wave decay conditions are simultaneously satisfied.

Figure 4 shows the threshold power for the instability as a function of the pumping frequency deviation for a modulation frequency of $f_m \sim 1.8$ MHz. It is seen that, for $\Delta f = 150$ MHz, the threshold power increases threefold. Far from the threshold, the effect of the modulation on the instability is less pronounced, as was also observed in the case of stochastic modulation.

The time evolution of the instability was studied in an experiment with the use of an S4-80 pulsed spectrum analyzer. The analyzer strobe duration was ~1 μs. In the experiment, we used pulsed pumping with a pulse duration of 15 μs and a simultaneously applied harmonic frequency modulation at a frequency of 1.8 MHz. Figure 5 shows the time behavior of the scattered-signal amplitude for various values of the pumping frequency deviation. As is seen in the figure, all of the curves demonstrate a well-defined exponential growth followed by saturation and, then, slow growth. The instability growth rate was determined from the exponential part of the curves. The dependence of the growth rate on the pumping frequency modulation is presented in Fig. 6. It is seen that, as the deviation increases to 100 MHz, the growth rate decreases only threefold. The figure also shows a similar dependence for the case of stochastic modulation. The difference in the growth rates in Fig. 6 again shows that the stochastic modulation has a less pronounced effect on the

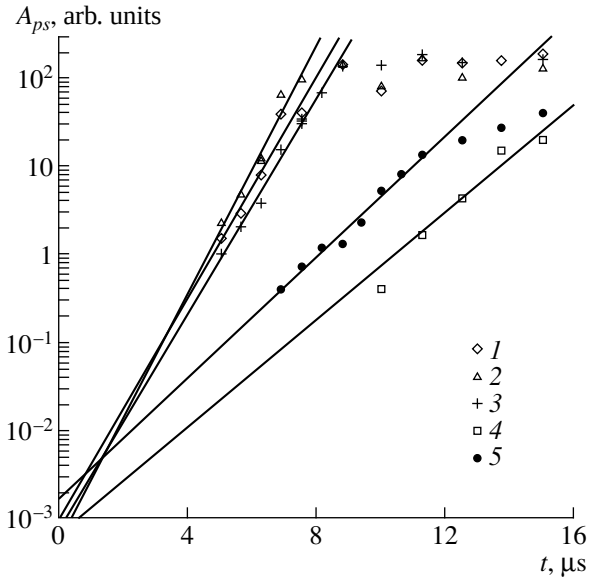

Fig. 5. Time dependence of the scattering-signal amplitude for different values of the frequency deviation: (*1*) 0, (*2*) 20, (*3*) 40, (*4*) 60, and (*5*) 80 MHz.

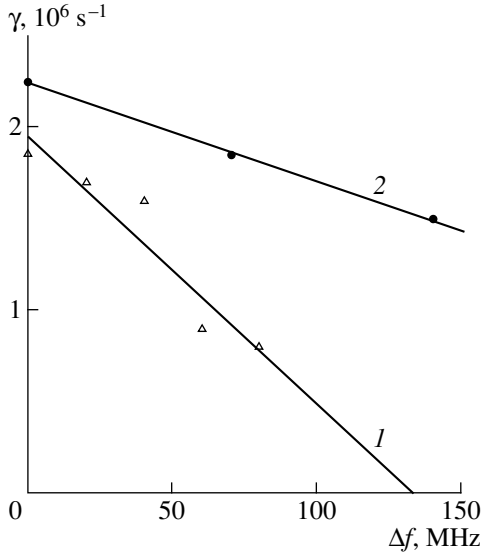

Fig. 6. Growth rate of absolute instability as a function of the frequency deviation for (*1*) harmonic modulation (f_m = 1.8 MHz) and (*2*) stochastic modulation.

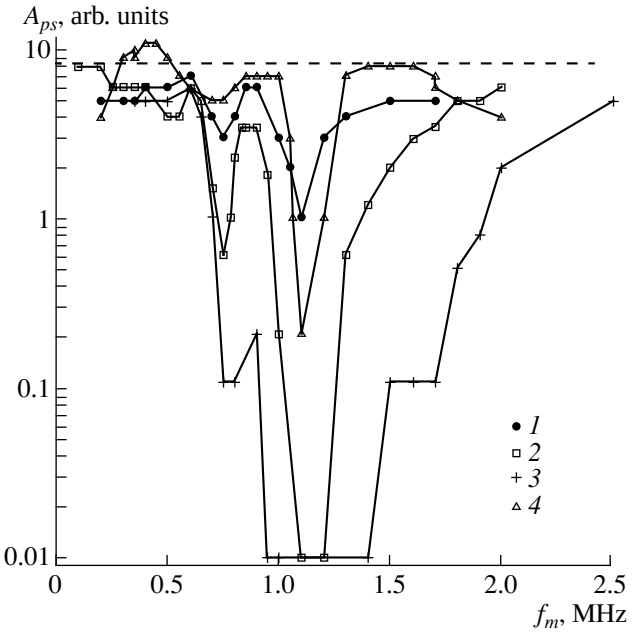

Fig. 7. Resonant suppression of the instability caused by harmonic frequency modulation of the pump wave for different values of the frequency deviation: (*1*) 15, (*2*) 30, (*3*) 60, and (*4*) 120 MHz.

absolute instability $l_0 \longrightarrow l_0' + s$ in comparison with the harmonic frequency modulation.

Figure 7 shows the scattered-signal amplitude as a function of the modulation frequency for different widths of the pump-wave spectrum. The dashed line parallel to the abscissa shows the level of the scattered signal for a monochromatic pump wave ($\Delta f = 0$). The signal is close to this level at $f_m > 1.5$ MHz and $f_m < 0.6$ MHz. However, around $f_m = 1$ MHz, within a wide range of deviation values, $10 < \Delta f < 100$ MHz, resonant suppression of the signal is observed. This is most pronounced within the range $40 < \Delta f < 80$ MHz.

This effect, along with an unexpectedly high stability of the stimulated-scattering coherent mode in the case of stochastic modulation, has yet to be explained, because a satisfactory theoretical interpretation of these effects is still lacking. The increase in the scattered signal for $\Delta f = 120$ MHz and $f_m = 0.5$ MHz (Fig. 5) is presumably related to the enhancement of decay instability occurring if the velocity of propagation of the decay point coincides with that of the ion-acoustic wave [10].

4. DISCUSSION OF RESULTS

The above experimental results show that the suppression of the absolute instability occurs when the frequency broadening of the pump-wave spectrum is equal to tens of megahertz, which is well above the ion-acoustic wave frequency and the maximum instability growth rate predicted by the theory for homogeneous plasma. Moreover, this broadening is considerably greater than the instability growth rate measured in the experiment. This contradicts the homogeneous-plasma theory, which predicts that suppression should occur for $2\pi\Delta f > \gamma$. Apparently, this discrepancy can be explained taking into consideration specific features of the three-wave interaction in an inhomogeneous plasma. The fact is that, in an inhomogeneous plasma, various spectral components of the pump wave can interact with the same ion-acoustic wave, generating daughter waves at the shifted frequencies satisfying the relation $f' = f_0 + \Delta f + f_s$. Such an interaction occurs in spatially shifted points; in the case of backward scattering, these points satisfy the decay condition $2k_0(f_0 + \Delta f, x + \Delta x) = k_s$. In the case of small frequency deviations, the shift is defined as $\Delta x = 4\pi\Delta f(l^2/v)$, where $l^2 = 2dk_0/dx$ and v is the group velocity of the daughter wave. Strong suppression of the absolute instability should take place when the shift is greater than the size of the feedback loop, L. According to [7], the instability growth rate is determined by the propagation time of the ion-acoustic wave through the feedback loop L/c_s and is defined by the relation $\gamma = \pi K(c_s/L)$, where $K = (\gamma_0 l)^2/(vc_s)$ and γ_0 is the instability growth rate predicted by the homogeneous-plasma theory. Combining the above equations, it is easy to obtain the criterion for suppression of the instability in an inhomogeneous plasma, $\Delta f > 0.25(\gamma_0^2/\gamma)$, which agrees with the observations described above.

5. CONCLUSION

The experiments have shown that, in an inhomogeneous plasma, the broadening of the pump frequency spectrum affects the parametric instability much more weakly than is predicted by the theory of decay instabilities in a homogeneous plasma [1, 2]. The suppression of the absolute instability is only observed for a pump-wave spectrum width of $2\pi\Delta f > 100\gamma$, which is much greater than the instability growth rate γ. It is suggested that the suppression of the absolute instability takes place when the spatial broadening of the parametric-decay region due to variations in the pumping frequency exceeds the size of the feedback loop responsible for the onset of the instability. It is found that stochastic pump-wave frequency modulation results in a high stability of coherent eigenmodes of the absolute instability.

ACKNOWLEDGMENTS

This work was supported in part by the Russian Foundation for Basic Research (project nos. 96-15-96367 and 99-02-17975) and the Foundation for Basic Research of the Republic of Belarus (project no. F98-046).

REFERENCES

1. E. Valeo and C. Oberman, Phys. Rev. Lett. **30**, 1035 (1973).
2. K. Mima and K. Nishikawa, in *Handbook of Plasma Physics*, Ed. by A. A. Galeev and R. Sudan (Moscow, Énergoatomizdat, 1984; North-Holland, Amsterdam, 1984).
3. S. P. Obenschain, Y. C. Luhmann, and P. T. Grieling, Phys. Rev. Lett. **36**, 1309 (1976).
4. K. Mizunok and J. S. De Groot, Phys. Rev. Lett. **39**, 608 (1977).
5. V. I. Arkhipenko, V. N. Budnikov, I. A. Romanchuk, *et al.*, Fiz. Plazmy **7**, 396 (1981) [Sov. J. Plasma Phys. **7**, 216 (1981)].
6. V. I. Arkhipenko, V. N. Budnikov, E. Z. Gusakov, *et al.*, Fiz. Plazmy **13**, 693 (1987) [Sov. J. Plasma Phys. **13**, 398 (1987)].
7. V. I. Arkhipenko, V. N. Budnikov, E. Z. Gusakov, *et al.*, Zh. Éksp. Teor. Fiz. **93**, 1221 (1987) [Sov. Phys. JETP **66**, 689 (1987)].
8. V. I. Arkhipenko, V. N. Budnikov, E. Z. Gusakov, *et al.*, Pis'ma Zh. Éksp. Teor. Fiz. **46**, 17 (1987) [JETP Lett. **46**, 18 (1987)].
9. V. I. Arkhipenko, V. N. Budnikov, E. Z. Gusakov, *et al.*, Plasma Phys. Controlled Fusion **40**, 215 (1998).
10. V. I. Arkhipenko, V. N. Budnikov, E. Z. Gusakov, *et al.*, Plasma Phys. Controlled Fusion **37**, 1353 (1995).

Translated by N. F. Larionova

Plasma Physics Reports, Vol. 26, No. 4, 2000, pp. 320–327. Translated from Fizika Plazmy, Vol. 26, No. 4, 2000, pp. 346–354.

LOW-TEMPERATURE PLASMAS

Long Laser Spark and Electric Gas Breakdown

A. V. Shelobolin

Lebedev Institute of Physics, Russian Academy of Sciences, Leninskiĭ pr. 53, Moscow, 117924 Russia

Received May 19, 1998; in final form, March 18, 1999

Abstract—Initiation of electric air breakdown under normal conditions by a long laser spark is studied experimentally. A qualitative model explaining the effects observed is presented. © *2000 MAIK "Nauka/Interperiodica".*

1. INTRODUCTION

When analyzing the discrepancies between the theory of electric gas breakdown (EGB) and experiments, we can distinguish three groups of problems. The first group concerns the problems for which the theory and experiments are in reasonable agreement, specifically, the main body of the energy estimates and calculations. These problems do not require the revision of the theory. The second group describes the gradually changing spatial and temporal breakdown-wave characteristics. In present-day EGB theory, most attention is focused on just these problems, which are surveyed in [1]. The restrained pessimism of the authors is primarily associated with the fact that the present-day theory still fails to explain some parameters of the EGB waves, the more so since the existing model is incapable of explaining the development of the EGB waves from the middle of the interelectrode gap and describes the inertial propagation of streamers as a pulse relaxation. That this group of problems is far from being completely solved calls for a significant revision of the EGB model, although attempts to quantitatively refine the existing model are still possible.

The third group of problems requires the revision of the basis of the model. This group deals with the processes in which the spatial and temporal EGB characteristics change stepwise. The well-known manifestations of these phenomena are the transition from the avalanche to a streamer, transverse nonuniformity of the streamer region of the leader, and the stepwise nature of the lightning leader and the leader of a long laboratory spark. The necessity of the revision of the model is determined by the fact that the mathematical apparatus of the present-day quasi-electrostatic model does not contain the necessary elements to obtain solutions adequately describing these phenomena.

It is desirable to base a new model on experiments in which the temporal stepwise nature and the spatial nonuniformity of EGB are pronounced most clearly. For this purpose, it is convenient to use the experiments on the initiation of EGB by a long laser spark (LLS). An additional argument in favor of using these experiments as a basis for a new model is the relatively soft requirements for spatial and temporal resolutions at the present stage of investigation. It is also important that the spatial location of the EGB wave is strongly determined and the timing accuracy of the diagnostics with respect to the laser pulse is very high. This paper is devoted to a description of these experiments. In addition, a qualitative model explaining the experimental results is proposed.

LLSs were first studied in [2]. They usually have a bead structure and propagate along the optical axis of the system with a velocity of $\sim 10^9$ cm/s. In order to avoid the bead structure of the spark, it was proposed in [3] to use a conical lens that focuses the laser beam into a line with a length of several diameters of the laser beam along the axis of the system. A bead LLS with a total length of several tens of meters was observed in [4]. As a rule, in order to obtain LLSs, either Q-switched neodymium-glass lasers or e-beam-controlled CO_2 lasers are used. Except for the energy and power requirements associated with the threshold for optical gas breakdown, no demands on other laser parameters, such as divergence, time contrast, and radiation uniformity over the beam cross section, are imposed. Thus, the LLS is a relatively cheep instrument for physical investigations.

The first experiment on EGB initiation with the use of an LLS is described in [5]. A 50-cm-long linear breakdown was obtained in air under normal conditions with a 10 kV/cm average electric field. The breakdown also occurred in the absence of an LLS, but the EGB wave evolved along a line markedly deviating from the straight line. Paper [5] and subsequent papers [6, 7] initiated a series of studies on high-voltage breakdown. In accordance with the basic effect obtained with the use of an LLS, this regime will be referred to as a guiding regime. Seemingly, this series can also include experiments on the initiation of EGB in long gaps by ultraviolet laser radiation, which causes no LLS but produces multiphoton gas preionization [8, 9].

The second line of investigation is the initiation of an EGB in superlong gaps, i.e., gaps whose length exceeds the LLS length [10–13]. This regime can be called a partially guiding regime, because the rectilin-

1063-780X/00/2604-0320$20.00

ear structure of the EGB wave is observed only in regions where the LLS exists.

A recently developed third line of investigation involves the use of conical lenses to produce elongated switches with an interelectrode gap up to 10 cm long [14–18]. This regime can be called the switch regime, taking into account the basic goal of the investigations and some unique properties of this type of switch. Finally, the fourth line of investigation of a low-voltage breakdown was started in [19–23], in which the average electric field was 1 kV/cm or less and no electric breakdown was observed in the absence of an LLS. We will refer to this regime as the initiation regime, in accordance with the basic effect obtained with the use of an LLS. Below, we will focus on this effect.

EGB modeling with the use of an LLS has considerable promise as is shown in [24], where three fundamental features of the EGB streamer stage were observed in the guiding regime: the development of a streamer from the middle of the interelectrode gap and the stepwise and inertial nature character of the streamer propagation. However, EGB modeling with the use of an LLS in the guiding regime did not reveal qualitatively new effects, in contrast to the initiation regime, in which such effects were observed. We note that, in the guiding regime, only one type of EGB wave can be modeled, whereas in the initiation regime, two types of EGB waves and the transition of one wave into another can be modeled. This is why the experiments carried out in the initiation regime are of greater interest. It should be noted that all of the experiments in the initiation regime were carried out in air under normal conditions.

2. CALCULATIONS OF THE INITIATION REGIME

In one of the first papers devoted to this line of investigation [19], it was shown that a spatial resolution of ~1 mm and temporal resolution of ~1 μs are sufficient to obtain important information. A present-day experimental facility can easily satisfy these conditions.

As a basic geometry of the experiment, we chose a coaxial line with a broken axis, in which, after the bridging of the gap, the discharge was excited on the axis of a chamber with a reverse-current conductor. Such geometry allowed us to eliminate both the influence of strays on the processes under study and the distortion of the gap field by foreign conducting objects and to carry out rather accurate calculations (due to the fixed chamber inductance). This also suggests the chance to test one of the controversial points of EGB theory—the problem of the streamer carrying away the electrode potential. One of the coaxial electrodes was a tube along which laser radiation propagated; another one was a needle whose potential was opposite in sign with respect to the potential of the reverse-current conductor. The streamer was assumed to propagate from the needle to the tube. In this case, if the electrode potential is carried away by the streamer, the value and the distribution of the field near the streamer head are continuously reproduced and the length of the breakdown gap is limited only by the LLS parameters.

The first experiments carried out to test this hypothesis showed that, if the LLS parameters are stable and the LLS length exceeds the length of the interelectrode gap, the threshold waiting voltage responsible for the electric phase of the breakdown depends weakly on the length of the interelectrode gap up to a certain (threshold) length and then sharply increases [20]. A similar result was independently obtained in [23] for a different electric-field geometry. It was established in [20] that the threshold gap length for the low-voltage breakdown is determined by both the physical properties of the plasma produced by an LLS and the technological parameters of the chamber design, in particular, the diameter of the reverse-current conductors. The obtained dependence of the threshold gap length on the applied voltage was found to be close to exponential and differed substantially from the analogous dependences for both the avalanche and streamer EGB models. Experimentally, this problem can be settled only with the use of high-speed photorecording of the breakdown wave emerging in the interval between the optical breakdown and electric discharge. This interval can exceed 100 μs [19]; therefore, this process can be recorded, e.g., by an SFR-2M high-speed photorecorder with a rotating mirror. In this case, the optical breakdown, which lasts about 10 ns for a neodymium laser and about 1 μs for a CO_2 laser, can be reliably distinguished from the final, arc-discharge phase.

The schematic of the experiment is presented in Fig. 1. Its basic elements listed in the figure caption were changed insignificantly from experiment to experiment. The polarity was changed by rotating the chamber with respect to the laser beam and subsequent change in the electrode locations. High-speed photorecording was carried out in both the continuous regime with the use of a Dove prism and the frame regime without a Dove prism. Typical pictures obtained by fast continuous recording of the process of EGB initiation by an LLS were presented in [19]. Similar pictures are also typical of the guiding regime [6]. The quantitative results obtained from these experiments are the number of points of the optical breakdown in the interelectrode gap, the afterglow time of these points, and the degree of correlation of the spatial positions of these points with the brightest points of a subsequent arc discharge. Obviously, this is information of secondary importance. The most important information concerning the onset of the electric-breakdown wave between the optical breakdown and arc discharge can be obtained only with frame-by-frame recording. These experiments were carried out with use of a 15-cm-diameter camera; the electrodes were a 36-mm-diameter tube and a 1-mm-diameter needle. The interelectrode distance was

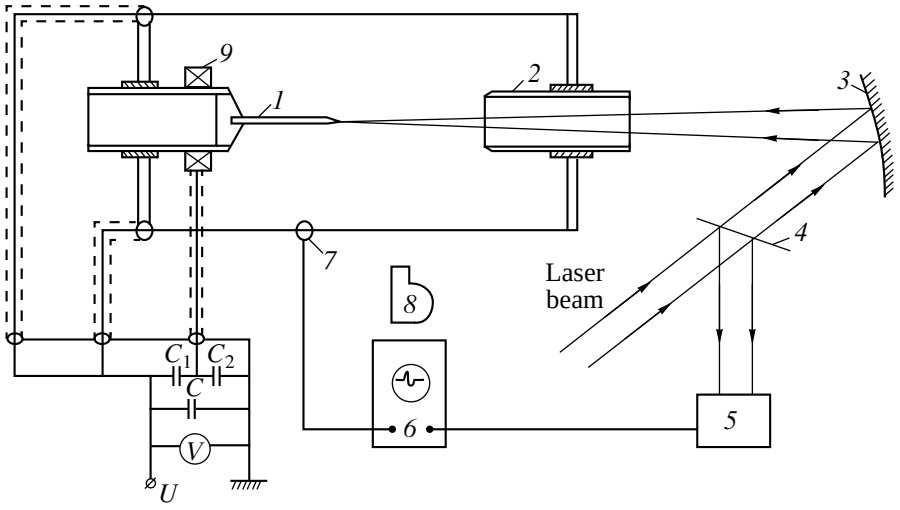

Fig. 1. Schematic of the experiment: (*1*) cathode, (*2*) anode, (*3*) focusing mirror, (*4*) splitting plate, (*5*) photodetector, (*6*) oscillograph, (*7*) Rogowski coil, (*8*) SFR, and (*9*) emitter of the longitudinal electric field.

12 cm. EGB was initiated by a CO_2 laser [25] (100-J energy and 1-μs pulse duration).

Figures 2 and 3 present typical images illustrating the onset of the EGB wave in two different experiments. The electrodes are also shown schematically, which allows one to see the direction of the wave propagation and determine the absolute dimensions of the breakdown wave by comparing it with the sizes of the electrodes and interelectrode gap. The frame exposure time and the time interval between frames were 4 μs. The instant (in μs) corresponding to the middle of the exposure time can be determined from the expression $t = 2 + 4N$, where $N = 0, 1, 2 \ldots$ is the frame number; $N = 0$ corresponds to the first occurrence of the LLS. The basic results of frame-by-frame recording are the following:

(i) Two basic types of EGB waves were observed: the primary wave (PW) and secondary wave (SW).

(ii) The PW has the shape of a piston with a characteristic size of 1 cm. For any electrode polarity, this wave moves from the tube to the needle with velocity of the order of 10^5 cm/s, corresponding to the thermal velocity of air ions. The size of a PW exceeds the characteristic size of the points of the optical LLS breakdown by almost one order of magnitude; the emission from these points lasts several microseconds. No effect of a discrete LLS structure on the PW shape and velocity was observed.

(iii) The SW is 1–2 mm in transverse size and propagated in the direction of the maximum preionization determined by the LLS optical-breakdown points. Before the occurrence of the SW, a uniform luminous channel less than 1 mm in diameter was seen between the front of the PW and the needle electrode (Fig. 2, frames 20, 24, 26). The time resolution was insufficient to determine the direction of the SW propagation but allowed us to estimate the SW velocity from below as $V \gtrsim 10^7$ cm/s; i.e., this velocity was on the order of the electron thermal velocity at a temperature close to room temperature and higher.

(iv) After the PW passed more than half of the interelectrode distance, it went over into the SW.

(v) The PW diameter changed only slightly in the course of propagation and was almost doubled in the final stage. This could be related to an increase in the emission intensity from the PW cylindrical boundary.

(vi) The EGB began with the formation of a cylindrical luminous region near the tube electrode. This was a standing wave that contracted near the electrode end and from which the PW detached. The diameter of the standing wave was either equal to the PW diameter or exceeded it threefold (Fig. 3, frames 2, 4, 6, 8, and 10). Moreover, during the formation of the standing wave, a cylindrical skin layer was observed (Fig. 3, frames 2, 4, and 6).

(vii) In the initial stage of propagation, the PW could have a double structure in the longitudinal direction, which further went over into a single one. The emission intensity from the leading part of the PW was lower than the intensity from the trailing one. This could be associated with the fact that the energy was supplied to the PW from the tube electrode and was partially absorbed in the trailing part of the PW (Fig. 2, frames 7, 10, 20, and 24).

(viii) In the final stage of the PW propagation, an additional wave process—a tail wave—occurred between the PW trailing edge and the SW (Fig. 2, frames 10, 18, 20, 24, and 26).

(ix) In some experiments, we observed the propagation of the reverse wave (a luminous spot of undefined configuration) from the needle electrode toward the tube electrode (Fig. 3, frames 12, 14). Such a shape of the reverse wave could be ascribed to the fact that it was

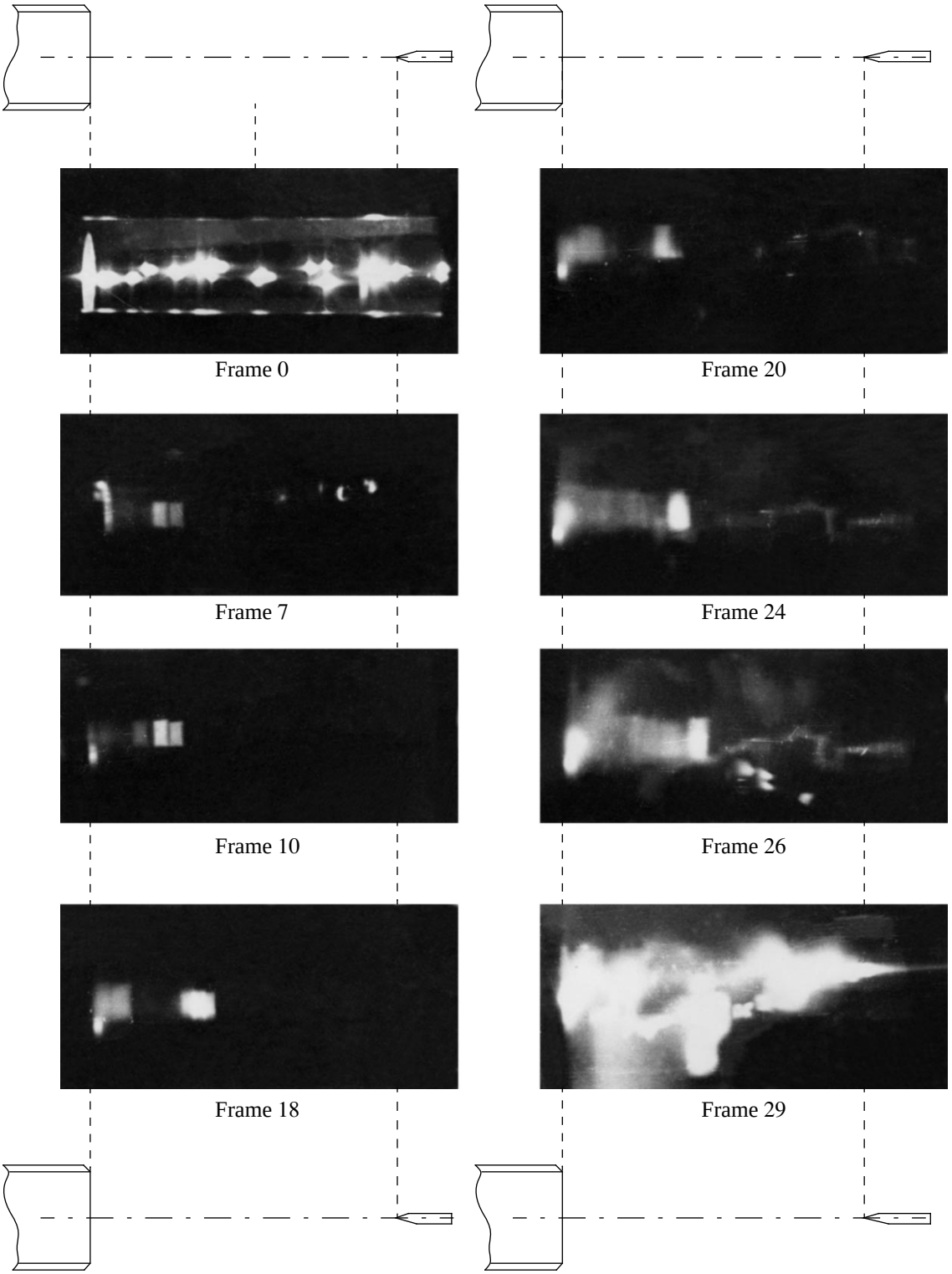

Fig. 2. Evolution of the EGB wave, $U = +50$ kV.

formed on the support of the needle (a tube with an X-shaped bridge), rather than on the needle itself.

(x) PWs were also observed before the LLS was produced. This was associated with air preionization by background laser radiation. The coma aberration of the focusing system was the reason why background radiation produced a 2-cm-diameter luminous spot in the focal plane; the PWs propagated from both sides of this

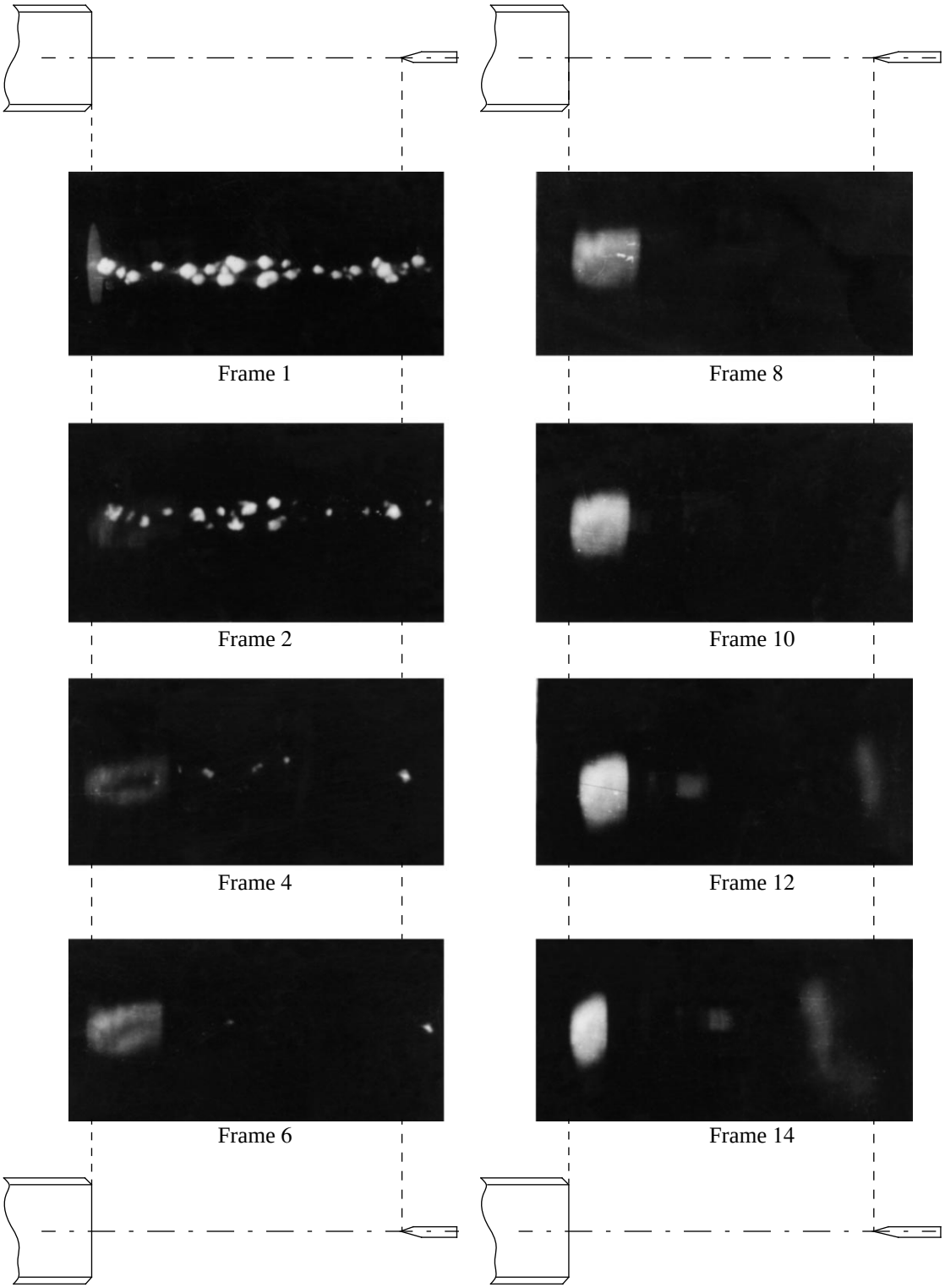

Fig. 3. Formation of the standing wave and the departure of the PW from the standing wave, $U = -39$ kV.

spot. The experimental conditions did not allow us to accurately measure the coordinates of these PWs.

(xi) Small metal fragments driven out from the support unit of the needle electrode by laser radiation had no appreciable effect on EGB waves (Fig. 2, frames 7, 26).

Figure 4 shows the PW propagation; the longitudinal coordinate is counted from the middle of a double

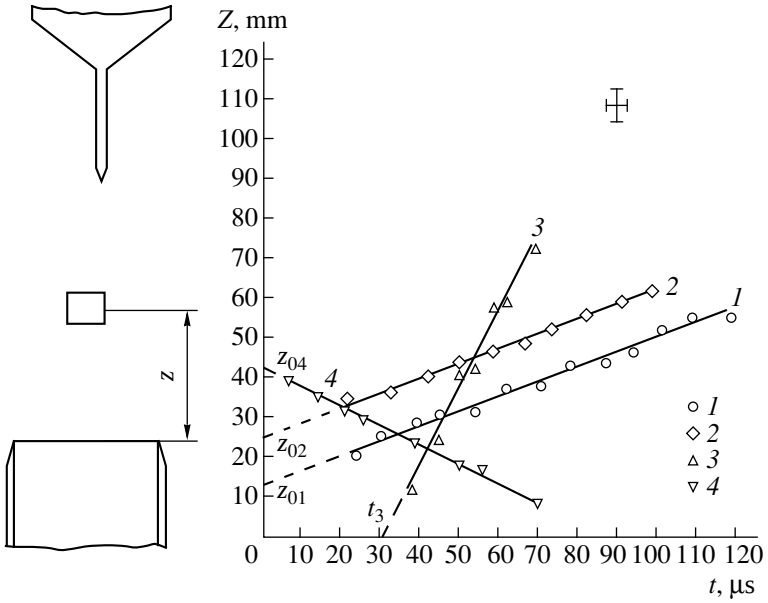

Fig. 4. Time dependence of the longitudinal coordinate of (*1–3*) the PWs and (*4*) the boundary of the standing wave: U = (*1*) + 50, (*2*) –39, (*3*) –39, and (*4*) –39 kV.

pistonlike PW or from the leading edge of a single PW. The voltage sign shows the polarity of the tube voltage. The spatial and temporal error bars correspond to the frame exposure time and the longitudinal size of the breakdown wave. This picture allows a more exact determination of the velocity of the breakdown wave and the coordinates where it starts and finishes, as well as the time when the standing wave forms. The processing of the figure gives the following values for the PW velocities: $V_1 = 3.2 \times 10^4$ cm/s, $V_2 = 3.7 \times 10^4$ cm/s, and $V_3 = 2.4 \times 10^5$ cm/s. The velocity with which the standing wave contracts is $V_4 = 5 \times 10^4$ cm/s. The initial PW coordinates are z_{01} = 1.4 cm, z_{02} = 2.4 cm, and z_{04} = 4.2 cm, and the time during which the standing wave is formed is t_3 = 30 μs.

3. QUALITATIVE MODEL

Although the PW and SW are similar in appearance to an avalanche–streamer transition, the factors listed above cannot be explained in the existing EGB model. The avalanche model should be completely rejected, because, in this model, the direction of the PW propagation is independent of the polarity of electrodes. In order to discard the streamer model, it should be taken into account that all of the well-known wave processes can be broken into two groups: frontal and coherent processes. In the former, the energy is deposited at the wave front; the latter are related to the action of a distant (point or volume) source. In order to describe the coherent processes, it is necessary to introduce the notion of the phase. In describing the frontal processes, this is not required. Therefore, the avalanche and streamer models developed for frontal waves cannot explain the phase effects observed during the evolution of PWs, standing waves, and tail waves. This is the reason why it is necessary to consider an alternative, plasma-waveguide model. Applied to the experiments in question, its basic concepts are the following:

(i) Due to emission from the points of optical breakdown, the laser spark forms a cylindrical plasma channel several centimeters in diameter.

(ii) The density of charge carriers in this channel decreases continuously until the resonance occurs with the electromagnetic oscillations produced in the channel under the action of the applied voltage. The channel diameter is stabilized, and the difference in the reflection coefficients for the electromagnetic wave at the ends of the channel determines the propagation direction of a solitary traveling wave.

(iii) The relative stabilization of the PW channel diameter allows us to assume that it is the surface (rather than space) dissipation that plays a decisive role. This dissipation occurs in the vicinity of a cylindrical surface where the charge-carrier density is close to the critical density for the characteristic frequency of the electromagnetic field generated in the channel.

(iv) It seems that the PW–SW transition, which is characterized by a jump in the propagation velocity and a decrease in the diameter of the breakdown wave, can be associated with the transition from an ion-acoustic wave to an electron Langmuir wave.

(v) The longitudinal propagation of a PW and its interaction with the channel medium suggest that there exists a substantial longitudinal component of the alternating electric field. Thus, the wave in question should be sought in the class of longitudinal surface waves.

This model allows us to qualitatively explain why curves *1*, *2*, and *3* in Fig. 4 do not pass through the coordinate origin. For a PW to develop, it is necessary to form a reflecting plasma mirror on the end of the tube electrode; the standing wave plays the role of such a mirror. Curves *1* and *2* are related to strong background laser radiation during which a standing wave is produced. Curve *3* corresponds to the case of weak background laser radiation, when the formation of the standing wave begins after the emergence of an LLS.

4. ADDITIONAL EXPERIMENTS

According to point (v) of the previous section, there should exist natural frequencies of the longitudinal electric field in the plasma waveguide produced by an LLS. It is seen from Fig. 3 that there must be no less than two such frequencies. An additional series of experiments was carried out to determine these frequencies [22]. The initial schematic of the experiment (Fig. 1) was somewhat changed. The chamber used had an 18-cm-diameter reverse-current conductor. In order to improve the quality of the plasma resonator produced by an LLS in the interelectrode gap, the electrodes used were two 12-mm-diameter tubes; the distance between the electrodes was either 7.5 or 10 cm. An emitter of the longitudinal electric-field component was mounted on one of the electrodes. The emitter was connected to one of the elements of the capacitive divider (C_2) connected in parallel with the basic capacitive storage C. The radiator winding and capacitor C_2 produced a high-quality resonant oscillatory circuit of positive feedback. This feedback was weak because of frequency–phase mismatching.

By varying the C_2 capacitance, we adjusted the eigenfrequency of the feedback circuit so that oscillations were excited in the cylindrical plasma resonator produced by an LLS and evolving in the applied electric field. The current oscillations in the plasma column were measured by a Rogowski coil and recorded by an S8-13 oscillograph. The LLS source was a neodymium laser (with 10-J energy and 3-ns pulse duration). A constant waiting voltage across the interelectrode gap (5–7 kV) was maintained at a level below the EGB threshold.

From traces of the electric current in the discharge gap (decaying sinusoids), we determined the oscillation period τ and the decay rate γ. We managed to record two low-frequency oscillation modes: the oscillation period and the decay rate of the first mode were $\tau = 0.5$ μs and $\gamma = (1.5 \pm 0.3)$ μs, respectively, and those of the second mode were $\tau = 1.5$ μs, $\gamma = (23 \pm 7)$ μs. The error in γ is the statistical scatter from different experiments. The scatter in τ was not observed, so the error in this quantity was evaluated by the time error in the oscillograph measurements; i.e., it was less than 10%. The absolute calibration of the Rogowski coil was not performed; however, the calculation of the Rogowski coil sensitivity allows us to estimate the current amplitude in the first maximum to be 0.2–0.4 A. Variations in the interelectrode distance from 7.5 to 10 cm had no effect on the recorded parameters.

5. ANALYSIS OF THE RESULTS

An analysis of the results obtained reduces mainly to the identification of the evolving primary EGB wave and determination of the state of the plasma channel in which it propagates. An additional analysis allows us to identify the secondary wave based on the available data.

The observed PW should be classified as an ion-acoustic wave, because photorecording shows that its propagation velocity corresponds to the thermal velocity of air ions; in this case, a substantial energy exchange between the wave and medium is observed. This wave can also be classified as a surface (rather than space) wave, because it follows from the measurements that the dependence of its decay rate on the frequency is stronger than linear. This agrees with the photorecording images in which a cylindrical skin layer is clearly seen in the initial stage of the formation of a standing wave. A monotonically increasing ion-acoustic dispersion curve $\omega(k)$ in a plasma waveguide [26], which goes over to the asymptote $\omega_i/\sqrt{2}$, qualitatively explains the mentioned difference in the velocities of PWs (see Section 2). However, based on the above dependence, the results of photorecording still cannot be interpreted as the lower spatial modes of ion plasma oscillations. This fact imposes additional requirements on both future theoretical developments and experiments.

When analyzing the structure of the channel in which the PW propagates, it is necessary to distinguish the region of admissible values of the temperature T and charge-carrier density n in the plane (T–n). From frame-by-frame photorecording, it follows that the Debye radius must be less than 0.1 cm. Therefore, we have $T/n < 4 \times 10^{-8}$ eV cm^3. On the other hand, any plasma component in the channel must have a temperature no less than room temperature; i.e., $T > 0.025$ eV. A simultaneous analysis of these requirements leads to the charge-carrier density $n > 6 \times 10^5$ cm^{-3}. Note that, since we did not make any assumptions about the mass of charge carriers, this condition must hold for both the electron and ion components.

Taking into account that the frequency of the surface wave is close to either the ion plasma frequency or the electron Langmuir frequency, we can determine the critical densities of ions and electrons on this surface under the conditions of the resonance experiments. For the electron component, the critical densities are 2.5×10^3 and 2.2×10^4 cm^{-3} for the first and second recorded modes, respectively. For the ions, the critical densities are four orders higher: 10^8 and 10^9 cm^{-3} for O_2^- and N_2^+ ions. This agrees with the results of [6], in which simi-

lar values for the charge-carrier densities were obtained under similar conditions from both the analysis of the balance equations and direct probe measurements.

By comparing the obtained values of the critical densities of charge carriers with admissible values of the charge-carrier densities, we can infer that it is the ions that are responsible for the collective effects in the PW, whereas the electrons behave as a background gas. The SW should be interpreted as an electron Langmuir wave. The reason for this is the coincidence of the SW velocity estimated from photorecording with the electron thermal velocity. This is also confirmed by the results of [6], in which EGB began with the excitation of an SW and the SW average velocity varied in the range 10^7–10^8 cm/s, depending on the applied voltage. Direct experimental measurements are insufficient to classify the SW as a surface or space wave. Nevertheless, the presented experimental data and estimates allow us to assume that the PW–SW transition is related to the increase in the electron density in the course of PW propagation until the electron resonator is produced on the axis of the ion-acoustic resonator. From an analysis of the admissible values of the charge-carrier densities, we can estimate the electron density in the SW and obtain the threshold conditions for the SW onset, $n > 10^8$–10^9 cm^{-3}, and to evaluate the range of the eigenfrequencies of the corresponding plasma waveguide as $\nu > 10^9$ Hz.

6. CONCLUSION

In conclusion, we note that there is no direct analogy between the PW and the avalanche or streamer. The analogy may be carried out only from a methodological standpoint, because it is necessary to take into account that all of the experimentally observed space–time EGB effects that cannot be explained in the avalanche–streamer model may be qualitatively interpreted with the use of phase and dispersion relations typical of plasma processes.

ACKNOWLEDGMENTS

I am grateful to the Shenth firm for help in preparing this paper and A.A. Rukhadze for fruitful discussions and helpful critiques.

REFERENCES

1. E. M. Bazelyan and Yu. P. Raizer, *Spark Discharge* (MFTI, Moscow, 1997; CRC, Boca Ratón, 1997).
2. N. G Basov, V. A. Boĭko, O. N. Krokhin, and G. V. Sklizkov, Dokl. Akad. Nauk SSSR, Fiz. **173**, 538 (1967).
3. B. Ya. Zel'dovich, B. F. Mul'chenko, and N. F. Pilipetskiĭ, Zh. Éksp. Teor. Fiz. **58**, 794 (1970) [Sov. Phys. JETP **31**, 425 (1970)].
4. V. A. Parfenov, L. N. Pakhomov, V. Yu. Petrun'kin, and V. A. Podlevskiĭ, Pis'ma Zh. Tekh. Fiz. **2** (16), 731 (1976) [Sov. Tech. Phys. Lett. **2**, 286 (1976)].
5. D. W. Koopman and T. D. Wilkerson, J. Appl. Phys. **42**, 1883 (1971).
6. D. W. Koopman and K. A. Saum, J. Appl. Phys. **44**, 5328 (1973).
7. J. R. Greig, D. W. Koopman, R. F. Fernsler, *et al.*, Phys. Rev. Lett. **41**, 174 (1978).
8. N. N. Kononov, G. P. Kuz'min, and V. I. Fisher, Pis'ma Zh. Tekh. Fiz. **14** (19), 1820 (1988) [Sov. Tech. Phys. Lett. **14**, 789 (1988)].
9. A. A. Antipov, A. Z. Grasyuk, A. K. Zhilkin, *et al.*, Zh. Tekh. Fiz. **61**, 200 (1991) [Sov. Phys. Tech. Phys. **36**, 490 (1991)].
10. G. N. Aleksandrov, V. L. Ivanov, G. D. Kadzov, *et al.*, Zh. Tekh. Fiz. **47**, 2122 (1977) [Sov. Phys. Tech. Phys. **22**, 1233 (1977)].
11. G. N. Aleksandrov, O. G. Ivanov, O. P. Ivanov, *et al.*, Pis'ma Zh. Tekh. Fiz. **15** (16), 19 (1989) [Sov. Tech. Phys. Lett. **15**, 587 (1989)].
12. K. Kincade, Laser Focus World **28** (11), 36 (1992).
13. P. Mortensen, Laser Focus World **33** (9), 38 (1997).
14. F. Bunkin, V. V. Korobkin, Yu. A. Kurinyĭ, *et al.*, Kvantovaya Électron. (Moscow) **10**, 443 (1983) [Sov. J. Quantum Electron. **13**, 254 (1983)].
15. M. Yu. Marin, V. I. Pil'skiĭ, L. Ya. Polonskiĭ, *et al.*, Zh. Tekh. Fiz. **57**, 1507 (1987) [Sov. Phys. Tech. Phys. **32**, 898 (1987)].
16. O. G. Ivanov, R. I. Okunev, L. N. Pakhomov, *et al.*, Zh. Tekh. Fiz. **57**, 2012 (1987) [Sov. Phys. Tech. Phys. **32**, 1212 (1987)].
17. V. V. Korobkin, L. Ya. Margolin, L. Ya. Polonskiĭ, and L. N. Pyatnitskiĭ, Kvantovaya Électron. (Moscow) **16**, 1885 (1989) [Sov. J. Quantum Electron. **19**, 1214 (1983)].
18. L. Ya. Polonskiĭ, A. Yu. Goltsov, and A. V. Morozov, Phys. Plasmas **3**, 2781 (1996).
19. V. D. Zvorykin, F. A. Nikolaev, I. V. Kholin, *et al.*, Fiz. Plazmy **5**, 1140 (1979) [Sov. J. Plasma Phys. **5**, 638 (1979)].
20. V. D. Zvorykin, F. A. Nikolaev, I. V. Kholin, *et al.*, Kratk. Soobshch. Fiz. **8**, 41 (1980).
21. A. Yu. Chugunov, F. A. Nikolaev, and A. V. Shelobolin, in *Proceedings of 25th International Conference on Phenomena in Ionized Gases, Minsk, 1981*, p. 797.
22. A. V. Shelobolin, Kratk. Soobshch. Fiz., No. 9–10, 10 (1997).
23. O. B. Danilov and S. A. Tul'skiĭ, Zh. Tekh. Fiz. **48**, 2040 (1978).
24. É. I. Asinovskiĭ, L. M. Vasilyak, and S. Yu. Unkovskiĭ, Zh. Tekh. Fiz. **62**, 184 (1992) [Sov. Phys. Tech. Phys. **37**, 339 (1992)].
25. V. A. Danilychev and V. D. Zvorykin, Tr. FIAN **142**, 117 (1983).
26. A. F. Alexandrov, L. S. Bogdankevich, and A. A. Rukhadze, *Principles of Plasma Electrodynamics* (Vysshaya Shkola, Moscow, 1978; Springer-Verlag, Berlin, 1984).

Translated by A. D. Smirnova[†]

[†] Now deceased.

Plasma Physics Reports, Vol. 26, No. 4, 2000, pp. 328–334. Translated from Fizika Plazmy, Vol. 26, No. 4, 2000, pp. 355–361.

LOW-TEMPERATURE PLASMAS

Scanning Calorimetry Measurements of the Gas Temperature in an RF-Discharge Fluorine-Containing Plasma

A. N. Magunov and O. V. Lukin

Institute of Microelectronics, Russian Academy of Sciences, ul. Universitetskaya 21, Yaroslavl, 150007 Russia

Received November 4, 1998; in final form, July 5, 1999

Abstract—The neutral-gas temperature in a low-pressure (50 Pa) capacitive RF discharge in a $CF_4 + O_2$ mixture is determined from the heating kinetics of a gallium arsenide single crystal, which is chemically inert to any radicals in a fluorine-containing plasma. Experimental methods are discussed that make it possible to confirm the absence of heat sources capable of additional heating of the calorimeter in the discharge. The features and applicability limits of the method of non-steady-state gas thermometry in a weakly ionized nonequilibrium plasma are discussed. The method proposed is compared with conventional steady-state methods based on measurements of the established temperature of a thermal probe in the discharge. Temperature scanning makes it possible to study dependences that cannot be investigated by steady-state methods, in particular, the temperature dependence of the calorimeter heating power, which is very important for diagnosing the processes of plasma–surface heat transfer. © *2000 MAIK "Nauka/Interperiodica".*

1. INTRODUCTION

Plasma and plasmochemical technologies can be successfully developed only if there is a sufficiently wide range of fast-operating diagnostics. The absence of such methods in microtechnology leads to a situation in which the regimes of plasma–surface interaction in the majority of research and commercial devices are sought for only from the final result, by the trial-and-error method for each individual device. One of the important discharge parameters is the neutral-gas temperature. At low pressures (~1 torr and below), the gas temperature T_g depends on the state of the reactor wall, because the rates of the surface processes involving excited states or radicals can vary over orders of magnitude depending on the composition and properties of the absorbed layers. The excited states can either substantially contribute to gas heating in the bulk of the discharge [1] or can be deactivated on the wall and the electrode surface. Therefore, the measurement of T_g in a discharge is one of the methods allowing one to control the reproducibility of microtechnological processes. The simplest and most frequently used measurement techniques are contact diagnostics. In recent years, contact thermometers (thermocouples and thermoresistors), the data from which are recorded by the electric signals, have been replaced with contact thermometers based on optical recording [2–4], whose advantage is that the signal is insensitive to electrical noise. Nonsteady-state methods provide more informative measurements as compared to steady-state ones, but with poorer spatial resolution. At present, these methods are employed only in large-volume plasmochemical reactors (10–20 cm in radius).

Previously, measurements of the gas temperature by scanning calorimetry were carried out with the use of a silicon single crystal. For some gases (He, Ar, N_2, O_2, or CF_4) at pressures from 10 to 100 Pa, measurements were carried out in an RF discharge [2, 5]. However, we failed to measure the gas temperature in mixtures of tetrafluorinemethane and oxygen ($CF_4 + O_2$) because of the surface exothermic reaction between atomic fluorine and silicon. This mixture (along with others) is widely used in plasmochemical microtechnology to etch silicon during the production of integrated microcircuits, optical devices, etc. Therefore, it is necessary to develop the methods for measuring the gas temperature in these chemically active media.

In this paper, we present the results of measuring the gas temperature in an RF discharge excited in a cylindrical reactor in a $CF_4 + O_2$ mixture. The calorimeter is made of a GaAs single crystal, which is chemically inert to fluorine-containing plasma. We also discuss some features of the method that are important for the interpretation of the experimental results.

2. EXPERIMENT

The measurements were carried out in a 45-cm-long cylindrical quartz reactor with an inner diameter of 19 cm (the schematic of the reactor is described in [6, 7]). Semicylindrical external electrodes excited an RF discharge at a frequency of 13.56 MHz. The electrodes were separated from the plasma by a 5-mm-thick quartz wall. The deposited power was 260 W. The pressure of the $CF_4 + O_2$ mixture was 50 Pa, and the circulation rate was ~100 cm^3/min. A small additive of oxygen in the discharge mixture led to a substantial

1063-780X/00/2604-0328$20.00

increase in the concentration of atomic fluorine compared to a discharge in pure tetrafluorinemethane, all other conditions being the same [8, 9]. The discharge in a mixture of the same composition but with a small amount of CF_4 results in a high degree of dissociation of oxygen [10]. The oxygen content in the mixture varied from zero to 100%. The calorimeter was made of a polished 0.43-mm-thick gallium arsenide monocrystalline plate 2×2 cm in size. The electric resistivity of the semi- insulating chromium-doped crystal was approximately 10 MΩ cm [11]. The crystal attached to two quartz rods 1.5 mm in diameter was located on the axis of the reactor. One end of the cylindrical reactor was a polished quartz plate, which served as an optical window. After the discharge was switched on and off, the crystal temperature $T(t)$ was measured by laser interferometry [12]. Probing radiation of an He–Ne laser with a wavelength of 1.15 μm fell on the crystal at an angle of 5° in order to eliminate interference in the optical window, which was also heated by thermal flux from the discharge, and was reflected to a photodetector (an FD-7G germanium photodiode operating in the photogalvanic regime). In addition to the 1.15-μm wavelength radiation, an LG-126 laser produced radiation at the 1.08-μm wavelength with the power one order of magnitude less than the radiation at the main wavelength. Both of these lines fall into the transparency range of the crystal; therefore, these waves interfered in the crystal and caused beating at the photodetector. In order to avoid this effect, an interference filter (with a maximum transparency at 1.15 μm) was placed in front of the photodetector to cut off the 1.08-μm line. The interferogram (Fig. 1) was recorded by an H-3021 recorder. The temperature was determined at the instants corresponding to the extremums of the interferogram. The random error of the temperature measurements was less than 0.1 K in the range $T = 300$–700 K.

In contrast to silicon single crystals (as well as quartz glass), the GaAs crystal does not interact with fluorine-containing radicals (including atomic fluorine). For this reason, the heating of a GaAs crystal in the fluorine-containing plasma is not accompanied by the thermal effect of plasmochemical reaction. Another advantage of gallium arsenide over silicon is a higher temperature sensitivity in laser-interferometry measurements [13]. This leads to a greater number of interference extremums per unit temperature interval for a GaAs crystal than for a silicon crystal of the same thickness. The third advantage of GaAs over Si is a wider band gap of the crystal ($E_g \approx 1.4$ eV for GaAs and $E_g \approx 1.1$ eV for Si). Therefore, the radiative loss at high temperatures is smaller with a GaAs calorimeter because thermal radiation from the crystal is caused by free carriers (electrons in the conduction band and holes in the valence band), whose concentration increases with temperature according to the Arrhenius law with the activation energy equal to the half-width of the band gap of the crystal [14]. Under the same discharge conditions, a GaAs calorimeter is heated to a higher temperature than a silicon one; i.e., the temperature scanning range for a GaAs calorimeter is wider than for a silicon calorimeter (and substantially wider than for a quartz calorimeter, which has the highest rate of radiative heat removal).

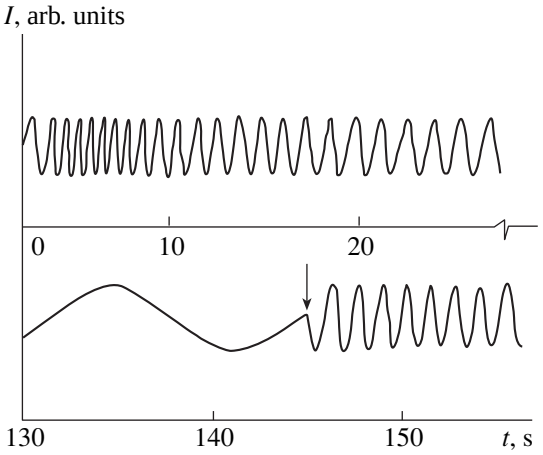

Fig. 1. Time dependence of the radiation intensity (λ = 1.15 μm) reflected from a 0.43-mm-thick GaAs single crystal inserted in an RF discharge in a $CF_4 + O_2$ mixture at a 50-Pa pressure. The measurements are carried out after the RF discharge was switched on and off. The arrow shows the instant the discharge was switched off.

3. RESULTS AND DISCUSSION

Time dependences of the crystal temperature after switching on and off the discharge are presented in Fig. 2. The discharge was excited in a $CF_4 + O_2$ mixture at different partial pressures of the components. It is seen that the crystal is heated to the highest temperature in the oxygen plasma. The temperature of a GaAs crystal in the discharge reaches 370°C, whereas the steady-state temperature of a silicon crystal is lower by 50°C under the same conditions; this is a result of lower radiative heat removal from GaAs.

An addition of tetrafluorinemethane to oxygen sharply decreases the steady-state crystal temperature in the discharge. By differentiating the dependences $T(t)$, we constructed the temperature dependences of the power density $D = c\rho h(dT/dt)$ spent on crystal heating in the discharge (here, c, ρ, and h are the specific heat, density, and thickness of the crystal, respectively). These dependences are presented in Fig. 3. In order to exclude time from the consideration and construct the temperature dependences, the heat transfer should be quasisteady; i.e., all of the processes should proceed as if the heating rate is zero. The coincidence of dependences $D(T)$ for calorimeters of different thicknesses (which differs by a factor of 3) proves that the heat-transfer rate is determined only by the instantaneous temperature of the surface and is independent of the

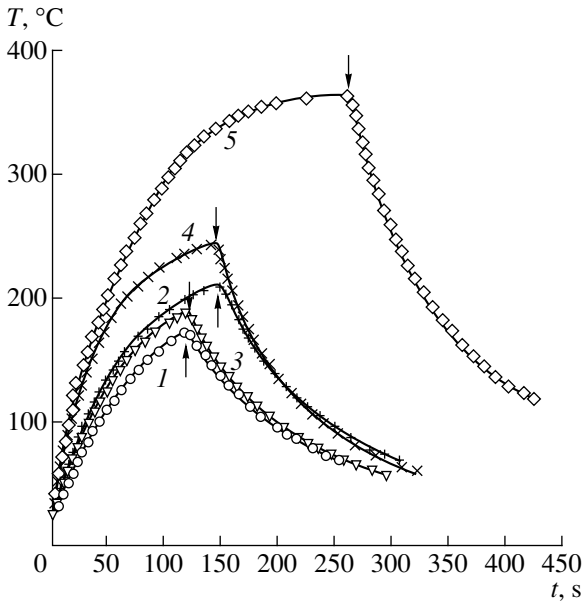

Fig. 2. Time dependence of the temperature of a GaAs crystal in a $CF_4 + O_2$ mixture at a 50-Pa pressure after the RF discharge was switched on and off. The vertical arrows show the instants the discharge was switched off. The oxygen content in mixture is (*1*) 20, (*2*) 40, (*3*) 60, (*4*) 90, and (*5*) 100%.

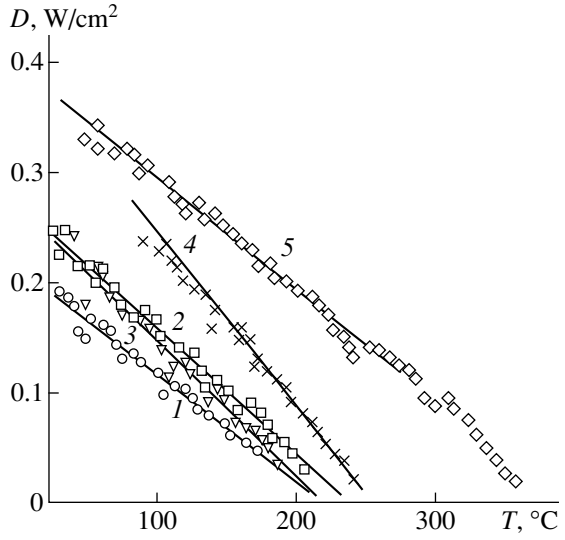

Fig. 3. Temperature dependence of the power density heating the calorimeter in the RF discharge in a $CF_4 + O_2$ mixture. The oxygen content in the mixture is (*1*) 20, (*2*) 40, (*3*) 60, (*4*) 90, and (*5*) 100%.

process duration; i.e., the heat transfer is actually quasisteady.

To determine the gas temperature, we extrapolate the linear dependence $D(T)$ to the point of intersection with the abscissa. The value of T at which the condition $dT/dt = 0$ holds is equal to the gas temperature. This method is based on the fact that almost the entire heat flux falling on the calorimeter surface is associated with a sole heat-transfer mechanism. This mechanism includes both the energy transport from the discharge to the surface by neutral-particle molecular heat conduction and the relaxation of the translational energy of particles in their collisions with the surface. This mechanism is characterized by the following features.

(i) The power deposited on the surface decreases with the surface temperature. It is usually assumed [15] that the dependence $D(T)$ must be nonlinear if the initial difference between the gas and surface temperatures is greater than several degrees. However, this is not the case at low gas pressures: the dependence $D(T)$ is linear even for an initial temperature difference of several hundred degrees [7]. We also observed the linear temperature dependence $D = A - BT$. Using an empirical approximation based on the plots $D(T)$ (Fig. 3), we determine both parameters A and B. If the heat-transfer rate is determined only by the transport and relaxation of the particle kinetic energy, the dependence has the form $D = 2\alpha(T_g - T)$, where α is the heat transfer coefficient and T_g is the gas temperature outside the thermal boundary layer. Thus, $B = 2\alpha$ and $A/B = T_g$. The deviation of the dependence $D(T)$ from linear points to the presence of additional heat sources (e.g., heat release in the surface plasmochemical reaction [16]).

(ii) The heat-transfer rate is limited by the rate of energy transfer across the boundary layer, whose thickness is comparable with the characteristic size of the calorimeter. To verify this, we examined how the heating rate constant $k\ (s^{-1}) = 2\alpha/c\rho h$ changes when the calorimeter size is varied. If the rate constant increases with decreasing the calorimeter size, then the limiting process is the diffusive heat transfer. The reason is that, as the calorimeter size decreases, the thickness of the boundary layer near the surface also decreases and the temperature gradient in the layer and the density of the heat flux on the surface increase. Hence, we obtain that the characteristic heating time $\tau = k^{-1}$ decreases with decreasing the crystal size.

(iii) The surface properties have no effect on the heat-transfer rate because the relaxation of the kinetic energy of particles in their collisions with the surface proceeds during a single collision and, thus, cannot be a limiting factor. We can verify this by comparing the heating kinetics for calorimeters of the same shape and mass but with different surface properties (e.g., with deposited thin films whose surface accommodation coefficients for kinetic energy are different; to ensure this, the surface material should include atoms with very different atomic masses [17]). It is difficult to check the calorimeter for this property, because any calorimeter surface is covered with an absorbed-water film, which is hard to remove.

(iv) When the power deposited in the discharge is varied, the changes in the parameters α and T_g correlate: an increase in the temperature T_g results in an

increase in the parameter $\alpha \sim \lambda \sim (T_g)^n$ (here, λ is the heat conductivity of a gas and $n \approx 0.7$–1, depending on the gas species). This fact allows us to distinguish the effect of gas heat conduction and thermal effects of the catalytic and chemical processes on the surface when the dependence $D(T)$ is linear because of the weak temperature dependence of the rates of heterogeneous processes. The influence of heat release due to heterogeneous processes on the heating manifests itself in the apparent increase in T_g and simultaneous apparent decrease in α with increasing the deposited power. Such behavior is unlikely to occur; therefore, there must be an additional heat source that is not related to the gas heat conduction. Just in this fashion, we found an additional heat source on the surfaces of an Si single crystal and SiO_2 film in a $CF_4 + O_2$ plasma. Thus, the limited applicability of a silicon calorimeter for the diagnostics of a fluorine-containing plasma was demonstrated. Figure 4 shows the parameters α and T_g as functions of the deposited power in a CF_4 discharge. Both parameters increase simultaneously with increasing the deposited power; this shows that the heat release due to deactivation of the excited levels on the crystal surface is insignificant.

Experiments carried out to verify each of the above features prove that, for a low deposited power, the calorimeter heating is associated with a sole heat-transfer mechanism. Thus, the calorimeter is catalytically and chemically inert. Therefore, the neutral gas temperature in the discharge can be determined from the heating kinetics of the calorimeter. The contribution of both the ion bombardment and charged-particle recombination on the surface to the crystal heating is less than 10^{-3} of the power of the integral heat source, because the degree of ionization in the discharge is fairly low ($\sim 10^{-6}$). Radiation from the discharge is also insignificant for the thermal balance in the crystal. This was confirmed in experiments with crystals covered with antireflective dielectric films with thicknesses from 0.2 to 1μm; in this case, the absorption of the optical radiation falling on the crystal increased by a factor of 1.5 to 2.

The gas temperature in the discharge and the heat transfer coefficient for different oxygen contents in a $CF_4 + O_2$ mixture are shown in Fig. 5. It is seen that α is a nonmonotonic function of the oxygen content. This is also seen in Fig. 3, where the inclination of the $D(T)$ curves changes nonmonotonically. The dependence of the heat transfer coefficient on the oxygen content in the mixture is related to the change in the degree of dissociation of the gas, which manifests itself in the change of the gas thermal conductivity. The degree of dissociation of O_2 is maximum when a small amount (approximately 10%) of CF_4 is added; in this case, the heat transfer coefficient is also maximum. The reason for the nonmonotonic dependence of the axial gas temperature in the reactor on the oxygen content is unknown, because we do not know all of the chemical processes contributing to the gas heating (the heating of molecules by elastic collisions with electrons is insignificant under the conditions of our experiment). The gas temperature in the oxygen discharge is ~150 K above that in the mixture. This may be associated with the different distributions of the RF power deposition in the discharges. With the same spatial distribution of the power deposition, the temperature on the reactor axis should be higher in a heavier gas with a lower thermal conductivity.

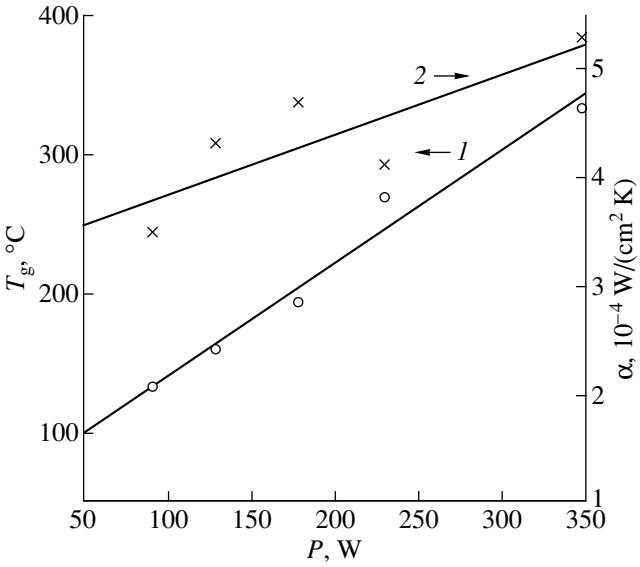

Fig. 4. (*1*) Gas temperature T_g and (*2*) the heat transfer coefficient α as functions of the power deposited in the RF discharge in CF_4. The pressure is 50 Pa.

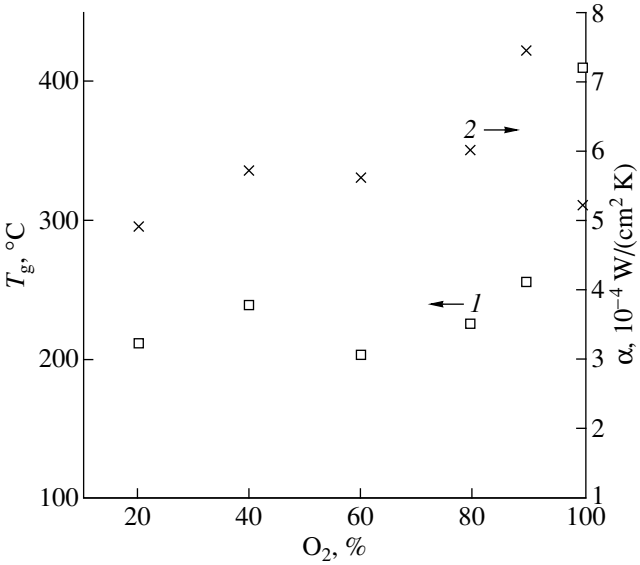

Fig. 5. (*1*) Gas temperature T_g and (*2*) the heat transfer coefficient α as functions of the oxygen content in the RF discharge in a $CF_4 + O_2$ mixture. The pressure is 50 Pa, and the deposited power is 260 W.

The measurement error in T_g is mainly determined by low-frequency (~0.01–0.1 Hz) fluctuations of the deposited power. The change in the deposited power causes a change in the gas temperature, which leads to the deviation of the $D(T)$ dependence from linear (Fig. 3, upper curve). Depending on the number of points that are used to determine the parameters of the empirical approximation $D = A - BT$, the obtained value of T_g falls within a range of 20–40 K. Therefore, the random measurement error is assumed to be ±20 K. Fluctuations of the energy deposition are peculiar to any individual device and discharge; therefore, the presented estimate for the error is only tentative and cannot serve as an actual characteristic of the method.

In the discharge with 80–100% CF_4, the quartz walls of the reactor are heated only slightly in contrast to O_2, N_2, or Ar discharges, in which the wall temperature increases by 20–40 K in 2–3 min with the same deposited power. The heat balance of the discharge is still unknown. The neutral particle gains, on average, 1–2-eV energy in the time it stays in the reactor (~0.1 s). The questions of where, in which process, and at which rate this energy is transferred to the solid body or released in some other way (e.g., in the pumping system outside the reactor) are still unanswered.

4. COMPARISON OF STEADY-STATE AND NONSTEADY-STATE MEASUREMENTS OF T_g

To perform contact measurements of the gas temperature in discharges, thermal probes with a size as small as possible are usually used [18]. The restrictions on the probe size are determined by the need to decrease perturbations introduced in the discharge by the thermal probe. However, this results in a loss of information necessary for the interpretation of the experimental data. Let us consider the simplest heat-balance equation for the thermal detector, assuming that the heterogeneous processes and corresponding heat release are absent:

$$cmdT/dt = \alpha S(T_g - T) - \varepsilon\sigma S(T^4 - T_0^4).$$

Here, m is the mass of the heat detector, S is its surface area, ε is the effective emission coefficient (with the geometry of the experiment being taken into account), σ is the Stefan–Boltzmann constant, and T_0 is the wall temperature. The temperature-relaxation time of a small-mass thermal detector (e.g., a thermojunction 0.2–0.4 mm in diameter or a portion of a 0.1-mm-diameter optical fiber) is comparable with the relaxation time of the discharge parameters (~0.1–1 s). Therefore, for analysis, we use only the established temperature of a thermal probe, when the heat flux from the discharge is balanced out by the radiative heat removal. Thermal equilibrium ($T = T_g$) is possible only for a nonemissive thermal probe. For $\varepsilon \neq 0$, the heat balance equation contains two unknowns (α and T_g), so that, in order to determine T_g, we need to know the heat transfer coefficient. In the previous section, it was shown that, in the non-steady-state method, the coefficient α is determined by the inclination of the curve $D(T)$ in each particular experiment. In steady-state measurements [18], the heat transfer coefficient is determined from the similarity theory. For small Knudsen numbers (Kn $\ll$ 1), we have $\alpha = \mathrm{Nu}\lambda/L \sim (T_g)^n L^{-1}$, where Nu is the Nusselt number determined from the probe shape, L is the characteristic size of the probe, and $n \leq 1$. In this case, the rate of the heat transfer between the gas and surface is independent of the surface properties, because the main resistance to the heat transport is offered by the boundary layer. However, for the gas pressures $p \leq$ 1–3 torr, the condition of the applicability of the continuous-medium model is violated for thermal probes with a characteristic size of $L \sim 1$ mm. In the intermediate pressure range, the coefficient α is lower than in the case when the continuous-medium model is valid. In addition, this coefficient depends on the pressure and on the accommodation coefficient γ of the kinetic energy: $\alpha \sim \gamma p (T_g)^{-1/2}$.

Extrapolation of the results of the similarity theory, which is valid for heat transfer in a continuous medium, to the intermediate pressure range (Kn ~ 1) results in a severalfold overestimation of the coefficient α and a too low value of T_g. This error seems to increase with decreasing the pressure and increasing the gas temperature. Thus, the steady-state methods for determining the gas temperature with the use of emissive thermal probes are inapplicable in the intermediate pressure range, because we failed to measure the heat transfer coefficient and the probe temperature simultaneously. For example, if the measured values are T = 700 K, T_0 = 300 K, and ε = 1, then, in a CF_4 discharge at p = 0.3 torr, we obtain $T_g \approx$ 770 or 1260 K, depending on which approximation for α is chosen for the measurements carried out with a spherical thermal probe 0.5 mm in diameter.

The detector (the data from which are recorded by an electric signal) is a thermocouple placed inside a quartz or glass tube 1 mm in diameter. The tube walls are approximately 0.1 mm thick and are optically thick in the spectral region $\lambda \geq$ 3–5 μm, where, at the temperature $T \leq$ 1000 K, the Planck function is maximum. The result of measuring T_g with this detector in the steady-state regime at pressures $p \leq$ 3 torr cannot be reliably interpreted because of a lack of exact data on the heat transfer coefficient. In order to substantially (almost to zero) decrease the emission coefficient of the detector, the thermocouple surface can be protected by a plasmochemically deposited dielectric coating several tens of μm thick. In this case, the emission coefficient of the detector is almost the same as that of metal and does not exceed 0.01–0.03 in the infrared spectral region (instead of $\varepsilon \approx 0.9$ for a glass tube). Thus, we can avoid the need for determining the heat transfer coefficient and go over from the measurements in the heat-flux

regime to the regime close to thermal equilibrium between the detector and the gas. However, the measurements still provide limited information. For example, in the steady-state regime, we cannot separate the experimentally measured total heat flux into components related to different heat-transfer mechanisms. Also, we cannot study the kinetics of the heat transfer between the plasma and the surface. The non-steady-state method, which allows us to obtain the entire phase trajectory of the plasma–surface system in the temperature–power variables in each experiment, is much more informative than the steady-state method providing a single point of the phase trajectory.

The relaxation method allows us to determine the temperature dependence of the power heating the calorimeter. Such dependences cannot be obtained by the steady-state methods. This is an important advantage of scanning calorimetry over ordinary thermocouple measurements in the discharge. Scanning calorimetry allows experimental verification of the hypotheses for the heat-transfer mechanisms, which is impossible with the use of thermocouples. The relaxation method, in which information is read remotely with the use of a laser, makes it possible to use calorimeters made of various materials (Si, GaAs, and sapphire single crystals; glasses; etc.) and to vary the calorimeter size and surface properties. Presumably, for any chemically active medium, it is possible to find the material either to produce a calorimeter (as is done in this paper) or deposit thin protective films on the calorimeter surface in order to eliminate the thermal effect of surface plasmochemical reactions.

The temperature dependence $D(T)$ can be obtained due to the fact that the heating time of the calorimeter substantially exceeds the time needed for the discharge parameters to reach the steady state. However, the high heat capacity that can be achieved only in large-size calorimeters results in a low spatial resolution. We have not yet considered the trade-off problem of the minimum size of the calorimeter against maximum information. In this paper, the high spatial resolution of measurements is of minor importance, because we study the temperature near the reactor axis, where the radial dependence is gently sloping. However, if there is a need to measure T_g in the region of large temperature gradients (e.g., near the reactor walls), the problem of the crystal size is important and requires special analysis.

5. CONCLUSION

The possibility of measuring the gas temperature in a discharge by the heating kinetics of the calorimeter is based on the fact that, under the conditions of our experiment, the basic heat flux is that resulting from the relaxation of translational (and maybe rotational) degrees of freedom of the particles. Evidence for this statement can be formulated in the form of several conditions that can be verified experimentally. One of the arguments in favor of the absence of additional thermal sources is the following. As the deposited power increases, the gas temperature increases, whereas the heating time constant of the calorimeter decreases. The reason for such behavior is that the time constant depends on the thermal conductivity (i.e., temperature) of the gas outside the thermal boundary layer. Therefore, as the gas temperature increases, the thermal resistance decreases and both the heat transfer coefficient and the heating time constant $\tau \sim (T_g)^{-n}$ $(n \sim 1)$ increase. If there is an additional heat source (e.g., heat release with the Arrhenius temperature dependence of the rate), the increase in the deposited power can result in an apparent increase in the heating time constant even to infinity (in this case, the curve $D(T)$ is in parallel to the abscissa). Since a simultaneous increase in T_g and τ is impossible, the observed deviation of the experimental data from the standard behavior can be evidence that the heat transport is associated not only with the relaxation of translational and rotational degrees of freedom of the particles on the surface but also with an additional heat source. Such a pattern was previously observed when T_g was measured in a $CF_4 + O_2$ plasma with a silicon single-crystal calorimeter covered with an oxide film.

To measure the gas temperature in a chemically active medium, the calorimeter should be made of materials that do not produce volatile reaction products in interactions with active particles. In this case, the thermal effect of the surface plasmochemical reaction is associated with the formation of one or more monolayers consisting of reaction products. After several layers are formed, the reaction slows down and then terminates, because the reagents (chemically active particles from the discharge and crystal-lattice atoms) are spatially separated by these layers. It is this technique that allows measurements in oxygen or nitrogen plasma with the use of a silicon calorimeter (silicon oxides and nitrides are nonvolatile at such low temperatures) or in a $CF_4 + O_2$ discharge with the use of a GaAs calorimeter (produced fluorides are nonvolatile). For discharges in mixtures containing chlorine and bromine, in which GaAs undergoes etching, other calorimeter materials should be used.

Obviously, any calorimeter measures its own temperature. For the lack of data on the heat-transfer kinetics, it is not always possible to find the relation between the steady-state temperature of the emissive thermal probe and the gas temperature. At pressures of 0.1–1 torr, T_g measurements with the use of thermocouples and other thermal detectors are almost always wrong (the gas temperature is underestimated by tens or hundreds of degrees due to the erroneous assumption of the heat transfer coefficient). Therefore, in order to carry out measurements in the intermediate pressure range in the regime of thermal equilibrium with a gas (rather than in the heat-flux regime), it is more appropriate to employ nonemissive thermal probes. None-

missive thermal detectors can be produced by standard plasmochemical methods that are widely used in microtechnology. A submicron dielectric film deposited on the surface of a metal probe serves two purposes: the surface becomes catalytically inert, and the emission coefficient of the obtained structure is lower by a factor of several tens than the emission coefficient of glass tubes that are presently being used in thermocouple measurements. However, even with the use of new technologies, it is impossible to make steady-state thermometry measurements in discharges more informative. The most that can be obtained by steady-state methods is the determination of T_g, whereas for nonsteady-state methods this is only the starting point from which the study of the mechanisms for plasma–surface heat transfer begins.

ACKNOWLEDGMENTS

This work was supported by the Russian Foundation for Basic Research, project no. 96-02-18164.

REFERENCES

1. V. V. Rybkin, A. B. Bessarab, and A. I. Maksimov, Teplofiz. Vys. Temp. **34**, 181 (1996).
2. A. N. Magunov, Pis'ma Zh. Tekh. Fiz. **18** (10), 44 (1992) [Sov. Tech. Phys. Lett. **18**, 317 (1992)].
3. S. R. Kidd, J. S. Barton, M. N. Inci, *et al.*, Meas. Sci. Technol. **5**, 816 (1994).
4. V. Everett, K. T. Jones, G. B. Scelsi, *et al.*, Aust. J. Phys. **48**, 527 (1995).
5. A. N. Magunov, O. V. Lukin, and A. Yu. Gasilov, Teplofiz. Vys. Temp. **37**, 202 (1999).
6. A. N. Magunov, Prib. Tekh. Éksp., No. 5, 131 (1995).
7. A. N. Magunov, Fiz. Plazmy **23**, 1018 (1997) [Plasma Phys. Rep. **23**, 940 (1997)].
8. W. R. Harshbarger and R. A. Porter, Solid State Technol. **21** (4), 99 (1978).
9. R. d'Agostino and F. Fracassi, in *Proceedings of the Piero Caldirola International School of Plasma Physics, Varenna, Italy, 1992*, Ed. by G. Bonizzoni, W. Hooke, and E. Sindoni (SIF, Bologna, 1993), p. 309.
10. O. Auciello, D. E. Ibbotson, and D. L. Flamm, Nucl. Instrum. Methods Phys. Res. B **23**, 419 (1987).
11. M. G. Mil'vidskiĭ, *Semiconductive Materials in Modern Electronics* (Nauka, Moscow, 1986).
12. A. N. Magunov and E. V. Mudrov, Teplofiz. Vys. Temp. **30**, 372 (1992).
13. A. N. Magunov, Prib. Tekh. Éksp., No. 3, 6 (1998).
14. A. N. Magunov, Pis'ma Zh. Tekh. Fiz. **20** (7), 65 (1994).
15. S. S. Kutateladze, *Handbook of Heat Transfer and Hydrodynamic Resistance* (Énergoatomizdat, Moscow, 1990).
16. A. N. Magunov, Pis'ma Zh. Tekh. Fiz. **21** (5), 44 (1995) [Tech. Phys. Lett. **21**, 185 (1995)].
17. R. G. Barantsev, *Interaction of Rarefied-Gas Flows with Surfaces* (Nauka, Moscow, 1975).
18. D. I. Slovetskiĭ, *Mechanisms for Chemical Reactions in Nonequilibrium Plasmas* (Nauka, Moscow, 1980).

Translated by A. D. Smirnova[†]

[†] Now deceased.

Plasma Physics Reports, Vol. 26, No. 4, 2000, pp. 335–343. Translated from Fizika Plazmy, Vol. 26, No. 4, 2000, pp. 362–370.

PLASMA ELECTRONICS AND NEW ACCELERATION METHODS

Plasma Electronics and Plasma Acceleration of Charged Particles[1]

Ya. B. Faĭnberg

National Science Center Kharkov Institute of Physics and Technology, Akademicheskaya ul. 1, Kharkov, 310108 Ukraine

Received September 6, 1999

Abstract—Preliminary results are summarized from studies on plasma electronics and plasma acceleration of charged particles, recent advances in this field are analyzed, and the challenging problems are outlined. *© 2000 MAIK "Nauka/Interperiodica".*

1. PLASMA ELECTRONICS

Plasma electronics and plasma methods of accelerating charged particles have become an integral part of plasma physics and accelerator science and technology [1–3]. Until recently, nonlinear and quasilinear theories of the beam–plasma interaction (BPI) and, accordingly, the theory of beam–plasma oscillators and amplifiers took into account only beam-related nonlinear effects and described plasma-related effects in the linear approximation. In the last few years, the generation and amplification of microwave radiation has been investigated self-consistently in the nonrelativistic approximation with allowance for the effect of microwaves excited in the BPI on the plasma parameters (primarily, on the plasma density). It was shown that plasma-related nonlinear effects (longitudinal and transverse ponderomotive forces and parametric resonances) cause the microwaves excited in the BPI to generate ion oscillations and waves, thereby changing the plasma density. As a result, the plasma becomes inhomogeneous[2] and unsteady, which may lower the intensity of the excited microwaves (or even stop their excitation) and substantially change the microwave spectrum [4, 5]. A theory developed with allowance for the ponderomotive forces in a plasma makes it possible to infer the processes that reduce the intensity of microwaves excited in the BPI or even prevent their excitation. The theoretical predictions agree well with the experimental data [6]. The next step in this direction is to investigate how to avoid unfavorable effects associated with the ponderomotive forces in the course of BPI in a plasma.

The way in which microwaves become coupled nonlinearly with low-frequency plasma oscillations and waves is well described in [7–9]. The main difficulty in constructing the relevant theory is the necessity of describing self-consistently not only the aforementioned processes but also (in the nonlinear approximation) the excitation of waves in the BPI and their evolution.

The influence of parametric instabilities on the BPI was studied by Karas' *et al.* [10, 11]. They investigated the problem of how a periodic plasma inhomogeneity affects the BPI by analyzing a three-wave interaction (involving ion acoustic, electromagnetic, and plasma waves) under the assumption that the ion acoustic wave is specified *a priori*. They showed in particular that, if the three waves stay synchronized with each other in time and space and if the plasma wave amplitude is smaller than the amplitude at which the plasma wave starts to trap the beam electrons, then the BPI may be more efficient.

In reviewing the recent progress in plasma electronics, it is necessary to point out the advances achieved in investigating and fabricating high-power long-pulse plasma-based microwave oscillators. Among the papers on this topic, we should, first of all, mention the paper by Goebel *et al.* [12], in which they described their work on creating a microwave Plasma-Assisted Slow-Wave Oscillator (PASOTRON). The PASOTRON is already capable of operating at a power of about 5 MW, the pulse duration being 100 μs. Such a high efficiency of the oscillator is, to a great extent, attributed to its operation with a plasma, although, as is seen from the literature, the advantages of using plasmas in electrodynamic systems (such as waveguides and resonators) are not employed in full measure. In particular, this concerns the possibility of controlling dispersion properties by varying plasma parameters. However, other plasma functions are well employed in the PASOTRON. First, the plasma created in a hollow cathode serves as a very efficient electron emitter, such

[1] Supplemented version of the address at the opening of the VI International Seminar on Plasma Electronics and New Acceleration Techniques, Kharkov, 1998.

[2] Recall that the plasma homogeneity is of crucial importance because of the resonant nature of the wave–particle interaction ($\nu_{ph} = \nu_{par}$), which underlies collective BPI. Consequently, the generation and amplification of microwaves in the BPI are very sensitive to the plasma inhomogeneity, which results, in particular, from nonlinear plasma processes.

1063-780X/00/2604-0335$20.00 © 2000 MAIK "Nauka/Interperiodica"

that it ensures current densities of 50–80 A/cm^2. Another important feature is the possibility of focusing an electron beam in the BPI region without using a magnetic field, in which case the role of the external magnetic field is played by beam self-pinching in the plasma. These results are great importance for studies carried out with traditional plasma-based microwave devices. However, with the aim of better realizing the advantages of plasma electronics, the beam electrons should also be accelerated in a plasma (rather than in a vacuum) in order to overcome the restrictions on the beam current magnitude that are associated with the electron space charge in the beam.

In recent years, interesting and important papers have been published on the radical modification of klystrons via the collective interaction of charged-particle beams with plasmas and on klystron bunching as a means of producing ultrashort (shorter than 100 fs) electron bunches, which are utilized in new plasma-based charged-particle acceleration schemes and can also be used to create intense sources of infrared radiation.

Katsouleas and Clayton [13] suggested to excite electromagnetic wake waves in a plasma by intense laser light, which can be used to ionize a neutral gas layer and create a plasma slab with controlled parameters. Momentum transfer from the electromagnetic wake field to a relativistic electron beam (REB) in a plasma slab causes the beam to propagate in the drift space and evolve into a periodic train of short electron bunches.

Pasour *et al.* [14] developed and created a high-power klystron, in which bunching occurs under the action of an electromagnetic wake wave excited by the leading edge of a high-current REB propagating in a plasma. The electric field modulates the wake wave of an REB with an initially uniform density and thus breaks the beam up into a periodic train of very short bunches, which excite an electromagnetic field in a conventional waveguide structure. The length and repetition rate of the bunches are controlled merely by varying the plasma density. The most important feature of this klystron, in which electromagnetic waves are actually generated during the BPI, is that there is no need to solve a complicated problem of converting electrostatic space-charge waves into the emitted electromagnetic radiation.

Another way of utilizing the plasma in order to substantially increase the efficiency of present-day (rather than conventional) oscillators and amplifiers (especially those operating in millimeter, submillimeter, and even shorter wavelength ranges) is to exploit oblique waves excited in the plasma of free electron lasers instead of mechanical wigglers, which restrict the possibility of shortening the wavelengths of the excited microwaves [15].

Despite the significant progress achieved in plasma electronics, there are still a number of questions that lack adequate answers. The most important problem here is that of investigating the interaction between stochastic electromagnetic radiation and matter both theoretically and experimentally. The development and creation of beam–plasma microwave oscillators and amplifiers have been the subject of significant research efforts. Now, the theory of microwave sources has been constructed (at least in the linear approximation) and the sources have been fabricated, so that an important step has been taken toward studying stochastization processes in the BPI and it has become relevant to examine the interaction of stochastic radiation with matter and, in particular, to continue investigations of the interaction between stochastic radiation with charged particles in a plasma. Bass *et al.* [16] demonstrated the possibility of efficient plasma heating by stochastic radiation in the BPI. The physical mechanism underlying such heating is trivial. It is well known that, in the course of interaction of a regular microwave field with a charged particle, the particle energy averaged over the microwave field period does not grow if binary collisions are neglected. In the presence of collisions, the averaged particle energy changes in proportion to the collision frequency. This effect can be explained in a trivial way as follows: since collisions change the phase of a particle in the microwave field, the averaged (over the field period) energy acquired by a particle due to collisions is nonzero. If the phase of an electromagnetic field undergoes a random jump, the phase of a particle in the field will change in the same manner as in the binary collision event. However, electromagnetic random-phase fields are a particular case of stochastic electromagnetic fields: in interactions with particles, they play a role similar to binary collisions; the rate at which the field phase undergoes jumps is an analogue of the frequency of binary collisions; and the averaged (over the field period) energy acquired by a particle is proportional to this rate. This simple example clearly illustrates one of the features of the interaction between charged particles and random electromagnetic fields.

Since the electromagnetic-field–particle interaction underlies many processes involving the interaction between radiation and matter, we may expect that the stochastic-radiation–charged-particle interaction will differ from the interaction of regular (in particular, microwave) radiation with charged particles in some important aspects. We can state that investigating the interaction between stochastic microwave fields and matter will serve to substantially generalize the theory of radiation–matter interaction and significantly extend the area in which this interaction may find practical applications. It is well known that stochastic electromagnetic fields can serve to efficiently accelerate charged particles and heat plasmas; they can also take part in many other processes that are important from the standpoint of plasma electronics. Recall that, even in the absence of binary collisions and even when particles and electromagnetic fields propagate in a nonres-

onant or asynchronous fashion, these phenomena are accompanied by energy transfer between stochastic microwave fields and charged particles. Of course, the average energy transferred from an electromagnetic field to charged particles increases in proportion to $\sqrt{t}$ rather than t, as in the case of resonant interaction. However, since the fraction of the energy exchanged between the field and the particles can be fairly significant, it is necessary to take into account the interaction between charged particles and stochastic electromagnetic fields together with other nonlinear effects that are described by terms proportional to $\sim E^2$. Comparing the expression for the energy acquired by a charged particle interacting with a regular microwave field in the presence of binary collisions with the relevant expression for the case of interaction with a stochastic electromagnetic field in the absence of binary collisions (the latter expression has been derived using a partially phenomenological, quasilinear theory of a weakly turbulent plasma with allowance for correlations among stochastic electromagnetic fields), we can see that these expressions are similar to each other and contain the inverse correlation time τ_{cor}^{-1} in place of the frequency of the binary collisions [16].[3]

Recall that there is both theoretical and experimental evidence (such as plasma heating and charged-particle acceleration) for possible efficient interaction of stochastic microwave radiation with charged particles. Then, the question naturally arises as to how much the interaction between stochastic radiation with matter differs from the interaction of regular microwave fields with charged particles. Let us list some relatively simple (not too involved) theoretical and experimental problems that are to be solved in the future:

1. Investigation of the absorption of stochastic microwave radiation in plasmas, metals, superconductors, semiconductors, dielectrics, and ferrites in the hydrodynamic and kinetic approximations.

2. Investigation of normal and anomalous skin effects in plasmas, metals, semiconductors, and ferrites.

3. Derivation of analogues of the Leontovich–Rytov boundary conditions for stochastic fields.

4. Investigation of the possibility of deriving an analogue of the Kramers–Kronig relation for stochastic fields.

5. Investigation of the parametric resonance in stochastic microwave fields.

6. Derivation of the expression for the microwave pressure force in stochastic electromagnetic fields.

7. Investigation of the characteristic features of the generation and amplification of stochastic radiation in millimeter, submillimeter, visible, ultraviolet (UV), and X-ray spectral ranges.

8. Investigation of the interaction of stochastic radiation with solid-state and space plasmas.

9. Investigation of the possibility of charged-particle acceleration by stochastic fields in vacuum.

10. Investigation of the effect of stochastic radiation on the processes in Josephson transitions.

11. Investigation of the "stochastic resonance" from the standpoint of applications to plasmas and devices based on the Josephson effect (SQUIDs, etc.).[4]

We should say a few words about the last problem. In the early 1980s, a very interesting phenomenon, which was called "stochastic resonance," was predicted theoretically and then confirmed experimentally. Although, in my opinion, this name is not quite correct and the physical mechanisms underlying this phenomenon have not yet been clarified in full measure, numerous theoretical and experimental investigations have shown that this fundamental phenomenon is peculiar to many nonlinear systems. In this connection, we refer the reader to original papers [17–19], very useful reviews [20, 21], and an interesting paper by Klimontovich [22], which was modestly entitled "Methodological Notes ...," but turned out to be of much greater importance.[5] Among the properties of stochastic resonance, the most important for practical applications is surely the following feature, which, at first glance, seems to be paradoxical: a stochastic perturbation acting on, e.g., a bistable system can increase the signal-to-noise ratio, the signal being a regular determinate perturbation. Hence, in contrast to the widely held opinion that a stochastic perturbation (noise) worsens the parameters of a dynamic system, such a perturbation in the case at hand can improve them. Note that it is not the only example of the favorable effect of stochastic perturbations: they can also be exploited for charged-particle acceleration (the Fermi mechanism), heating of collisionless plasmas, and other applications. For example, stochastic resonance may be used in a new generation of devices—SQUIDs—despite considerable natural and technological noises.

The phenomenon of the phase synchronization of a system of stochastic oscillators is closely related to the phenomenon of stochastic resonance. Phase synchronization is now being actively studied [23], in particular, with the aim to synchronize numerous generators of stochastic oscillations and waves.

[3] In [16], the plasma nonlinearity was taken into account merely by introducing a correlator of the Fourier components of a stochastic electric field, while the other nonlinear effects were neglected.

[4] In recent years, considerable interest has arisen regarding the following two problems:
(i) Investigation of the reasons for the shortening of a pulse in high-power relativistic microwave oscillators.
(ii) Investigation of the processes in plasma opening switches.

[5] The papers by A.A. Andronov, A.A. Vitt, and L.S. Pontryagin (1933) and H.A. Kramers (1940) also stand out as significant contributions to the theory of the effect of stochastic perturbations on nonlinear systems.

The next problem (the most important problem being the study of the interaction between stochastic radiation and matter) in plasma electronics is to achieve the generation and amplification of microwaves in millimeter, submillimeter, and even shorter wavelength ranges by either increasing the plasma density or by changing the frequency with the help of either Doppler or Compton effects associated with relativistic electron motion. At present, novel methods of upshifting the frequency (the so-called photon acceleration) are being actively studied. Increasing the plasma density involves considerable difficulties because binary collisions and collective interactions increase the dissipation of the energy of beam electrons, plasma electrons, and excited electromagnetic waves.

For example, even in a fully ionized plasma, the collision frequency is $\nu_{st} \sim n_p/T_e^{3/2}$, while the Langmuir frequency of the oscillations increases according to the law $\omega_p \sim n_p^{1/2}$. The way of lowering the collision frequency ν by increasing the electron temperature is inefficient. Of course, the unfavorable effect of collisions may be overcome by using short pulses (such that $\tau_{pul} < \nu_{st}^{-1}$), in which case, however, the pulses should be extremely short. We emphasize that, in plasma-based schemes for particle acceleration by space-charge wake fields, the relevant wake waves were already excited in a gas plasma of density 10^{17}–10^{18} cm^{-3} (but the lifetime of such a plasma was very short).

Millimeter and centimeter waves were successfully generated in the interaction between an REB and a dense (~10^{14}–10^{16} cm^{-3}) plasma, the beam pulse duration being about 2 μs.

The most natural way to shorten the wavelength of the excited microwave radiation is to generate microwaves in fairly homogeneous, solid-state, "quiescent" plasmas with very high densities (10^{14}–10^{18} cm^{-3} for semiconductors and 10^{22}–10^{23} cm^{-3} for metals). The very first experiments on the generation of electromagnetic waves in a semiconductor plasma in the collective BPI were carried out by Kornilov *et al.* [24], who took into account the remark made by Mandel'shtam (which is often cited in the literature) that, if the channel radius in a solid body is smaller than the wavelength, then an electromagnetic wave will propagate as if there is no channel. In those experiments, the authors succeeded in generating electromagnetic waves at a frequency of 3.7×10^{10} Hz by injecting electron beams into a 2-mm-wide channel in a semiconductor (germanium) at liquid-nitrogen temperature. The generation was governed by the beam–plasma dissipative instability (the temperature of a semiconductor sample was varied from 250 to 300 K and the plasma density in a semiconductor was varied from 2.3 to 2.6×10^{13} cm^{-3}).

We can expect that increased interest in a somewhat exotic scheme of particle acceleration in crystals (in which case the plasma density is as high as 10^{22}–10^{23} cm^{-3}) will stimulate active theoretical and experimental investigations on the generation of microwave radiation with very short wavelengths in solid-state plasmas.

It is well known that the frequency of the oscillations excited in a plasma of an REB in the absence of a magnetic field is no higher than ω_p, so that the problem arises as to how to convert oscillations with frequencies below the Langmuir frequency into those in the frequency range far above ω_p. This problem can be solved with the help of the Doppler effect and stimulated Compton effect associated with the motion of an REB and the effect of stimulated Raman scattering. In this way, it might be expedient to create a plasma-based free electron laser in which the role of the wiggler will be played by an oblique plasma wave [15]. The methods based on the reflection of microwave radiation from a moving plasma or propagating ionization front are decidedly promising in terms of increasing the frequency of the waves emitted from plasma-filled or gas-filled sources [25–28].

Among the recent works on relativistic plasma electronics, we should mention the fundamental paper presented at this seminar by A.A. Rukhadze and P.S. Strelkov and very important studies by E. Shamiloglu *et al.* and V.L. Granatstein *et al.*, which were published in the collection of papers *Digest of Technical Papers of International Workshop on High-Power Microwave Generation and Pulse Shortening, Edinburgh, 1997*, Ed. by F.I. Ogee *et al.*

2. PLASMA ACCELERATION OF CHARGED PARTICLES

One of the most promising present-day methods for collective acceleration [29–37] is a plasma-based scheme for particle acceleration by space-charge waves [34], which has already been investigated in many papers [30–37]. Among them is [34], in which the scheme was proposed; a very important paper [38], in which Tajima and Dawson suggested new efficient methods for exciting plasma waves by laser light [plasma beat-wave accelerator (PBWA) and laser wake-field accelerator (LWFA) schemes] and analyzed some relevant problems of particle acceleration; and a paper by Chen *et al.* [39], who proposed to excite plasma waves by a short electron bunch or a periodic train of electron bunches [plasma wake-field accelerator (PWFA)]. An important point here is that it was suggested to accelerate particles by wake plasma waves. Theoretical investigations [40, 41] (see also [42, 43]) and experimental works [44–47] (see also [48]) also substantially contributed to the development of acceleration schemes based on laser-driven plasma waves, and papers [49, 50] made significant contributions to research on the excitation of wake plasma waves by electron bunches in PWFA schemes. In recent years, the wake-field acceleration (WFA) method has been

substantially modified: a new version—self-modulated WFA (SMWFA), which is based on the self-modulation of a laser pulse—was proposed in [51, 52] (see also [53–55]). The most impressive results on plasma acceleration of charged particles were obtained in experiments described in [56, 57], in which the accelerating fields at short distances were as strong as 1.5–20 $\times$ 10^8 V/cm and particles were accelerated to energies of 100–300 MeV over distances of about 1 cm. Thus, the LWFA acceleration scheme is now being actively developed. The results achieved in the acceleration method based on relativistic electron bunch–driven wake plasma waves are not so significant: the accelerating fields are about 50 kV/cm, the bunch charge being about 4 nC. Recent progress in producing short dense electron bunches raises the hope that very strong accelerating fields will be achieved in PWFA research [13, 58].[6]

We should also say a few words about new possibilities of further increasing the accelerating field. Recall that the maximum electric field of a relativistic space-charge wave in a plasma is $E_{\max} = \frac{n_{\sim p}}{n_{0p}} = \sqrt{4\pi e^2 n_{0p} m c^2 \gamma}$, where $n_{\sim p}$ is the maximum density in the space-charge wave. The ratio $n_{\sim p}/n_{0p}$ is governed by the way in which the space-charge wave is initiated. In experiments on laser excitation, this ratio is less than 15% (LWFA), and in experiments on the generation of plasma waves by electron bunches it is about 3% (PWFA). According to [57], for LWFA, we have $n_{\sim p}/n_{0p} = a^2/\sqrt{1+a^2}$, where $a = \frac{eE_L\lambda_L}{2mc^2}$, E_L is the electric field, and λ_L is the laser wavelength. For the excitation of wake plasma waves by electron bunches (PWFA), this ratio is known to be equal to $n_{\sim p}/n_{0p} \sim n_b/n_{0p}$ [66], where n_b is the beam density.[7] Consequently, the maximum electric field in a plasma wave can be increased by increasing the laser field and/or laser wavelength as well as the density of the electron bunch exciting the plasma wave (or by searching for new ways of generating plasma waves). Comparing the ratios $n_{\sim p}/n_{0p}$ for LWFA and PWFA gives $\left(\frac{eE_L\lambda_L}{2mc^2}\right)^2 \approx \frac{n_b}{n_{0p}}$, thereby determining the electron density in the bunch n_b that is required to excite a plasma wave with the same maximum electric field as that of a laser-driven plasma wave. This relationship implies that, in order to generate such a plasma wave in PWFA, it is necessary to make the ratio n_b/n_{0p} as large as possible. Note that the case $n_b/n_{0p} \sim 1$ goes beyond the applicability range of the above expression for $E_{\max}$ in LWFA, because it was derived under the assumption $a \ll 1$.

Another trivial way for increasing $E_{\max}$ is to initiate waves in higher density plasmas, in particular, in a solid-state plasma. Recall that, by virtue of the relationship $\omega_p \approx \sqrt{n_p}$, the wavelength of the wave excited in the plasma can be made shorter only by increasing the plasma density (see the first part of the review presented), so it becomes clear that increasing the maximum electric field of a space-charge wake wave also requires the plasma density to be increased. Hence, the plasma-based schemes for the generation and amplification of microwave radiation and for the acceleration of charged particles should utilize higher density plasmas, in particular, solid-state and semiconductor [24] plasmas. However, the plasma density in semiconductors ($n_p \sim 10^{14}$–10^{18} cm^{-3}) is lower than the gas plasma density that has already been achieved in experiments on LWFA (~10^{19} cm^{-3}). Consequently, in developing plasma-based particle accelerators, it seems natural to turn to the plasma of metals, in which the density of free electrons is as high as 10^{22}–10^{23} cm^{-3}. Chen and Nable [67, 68] proposed a very daring but somewhat exotic[8] idea of implementing LWFA, which, however, involves solving the following challenging problems:

(i) launching laser light into a metal,

(ii) exciting space-charge waves in a metal plasma by laser light,

(iii) weakening the effect of multiple scattering of a beam of accelerated particles by the plasma electrons that occur between the channeling planes, and

(iv) solving a very important problem of preventing the destruction of crystals affected by extremely powerful laser radiation via utilizing very short (~ω_p^{-1}) laser pulses.

According to the estimates made in [67], the energy density required to generate accelerating fields of about 100 GeV/cm should be as high as 3×10^7 J/cm^3.

Recall that the electric field of a space-charge wave is governed by the way in which it is generated. Chen and Nable [68] proposed to excite a plasma wave by laser light via either the method used in LWFA or the method suggested by Katsouleas *et al.* [69], which involves the interaction between laser radiation and a plasma whose density is made periodically nonuniform in space by an acoustic wave or with the help of a diffraction grating. The latter method is based on the

[6] Theoretical and experimental advances in PWFA research were reviewed in papers [53–64] and other works and its present status was discussed in detail by Andreev and Gorbunov [65] (see also [57]).

[7] This relationship is valid only in the linear approximation, when $n_b/n_{0p} \ll 1$.

[8] Note that there are things that seem to be exotic at the time they appear but presently become conventional. Thus, the methods of collective acceleration (in particular, the scheme for accelerating charged particles by space-charge waves in a plasma), which were proposed in 1956, appeared to be even more exotic at that time.

three-wave interaction involving a laser wave, ion acoustic wave, and Langmuir plasma wave. The wave interaction can give rise to a plasma wave with the frequency ω_p and wavenumber k_p only under the following conditions: $\omega_L \approx \omega_p$, $\omega_s \ll \omega_p$, $k_L\omega_L$ is close to zero, and the wavenumber of an ion acoustic wave is equal to k_p. The phase velocity $v_{ph} = \omega_p/k_p$ of the excited plasma wave is close to c.

The first method suggested by the authors of [68] is the generation of wake plasma waves by short laser pulses (as is done in the LWFA scheme), in which case the condition $\omega_L \gg \omega_p$ should be satisfied. Since $\omega_p \approx 10^{16}$ in both methods, it is necessary to develop and create extrapowerful UV lasers. It is suggested that a plasma density of about $\sim 10^{23}$ cm^{-3} will be achieved by ionizing the atoms of a solid body by the same UV laser. In this way, however, the fact that laser light will be strongly damped because of the strong absorption should also be taken into account. To answer the question of whether the very daring and interesting ideas expounded by Chen and Nable [67, 68] can be implemented in practice, it is necessary to determine how deep intense UV laser light can penetrate into a metal with allowance for the losses from ionization and photoeffect. Keeping in mind the fact that even very short laser pulses of enormous power will destroy a solid body, Chen and Nable [67, 68] proposed to accelerate charged particles in optical fibers or thin metal films, in which case laser radiation may become easier to launch into a crystal. They are justified in suggesting that preliminary experiments in this direction can be performed with semiconductors in which the electron density is as high as $\sim 10^{18}$ cm^{-3}. In this connection, we must point out very interesting works [70, 71], in which the phenomenon of anomalous penetration of visible laser pulses into a semiconductor was predicted theoretically and discovered experimentally. In the opinion of the authors of [70, 71], this anomaly can be attributed to the excitation of surface plasma waves.

Note that the maximum possible electric field in a steady-state space-charge wave in a plasma is limited by the condition that the velocity acquired by the plasma electrons in the field of this wave is equal to the wave phase velocity, $v_e = v_{ph}$, so that $E_{\max} = \sqrt{4\pi n_{0p} mc^2(2\gamma - 1)}$ [72].

Another idea (of no less importance) originated by Chen and Nable [67, 68] is that of utilizing solid-state crystal bodies in order to raise the electric field via laser-driven plasma waves, in which case the crystalline properties may also help to generate high-brightness beams of accelerated particles through the channeling effect. In fact, under the channeling conditions, strong accelerating fields and the very high rates at which accelerated particles acquire energy can substantially lower the emittance of a beam of accelerated particles; however, it is necessary to take into account the fact that the channeling angle is equal to $\psi \sim \sqrt{eV/\varepsilon_p}$, where eV is the depth of the potential well (or the height of the potential barrier that forms between the lattice planes of the crystal). For very high energies ε_p, this angle is very small. For this and other reasons, the method of lowering the emittance of a beam of charged particles accelerated to extremely high energies in crystals requires more detailed theoretical and experimental investigations.

It may be that Chen and Nable's ideas will not be implemented in full measure in the near future. However, some of the aspects of this acceleration method can be used to create very high energy (about 10^{13}–10^{18} eV) particle accelerators.

Another scheme for charged-particle acceleration in crystals was proposed by Tajima *et al.* [73, 74] and was further developed in subsequent works. This scheme is based on the analogy with particle acceleration in microwave waveguides with periodically spaced metal or dielectric disks and implies acceleration via hard X radiation, for which a periodic crystalline structure plays the same role that periodically spaced disks play for microwave radiation in waveguides. The use of crystals for particle acceleration via hard X radiation on the basis of the Borman effect [73] eliminates the problems of launching laser radiation into a crystal and of guiding laser pulses over relatively large distances in a crystal. Tajima and Covenago [73] proposed to channel accelerated charged particles in a crystal in order to reduce their scattering. They also noted that Hofstadter had already originated analogous ideas in his unpublished paper.

Now, we will say a few words about research on charged-particle acceleration in solids. Grishaev and Nasonov [75] suggested to accelerate charged particles by longitudinal polarization waves of an optically active matter that are driven by beatings of two electromagnetic waves and noted that the channeling effect can serve to reduce the divergence of a beam of accelerated particles due to their multiple scattering. Tajima and Covenago [73] proposed to accelerate charged particles in crystals by hard X radiation and to lower the divergence of a beam of accelerated particles by channeling them. They also studied some other aspects of this acceleration method.

Above, we have briefly reviewed the results obtained by Chen and Nable in their papers [67, 68], which were published under promising titles and now seem to be of even greater importance. Let us say some more words about those papers. Examining the prospects for the new concept of accelerating charged particles by laser radiation in a solid body, Chen and Nable determined the electric field of a plasma wave in a metal from the relationship that was obtained for the maximum field of a nonlinear wave propagating in a plasma by solving the problem of natural waves. However, the electric field should clearly be estimated by solving the problem of induced oscillations and waves.

Since the electric field of the plasma wave is very sensitive to the way in which the wave is excited (see above), deriving the final expression for the electric field of the plasma wave requires solving the problem of its excitation in the case at hand.

3. ACCELERATION OF CHARGED PARTICLES IN VACUUM[9]

Despite substantial progress in the acceleration of charged particles in media (in particular, in plasmas), the question of whether the potentialities of particle acceleration in vacuum have already been exhausted is still relevant, especially, in connection with the fabrication of lasers, whose power can now be as high as several hundred terawatts. Terawatt lasers are capable of generating pulses whose power density at the focus is 10^{19}–10^{20} W/cm^2 and electric field is about 10^{12} V/cm^2, which is higher than the atomic electric field. This brings up the question of whether such strong fields can serve to accelerate charged particles in vacuum to high energies such that the velocity of the accelerated particles is close to the speed of light c and, accordingly, the phase velocity of the accelerating laser wave, which is synchronized with the velocity of the accelerated particles, is equal to c. The paper by Lawson [76] contributed substantially to research on vacuum accelerators. Now, it is clear that, in a vacuum, neither internal waves nor their complex superpositions such that the forces accelerating a particle are linear in the electric field can be used to accelerate charged particles [77, 78], because it is impossible to maintain a prolonged synchronization between the accelerating electromagnetic wave and the motion of accelerated particles (or because electromagnetic-field configurations required for acceleration are lacking). On the other hand, in vacuum, charged particles can be accelerated via forces that are nonlinear (e.g., quadratic) in the electric field using stimulated Compton scattering (the Kapitsa–Dirac effect, i.e., acceleration by radiation pressure–driven ponderomotive forces) [77, 78]. Note that Gaponov and Miller [79] were the first to propose charged particle acceleration by a moving potential well formed by two oppositely propagating electromagnetic waves in an unrippled waveguide.

The results of computer simulations carried out in [80] are also of great importance for studying particle acceleration in vacuum. Katsouleas *et al.* [80] showed that, depending on the value of the nonlinearity factor $\mu = eE_L\lambda_L/2\pi mc^2$, the particles either cannot be accelerated (at $\mu = 0.4$) or can be involved in the acceleration process (at $\mu = 4.0$). They also found that the transverse component of the electric field of a laser wave plays a decisive role in particle acceleration. However, it is not clear whether the emission of photons by an electron in a laser wave field was taken into account in [80].

In my opinion, among the most interesting methods for accelerating charged particles in vacuum are acceleration with the help of a light spot [78] and acceleration in the AXION device [81].

[9] Here, we will be interested in acceleration in free vacuum either in the absence of waveguides, mirrors, diffraction gratings, etc., or when they are positioned at distances long enough for surface waves to be neglected.

ACKNOWLEDGMENTS

I am grateful to V.I. Karas' for his gentle but implacable pressure in writing this paper. I would like to thank N.F. Shul'ga for fruitful discussions of the problems related to the channeling of relativistic charged particles in crystals. This work was supported in part by the International Science Foundation, grant no. EPU 052021.

REFERENCES

1. Ya. B. Faĭnberg, Fiz. Plazmy **11**, 1398 (1985) [Sov. J. Plasma Phys. **11**, 803 (1985)].
2. Ya. B. Faĭnberg, Fiz. Plazmy **20**, 613 (1994) [Plasma Phys. Rep. **20**, 549 (1994)].
3. Ya. B. Faĭnberg and A. A. Rukhadze, in *Encyclopedia of Physics* (Rossiĭskaya Éntsiklopediya, Moscow, 1992), Vol. 3, p. 606.
4. Yu. P. Bliokh, M. G. Lyubarskiĭ, and V. O. Podobinskiĭ, Fiz. Plazmy **20**, 910 (1994) [Plasma Phys. Rep. **20**, 817 (1994)].
5. Yu. P. Bliokh, Ya. B. Faĭnberg, M. G. Lubarsky, *et al.*, in *Proceedings of International Conference on High-Power Particle Beams, Haifa, 1998*, Vol. 2, p. 699.
6. V. S. Antipov, A. N. Antonov, V. A. Balakirev, *et al.*, in *Proceedings of International Conference on High-Power Particle Beams, Haifa, 1998*, Vol. 2, p. 760.
7. V. E. Zakharov, Zh. Éksp. Teor. Fiz. **62**, 1745 (1972) [Sov. Phys. JETP **35**, 908 (1972)].
8. V. N. Oraevskiĭ and R. Z. Sagdeev, Zh. Tekh. Fiz. **32**, 1291 (1962) [Sov. Phys. Tech. Phys. **7**, 955 (1962)].
9. V. P. Silin, Zh. Éksp. Teor. Fiz. **48**, 1669 (1965) [Sov. Phys. JETP **21**, 1121 (1965)].
10. V. I. Karas', V. A. Balakirev, Ya. B. Fainberg, *et al.*, in *Proceedings of International Conference on High-Power Particle Beams, Haifa, 1998*, Vol. 1, p. 392.
11. V. A. Balakirev, V. I. Karas', E. A. Kornilov, and Ya. B. Faĭnberg, Fiz. Plazmy **24**, 738 (1998) [Plasma Phys. Rep. **24**, 684 (1998)].
12. O. M. Goebel, R. W. Schumacher, J. M. Butler, *et al.*, Proc. SPIE (Intense Microwave and Particle Beams) **2843**, 69 (1996).
13. T. Katsouleas and C. Clayton, IEEE Trans. Plasma Sci. **24**, 443 (1996).
14. J. A. Pasour, R. Seeley, D. Smithe, and K. Nguen, Rev. Sci. Instrum. **68**, 3229 (1997).
15. V. A. Balakirev, V. I. Miroshnichenko, and Ya. B. Faĭnberg, Fiz. Plazmy **12**, 983 (1986) [Sov. J. Plasma Phys. **12**, 563 (1986)].
16. F. G. Bass, Ya. B. Faĭnberg, and V. D. Shapiro, Zh. Éksp. Teor. Fiz. **49**, 329 (1965) [Sov. Phys. JETP **22**, 230 (1965)].

17. A. Hibbs, A. L. Singsaag, E. W. Jacobs, *et al.*, J. Appl. Phys. **77**, 2582 (1995).
18. M. I. Dykman, P. V. E. McClinton, P. Manella, and N. Stokes, Pis'ma Zh. Éksp. Teor. Fiz. **52**, 780 (1990) [JETP Lett. **52**, 141 (1990)].
19. R. Bensi, A. Sutera, and A. Vulpiani, J. Phys. A **14**, L453 (1981).
20. V. S. Anishchenko, A. B. Neĭman, F. Moss, and L. Shimansky-Gayer, Usp. Fiz. Nauk **169**, 8 (1999).
21. A. Bulsara and J. Yammaitoni, Phys. Today **49** (3), 36 (1996).
22. Yu. L. Klimontovich, Usp. Fiz. Nauk **169**, 39 (1999).
23. M. Rosenblum, Phys. Rev. Lett. **76**, 1804 (1996).
24. E. A. Kornilov, S. A. Nekrashevich, Ya. B. Faĭnberg, and N. A. Shokhovtsev, Pis'ma Zh. Éksp. Teor. Fiz. **11**, 284 (1970) [JETP Lett. **11**, 185 (1970)].
25. O. G. Zagorodnov, A. M. Egorov, and Ya. B. Faĭnberg, Zh. Éksp. Teor. Fiz. **38**, 7 (1960) [Sov. Phys. JETP **11**, 4 (1960)].
26. V. I. Semenova, Izv. Vyssh. Uchebn. Zaved., Radiofiz. **10**, 1077 (1967) [Sov. Radiophys. Quantum Electron. **10**, 399 (1967)].
27. T. Katsouleas, J. Dawson, *et al.*, AIP Conf. Proc. **335**, 584 (1994).
28. S. C. Wilks, J. M. Dawson, W. B. Mori, *et al.*, Phys. Rev. Lett. **62**, 2600 (1989).
29. V. I. Veksler, in *Proceedings of CERN Symposium on High-Energy Physics, Geneva, 1956*, Vol. 1, p. 80.
30. V. I. Veksler, At. Énerg. **2**, 427 (1957).
31. V. I. Veksler and V. P. Sarantsev, At. Énerg. **24**, 317 (1968).
32. G. I. Budker, in *Proceedings of CERN Symposium on High-Energy Physics, Geneva, 1956*, Vol. 1, p. 68.
33. G. I. Budker, At. Énerg. **1**, 9 (1956).
34. Ya. B. Faĭnberg, in *Proceedings of CERN Symposium on High-Energy Physics, Geneva, 1956*, Vol. 1, p. 84.
35. Ya. B. Faĭnberg, At. Énerg. **6**, 431 (1959).
36. Ya. B. Faĭnberg, Usp. Fiz. Nauk **93**, 617 (1967) [Sov. Phys. Usp. **10**, 750 (1967)].
37. Ya. B. Faĭnberg, Part. Accel. **6**, 95 (1975).
38. T. Tajima and J. M. Dawson, Phys. Rev. Lett. **43**, 267 (1979).
39. P. Chen, J. M. Dawson, T. Katsouleas, *et al.*, Phys. Rev. Lett. **54**, 693 (1985).
40. L. M. Gorbunov and V. I. Kirsanov, Zh. Éksp. Teor. Fiz. **93**, 509 (1987) [Sov. Phys. JETP **66**, 290 (1987)].
41. P. Sprangle, E. Esarey, A. Ting, and G. Joyce, Appl. Phys. Lett. **53**, 2146 (1988).
42. S. V. Bulanov, V. I. Kirsanov, and A. S. Sakharov, Fiz. Plazmy **16**, 935 (1990) [Sov. J. Plasma Phys. **16**, 543 (1990)].
43. O. V. Batishchev, V. I. Karas', and Yu. S. Sigov, Fiz. Plazmy **20**, 654 (1994) [Plasma Phys. Rep. **20**, 587 (1994)].
44. C. Joshi, T. Tajima, J. M. Dawson, *et al.*, Phys. Rev. Lett. **47**, 1285 (1981).
45. C. E. Clayton, C. Joshi, C. Darrow, and D. Umstadter, Phys. Rev. Lett. **54**, 2343 (1983).
46. C. Joshi, W. B. Mori, T. Katsouleas, *et al.*, Nature (London) **311**, 525 (1984).
47. C. E. Clayton, K. A. Marsh, A. Dyson, *et al.*, Phys. Rev. Lett. **70**, 37 (1993).
48. F. Amiranoff, M. Laberge, J. R. Marques, *et al.*, Phys. Rev. Lett. **68**, 3710 (1992).
49. J. B. Rosenzweig, Preprint No. 90/40 (Fermi National Accelerator Laboratory, Batavia, IL, 1990).
50. A. Ts. Amatuni, M. R. Magomedov, E. V. Sekhposyan, and S. S. Élbakyan, Fiz. Plazmy **5**, 85 (1979) [Sov. J. Plasma Phys. **5**, 49 (1979)].
51. N. E. Andreev, Pis'ma Zh. Éksp. Teor. Fiz. **55**, 551 (1992) [JETP Lett. **55**, 571 (1992)].
52. J. Krall, A. Ting, E. Esarey, and P. Sprangle, Phys. Rev. E **48**, 2157 (1993).
53. T. Antonsen and P. Mora, Phys. Rev. Lett. **69**, 2204 (1992).
54. P. Sprangle, E. Esarey, J. Krall, and J. Joyce, Phys. Rev. Lett. **69**, 2200 (1992).
55. V. A. Balakirev *et al.*, Vopr. At. Nauki Tekh., Ser.: Yadernofiz. Metody, No. 6, 168 (1990).
56. A. Modena, Z. Najimidin, A. E. Dangor, *et al.*, Nature (London) **337**, 606 (1995).
57. K. Nakajma, D. Fisher, T. Kawakubo, *et al.*, Phys. Rev. Lett. **74**, 4428 (1995); K. Nakajma and A. Ogata, in *Proceedings of 11th Symposium on Accelerator Science and Technology, Harima, 1997*, p. 36.
58. D. Umstadter, J. K. Kim, and E. Dodd, Phys. Rev. Lett. **76**, 2073 (1996).
59. S. V. Bulanov, V. A. Vshivkov, G. I. Dudnikova, *et al.*, Fiz. Plazmy **23**, 284 (1997) [Plasma Phys. Rep. **23**, 259 (1997)].
60. N. E. Andreev, L. M. Gorbunov, and A. A. Frolov, Fiz. Plazmy **24**, 888 (1998) [Plasma Phys. Rep. **24**, 825 (1998)].
61. V. I. Karas', I. V. Karas', V. D. Levchenko, *et al.*, Fiz. Plazmy **23**, 311 (1997) [Plasma Phys. Rep. **23**, 285 (1997)].
62. Ya. B. Faĭnberg, Fiz. Plazmy **23**, 275 (1997) [Plasma Phys. Rep. **23**, 251 (1997)].
63. T. Katsouleas and W. Mori, AIP Conf. Proc. **335**, 112 (1994).
64. P. Sprangle, E. Esarey, and A. Ting, Phys. Rev. A **41**, 4463 (1990).
65. N. E. Andreev and L. M. Gorbunov, Usp. Fiz. Nauk **169**, 53 (1999).
66. T. Katsouleas, Phys. Rev. A **33**, 2066 (1986).
67. P. Chen and R. Nable, *Advanced Acceleration Concepts*, Ed. by S. Chattopadhyay, S. McCullough, and P. Dane (AIP, New York, 1997), p. 273.
68. P. Chen and R. Nable, *New Modes of Particle Acceleration*, Ed. by Z. Parsa (AIP, New York, 1997), p. 95.
69. T. Katsouleas, J. Dawson, D. Sultana, and Y. Yan, IEEE Trans. Nucl. Sci. **32**, 3554 (1985).
70. S. C. Kitson, W. L. Barnes, J. R. Sambles, Phys. Rev. Lett. **77**, 2670 (1996).
71. T. W. Ebessen, H. J. Lezec, and H. F. Ghaemi, Nature (London) **391**, 667 (1998).
72. A. I. Akhiezer and R. V. Polovin, Zh. Éksp. Teor. Fiz. **30**, 915 (1956) [Sov. Phys. JETP **3**, 696 (1956)].

73. T. Tajima and M. Covenago, Phys. Rev. Lett. **59**, 1440 (1987).
74. T. Tajima and B. S. Newberger, Phys. Rev. A **40**, 6897 (1989).
75. I. A. Grishaev and N. N. Nasonov, Pis'ma Zh. Tekh. Fiz. **3**, 1084 (1977) [Sov. Tech. Phys. Lett. **3**, 446 (1977)].
76. J. Lawson, IEEE Trans. Nucl. Sci. **26**, 4217 (1979).
77. R. Palmer, AIP Conf. Proc. **335**, 90 (1994).
78. N. B. Baranova, M. O. Skully, and B. Ya. Zel'dovich, Zh. Éksp. Teor. Fiz. **105**, 469 (1994) [JETP **78**, 249 (1994)].
79. A. V. Gaponov and M. A. Miller, Zh. Éksp. Teor. Fiz. **34**, 242 (1958) [Sov. Phys. JETP **7**, 168 (1958)].
80. T. Katsouleas, W. B. Mori, J. S. Wurtele, *et al.*, in *New Modes of Particle Acceleration*, Ed. by Z. Parsa (AIP, New York, 1997), p. 21.
81. L. C. Steinhauer and W. D. Kimura, J. Appl. Phys. **72**, 3237 (1992).

Translated by G. V. Shepekina

Plasma Physics Reports, Vol. 26, No. 4, 2000, pp. 344–350. Translated from Fizika Plazmy, Vol. 26, No. 4, 2000, pp. 371–377.

PLASMA ELECTRONICS AND NEW ACCELERATION METHODS

Theoretical and Experimental Investigations of the Excitation of High-Frequency Oscillations in an Ion Collective Accelerator Model Based on the Doppler Effect

V. I. Butenko, D. V. Gorozhanin, A. M. Egorov, B. I. Ivanov*, V. V. Ognivenko, I. N. Onishchenko, and V. P. Prishchepov

Kharkov Institute for Physics and Technology, National Science Center, Akademicheskaya ul. 1, Kharkov, 310108 Ukraine
**e-mail: ivanovbi@kipt.kharkov.ua*

Received April 30, 1999

Abstract—Results are presented from studies of a two-beam scheme of ion acceleration by a high-frequency field excited by an electron beam due to the instabilities associated with anomalous and normal Doppler effects. The dynamics of the excitation of eigenmodes in a periodic slow wave structure (SWS) by a relativistic electron beam via the anomalous Doppler effect is investigated theoretically. Mechanisms for the saturation of the instability are considered, analytical expressions for the maximum field amplitude and the efficiency with which the energy of beam electrons is converted into the energy of the excited wave are derived, and the results of numerical simulations of such excitation are presented. An experimental stand designed to test the principles and possibility of proton acceleration up to an energy of 8 MeV at a current up to 3 A is described. A double resonance (associated with anomalous and normal Doppler effects) occurring in the interaction of an electron beam with a helical SWS is studied experimentally. In this case, an increase in the efficiency with which the accelerating high-frequency field is excited is observed. © *2000 MAIK "Nauka/Interperiodica"*.

1. INTRODUCTION

Many problems of plasma physics and technology have much in common with the problems of the physics and technology of charged-particle accelerators, such as the interaction of charged particles with electromagnetic fields, collective effects, instabilities, production of high-power particle beams for plasma heating and inertial confinement fusion, and radiation stability of reactor materials. In this connection, the importance of the development of new acceleration methods, in particular, plasma accelerators and two-beam accelerators (see, e.g., [1, 2]), should be emphasized.

An increase in the current in existing linear accelerators is limited in particular by the fact that the accelerating RF field is defocusing in the radial direction [3]. This limitation is overcome in collective (plasma) accelerators in which the particles are accelerated by space electromagnetic E-waves whose amplitude is maximum on the axis [1]. In the two-beam linear electron–ion accelerator under consideration, a high-power electron beam can excite an RF field that is both accelerating and focusing. In this case, a substantial increase in both the current of the accelerated ions and the acceleration rate can be achieved.

The concept of a two-beam high-current ion accelerator based on the Doppler effect was proposed in [4, 5]. According to this concept, an RF field that is both accelerating and focusing is generated by means of an intense electron beam injected into a spatially periodic structure of a linear accelerator along its axis. Simultaneously and in the same way, the ion beam to be accelerated is injected. The RF field is excited due to the cyclotron instability associated with anomalous and normal Doppler effects (ADE and NDE, respectively). Thus, in order to excite an RF field via ADE or NDE, the transverse field of a certain spatial harmonic of the slow wave structure (SWS) is employed, whereas the longitudinal field of the corresponding resonant spatial harmonic is used to accelerate the ions. The corresponding diagram is presented in Fig. 1, where the periodic function $\omega(k_z)$ shows the dispersion relation for the electrodynamic structure. The points of intersection of this curve with the straight lines $\omega = k_z v - \omega_c$, $\omega = k_z v + \omega_c$, and $\omega = k_z v_i$ correspond, respectively, to the ADE and NDE excitation of the RF field and ion acceleration by the excited wave. Here, z is the longitudinal coordinate, k_z is the longitudinal wavenumber, v is the electron velocity, ω is the frequency of excited oscillations (which is equal to the eigenfrequency of the structure), ω_c is the electron cyclotron frequency, and v_i is the ion velocity.

This acceleration scheme, which is intermediate (or hybrid) between conventional and collective accelerators, uses the well-studied and technologically developed electrodynamic structure of the former and intense accelerating and focusing RF fields of the latter. Its basic advantages are the following. (i) Near the axis (i.e., in the region occupied by the electron beam with

1063-780X/00/2604-0344$20.00 © 2000 MAIK "Nauka/Interperiodica"

the space-charge cyclotron wave excited in it), the resonantly excited field is spatial; this provides (as in a plasma waveguide [1]) both radial and phase stability of the accelerated ion beam. (ii) The intensity of the accelerated field on the axis is higher than at the ends of the drift tube (in conventional accelerators, the situation is opposite). (iii) The ADE excitation of the accelerating and focusing RF fields can proceed without a change in the eigenfrequency of the resonator and phase velocity of the wave; this substantially facilitates the calculations and the maintenance of the accelerator parameters. (iv) Correlated variations in both the wave phase velocity and the magnetic field along the accelerator provide the resonant ADE excitation of the required type of oscillations and the suppression of other instabilities (due to the nonuniformity of the excitation conditions for the latter). (v) There is the possibility of the excitation of an accelerating wave with a low phase velocity by a relativistic electron beam; in this case, the nonlinear effects associated with the trapping of the beam electrons by the excited wave can be neglected up to field values on the order of 10^5–10^6 V/cm.

Preliminary estimates showed that this type of ion accelerator has considerable promise. The design and working tolerances are basically the same as in conventional linear accelerators and powerful microwave devices (i.e., it is achievable in practice). An accelerating field of about 10^5 V/cm was obtained experimentally in [6] using an H-type structure (with the drift tubes placed on reversed hangers) excited by an intense electron beam via ADE. In order to develop such an acceleration method, we carried out theoretical and experimental studies and computer simulations and designed an experimental acceleration stand.

This paper is organized as follows. In Section 2, we theoretically study the ADE excitation of the accelerating field in a periodic SWS by a relativistic electron beam. In Section 3, we describe an experimental acceleration stand designed to test this acceleration scheme. In order to increase the acceleration efficiency, it seems advantageous to excite RF oscillations under the conditions of ADE–NDE double resonance. The results of experiments on the interaction of an electron beam with a helical SWS under these resonance conditions are presented in Section 4.

2. ADE EXCITATION OF THE ACCELERATING FIELD BY A RELATIVISTIC ELECTRON BEAM

Let us consider the ADE excitation of an axially symmetric E-mode by an electron beam in a periodic SWS. A monoenergetic annular relativistic electron beam is injected at $z = 0$ with the velocity $\mathbf{v}(z = 0) = \mathbf{e}_z v_0$ along the symmetry axis (the z-axis) of the system. The beam current density is

$$j_{zb}(r) = \frac{I_b}{2\pi r}\delta(r - r_b),$$

where I_b and r_b are the current and the radius of the beam, respectively, and $\mathbf{e}_z$ is the unit vector along the z-axis.

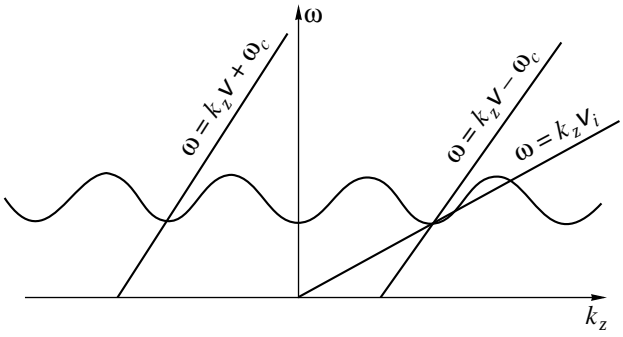

Fig. 1. Dispersion curves for a periodic SWS.

We assume that the beam and the SWS are in a uniform external magnetic field $\mathbf{H} = \mathbf{e}_z H_0$. We consider the spatial amplification of an axially symmetric E-wave by this beam under the condition of the ADE resonance

$$\omega = k_z v_0 - \omega_H/\gamma_0, \tag{1}$$

where ω and k_z are the frequency and the longitudinal wavenumber, respectively; $\omega_H = |e|H_0/mc$, $\gamma_0 = (1 - v_0^2/c^2)^{-1/2}$; e and m are the charge and mass of an electron; and c is the speed of light in a vacuum.

The electric field of the wave propagating in a periodic SWS in the positive direction along the z-axis can be represented as a superposition of spatial harmonics

$$\begin{aligned}\mathbf{E}(\mathbf{r}, t) &= \mathrm{Re}[C_s(z)\mathbf{E}_s(r)\exp(-i\omega t)],\\ \mathbf{E}_s(r) &= \sum_{n=-\infty}^{\infty}\alpha_{sn}\mathbf{E}_s^{(n)}(r)\exp[ik_{sn}z],\end{aligned} \tag{2}$$

where $C_s(z)$ is the slowly varying (along the z-axis) field amplitude, $k_{sn} = h_s + 2\pi n/L$ is the longitudinal wavenumber of the nth spatial harmonic, L is the structure period, and α_{sn} are the dimensionless coefficients characterizing the relative amplitude of the nth spatial harmonic. The axially symmetric E-wave in question has the components E_z, E_r, and H_φ, and the functions $\mathbf{E}_s^{(n)}(r)$ and $\mathbf{H}_s^{(n)}(r)$ in the region of the beam–wave interaction can be written as

$$\begin{aligned}E_{sz}^{(n)} &= I_0(k_\perp r), \quad E_{sr}^{(n)} = -i\frac{k_{sn}}{k_\perp}I_1(k_\perp r),\\ H_{s\varphi}^{(n)} &= -i\frac{k}{k_\perp}I_1(k_\perp r),\end{aligned} \tag{3}$$

where $k = \omega/c$; $k_\perp = \sqrt{k_{sn}^2 - k^2}$ is the transverse wavenumber specified by the boundary conditions for the field on the waveguide wall and I_0 and I_1 are the modified Bessel functions.

Below, we assume that the electron beam is in resonance (1) with the mth spatial harmonic of the field, $k_z = k_{sm} \equiv k_m$. Then, taking into account only the resonant terms, we can write the nonlinear equations of motion of the beam electrons in Lagrangian variables and the equation for the slowly varying wave amplitude in the following form [7]:

$$\frac{d}{d\xi}p_3 = -\frac{k_\perp c}{\omega_H}\left(\gamma - \frac{\omega_H\omega}{k_\perp^2 c^2}\right)\mathrm{Re}\left(\frac{p_1^*}{p_3}A\right), \quad (4)$$

$$\frac{d}{d\xi}p_1 + i\left(1 - \frac{\omega + \omega_H/\gamma}{k_m v_z}\right)p_1 = \frac{k_m}{k_\perp}(\beta_z^{-1} - \beta_{ph})A, \quad (5)$$

$$\frac{d}{d\xi}A = \nu\frac{\omega_H k_\perp}{\omega k_m}\int_0^1 d\tau_0 p_1\left(\frac{k_\perp^2 c}{k_m\omega_H} - \frac{1}{p_3}\right), \quad (6)$$

$$p_1(0, t_0) = 0, \quad p_3(0, t_0) = \beta_0\gamma_0, \quad A(0) = A_0. \quad (7)$$

Here, $p_1 = \beta_+\gamma\exp[i(\omega t_\wedge - k_m z - \varphi(0, t_0))]$, $p_3 = \beta_z\gamma$, $\xi = k_m z$, $v_+ = v_x + iv_y$, $\beta_+ = v_+/c$, $\gamma = (1 - \beta_z^2 - \beta_\perp^2)^{-1/2}$, $\beta_\perp = |\beta_+|$, $A = \dfrac{i|e|\alpha_{sm}I_1(k_\perp r_b)}{2mc^2 k_m}C_s$, $\nu = \dfrac{\omega c\alpha_{sm}^2 I_1^2(k_\perp r_b)}{2\omega_H k_\perp^2|N_s|}\dfrac{I_b}{I_A}$, $\varphi = \arctan[y_\wedge(z, t_0)/x_\wedge(z, t_0)]$, $x_\wedge(z, t_0)$ and $y_\wedge(z, t_0)$ are the transverse coordinates of an electron, $\tau_0 = \omega t_0/2\pi$, t_0 is the time the electron enter the region $z > 0$, $N_s = \dfrac{c}{4\pi}\int_{S_\perp} dS\mathbf{e}_z\{[\mathbf{E}_s\mathbf{H}_{-s}] - [\mathbf{E}_{-s}\mathbf{H}_s]\}$ is the norm for the wave with index s, and $I_A = mc^3/|e| = 17$ kA.

Note that, when deducing equations (4)–(6), the expression for the longitudinal component of the electric field $E_{\pm sz}^{(n)}(r)$ was expanded into a series in the small parameter $k_\perp r_L$ near the initial electron coordinates; here, $r_L = |v_+|\gamma/\omega_H$ is the electron Larmor radius.

Equations (4)–(6) have the following integrals [7, 8]:

$$|A(\xi)|^2 - |A_0|^2 = 2\nu\frac{\omega_H k_\perp^2}{\omega k_m^2}(\gamma_0 - 1)\eta(\xi), \quad (8)$$

$$\frac{k_\perp^2 c}{2k_m\omega_H}\beta_\perp^2\gamma^2 + (\beta_z - \beta_{ph})\gamma = (\beta_0 - \beta_{ph})\gamma_0, \quad (9)$$

$$|A|\beta_\perp\gamma\sin\psi = \frac{\omega_H}{k_\perp c}[(\gamma_0 - \gamma) - (\beta_0\gamma_0 - \beta_z\gamma)\beta_{ph}]. \quad (10)$$

Here, $\psi = \arg(p_1^* A)$, $\beta_{ph} = \omega/k_m c$, $\eta(\xi)$ is the electron efficiency, and

$$\eta = \frac{\gamma_0}{\gamma_0 - 1}\int_0^1 d\tau_0\left[1 - \frac{\gamma(z, t_0)}{\gamma_0}\right]. \quad (11)$$

Relation (10) is obtained in the hydrodynamic approximation, assuming that the absolute value of the electron momentum is independent of the injection time t_0.

From equations (5) and (6) it follows that, in the initial stage of the instability (in the linear approximation), the wave amplitude increases according to the law

$$A(\xi) = A_0\cosh(\rho\xi), \quad (12)$$

where $\rho = (\beta_0^{-1} - \beta_{ph})\sqrt{\nu}$ and $\cosh(x)$ is the hyperbolic cosine.

It is seen that the spatial growth rate of the instability is proportional to $I_b^{1/2}$. Such a dependence of the growth rate on the beam current is also characteristic of the ADE instability of a transverse wave [9].

We now consider the nonlinear stage and regimes of the instability saturation. From equations (4) and (6), it follows that the instability saturates if one of the conditions $\cos\psi = 0$ or $\beta_z\gamma = p_{3*} = k_m\omega_H/k_\perp^2 c$ is satisfied [7, 8]. Let the instability saturate at $\cos\psi = 0$ and $p_3 > p_{3*}$. In this case, the right-hand side of equation (10) is negative; consequently, in the saturation state, the helical phase is equal to $-\pi/2$. For $\psi = -\pi/2$, from equations (8)–(10), we can obtain the maximum values of the energy, momentum, and amplitude of the wave. In the case when the beam–electron energy loss is small, $\eta \ll 1$, we also obtain from these equations the electron efficiency and the wave amplitude in the saturation state,

$$\eta_{\max} = \frac{4\gamma_0}{\gamma_0 - 1}\beta_{ph}\gamma_{ph}^2(\beta_0 - \beta_{ph})\rho, \quad (13)$$

$$A_{\max} = \left[|A_0|^2 + 8\beta_0^2\gamma_0^2\frac{(\beta_0 - \beta_{ph})^2}{(1 - \beta_0\beta_{ph})^2}\rho^3\right]^{1/2}, \quad (13a)$$

where $\gamma_{ph} = k_m/k_\perp$. It is seen from (13) that, in the case in question, the efficiency increases with increasing the beam current.

Now, we consider the case when the saturation of the instability occurs at $p_3 = p_{3*}$. From equation (9), we determine the corresponding value of γ and find the expressions for the efficiency and maximum wave amplitude in the saturation regime in question:

$$\eta_{\max} = \frac{\gamma_0\gamma_{ph}^2}{\gamma_0 - 1}\frac{1 - \beta_0\beta_{ph}}{1 + \gamma_{ph}^{-1}}\beta_{ph}^2, \quad (14)$$

$$A_{\max} = \left[|A_0|^2 + \frac{2\beta_0^2\gamma_0^2}{1+\gamma_{ph}^{-1}} \frac{(\beta_0 - \beta_{ph})}{(1-\beta_0\beta_{ph})} \beta_{ph}\rho^2 \right]^{1/2}. \quad (14a)$$

It is seen from (14) that, in this case, the efficiency is independent of the beam current. For $\beta_{ph} \ll 1$, expression (14) takes a simpler form:

$$\eta_{\max} = \gamma_0\beta_{ph}^2/2(\gamma_0 - 1). \quad (15)$$

The expression for the threshold value of the parameter ρ_* separating the two above instability regimes is

$$\rho_* = \frac{(1-\beta_{ph}\beta_0)\gamma_{ph}}{2\beta_0\sqrt{1+\gamma_{ph}}}\beta_{ph}. \quad (16)$$

For $\rho < \rho_*$, the instability saturates at $\psi = -\pi/2$ and the efficiency is determined by (13). For $\rho > \rho_*$, the instability saturates when the longitudinal momentum takes the value $p_3 = p_{3*}$; in this case, the efficiency is determined by (14).

The results of the numerical solution of equations (4)–(6) for an initial electron beam energy of 300 keV ($\gamma_0 = 1.6$), wave amplitude of $\varepsilon_0 = 5 \times 10^{-3}$ ($\varepsilon = A/\rho$), and phase velocity of $v_{ph} = 0.1c$ are presented in Figs. 2 and 3. Figure 2 shows the dimensionless wave amplitude ε as a function of the longitudinal coordinate ζ ($\zeta = \rho\xi$) for the amplification coefficient that is lower (curve *1*, $\rho = 0.003$) and higher (curve *2*, $\rho = 0.1$) than the threshold one. For the above wave and beam parameters, the threshold value of ρ is $\rho_* = 0.042$. It is seen that the maximum value of the wave amplitude in the saturation state increases with increasing ρ. For $\rho < \rho_*$, the wave amplitude reaches its maximum and then monotonically decreases to the initial value. For $\rho > \rho_*$, the longitudinal profile of the wave amplitude in the saturation state is nonmonotonic; this is due to the competition of the two above saturation mechanisms.

Figure 3 presents the maximum efficiency as a function of the normalized amplification coefficient ρ. It is seen that, for $\rho < \rho_*$, the maximum efficiency increases with increasing ρ. For $\rho \ll \rho_*$, the efficiency increases linearly with increasing ρ [see (13)], and, for $\rho > \rho_*$, $\eta_{\max}$ is independent of ρ [cf. (14)]. The values of $\eta_{\max}$ and $A_{\max}$ calculated by formulas (13)–(14a) for the corresponding values of the parameter ρ and the above beam and wave parameters are in good agreement with the results of numerical calculations.

Thus, formula (16) determines the threshold value of the spatial growth rate; this value separates the qualitatively different saturation regimes. For a growth rate less than the threshold one, the efficiency is proportional to the spatial amplification coefficient and increases with increasing the beam current. For spatial growth rates larger than the threshold one, the efficiency in the saturation state reaches its maximum value proportional to the square of the ratio of the phase velocity of the field harmonic that is in synchronism with the beam to the speed of light; as the beam current increases further, the efficiency remains unchanged. The maximum achievable values of the electron efficiency in this regime correspond to the excitation of an axially symmetric E-wave by a relativistic electron beam in both ADE-based amplifiers and oscillators.

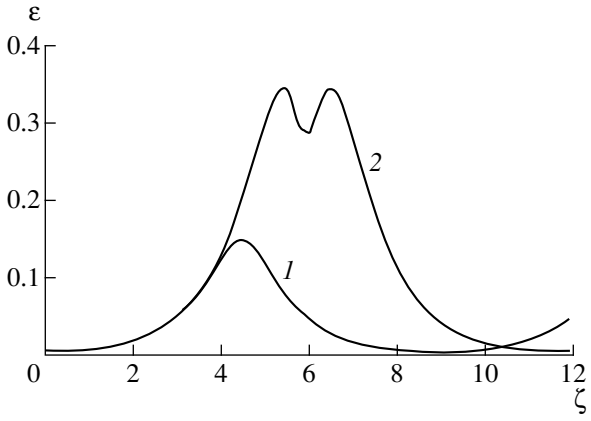

Fig. 2. Normalized wave amplitude as a function of the longitudinal coordinate ζ for ρ = (*1*) 0.03 and (*2*) 0.1.

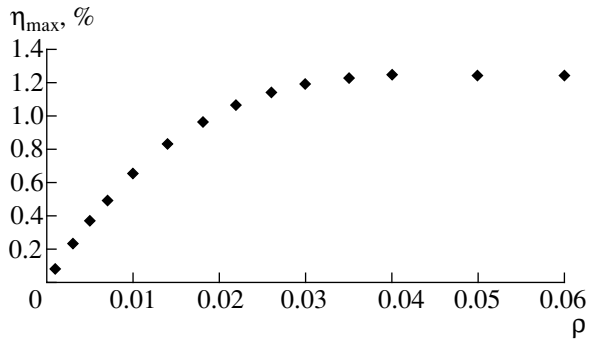

Fig. 3. Maximum efficiency as a function of the normalized amplification coefficient ρ.

3. EXPERIMENTAL ACCELERATION STAND

To test the proposed acceleration scheme, an experimental acceleration stand (EAS) is currently being created in which protons can be accelerated up to 8 MeV at a current up to 3 A. To save money, we used the available 5-MeV-energy 30-mA-current Ural-5 proton accelerator as an injector. With an appropriate injector, the EAS current can attain 3 A. In the EAS, the ADE excitation of the accelerating and focusing RF field in the H-type periodic structure will be produced by a high-current electron beam (the preliminary experiments are described in [6, 10, 11]). Resonant space-charge waves excited in the electron beam ensure both

radial and phase stability of the proton beam. The schematic, description, and parameters of the EAS are presented in [4, 5]. When determining the EAS parameters, we assumed that the frequency of the resonator loaded with a beam is equal to the frequency of the resonator without a beam. In our case, this assumption is valid because, for the ADE cyclotron instability, we can choose the conditions under which the shift of the resonator frequency is equal to zero.

The ADE excitation of RF oscillations is accompanied by an increase in the Larmor radius of the beam electrons (this effect was experimentally studied in [12]). As the electron beam propagates in the resonator, both its radius and the radius of the drift tubes increase. The simultaneous increase in both the radius of the drift tubes and the period of the accelerating structure from the input to output end of the resonator facilitates the maintenance of the constant acceleration rate over the resonator.

In order to avoid excessive longitudinal deceleration and an increase in the beam radius, the beam current and energy are chosen to be sufficiently large. To simplify calculations and increase their reliability, as well as to facilitate the adjustment of the accelerator, in this stage of investigations, we chose conditions under which the energy loss of the electron beam is small; therefore, the efficiency of the energy transfer from the electron beam to the ion beam is also small (less than 1%). The methods of substantially increasing the efficiency are discussed in [4].

In the EAS, the H-type resonator is excited by an electron beam produced by a transverse-compression electron gun. The electron beam is focused by magnetic coils and a solenoid. The electron-gun voltage is supplied from a high-voltage pulse transformer. The proton beam of the Ural-5 accelerator is injected through the central aperture in the cathode of the electron gun and passes along the axis of the H-resonator, where it is accelerated to 8 MeV. The solenoid, which consists of 15 coils, produces a resonant, longitudinally nonuniform magnetic field. Magnetic-discharge and turbomolecular pumps maintain a vacuum at a level of 10^{-7} torr. At the output, there are an electron collector, an ion collector with a movable bottom, and pump pipes. The electron injector consists of an electron gun and an industrially produced supply unit of a high-power klystron. The main element of the accelerating unit is an H-type resonator with the drift tubes mounted on counter hangers. The basic parameters of the Ural-5 accelerator–injector and designed EAS are the following: the initial proton energy is 5 MeV; the ion current is 30 mA; the electron-beam energy is 350 keV; the electron-beam current is 150 A; the pulse duration is 2.5 μs; the pulse repetition rate is 1 Hz; the initial and final electron-beam radii are 1.3 and 2.4 cm, respectively; the magnetic fields at the input and output are 609 Oe and 439 Oe, respectively; the resonator length is 161 cm; the working frequency is 148.5 MHz; the accelerating field is 56 kV/cm; the synchronous phase is 65°; and the shunt impedance is 35 MΩ/m.

At present, a one-to-one model of the accelerator resonator has been produced and the RF-field distribution along the resonator has been measured. Using adjusting elements, we obtained the required uniform RF-field distribution in the gaps. A solenoid with the required distribution of the magnetic field was calculated in [12] by the regularization method developed for the solution of ill-posed inverse problems [14].

4. INCREASING THE EFFICIENCY OF THE RF FIELD EXCITATION VIA THE DOPPLER EFFECT

To increase the excitation efficiency of RF oscillations in the SWS, it seems promising to produce the double-resonance conditions, when, for the given frequency, the resonance conditions for ADE ($\omega = k_{z1}v - \omega_H$) and NDE ($\omega = k_{z2}v + \omega_H$) are simultaneously satisfied. Here, ω is the circular frequency, k_z is the wavenumber, v is the electron-beam velocity, and ω_H is the electron cyclotron frequency. In [15], it was theoretically shown that, in a spatially periodic SWS, the amplification coefficient of RF oscillations increases substantially in the case of double resonance; consequently, the kinetic energy lost by the electron beam also increases. Here, we present the results from experimental studies of the double resonance with the use of a helical resonator, which allows us to satisfy the resonance conditions for ADE and NDE simultaneously. This is possible due to the specific shape of the dispersion curves of azimuthally asymmetric waves in a heli-

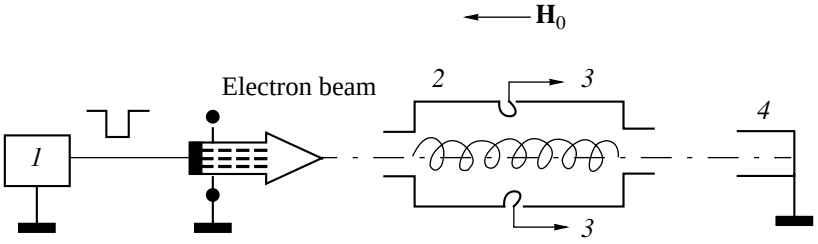

Fig. 4. Schematic of the experiment: (*1*) source of the accelerating voltage, (*2*) resonator, (*3*) RF measuring units, and (*4*) beam collector.

cal SWS. ADE excitation of this type of wave by an electron beam was studied experimentally and theoretically in [12, 16].

The schematic of the experiment is presented in Fig. 4. An electron beam (with an energy up to 50 keV and current up to 1 A) focused by an external magnetic field (up to 1 kOe) was injected into the SWS along the axis of the system. The SWS was a spiral segment placed into a multimode cylindrical resonator. The parameters of the experiment were chosen such that, for the given frequency and phase velocity of the azimuthally asymmetric helical mode, the ADE resonance conditions hold. (Note that, in the case of rectilinear motion of charged particles, the ADE instability can develop in the system even without the preliminary spinup of the beam electrons [9].)

The experiment showed (see Fig. 5) that RF oscillations were excited most efficiently in a rather narrow range of the parameter v/v_{ph}, where v_{ph} is the phase velocity of the SWS mode. Keeping in mind the aim of the paper and in order to explain this fact quantitatively, we carried out "cold" measurements of the dispersion properties of the SWS. The results obtained showed that, at the frequency of RF oscillations generated by the beam, the degeneration of the dispersion curve with respect to three characteristic wavenumber values occurred. The longitudinal distribution of the electric field $|E(z)|^2$, which was measured by the perturbation method, was compared with the field distribution obtained by computer simulations (Fig. 6). The total electric field was represented as

$$|E(z)|^2 = \left|A_1 \sin\frac{2\pi}{\lambda_1}z + A_2 \sin\frac{2\pi}{\lambda_2}z + A_3 \sin\frac{2\pi}{\lambda_3}z\right|^2,$$

where A is the weight coefficient (for the waveguide mode and two asymmetric helical modes) and λ is the corresponding wavelength; the ADE and NDE resonance conditions were satisfied for the asymmetric helical modes with λ_1 and λ_2, respectively. Graphically, this situation is presented in Fig. 7, where the dispersion curves for (*1*) the waveguide mode, (*2*) the asymmetric helical mode, and (*3*, *4*) the beam cyclotron waves are plotted. The region of intersection of the beam cyclotron waves with curve *2* corresponds to the resonance conditions for the ADE and NDE excitation. Straight line *5* shows the asymptote $\omega = k_z c/\sqrt{\varepsilon_{\text{eff}}}$, where $\varepsilon_{\text{eff}} \approx 2$ is the effective dielectric constant and c is the speed of light.

At certain values of λ and A, the measured and modeled distributions of $|E(z)|^2$ almost coincide (the discrepancy is less than 10%). Calculations showed that, in the experiment, the coupling of the ADE and NDE branches of the beam–SWS system occurred; i.e., the resonance conditions for ADE and NDE were satisfied simultaneously. As a result, conditions for the excitation of RF oscillations were optimum with respect to the parameter v/v_{ph1} (or ω/ω_H).

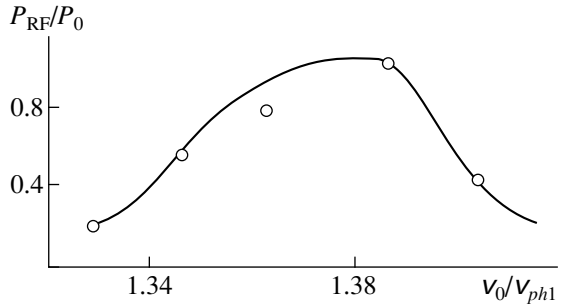

Fig. 5. Generated power as a function of the ratio of the beam velocity to the wave phase velocity.

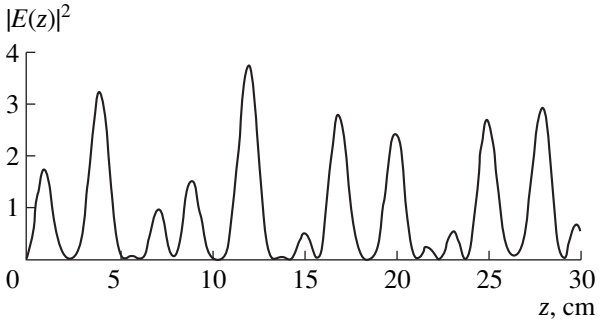

Fig. 6. Distribution of the electric field along the resonator.

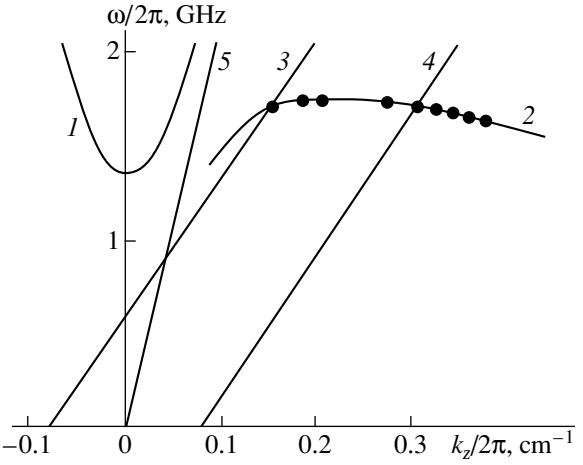

Fig. 7. Dispersion curves in the case of a helical SWS.

The physical meaning of the increase in the efficiency with which the beam kinetic energy is converted into the RF field oscillation energy in the case when the ADE and NDE resonances are satisfied simultaneously is the following. A rectilinear electron beam excites RF oscillations in the SWS under conditions of the ADE resonance. According to the theory of ADE [17], this is accompanied by the increase in the transverse (azi-

muthal) beam-electron energy, which can also be converted via NDE into the energy of the excited RF field.

Thus, in the experiment, the ADE–NDE double resonance is realized. In this case, the power of the excited RF oscillations increases, which is accompanied by an increase in the electron-beam energy loss. All of these results hold promise for using this mechanism in the two-beam accelerators in question.

5. CONCLUSION

In this paper, the results from theoretical investigations of the ADE excitation of an RF field and experiments on the excitation of RF oscillations under the conditions of ADE–NDE double resonance are presented and the experimental acceleration stand is described.

ACKNOWLEDGMENTS

We are grateful to Ya.B. Faĭnberg for fruitful discussions and A.M. Sessler for encouraging this work. This work was supported in part by the Lawrence Berkeley National Laboratory, the State Committee for Science and Technology of Ukraine (project no. 9.02.02/059), and the International Science Foundation and the Government of Ukraine (grants nos. UA-1000 and UA-1200).

REFERENCES

1. Ya. B. Faĭnberg, At. Energ. **6**, 431 (1959).
2. A. M. Sessler and S. S. Yu, Phys. Rev. Lett. **58**, 2439 (1987).
3. Ya. B. Faĭnberg, in *Theory and Computation of Linear Accelerators* (Gosatomizdat, Moscow, 1962), p. 19.
4. B. I. Ivanov, V. I. Butenko, A. M. Egorov, *et al.*, AIP Conf. Proc. **335**, 429 (1995).
5. V. I. Butenko, A. M. Egorov, B. I. Ivanov, *et al.*, Fiz. Plazmy **23**, 359 (1997) [Plasma Phys. Rep. **23**, 332 (1997)].
6. V. G. Gapanovich, B. I. Ivanov, M. I. Kapchinskiĭ, *et al.*, Zh. Tekh. Fiz. **60**, 193 (1990) [Sov. Phys. Tech. Phys. **35**, 116 (1990)].
7. V. V. Ognivenko, Vopr. At. Nauki Tekh., Ser: Yadernofiz. Issled., No. 4–5, 143 (1997).
8. V. V. Ognivenko, Ukr. Fiz. Zh. **43** (2), 177 (1998).
9. V. V. Zheleznyakov, Izv. Vyssh. Uchebn. Zaved., Radiofiz. **3**, 57 (1960).
10. D. V. Gorozhanin, B. I. Ivanov, V. A. Miroshnichenko, *et al.*, Vopr. At. Nauki Tekh., Ser: Tekh. Fiz. Éksp., No. 2, 72 (1984).
11. D. V. Gorozhanin, I. A. Dobranos, and B. I. Ivanov, Izv. Vyssh. Uchebn. Zaved., Radiofiz. **35**, 334 (1992).
12. B. I. Ivanov and D. V. Gorozhanin, Zh. Éksp. Teor. Fiz. **98**, 1018 (1990) [Sov. Phys. JETP **71**, 567 (1990)].
13. V. I. Butenko, Zh. Tekh. Fiz. **62** (7), 157 (1992).
14. A. N. Tikhonov and V. Ya. Arsenin, *Solutions of Ill-Posed Problems* (Nauka, Moscow, 1979; Halsted, New York, 1977).
15. Yu. P. Bliokh, A. V. Borodkin, B. I. Ivanov, *et al.*, Vopr. At. Nauki Tekh.: Ser: Tekh. Fiz. Éksp., No. 2, 69 (1984).
16. D. V. Gorozhanin, B. I. Ivanov, and M. I. Kapchinskiĭ, Izv. Vyssh. Uchebn. Zaved., Radiofiz. **27**, 880 (1984).
17. V. L. Ginzburg and I. M. Frank, Dokl. Akad. Nauk SSSR **56**, 583 (1947).

Translated by A. D. Smirnova[†]

[†] Now deceased.

Plasma Physics Reports, Vol. 26, No. 4, 2000, pp. 351–355. Translated from Fizika Plazmy, Vol. 26, No. 4, 2000, pp. 378–382.

PLASMA ELECTRONICS AND NEW ACCELERATION METHODS

Focusing of High-Energy Particles by a Plasma Current Lens Controlled by an External Magnetic Field

V. N. Belan, V. I. Butenko, A. M. Egorov, B. I. Ivanov*, V. A. Kiselev, A. F. Linnik, I. N. Onishchenko, and V. P. Prishchepov

Kharkov Institute for Physics and Technology, National Science Center, Akademicheskaya ul. 1, Kharkov, 310108 Ukraine
**e-mail: ivanovbi@kipt.kharkov.ua*

Received April 22, 1999

Abstract—Plasma current lenses in a nonuniform, programmed longitudinal magnetic field are considered. The longitudinal magnetic field determines the variations in the radius of the current channel, the current density, and the focusing azimuthal magnetic field. The efficiency of such plasma lenses can be increased by simultaneously decreasing the radii of both the current channel and the focused beam. © *2000 MAIK "Nauka/Interperiodica".*

1. INTRODUCTION

Plasma current lenses, in which charged-particle beams are focused by the azimuthal magnetic field produced by the longitudinal plasma current, show promise for investigations related to inertial confinement fusion [1] and the physics of high-energy particles [2]. The basic advantages of these lenses are their high focusing power and neutralization of the beam space charge.

Beam focusing by a cylindrical, longitudinally and radially uniform plasma current lens was studied in [3–5]. In particular, in experiments [5], carried out under a heavy-ion fusion program, a 2.2-GeV gold-ion beam was focused to a 0.25-mm-diameter spot at a focal distance of 14 cm, the spot diameter being determined only by the initial emittance of the beam. In this paper, we consider a "thick," longitudinally nonuniform adiabatic plasma lens in which, by means of an external magnetic field, the current-channel diameter is reduced as the diameter of the focused beam decreases; as a result, the efficiency of the lens increases. In some aspects, this scheme is similar to a "passive" adiabatic plasma lens in which the plasma density changes in the longitudinal direction [6].

2. CALCULATION OF FOCUSING IN NONUNIFORM PLASMA LENSES

2.1. Plasma Current Lens in an Arbitrary Solenoid

Let us consider the focusing of an ion beam in the azimuthal magnetic field produced by a longitudinal current in a plasma. We will investigate the case when the current-channel radius is determined by an external nonuniform magnetic field. The problem will be solved in the paraxial approximation. In this case, the equation for the magnetic surfaces is (see, e.g., [7, 8])

$$a^2(z) = \frac{a^2(0)B_z(0)}{B_z(z)}, \qquad (1)$$

where $a(z)$ is the running radius of the magnetic surface and $B_z(z)$ is the longitudinal magnetic field on the axis; $B_z(0)$ and $a(0)$ are determined by the boundary conditions at $z = 0$. We assume that the magnetic field is strong enough so that the electrons carrying the plasma current move along the nested magnetic surfaces. In this case, the boundary condition at $z = 0$ takes the form $a(0) = b$, where b is the outer radius of the electrode producing the plasma current (e.g., it may be the inner electrode of the plasma gun, which is at the capacitor-battery potential and whose output end is located at $z = 0$; see below). From equation (1), it is easily seen that, if the magnetic surfaces are equally spaced in a certain cross section, then they are equally spaced in any other cross section. As a result, if the current density is uniform throughout the cross section near the electron emitter, it will be uniform in any cross section, which is necessary for the focusing free of spherical aberration. The equation for the trajectories of the focused ions is

$$r'' + k^2\frac{B_z(z)}{B_z(0)}r = 0, \quad k^2 = \frac{2IZe}{Mc^2v_b^2}, \qquad (2)$$

where I is the plasma current, Ze and M are the ion charge and mass, c is the speed of light, v is the ion velocity, and $B_z(0)$ is the magnetic field near the plasma-gun end. In the Plasma Lens device (see below), the ratio $B_z(z)/B_z(0)$ is determined by the magnetic-field geometry; in our case, it is a short solenoid. As the ions are focused and the current channel in the

1063-780X/00/2604-0351$20.00 © 2000 MAIK "Nauka/Interperiodica"

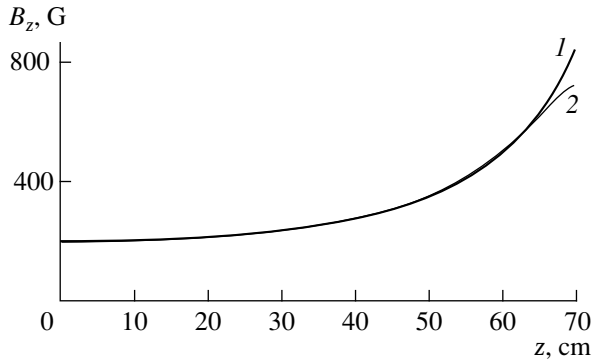

Fig. 1. Longitudinal profile of the external magnetic field in the case of a parallel beam: (*1*) the required field and (*2*) the field created by an optimized solenoid.

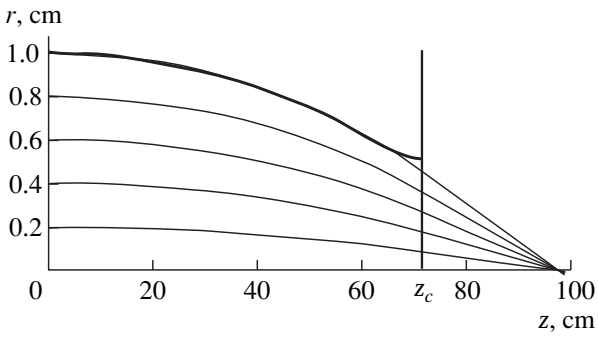

Fig. 2. Trajectories of the focused protons.

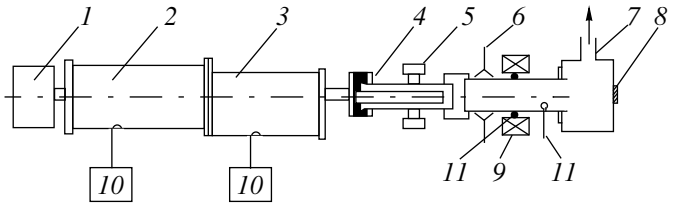

Fig. 3. Schematic of the device: (*1*) proton injector, (*2*) first stage of the accelerator, (*3*) the output stage of the accelerator, (*4*) plasma gun, (*5*) gas valve, (*6*) horn antenna, (*7*) chamber, (*8*) fluorescent screen, (*9*) solenoid, (*10*) RF sources, and (*11*) magnetic-field detectors.

plasma is compressed by the magnetic field of a short solenoid, a fraction of the ions (injected at large radii) can move outside the current channel for a certain time. These ions are also deflected toward the axis but do not attain the common focus. Outside the current channel, the equation of motion for them is

$$r'' + \frac{\kappa}{r} = 0, \quad \kappa = \frac{2ZeI}{c^2 M v}. \qquad (3)$$

An example of the calculated trajectories of the 5-MeV protons is presented below; the results are compared with the experiment.

2.2. Plasma Current Lens with an Optimized Solenoid

In order to increase the efficiency of the plasma lens, it is necessary to optimize the longitudinal profile of the external magnetic field so that the current-channel radius coincides with the radius of the focused beam. Then, it is required to calculate the parameters of a solenoid producing such a magnetic surface and determine the trajectory of the focused ions. We carried out calculations for the paraxial ion trajectories and paraxial magnetic surfaces. For the outer ions, which determine the radius of the focused beam, the boundary magnetic surface, and the current-channel radius, the motion equation has the form of (3) at $r \equiv r_{ms}$. This equation was solved by the Runge–Kutta method. As a result, we found the function $r_{ms}(z)$, which determines the sought-for magnetic surface in the case when the ions are injected parallel to the z-axis. For the boundary conditions $B_z(0) = 200$ G and $r_{ms}(0) = 1$ cm, from equation (1) we found the profile of the magnetic field on the axis of the system (Fig. 1) for the parameters of our experiment (see below).

The parameters of the solenoid producing the required magnetic field were calculated by Tikhonov's regularization procedure [9] (Fig. 1, curve *2*) by using the technique developed in [10]. The trajectories of ions propagating inside the current channel are described by equation (2), where $b = r_{ms}(0) = 1$ cm.

The results of the computer modeling of the focusing of a parallel proton beam (with account of the parameters of the plasma lens taken from the experiment) are presented in Fig. 2. The heavy line shows the current-channel boundary formed by the calculated nonuniform solenoid. The vertical line $z = z_c$ shows the position of the cathode, which can be, e.g., a wire mesh emitting electrons in order to maintain the plasma current. Behind the mesh, the focusing power of the lens is equal to zero so that the so-called inertial proton focusing takes place. In this scheme, the protons move inside the channel in which the current density is radially uniform; therefore, all of the protons are focused at the same point.

3. PLASMA LENS DEVICE AND URAL-5 ACCELERATOR

Experiments on the focusing of a 5-MeV proton beam were carried out in the Plasma Lens device and the Ural-5 accelerator (some of these results are presented in [11]). The Plasma Lens device (Fig. 3) includes a coaxial plasma gun (*4*) with two 40-cm-long electrodes, 3 and 7 cm in diameter. The inner annular electrode has a 2.5-cm-diameter aperture, through which a 5-MeV proton beam enters the plasma lens

chamber. The chamber is a 70-cm-long glass tube 10 cm in diameter. A short solenoid (*9*) 19 cm long and 15 cm in inner diameter encloses the tube. The maximum value of the magnetic field is 1 kG. The plasma gun is supplied from a capacitor battery with a 30-μF capacitance and charging voltage up to 10 kV. The working gas (hydrogen) enters the gun through a pulsed electromagnetic valve (*5*). The optimum amount of injected gas is 2–3 cm^3. The plasma temperature $T_e \sim$ 1–3 eV was measured by the Stark broadening of the H_β and H_γ spectral lines. For a 4- to 8-kV gun voltage, the plasma-flow velocity varied from 6×10^6 to 10^7 cm/s. The plasma density reached a value of 10^{16} cm^{-3} and then decreased to 10^{11} cm^{-3} over 100–200 μs.

The injected 5-MeV protons were produced in the Ural-5 accelerator, which is one of the first accelerators with high-frequency quadrupole focusing proposed by Kapchinskiĭ and Teplyakov (see, e.g., [12, 13]). The accelerator consists of the following basic elements (Fig. 3): (*1*) a proton injector (100-keV proton energy, 100-mA proton current, and 50-μs pulse duration), (*2*) the first stage of the accelerator (700-keV energy, 100-mA proton current, and 30-μs pulse duration), (*3*) the output stage of the accelerator (5-MeV energy, proton current to 30 mA, and 30-μs pulse duration), and (*10*) RF power amplifiers (RF power of ~1 MW and pulse duration of 100 μs). In order to improve the parameters as well as the reliability and stability of operation with the plasma lens, the Ural-5 accelerator was specially modernized.

4. EXPERIMENTS ON THE FOCUSING OF A 5-MeV PROTON BEAM

In addition to experiments described in [11], we performed measurements of the radial distribution of the azimuthal magnetic field at a distance of 42 cm from the plasma-gun output. The measurements were carried out using a 3-mm-diameter magnetic probe, which was introduced into the chamber through a 5-mm-diameter glass tube; this allowed us to move the probe along the chamber radius. The results of measurements are shown in Fig. 4. As is seen, the current-channel radius is ≈1 or 2 cm and the maximum magnetic field is ≈250 or 115 G for the switched-on and switched-off solenoid, respectively.

In experiments, we measured the diameter of a 5-MeV proton beam passing through the plasma at different instants with respect to the instant the plasma gun is switched on. For measurements, we used a 6-cm-diameter and 8-mm-thick fluorescent polystyrene screen. The screen was positioned 90 cm from the plasma-gun output and was protected against plasma radiation by a 12-μm aluminum foil, which was transparent for the 5-MeV protons. In all experiments, at the initial instant, the central electrode was positively charged. The gun voltage was 6 kV. The focusing was observed at 12- to 16- and 24- to 28-μs delays with respect the start of the gun discharge, which corresponded to the maximums of the plasma current measured by the Rogowski coil. The image of the proton beam on the screen was recorded by a digital camera. The average radius of the focused beam was 0.7 cm (in the absence of a plasma, it was equal to 3 cm). Calculation of the beam radius on the screen using equations (1) and (2) and the measured values of the current channel radius (1.3 cm), magnetic field (250 G), and initial

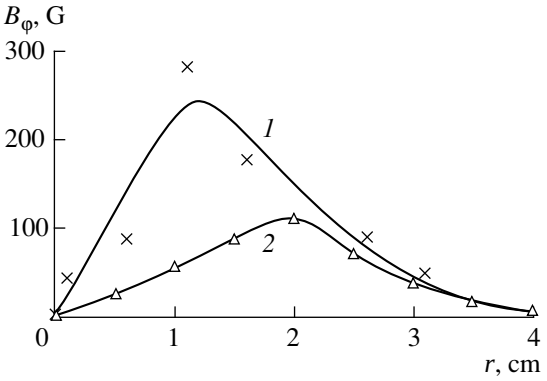

Fig. 4. Radial profile of the azimuthal magnetic field (curves *1* and *2* correspond to the switched-on and switched-off solenoids, respectively).

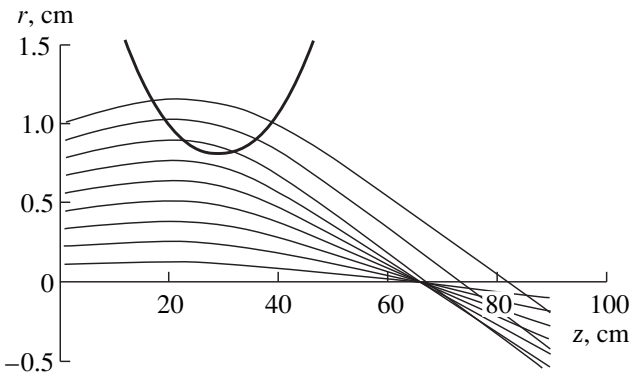

Fig. 5. 5-MeV proton trajectories calculated for the experimental conditions.

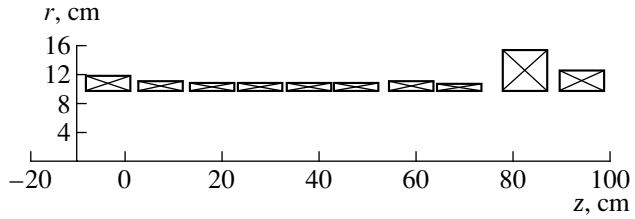

Fig. 6. Schematic of an optimized solenoid in the case of a diverging beam.

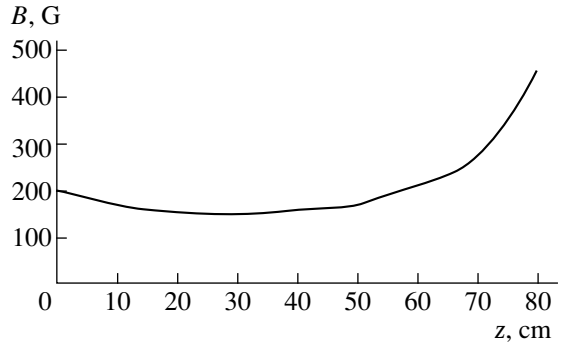

Fig. 7. Longitudinal profile of the external magnetic field created by an optimized solenoid.

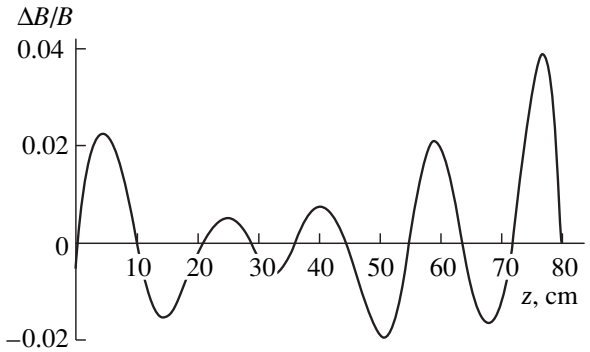

Fig. 8. Relative deviation of the magnetic field produced by an optimized solenoid from the calculated magnetic field.

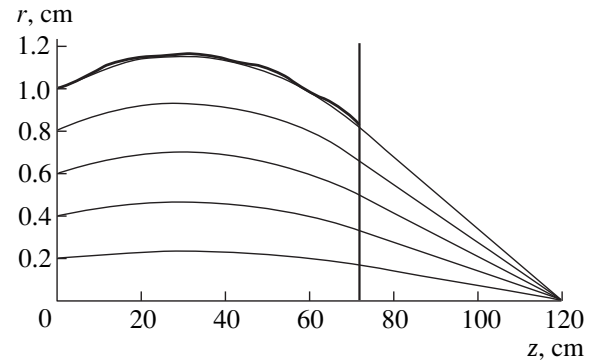

Fig. 9. Proton trajectories in the field of an optimized solenoid in the case of a diverging beam.

beam divergence (0.015 rad) gives the value of 0.6 cm (Fig. 5), which agrees with the experimental result. A parabolic curve at the top of Fig. 5 presents the radius of the current channel formed by the short solenoid used in this experiment. The protons injected at a radius of <0.7 cm are focused at z = 70 cm. The screen was positioned at z = 90 cm, and the second electrode of the current channel (a copper wire mesh) was located at z = 60 cm. It is seen in Fig. 5 that the protons injected at large radii propagate outside the current channel and do not get the focus.

5. OPTIMIZATION OF THE SOLENOID IN THE CASE OF A DIVERGING PROTON BEAM

By analogy with the method used in Section 2, we calculated the solenoid for the case of a diverging proton beam with zero emittance and the beam divergence as a function of radius, $\alpha(r) = \alpha_0 r/r_0$, where α_0 = 0.015 rad is the angle of deflection of the outer injected protons from the axis. We calculated the solenoid parameters for which the outer-proton trajectories coincide with the current-channel boundary formed by the corresponding magnetic surface. Figure 6 shows the calculated size and position of the solenoid coils for a current density in the coils of 1.6 A/mm^2.

Figure 7 shows the longitudinal magnetic field $B_c(z)$ produced by an optimized solenoid as a function of the longitudinal coordinate. Figure 8 shows the relative deviation of the magnetic field, $\Delta B/B(z) = [B(z) - B_c(z)]/B(z)$, where $B(z)$ is the required magnetic field obtained from the condition of coincidence between the outer-proton trajectory and the magnetic surface.

The proton trajectories in the current channel produced by the magnetic field of an optimized solenoid are presented in Fig. 9. The heavy curve shows the calculated current-channel boundary produced by a nonuniform solenoid. The vertical line at z = 72 cm shows the position of the cathode for the current flowing through the plasma. The cathode (wire mesh) was assumed to be transparent to the focused beam. Since we assume the density to be radially uniform, all the protons are focused at the same point.

A subsequent experimental study will be devoted to the proton focusing in an optimized magnetic field. The efficiency of the plasma lens can be increased due to the simultaneous consistent decrease in the radii of both the current channel and the focused beam.

ACKNOWLEDGMENTS

This work was supported by the Science and Technology Center of Ukraine, project no. 298.

REFERENCES

1. J. Meyer-ter-Vehn, S. Witkowski, R. Bock, *et al.*, Phys. Fluids B **2**, 1313 (1990).
2. G. Hairapetian, in *Proceedings of 5th Workshop on Advanced Acceleration Concepts, Woodbury, NY, 1994*, p. 174 [AIP Conf. Proc. **335**, 174 (1994)]; W. Barletta, S. Chattopadhyay, P. Chen, *et al.*, *ibid.*, p. 606.
3. W. K. H. Panofsky and W. R. Baker, Rev. Sci. Instrum. **21**, 445 (1950).
4. A. A. Goncharov, I. M. Protsenko, and V. V. Tsiolko, Zh. Tekh. Fiz. **50**, 2556 (1980) [Sov. Phys. Tech. Phys. **25**, 1499 (1980)].

5. E. Boggasch, A. Tauschwitz, H. Wahl, *et al.*, Appl. Phys. Lett. **60**, 2475 (1992).
6. P. Chen, K. Oide, A. M. Sessler, and S. S. Yu, Phys. Rev. Lett. **64**, 1231 (1990).
7. A. I. Morozov and L. S. Solov'ev, in *Reviews of Plasma Physics*, Ed. by M. A. Leontovich (Gosatomizdat, Moscow, 1963; Consultants Bureau, New York, 1965), Vol. 2.
8. A. I. Morozov and S. V. Lebedev, in *Reviews of Plasma Physics*, Ed. by M. A. Leontovich (Atomizdat, Moscow, 1974; Consultants Bureau, New York, 1980), Vol. 8.
9. A. N. Tikhonov and V. Ya. Arsenin, *Solutions of Ill-Posed Problems* (Nauka, Moscow, 1979; Halsted, New York, 1977).
10. V. I. Butenko, Zh. Tekh. Fiz. **62** (7), 157 (1992).
11. V. N. Belan, V. I. Butenko, B. I. Ivanov, *et al.*, Rev. Sci. Instrum. **69**, 1110 (1998).
12. I. M. Kapchinskiĭ and V. A. Teplyakov, Prib. Tekh. Éksp., No. 4, 17 (1970).
13. A. A. Egorov, A. P. Mal'tsev, V. A. Teplyakov, *et al.*, Zh. Tekh. Fiz. **51**, 1643 (1981) [Sov. Phys. Tech. Phys. **26**, 942 (1981)].

Translated by A. D. Smirnova[†]

[†] Now deceased.

Plasma Physics Reports, Vol. 26, No. 4, 2000, pp. 356–359. Translated from Fizika Plazmy, Vol. 26, No. 4, 2000, pp. 383–386.

PLASMA ELECTRONICS AND NEW ACCELERATION METHODS

The Maximum Electron Energy Achievable in Conventional Resonant Linear Accelerators

A. N. Opanasenko

National Science Center Kharkov Institute for Physics and Technology, Akademicheskaya ul. 1, Kharkov, 310108 Ukraine

Received April 27, 1999

Abstract—It is shown that, in resonant high-energy electron linear accelerators, undulator radiation should be observed, which is emitted by off-axis beam particles interacting with the transverse field of nonsynchronous spatial harmonics of the fundamental axisymmetric mode of a periodic accelerating structure. The mean power emitted by an individual electron is proportional to the squared distance between the electron and the accelerator axis and to the squared electron energy. This circumstance may limit the maximum energy to which off-axis beam electrons can be accelerated. © *2000 MAIK "Nauka/Interperiodica".*

1. INTRODUCTION

A major advantage of linear accelerators (linacs) over cyclic accelerators is that the power emitted by the accelerated particles is independent of their kinetic energy. At present, the maximum achievable energies in linacs are limited primarily by the mean acceleration rate and realistic acceleration lengths so that linacs capable of accelerating electrons (positrons) to teraelectronvolt energies are now being actively developed around the world. In this area, significant progress has been achieved in developing resonant linacs with periodic structures providing high accelerating gradients [1]. We should, however, mention an important factor that limits the maximum achievable energy in periodic structures: off-axis particles lose their kinetic energy via undulator photon emission [2, 3] in the transverse field of nonsynchronous spatial harmonics of the fundamental mode of a periodic linear accelerating structure.

Here, we apply the classical electrodynamic approach in order to consider the mechanism for this kind of photon emission and to derive an expression for the maximum energy to which the particles in resonant linacs can be accelerated.

2. MAXIMUM ENERGY OF AN OFF-AXIS PARTICLE IN A PERIODIC ACCELERATING STRUCTURE

The total power emitted by an ultrarelativistic electron moving along the z-axis of an accelerated structure can be represented as [4]

$$P \simeq \frac{2e^2}{3c^3}\left(\gamma^6\left(\frac{dv_z}{dt}\right)^2 + \gamma^4\left(\frac{dv_\perp}{dt}\right)^2\right), \qquad (1)$$

where c is the speed of light in a vacuum, e is the charge of an electron or a positron (below, we will speak only about electrons), γ is the Lorentz factor, and v_z and $v_\perp$ are the longitudinal and transverse electron velocities such that $v_z \approx c$ and $v_z \gg v_\perp$.

It is well known that the power emitted by a particle accelerated in the longitudinal direction is independent of its energy and is extremely low [4, 5]. The possible effect of the transverse fields on the emission from a particle in linacs has not yet been considered. However, because of the finite transverse dimensions of real beams and/or the deviation of beams from the linac axis, off-axis beam particles should experience rapidly oscillating transverse forces driven by nonsynchronous spatial modes inherent (by virtue of the Floquet theorem) in periodic accelerating structures.

We consider axisymmetric accelerating structures that are traditionally used in acceleration techniques. In the paraxial approximation, the radial force acting upon an ultrarelativistic particle can be written as [4]

$$F_r \simeq -\frac{er}{2}\frac{d}{dz}E_z, \qquad (2)$$

where E_z is the longitudinal electric field at the axis of the structure and r is the distance between the accelerated particle and the axis. Without loss of generality, we will deal with a traveling-wave periodic structure. We represent the field at the axis in the Floquet form [4]:

$$E_z = E_0 \sum_{n=-\infty}^{\infty} b_n \cos(h_n z - \omega t), \qquad (3)$$

where $h_n = \omega/c + 2\pi n/D$ is the longitudinal wavenumber, ω is the angular frequency of the electromagnetic field, and D is the period of the structure. The relative amplitude b_n of the nth spatial harmonics is normalized

1063-780X/00/2604-0356$20.00

to the amplitude E_0 of the fundamental accelerating harmonic so that $b_0 = 1$.

We substitute (3) into (2) and assume that the longitudinal coordinate of an ultrarelativistic particle depends on time as $z = c(t - t_0)$. As a result, we arrive at the equation of radial electron motion [6, 7]:

$$\frac{d^2r}{dt^2} = \frac{eE_0}{m\gamma}\frac{\pi r}{D}\sum_{n=-\infty}^{\infty} nb_n \sin\left(\frac{2\pi}{D}cnt - \varphi_n\right), \qquad (4)$$

where $\varphi_n = \varphi_0 + 2\pi nct_0/D$ and $\varphi_0 = \omega t_0$ is the particle phase with respect to the phase of the synchronous harmonic.

Note that the mean energy of an accelerated particle changes on a time scale longer than the oscillation period D/c. This indicates that the rapidly oscillating rate (4) of particle acceleration in the radial direction is inversely proportional to the relativistic mass of the particle.

Inserting the radial acceleration rate (4) into (1) and averaging the resulting formula over the period D/c, we obtain the following expression for the mean power emitted by a charged particle accelerated in a periodic linear structure:

$$P_{\text{rad}} = \frac{\pi^2}{3}\frac{e^4}{m^2c^3}\left(\frac{r}{D}\right)^2 E_0^2 \nu(\varphi_0)\left(\frac{W}{mc^2}\right)^2, \qquad (5)$$

where $W = mc^2\gamma$ is the net particle energy and the coefficient $\nu(\varphi_0) = \sum_{n=-\infty}^{\infty} n^2 [b_n^2 + b_n b_{-n}\cos(2\varphi_0)]$ is determined by the spectral content of the spatial harmonics of a periodic structure.

Expression (5) implies that a particle moving at a finite distance r from the axis of the accelerating structure should emit photons. Since the emission power increases in proportion to the squared kinetic energy of the particle, we may anticipate that the particle can only be accelerated to a certain limiting energy at which the power emitted by the particle equals the power the particle gains in an accelerating wave field. This corresponds to the power balance relation

$$P_{\text{rad}} = ceE_0\cos\varphi_0. \qquad (6)$$

Substituting (5) into (6) gives the maximum energy of an off-axis particle,

$$W_m = mc^2\frac{D}{\pi r}\sqrt{\frac{3mc^2}{eE_0 r_0}\frac{\cos\varphi_0}{\nu(\varphi_0)}}, \qquad (7)$$

where r_0 is the classical radius of an electron.

Now, we analyze the applicability condition for the validity of the classical electrodynamic description of the emission from an ultrarelativistic electron. According to [2, 8], the electrodynamic approach is valid if the electromagnetic wave energy in the rest frame of an electron is much lower than the electron rest energy:

$$\frac{h\gamma c/D}{mc^2} \ll 1. \qquad (8)$$

If we examine condition (8) in the context of the development of linear colliders operating in the X-ray range and for which $D \sim 1$ cm, we will find that relationship (7) is valid for electron energies satisfying the condition

$$W \ll mc^2\frac{D}{\Lambda_c} \simeq 0.5\times 10^6 \text{ eV}\frac{1 \text{ cm}}{2.4\times 10^{-10} \text{ cm}}$$
$$\simeq 2\times 10^3 \text{ TeV},$$

where h is Planck's constant and Λ_c is the Compton wavelength of an electron.

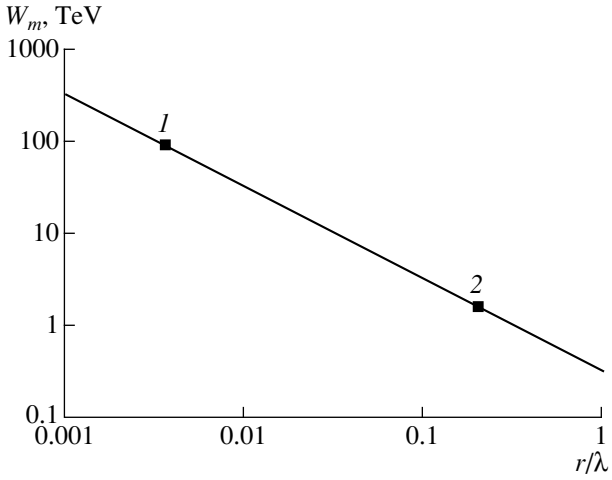

Maximum attainable energy W_m as a function of the radial position r/λ of an electron with respect to the axis of the accelerating structure. Point *1* corresponds to $r/\lambda = \delta r/\lambda = 0.0036$ and point *2*, to $r/\lambda = a/\lambda = 0.2$.

The figure shows the maximum energy of a particle as a function of its radial position r/λ with respect to the axis over the interval from $\delta r/\lambda$ (the relative amplitude of the betatron oscillations of the beam particles in the focusing system of an accelerator) to a/λ (the relative aperture width of the accelerating structure; usually, $a/\lambda \simeq 0.2$ [11]) in the radial direction. The profile of the maximum energy was obtained from expression (7) taken with the parameter values characteristic of the next generation of resonant linear colliders ($E_0 \sim$ 100 MV/m [1] and $D = \lambda/3$) and with the coefficient $\nu(0) = 0.154$, which was computed with the SUPERFISH code [9] for a SLAC-like structure [10]. We can see that, for typical permissible relative deviations from the axis, $\delta r/\lambda \simeq 0.0036$ [11], the maximum energy to which the particles can be accelerated is about 90 TeV, which is almost two orders of magnitude

higher than the desired attainable energies in linear colliders currently under development. However, expression (7) implies that the stronger the accelerating field E_0 (i.e., the higher the acceleration rate), the lower the maximum achievable energy. Additionally, if we take into account the fact that, according to the estimates presented in [11], the relative deviation of the beam particles from the axis is essentially independent of the wavelength λ of the accelerating wave, $\delta r/\lambda \simeq$ const, then, with allowance for the dependence $E_0 \sim \lambda^{-7/8}$ [12], we find that the maximum achievable energy will fall off with λ according to the law

$$W_m \propto \lambda^{7/16}. \tag{9}$$

3. EMISSION FROM AN ACCELERATED ELECTRON BUNCH

Here, we consider the power emitted by an accelerated electron bunch. High-energy accelerated particles for which the characteristic wavelength of the emitted photons is much shorter than the mean distance between the particles in the bunch emit photons independently of each other. In this case, the total power emitted by the bunch is equal to the sum of the powers emitted by the electrons [2]:

$$P_{\text{tot}} = \frac{\pi^2}{3}\frac{e^4}{m^2c^3}E_0^2\sum_i\left(\frac{r_i}{D}\right)^2\nu(\varphi_{0,i})\left(\frac{W_i}{mc^2}\right)^2, \tag{10}$$

where the summation is carried out over all bunch electrons.

Expression (10) shows that either a bunch with finite transverse dimensions or a bunch accelerated at a certain distance from the axis will emit radiation. One can see that, when the bunch particles are accelerated to such energies that the power emitted by the bunch becomes comparable to the power acquired by bunch in the accelerating wave field, the acceleration process ceases to be efficient, which corresponds to the condition

$$P_{\text{tot}} = \sum_i ceE_0\cos\varphi_{0,i}. \tag{11}$$

Let us derive an expression for the maximum achievable root-mean-square energy of the bunch under the balance relation (11) between the radiated and absorbed powers. We consider the case in which the correlations between the energy of the particle and its radial coordinate can be neglected. This case is typical of, e.g., coherent betatron oscillations of the beam particles in the focusing system of an accelerator, which the bunch being displaced from the axis as a single entity. Note that, according to (11), the microwave power absorbed by a bunch that is displaced from the axis as a single entity will be completely converted into the power of the emitted photons. We substitute (10) into the power balance relation (11) and average the resulting expression over all bunch particles to obtain the maximum achievable root-mean-square energy of a particle in the bunch,

$$W_m \equiv \sqrt{\langle W^2\rangle} \simeq mc^2\frac{D}{\pi\sigma_r}\sqrt{\frac{3mc^2}{eE_0r_0}\frac{\langle\cos\varphi_0\rangle}{\nu(\varphi_0)}}, \tag{12}$$

where the angle brackets denote averaging over the bunch particles and $\sigma_r \equiv \sqrt{\langle r^2\rangle}$ is the standard deviation of the particles from the axis of the structure. Since the coefficient $\nu(\varphi_0)$ depends weakly on the particle phase, it is taken with the phase φ_0 corresponding to the bunch center.

4. CONCLUSION

We have analyzed the mechanism for conversion of the kinetic energy of particles accelerated in the longitudinal direction into the energy of photons emitted by the particles in the course of their interaction with comparatively weak transverse fields of the nonresonant spatial harmonics in periodic accelerating structures. We have also studied the conditions under which this conversion occurs. It is evident that, in the conversion mechanism, a major role is played by high particle energies and by a rapidly oscillating transverse (undulator) force along the path of the beam.

It should be noted that the problem of longitudinal and transverse dynamics of accelerated particles in the energy range in which the power loss due to photon emission becomes dominant (i.e., when the decelerating force arising from photon emission should be incorporated into the motion equations) requires further research. It is also of interest to study how the fluctuations associated with the quantum character of photon emission from accelerated particles affect the beam dynamics.

ACKNOWLEDGMENTS

I am grateful to S.V. Peletminskiĭ for a valuable consultation on the possibility of applying the classical electrodynamic approach to the study of photon emission. I wish to thank N.I. Aĭzatskiĭ, V.F. Zhiglo, V.I. Kurilko†, V.A. Kushnir, N.A. Khizhnyak, and S.A. Cherenshchikov for fruitful discussions and useful remarks.

REFERENCES

1. J. P. Delahaye, in *Proceedings of 5th European Particle Accelerator Conference, Barcelona, 1996*, Vol. 1, p. 37.
2. V. L. Ginzburg, *Theoretical Physics and Astrophysics* (Nauka, Moscow, 1987; Pergamon, Oxford, 1979); Izv. Akad. Nauk SSSR, Ser. Fiz. **11**, 165 (1947).

† Deceased.

3. N. D. Devyatkov, E. D. Naumenko, A. A. Rukhadze, *et al.*, Zh. Tekh. Fiz. **67** (11), 131 (1997) [Tech. Phys. **42**, 1360 (1997)].
4. *Linear Accelerators*, Ed. by P. M. Lapostolle and A. L. Septier (Elsevier, Amsterdam, 1970).
5. J. D. Jackson, *Classical Electrodynamics* (Wiley, New York, 1962; Inostrannaya Literatura, Moscow, 1965).
6. É. L. Burshteĭn and G. V. Voskresenskiĭ, *Linear Accelerators of Intense Electron Beams* (Atomizdat, Moscow, 1970).
7. S. C. Hartman and J. B. Rosenzweig, Phys. Rev. E **47**, 2031 (1993).
8. L. D. Landau and E. M. Lifshitz, *The Classic Theory of Fields* (Nauka, Moscow, 1973; Pergamon, Oxford, 1975).
9. J. H. Billen and L. M. Young, in *Proceedings of 1993 Particle Accelerator Conference, Washington, 1993*, Vol. 2, p. 790.
10. G. Loew, R. H. Miller, R. A. Early, and K. L. Bane, Report No. SLAC-PUB-2295 (Stanford Linear Accelerator Center, Stanford, CA, 1979).
11. R. B. Palmer, in *Proceedings of Workshop on New Developments in Particle Acceleration Techniques, Orsay, 1987*, Vol. 1, p. 80.
12. W. Schnell and A. M. Sessler, in *Proceedings of Workshop on New Developments in Particle Acceleration Techniques, Orsay, 1987*, Vol. 1, p. 137.

Translated by O. E. Khadin

Plasma Physics Reports, Vol. 26, No. 4, 2000, pp. 360–362. Translated from Fizika Plazmy, Vol. 26, No. 4, 2000, pp. 387–389.

PLASMA ELECTRONICS AND NEW ACCELERATION METHODS

Formation and Emission of Intense Electromagnetic Pulses by Means of an Insulated Rod Antenna Excited by a Short-Duration High-Current Relativistic Electron Beam

N. I. Gaponenko, A. M. Gorban', D. V. Gorozhanin, V. I. Kurilko†, S. M. Latinskiĭ, Yu. F. Lonin, and I. F. Kharchenko†

Kharkov Institute for Physics and Technology, National Science Center, Academicheskaya ul. 1, Kharkov, 310108 Ukraine

Received April 30, 1999; in final form, September 17, 1999

Abstract—The possibility of forming and emitting high-power electromagnetic pulses by means of an insulated rod antenna excited by a short-duration high-current electron beam is studied. It is found experimentally that the amplitude of the emitted pulses and their characteristic period depend on the antenna length. The potentialities of the method proposed as applied to the generation of intense videopulses are discussed. © *2000 MAIK "Nauka/Interperiodica".*

1. INTRODUCTION

The principles of the formation of high-power electromagnetic radiation in beam–plasma systems were first formulated in theoretical works by Faĭnberg [1–3] and confirmed experimentally in [4–6]. Further development of these ideas and advances in the production of superintense charged-particle beams have provided considerable progress in super-high-power electronics.

An important line of investigations in this field is the production of intense electromagnetic (EM) pulses by converting the energy of a high-current relativistic electron beam (REB) into EM energy through direct excitation of an antenna–feeder system (AFS). Experiments with a premodulated beam [7] demonstrated that the efficiency of this conversion mechanism is fairly high (higher than 50%). In [8], direct excitation of an AFS by a modulated beam was used to measure the modulation depth of a beam propagating in a plasma. Of particular interest is to examine the potentialities of the method of direct excitation of an AFS by an electron beam for generating short-duration high-power EM pulses. As is known [9, 10], such pulses contain intense low-frequency spectral components, which are very promising for near-surface introscopy of the Earth, geological surveys of the sea shelf, and other investigations in which conventional high-frequency probing is inefficient.

The objective of this paper is to experimentally study the possibility of emitting high-power nanosecond EM pulses by exciting an AFS (in particular, a rod antenna) by an unmodulated short-duration high-current REB.

2. EXPERIMENT

Experimental studies of the excitation of a rod antenna by a short-duration high-current relativistic electron beam were carried out in a device producing pulsed electron beams with the following parameters: energy E = 0.5–1.5 MeV, current I = 5–15 kA, pulse duration up to 15 ns, and current rise duration ~0.5–1 ns.

In the experiments, we used 1- to 3-m-long rod antennas, 10–20 mm in diameter. The field of the emitted radiation was measured by a TEM horn antenna located ~5 m from the middle of the emitting antenna.

Figure 1 shows the schematic of the experiment. The electron flux is emitted from the cathode *1* when the accelerating voltage is applied across the anode–cathode gap. An anode *2* is made from a stainless steel grid with a transmittance of 85%. The beam current was measured by the Rogowski coil *4*. To prevent electric breakdown and give the necessary shape to the electron beam, we used a 0.5- to 1.5-kOe magnetic field created by coils *3*. The beam current was shorted to a cylindrical graphite collector *5* located 20 mm from the anode grid and mounted on a hemispheric insulator protecting the collector from electric breakdown. A rod antenna *7* was connected directly to the collector; in the experiments, the antenna length varied from 1 to 3 m.

At the horn of a receiving antenna *8*, the input impedance was equal to 377 Ω; near the cable connection, it was equal to 77 Ω. The angle between the axes of the emitting and receiving antennas was 25°–30°.

† Deceased.

1063-780X/00/2604-0360$20.00 © 2000 MAIK "Nauka/Interperiodica"

The aim of the experiments was to study the dependence of the characteristics of the generated EM pulses on the length of the emitting rod antenna. Figures 2–4 show the traces of signals detected by the receiving antenna for rod lengths of 1, 2, and 3 m, respectively, and the traces of the beam current at the collector. To specify the time scale, a calibration signal with a period of 20 ns is also shown.

As is seen from Figs. 2–4, the signal detected by the receiving antenna consists of irregular oscillations with a characteristic period on the order of the beam-current duration. It is clearly seen that the characteristic period and amplitude of the signal depend on the length of the emitting rod. Note that the recorded signal is similar in shape to the optimum signal for the superbroadband location with $\mu = \Delta f/f \approx 4/N = 0.66$ [11]. The measured electric field at the horn of the receiving antenna was ~10–30 V cm^{-1} for a 3-m-long emitting rod, and the amplitudes of signals emitted by 2- and 3-m-long antennas exceeded by 10 and 15 dB, respectively, those of signals emitted by a 1-m-long antenna. The characteristic period of oscillations also increased in proportion $\tau_2/\tau_1 \approx 1.3$ and $\tau_3/\tau_1 \approx 1.5$, where τ_1, τ_2, and τ_3 are the characteristic periods of signals emitted by the antennas with lengths of 1, 2, and 3 m, respectively. The emitted pulses were rather short, which is typical of videopulses. We analyzed the experimental data assuming the dipole character of the antenna emission. Such an approximation is based on the fact that, in the experiment, the characteristic emission wavelength is much longer than the antenna length, $\lambda \gg L$. Therefore, from the measured value of the electric field at the horn of the receiving antenna, we can estimate both the characteristic value of the current flowing through the rod and the emitted power. In our case, the expressions for the electric and magnetic field components lying in the horn plane of the receiving antenna are

$$E = \frac{ik^2 IL}{4\pi\omega\varepsilon_0 r}\sin\vartheta e^{i\omega t - ikr},$$

$$H = \frac{ikIL}{4\pi\mu_0 r}\sin\vartheta e^{i\omega t - ikr},$$

where I is the current flowing through the rod antenna, r is the distance from the rod center to the receiving antenna, ϑ is the angle between the axes of the rod and the receiving antenna, and ω and $k = \frac{2\pi}{\lambda}$ are the characteristic frequency and wavenumber of the rod emission. Then, for the parameter values $r \approx 4$ m, $\lambda \approx 12$ m, $\vartheta \approx 25°$, and $L = 3$ m, we obtain that the characteristic current through the rod antenna is ~1 kA. The total emitted power for the given parameters is equal to 10–20 MW.

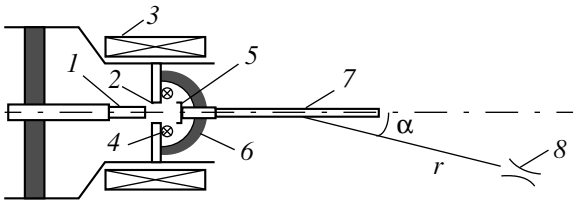

Fig. 1. Schematic of the experiment.

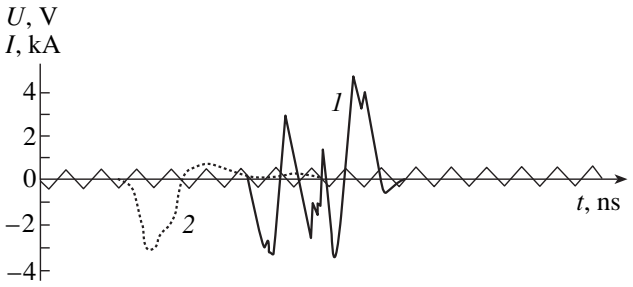

Fig. 2. Traces of (*1*) the emission signal and (*2*) beam current for an antenna length of 1 m and attenuation of 10 dB. The frequency of the calibration signal is 50 MHz.

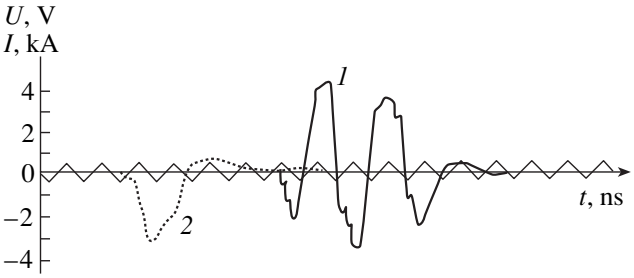

Fig. 3. Same as in Fig. 2 for an antenna length of 2 m and attenuation of 20 dB.

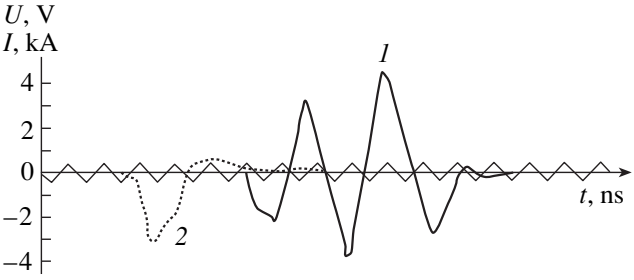

Fig. 4. Same as in Fig. 2 for an antenna length of 3 m and attenuation of 20 dB.

3. CONCLUSION

It is experimentally shown for the first time that intense nanosecond EM pulses can be generated by means of an insulated rod antenna excited directly by a short-duration high-current REB. The characteristic period and amplitude of the pulses increase with increasing the length of the emitting rod, provided that the pulse duration is kept constant.

To clarify the generation mechanism and determine the optimum generation conditions, we plan to carry out a series of experimental and theoretical investigations.

REFERENCES

1. A. I. Akhiezer and Ya. B. Faĭnberg, Dokl. Akad. Nauk SSSR **69**, 555 (1949).
2. A. I. Akhiezer and Ya. B. Faĭnberg, Zh. Éksp. Teor. Fiz. **21**, 1262 (1951).
3. Ya. B. Faĭnberg, At. Energ. **11**, 13 (1961).
4. I. F. Kharchenko, Ya. B. Faĭnberg, E. A. Kornilov, *et al.*, Zh. Éksp. Teor. Fiz. **38**, 685 (1960) [Sov. Phys. JETP **11**, 493 (1960)].
5. I. F. Kharchenko, Ya. B. Faĭnberg, E. A. Kornilov, *et al.*, Zh. Tekh. Fiz. **31**, 761 (1961) [Sov. Phys. Tech. Phys. **6**, 551 (1962)].
6. E. G. Shustin, V. P. Popovich, and I. F. Kharchenko, Zh. Éksp. Teor. Fiz. **59**, 657 (1970) [Sov. Phys. JETP **32**, 358 (1971)].
7. M. Friedman, J. Krall, J. J. Lau, and V. Serlin, Rev. Sci. Instrum. **61**, 171 (1990).
8. Yu. V. Tkach, I. I. Magda, G. V. Skachek, *et al.*, Fiz. Plazmy **6**, 586 (1980) [Sov. J. Plasma Phys. **6**, 321 (1980)].
9. H. F. Harmut, *Nonsinusoidal Wave for Radar and Radio Communication* (Academic, New York, 1981).
10. H. F. Harmut and D. R. Shao, IEEE Trans. **EMS-25**, 123 (1983).
11. L. Yu. Astanin and A. A. Kostylev, *Principles of Super-Wideband Radar Measurements* (Radio i Svyaz', Moscow, 1989).

Translated by N. F. Larionova

Plasma Physics Reports, Vol. 26, No. 4, 2000, pp. 363–365. Translated from Fizika Plazmy, Vol. 26, No. 4, 2000, pp. 390–393.

PLASMA ELECTRONICS AND NEW ACCELERATION METHODS

Multimode Parametric Instability during Electron Cyclotron Heating

Yu. R. Alanakyan, A. A. Ivanov, A. A. Luk'yanov, K. S. Serebrennikov, and V. Yu. Fedotov

Russian Research Centre Kurchatov Institute, pl. Kurchatova 1, Moscow, 123182 Russia

Received April 30, 1999

Abstract—A study is made of the generation of electron Bernstein waves in the interaction of a microwave field with a magnetized plasma during electron cyclotron heating. Parametric resonance accompanied by simultaneous conversion of microwave-field energy into the energy of numerous waves is analyzed. The relevant dispersion relation is investigated using the Hill method, which has recently been applied for the first time to examine the parametric interaction between high-power microwave radiation and plasmas. It is shown that the dispersion relation can be used to describe the onset of modulational instability at multimode parametric resonance. The growth rate of the modulational instability is obtained. Efficient energy transfer from the microwave field into Bernstein modes and, accordingly, into plasma electrons may be one of the main mechanisms for electron cyclotron resonance plasma heating. © *2000 MAIK "Nauka/Interperiodica".*

The nonlinear parametric interaction of microwave radiation with a plasma, which gives rise to a resonant instability, was investigated in detail by Silin [1]. Gradov and Zyunder [2] applied the method developed by Silin to consider the parametric excitation of waves propagating approximately along the magnetic field, when the pump wave frequency is close to the electron cyclotron frequency. Here, we study the problem of the generation of Bernstein modes under electron cyclotron heating conditions. Interest in this problem stems primarily from the fact that, under these conditions, all of the modes of the pump wave resonantly generate numerous waves, in which case the wave excitation is very sensitive to the frequency detuning $\Delta = \omega_0 - \Omega$ (where ω_0 is the pump wave frequency and Ω is the electron cyclotron frequency): the value of Δ determines which particular wave is preferentially generated.

We consider a homogeneous plasma that is affected by an alternating electric field $\mathbf{E}(t) = \mathbf{E}_0 \sin\omega_0 t$ whose frequency is close to the electron cyclotron frequency, $\omega_0 \approx \Omega \equiv eB/mc$, and which is directed transverse to a constant magnetic field **B**.

The growth rate of the excited waves is determined from the equation [1]

$$D(\omega, \mathbf{k}) = \begin{vmatrix} I_{nm} & D^e_{nm} \\ D^i_{nm} & I_{nm} \end{vmatrix} = 0, \quad (1)$$

where I_{nm} is the identity matrix, D $D^e_{nm} = R^{(n)}_e J_{n-m}(\mu)$, $D^i_{nm} = R^{(n)}_i J_{m-n}(\mu)$, $\mu = |\mathbf{ka}|$, **k** is the wave vector (which is the same for all of the generated waves), **a** is the amplitude of the electron oscillations in the pump field, $J_n(\mu)$ is an *n*th order Bessel function of the first kind,

$$R^{(n)}_\alpha = \frac{\delta\varepsilon_\alpha(\omega + n\omega_0, \mathbf{k})}{1 + \delta\varepsilon_\alpha(\omega + n\omega_0, \mathbf{k})}, \quad (2)$$

and $\delta\varepsilon_\alpha(\omega + n\omega_0, \mathbf{k})$ is the contribution of the plasma particles of species $\alpha = e, i$ to the longitudinal dielectric function. In the case of a high-frequency pump wave, the ion contribution to the longitudinal dielectric function can be written as

$$\delta\varepsilon_i = -\frac{\omega^2_{Li}}{\omega^2}, \quad (3)$$

where ω_{Li} is the Langmuir frequency of the plasma ions (which are assumed to be unmagnetized).

Note that the infinite-order determinant $D(\omega, \mathbf{k})$ is a periodic function of frequency with the period ω_0, in which case the simple poles are the only singular points of the matrix elements in (1) on the complex plane ω. Baitin and Ivanov [3] proposed an efficient approach for investigating infinite-order determinants. This approach is based on the Hill method [4] and makes it possible to find the roots of the dispersion relation without any *a priori* assumptions regarding the presence of small parameters. Following this approach, we represent the meromorphic function $D(\omega, \mathbf{k})$ as an infinite series,

$$D(\omega, \mathbf{k}) = 1 + \sum_\alpha \sum_n \frac{K_{\alpha n}}{\sin^2(\pi\omega/\omega_0) - \sin^2(\pi\omega_{\alpha n}/\omega_0)} = 0, \quad (4)$$

1063-780X/00/2604-0363$20.00

where $K_{\alpha n} = \dfrac{\pi D_{\alpha n}\sin(2\pi\omega_{\alpha n}/\omega_0)}{\omega_0 \partial\delta\varepsilon_\alpha(\omega, k)/\partial\omega|_{\omega=\omega_{\alpha n}}}$, $\omega_{\alpha n}$ are the roots of the equations $1 + \delta\varepsilon_\alpha(\omega, k) = 0$, and $D_{\alpha n}$ is the determinant of the matrix $D(\omega = \omega_{\alpha n})$ in which the row where a singularity at $\omega = \omega_{\alpha n}$ is present is assumed to be regularized by replacing unity with zero and $R_\alpha^{(0)}$ with minus unity.

Substituting the explicit expression (3) for $\delta\varepsilon_i(\omega)$ into (4) yields

$$D(\omega, \mathbf{k}) = 1 + \left(\frac{\pi\omega_{Li}}{\omega_0}\right)^2 \sum_{m=-\infty}^{\infty} (-1)^m J_{m+\frac{\omega_{Li}}{\omega_0}}(\mu) J_{-m-\frac{\omega_{Li}}{\omega_0}}(\mu) \frac{R_e^{(m)}(\omega_{Li})}{\sin^2\left(\pi\frac{\omega}{\omega_0}\right) - \left(\pi\frac{\omega_{Li}}{\omega_0}\right)^2 \cos^2\left(\pi\frac{\omega}{\omega_0}\right)}$$
$$- \frac{\pi}{\omega_0}\left(\frac{\pi\omega_{Li}}{\omega_0}\right)^2 \sum_{n=1}^{\infty} J_{\frac{\omega_{en}}{\omega_0}}(\mu) J_{-\frac{\omega_{en}}{\omega_0}}(\mu) \frac{\cos\left(\pi\frac{\omega_{en}}{\omega_0}\right)\sin\left(2\pi\frac{\omega_{en}}{\omega_0}\right)}{\left.\frac{\partial\delta\varepsilon_e}{\partial\omega}\right|_{\omega=\omega_{en}} \left(\sin^2\pi\frac{\omega_{en}}{\omega_0} - \left(\frac{\pi\omega_{Li}}{\omega_0}\right)^2 \cos^2\pi\frac{\omega_{en}}{\omega_0}\right)\left(\sin^2\pi\frac{\omega}{\omega_0} - \sin^2\pi\frac{\omega_{en}}{\omega_0}\right)}. \quad (5)$$

Using the Mittag–Leffler theorem of the series expansion of a meromorphic function [4], we can show that (5) is a representation of the meromorphic function

$$D(\omega, \mathbf{k}) = 1 + \left(\frac{\pi\omega_{Li}}{\omega_0}\right)^2 \sum_{m=-\infty}^{\infty} (-1)^m J_{m+\frac{\omega}{\omega_0}}(\mu) \times J_{-m-\frac{\omega}{\omega_0}}(\mu) \frac{R_e^{(m)}(\omega)\cos\left(\frac{\pi\omega}{\omega_0}\right)}{\sin^2\left(\frac{\pi\omega}{\omega_0}\right) - \left(\frac{\pi\omega_{Li}}{\omega_0}\right)^2 \cos^2\left(\frac{\pi\omega}{\omega_0}\right)}. \quad (6)$$

Note that expression (6) is valid for arbitrary values of ω. In the limit of small ω values, our equation $D(\omega, \mathbf{k}) = 0$ passes over to the familiar equation

$$1 = R_i^{(0)} \sum_{n=-\infty}^{\infty} J_n^2(\mu) R_e^{(n)}, \quad (7)$$

which was derived by Silin [1] for $\omega \ll \omega_0$. The quantity $R_i^{(0)}$ in (7) is described by formula (2) with expression (3).

In our problem of the excitation of Bernstein modes, the wave vector $\mathbf{k}$ is perpendicular to the magnetic field and the electron contribution to the longitudinal dielectric function is (see, e.g., [5])

$$\delta\varepsilon_e(\omega, k) = -2\sum_{n=1}^{\infty} \frac{n^2\Omega^2\Phi_n(k)}{\omega^2 - n^2\Omega^2}, \quad (8)$$

where $\Phi_n = I_n(k^2\rho_e^2)\exp(-k^2\rho_e^2)/k^2 r_{De}^2$, r_{De} is the electron Debye radius, ρ_e is the electron gyroradius, and $I_n(x)$ is an nth order Bessel function of the imaginary argument. The dispersion relation $1 + \delta\varepsilon_e = 0$ gives the following spectrum of the eigenfrequencies of the Bernstein modes:

$$\omega_{en}(k) = n\Omega(1 + \Phi_n(k)). \quad (9)$$

Formula (9) is valid for strongly magnetized electrons ($\rho_e < r_{De}$), in which case we have $\Phi_n(k) \ll 1$ so that the pump field harmonics are in resonance with all of the Bernstein modes.

The roots of the equation $D(\omega, \mathbf{k}) = 0$ lie near the poles of the function in (5) [or (6)]; i.e., we have $\omega \approx n\omega_0$ with $n = 0, \pm1, \pm2, \ldots$. Consequently, the periodicity of the determinant allows us to consider only the case of small ω values. Generally, it seems to be more convenient to use equation (5) rather than equation (7), because ω does not enter the expression for $R_e^{(n)}$. However, for the specific electron contribution (8), both of these equations are equivalent.

Below, we will be concerned with an aperiodic instability, assuming that ω is purely imaginary. Substituting (8) and (9) into (5) or (7) gives the final dispersion relation

$$1 + \frac{\omega_{Li}^2}{\omega^2 - \omega_{Li}^2}\left(\sum_{n=1}^{\infty} \frac{2n^2\Omega(\Delta - \Omega\Phi_n)\Phi_n}{\omega^2 - n^2(\Delta - \Omega\Phi_n)^2} J_n^2(\mu) + J_0^2(\mu)\frac{1/k^2 r_{De}^2 - \Phi_0}{1 + 1/k^2 r_{De}^2 - \Phi_0}\right) = 0, \quad (10)$$

where Δ is the detuning defined above and, under the conditions adopted ($\rho_e < r_{De}$), the second term in parentheses is small for all values of the wave vector.

We investigate equation (10) starting with the limit of short wavelengths, $k\rho_e \gg 1$, in which the asymptotic expressions for all of the functions $\Phi_n(k)$ are the same regardless of n: $\Phi_n(k) \approx 1/(\sqrt{2\pi}\, k^3 r_{De}^2 \rho_e) \equiv \Phi(k)$. In this

case, the series in equation (10) can be summed up using the formula [1, 6]

$$\sum_{n=-\infty}^{\infty} \frac{nJ_n^2(\mu)}{n+\nu} = 1 - \frac{\pi\nu}{\sin\pi\nu} J_\nu(\mu) J_{-\nu}(\mu).$$

As a result, we obtain

$$1 - \frac{\omega_{Li}^2}{\omega^2 - \omega_{Li}^2} \frac{\Omega\Phi(k)}{\Delta - \Omega\Phi(k)} \times \left(1 - \frac{\pi\nu}{\sin\pi\nu} J_\nu(\mu) J_{-\nu}(\mu)\right) = 0, \quad (11)$$

where $\nu = \omega/(\Delta - \Omega\Phi)$. A completely analytic treatment of equation (11) is possible only in the case $\mu < 1$. In the limit $|\omega| \ll \omega_{Li}$, this equation can be reduced to a quadratic equation, which has unstable solutions only in a narrow range of detunings ($\Omega\Phi(k)(1 - \mu^2/2) < \Delta < \Omega\Phi(k)$, and the growth rate is maximum,

$$\gamma_{\max} = \frac{\mu^2}{4}\Omega\Phi(k), \quad (12)$$

at $\Delta = \Omega\Phi(k)(1 - \mu^2/4)$ (here, $\gamma = -i\omega$). Formula (12) shows that, as the wave vector increases, the maximum growth rate decreases in proportion to $1/k$. Consequently, it is expedient to examine the range of small $k\rho_e$ values.

To do this, we again restrict ourselves to the limit $|\omega| \ll \omega_{Li}$, in which the solutions to equation (10) lie close to the roots of the denominators in the series. To find the nth root, it suffices to equate the denominator of the nth term in the series to zero and to solve the resulting equation. In this case, unstable solutions exist in the range $\Omega\Phi_n(k)(1 - 2J_n^2(\mu)) < \Delta < \Omega\Phi_n(k)$ and the growth rate is maximum,

$$\gamma_{\max} = n\Omega J_n^2(\mu)\Phi_n(k), \quad (13)$$

at $\Delta = \Omega\Phi_n(k)(1 - J_n^2(\mu))$. For $n = 1$, the growth rate, as a function of the wave vector, is maximum at $k\rho \approx 2$.

The problem that we have analyzed here may be important for electron cyclotron heating of plasmas confined in magnetic devices. Thus, in the case in which an electromagnetic wave enters the device by crossing its end and propagates along its axis, the physical picture will be as follows. Since the magnetic field changes along the device axis, the electron cyclotron frequency and hence the value of the detuning will change accordingly. As the pump wave penetrates into the plasma, different Bernstein modes are excited one after another and propagate across the magnetic field.

Using the Hill method for regularizing infinite-order determinants, we have derived dispersion relations (5) and (6), which describe the parametric interaction between long-wavelength microwave radiation and a plasma. These fairly general dispersion relations, which were obtained only under the assumption that the plasma ions are unmagnetized, possess all of the properties of the determinant in (1); in particular, they are periodic in frequency, the period being equal to that of the pump wave.

REFERENCES

1. V. P. Silin, *Parametric Action of High-Power Radiation on a Plasma* (Nauka, Moscow, 1973).
2. O. M. Gradov and D. Sünder, Zh. Éksp. Teor. Fiz. **58**, 979 (1970) [Sov. Phys. JETP **31**, 526 (1970)].
3. A. V. Baitin and A. A. Ivanov, Pis'ma Zh. Éksp. Teor. Fiz. **59**, 389 (1994) [JETP Lett. **59**, 416 (1994)]; A. V. Baitin and A. A. Ivanov, Preprint No. IAE-5792/1 (RRC Kurchatov Inst. of Atomic Energy, Moscow, 1994).
4. E. T. Whittaker and G. N. Watson, *A Course of Modern Analysis* (Cambridge University Press, Cambridge, 1952; Fizmatgiz, Moscow, 1962), Chaps. 1, 2.
5. A. F. Alexandrov, L. S. Bogdankevich, and A. A. Rukhadze, *Principles of Plasma Electrodynamics* (Vysshaya Shkola, Moscow, 1978; Springer-Verlag, Berlin, 1984).
6. B. S. Newberger, J. Math. Phys. **23**, 1278 (1982).

Translated by I. A. Kalabalyk

Plasma Physics Reports, Vol. 26, No. 4, 2000, pp. 366–368. Translated from Fizika Plazmy, Vol. 26, No. 4, 2000, pp. 393–395.

PLASMA ELECTRONICS AND NEW ACCELERATION METHODS

Effect of an External RF Field on the Beam–Plasma Discharge in a Magnetic Field

A. A. Ivanov, L. N. Knyazev, A. A. Luk'yanov, S. V. Murav'ev, A. A. Serov, and V. Yu. Fedotov

Russian Research Centre Kurchatov Institute, pl. Kurchatova 1, Moscow, 123182 Russia

Received April 27, 1999

Abstract—The effect of an RF field on a steady-state beam–plasma discharge with a plane electrode placed parallel to a sheetlike electron beam is studied experimentally. The plasma parameters were measured by a single probe, and the electron distribution function was determined with the use of an electrostatic analyzer. The energy and current of the electron beam were E_B = 2.5 keV and J_B = 0.05–1.5 A, respectively. The working pressure was $p = 2 \times 10^{-5}$–10^{-3} torr. The frequency of the external RF field was 13.56 MHz. Both the steady-state regimes in which the RF field had no effect on the plasma parameters and regimes with a pronounced effect of the RF field were observed. The experiments show that the regime of the discharge depends strongly on the plasma density and the magnetic field. The parametric instability is studied theoretically in the weak-turbulence approximation. It is shown that, due to the decay nature of the spectrum of plasma oscillations, the onset of instability is accompanied by the transfer of the energy of fluctuations over the spectrum, from the pump frequency toward its harmonics. © *2000 MAIK "Nauka/Interperiodica".*

A low-pressure steady-state beam–plasma discharge (BPD) in a longitudinal magnetic field is an efficient tool for producing plasmochemical dissociation reactions [1, 2]. It can also be used in technology for surface treating. The efficiency of surface treating increases in the presence of flows of high-energy ions, which can be produced by combining a BPD with an RF discharge (combined BPD–RF discharge). The interaction of an RF electric field with a magnetized plasma is also of great interest for heating plasma electrons and ions.

In this paper, we consider a combined BPD–RF discharge, in which a potential RF electric field ($\Omega = 8.5 \times 10^7\ s^{-1}$) perpendicular to the magnetic field is applied to a conventional BPD. The schematic of the experiment is presented in Fig. 1 (see [3] for details).

The plasma was produced in argon at a pressure of 10^{-4}–10^{-3} torr by a sheetlike electron beam with an energy of 2 keV and current of 0.05–1 A and was confined by a 300- to 500-G magnetic field. An electron beam propagated along the magnetic field. In the absence of an RF field, the shape of the beam-electron distribution function (BEDF) on the whole varied according to the one-dimensional quasilinear theory (Fig. 2). However, in developed BPDs, the relaxation length was several times greater than that predicted by the theory. (This well-known discrepancy has led to the development of the theory of strong turbulence, which, however, predicts a relaxation length substantially larger than that observed in experiments [4].)

In some cases, when an external RF field was applied to a BPD plasma, the discharge was quenched. This occurred when the plasma density and temperature were low, $n < (2–3) \times 10^{11}$ cm^{-3} and $T_e < 2–3$ eV. The quenching manifested itself in a decrease in the plasma density by more than one order of magnitude when the RF field was switched on. In this case, near the electron beam, at distances more than several electron cyclotron radii from the field source, the electric field was 1–2 V/cm. The plasma parameters and the

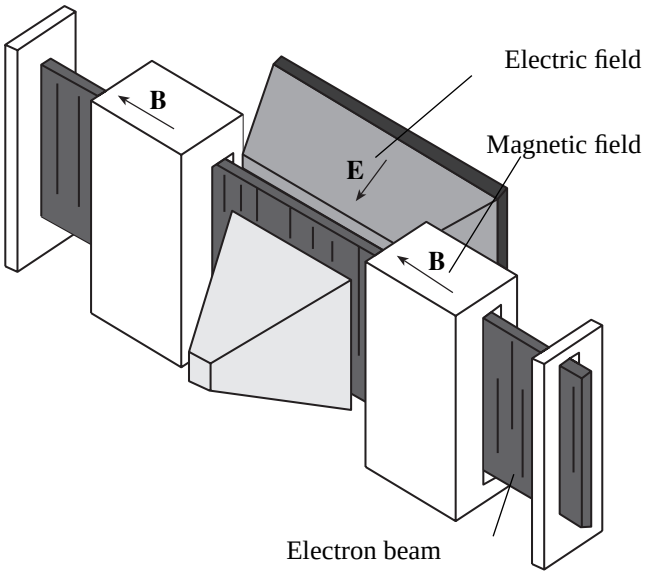

Fig. 1. Beam–plasma discharge device with a sheetlike beam.

1063-780X/00/2604-0366$20.00 © 2000 MAIK "Nauka/Interperiodica"

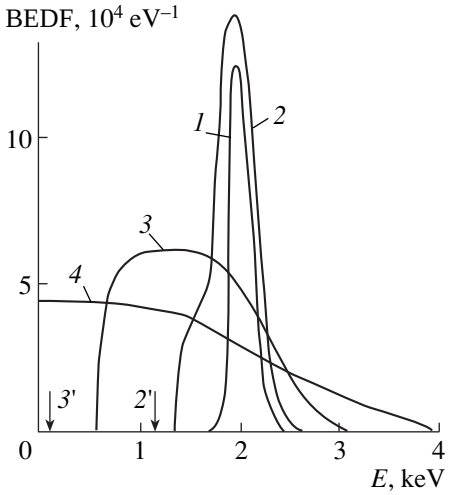

Fig. 2. (*1*) Initial BEDF and (*2–4*) BEDFs measured at the device output in the absence of an RF field for the beam currents I = (*2*) 0.05, (*3*) 0.25, and (*4*) 0.7 A. The arrows show the lower beam energy calculated by the quasilinear theory.

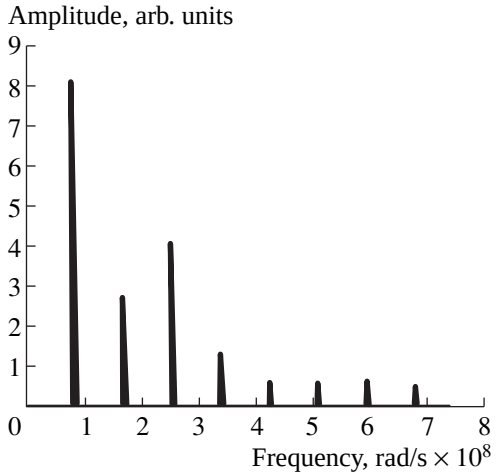

Fig. 3. The spectrum of plasma oscillations excited under the parametric action of an external RF field.

local potential of the RF field were measured by a Langmuir probe. To measure the plasma density n_p and the electron temperature T_e, a high-frequency filter was introduced into the probe circuit. The probe could be moved in the direction perpendicular to the direction of electron-beam propagation, which allowed us to measure the spatial distributions of the plasma parameters. The RF potential $\tilde{V}$ was measured by the shift of the probe floating potential V_S according to the expression $V_S = -(T_e/e)\ln(e\tilde{V}/T_e)$ [5]. The beam-electron energy analyzer based on the retarding-field method was positioned at the end of the experimental chamber and measured the BEDF. The spectra of plasma oscillations excited under the parametric action of the RF field were also analyzed (Fig. 3). The spectrum consisted of a series of peaks localized near harmonics of the pump frequency. This is evidence of the transfer of the energy of fluctuations to the high-frequency region of the spectrum.

Such a spectrum is very different from that predicted by the well-known theoretical models (see, e.g., [6, 7]). According to those models, the energy of fluctuations must be transferred toward low frequencies (down to the lower hybrid frequency Ω_{LH}) and small wavenumbers $k \approx 0$. After that, the plasma should come to a highly turbulent state, which should be accompanied by the formation of a Langmuir condensate. In the above papers, the basic nonlinear process leading to saturation of the parametric instability is the induced scattering of plasma waves by ions.

Here, we propose another scenario of the onset of the instability. In the magnetic field, the plasma oscillations in the frequency range under study are described by the following dispersion relation [8]:

$$\omega^2(\mathbf{k}) = \frac{\omega_{pi}^2(1 + y^2 A_0)}{1 + (1 - A_0)/k^2\rho_{De}^2}, \qquad (1)$$

where $\Omega_{LH} \le \omega < \omega_{ce}$, ω_{ce} is the electron cyclotron frequency; $A_0 = I_0(k_\perp^2\rho_e^2)\exp(-k_\perp^2\rho_e^2)$, ρ_e is the electron cyclotron radius; $I_0(x)$ is the modified Bessel function; $y = (k_z/k)\sqrt{\frac{M}{m}}$, M and m are the ion and electron masses, respectively; $\omega/|k_z| > v_{Te}$; $k = |k|$; and $k_\perp$ is the wave-vector component perpendicular to the magnetic field. The magnetic field is directed along the z-axis.

The dispersion curve $\omega(\mathbf{k})$ can be conventionally divided into two regions: the electron region ($k \ll 1$ and the ion-acoustic region ($k > 1$).

The external RF field drives the parametric instability with the maximum growth rates

$$\gamma_{\max} = \frac{1}{8}\frac{u_e^2\Omega_{LH}^2}{c_s^2\Omega}$$

in the electron region and

$$\gamma_{\max} = \frac{1}{8}\frac{u_e^2}{c_s^2}\Omega$$

in the ion region (here, u_e is the electron drift velocity and c_s is the speed of sound), which results in the excitation of the wave packets P_{1e} and P_{1i} in the electron and ion-acoustic regions, respectively. Two waves both belonging to any of these packets and having the frequencies $\omega_1 \approx \omega_2 \approx \Omega$ generate long-wavelength oscilla-

tions with the frequency ω in the electron region such that

$$\omega = \omega_1 + \omega_2, \quad \mathbf{k} = \mathbf{k}_1 + \mathbf{k}_2.$$

These conditions, which are usually referred to as the decay conditions, are consistent with equation (1). Evidently, $\omega \approx 2\Omega$; thus, a packet P_2 emerges near the second harmonic of the pump frequency. Similarly, two waves belonging to the packets P_{1e} and P_2 generate the wave with frequency $\approx 3\Omega$, etc. Thus, we obtain the set of packets near the harmonics of the pump frequency. Since these packets relate to the long-wavelength electron region, they can be easily recorded in the experiment.

As for short-wavelength oscillations excited in the ion-acoustic region, it is difficult to observe them directly. Nevertheless, they manifest themselves indirectly through their strong effect on the beam–plasma instability. Since the growth rate of the instability is proportional to $\omega_{pe}^2 c_s^2/\Omega^2 u^2 \sim k_\parallel^2/k_\perp^2$ (where u is the beam velocity), it strongly decreases in the presence of short-wavelength oscillations, so that the beam relaxation is suppressed.

REFERENCES

1. A. A. Ivanov and T. K. Soboleva, *Nonequilibrium Plasmochemistry* (Atomizdat, Moscow, 1978).
2. Yu. F. Nasedkin, L. N. Knyazev, A. N. Korukov, and A. A. Serov, *Proceedings of Interindustry Seminar on Physical Principles of Innovative Plasma Technologies in Microelectronics, Kharkov, 1991*, p. 51.
3. V. M. Atamanov, G. B. Levadnyi, A. A. Ivanov, *et al.*, Beitr. Plasmaphys. **22**, 509 (1982).
4. A. K. Berezin, E. V. Lifshits, Ya. B. Fainberg, *et al.*, Fiz. Plazmy **21**, 241 (1995) [Plasma Phys. Rep. **21**, 227 (1995)].
5. V. A. Godyak, A. N. Ivanov, and A. A. Kuzovnikov, Zh. Tekh. Fiz. **37**, 1063 (1967) [Sov. Phys. Tech. Phys. **12**, 766 (1967)].
6. S. L. Musher, A. M. Rubenchik, and B. I. Sturman, Plasma Phys. **20**, 1131 (1978).
7. B. D. Ogirov and A. M. Rubenchik, Zh. Éksp. Teor. Fiz. **81**, 159 (1981) [Sov. Phys. JETP **54**, 79 (1981)].
8. A. B. Mikhaĭlovskiĭ, *Theory of Plasma Instabilities* (Atomizdat, Moscow, 1971; Consultants Bureau, New York, 1974).

Translated by A. D. Smirnova[†]

[†] Now deceased.

Plasma Physics Reports, Vol. 26, No. 4, 2000, pp. 369–371. Translated from Fizika Plazmy, Vol. 26, No. 4, 2000, pp. 396–398.

PLASMA ELECTRONICS AND NEW ACCELERATION METHODS

Nonlinear Electromagnetic Pulse with a Superwide Frequency Bandwidth

A. M. Egorov and V. I. Maslov

National Science Center Kharkov Institute for Physics and Technology, Akademicheskaya ul. 1, Kharkov, 310108 Ukraine

Received April 30, 1999; in final form, October 21, 1999

Abstract—A nonlinear equation is derived and its analytic solution describing a soliton-like perturbation propagating at velocity close to the speed of light is found. It is shown that the rate at which the amplitude of a soliton excited by a cold electron beam in a magnetized plasma-filled waveguide grows is proportional to $(n_b/n_0)^{1/3}$, as is the linear growth rate of the beam–plasma instability. © *2000 MAIK "Nauka/Interperiodica".*

In studying the generation of wake plasma waves, Bulanov *et al.* [1] focused most of their attention on the formation of electromagnetic solitons that cannot be described in the envelope approximation. The soliton is generated in the wake of an electromagnetic pulse in the form of a nonlinear wideband electromagnetic pulse. In recent years, ultrashort wideband wave pulses and their applications have been analyzed in a number of papers (see, e.g., [2, 3]).

The interaction of high-power laser radiation with a plasma is characterized by qualitatively new effects, in particular, the formation of soliton-like perturbations. There is experimental evidence that solitons are generated when the dispersion curve for the excited oscillations has a straight line segment.

Analytic solutions describing solitons propagating at the speed of light in an unbounded plasma have been sought in many papers (see, e.g., [2]). Here, we analytically study a soliton-like perturbation propagating in a plasma waveguide. In a magnetized plasma, one of the modes of high-frequency oscillations is described by the dispersion law

$$\omega = ck\omega_p/(\omega_p^2 + c^2k^2)^{1/2}, \quad (1)$$

where ω_p is the Langmuir frequency of the plasma electrons, ω and k are the frequency and wave vector of the wave, and c is the speed of light. We can see that, for $\omega_p \gg ck$, the dispersion relation is almost linear, $\omega \approx ck$. Consequently, we can expect that this mode can give rise to a soliton-like perturbation. Let us construct a nonlinear equation describing such a soliton.

We consider a plane plasma-filled metal waveguide of length a in the y direction. Let a soliton-like perturbation of the electric potential φ propagate with the velocity V_s along the z-axis. We assume that the solution amplitude $-\varphi_0$ is small and that the soliton is symmetric; i.e., the potential φ is independent of the coordinates in the plane orthogonal to the vector $\mathbf{V}_s$. We start by analyzing a soliton that is steady-state in the comoving frame of reference. From the Maxwell equations, we obtain the following equation for the electric field $\mathbf{E}$ of a soliton:

$$\Delta\mathbf{E} - (\mathbf{V}_s\nabla)^2\mathbf{E}/c^2 + 4\pi e[\nabla n - (\mathbf{V}_s\nabla)n\mathbf{v}/c^2] = 0, \quad (2)$$

where n and $\mathbf{v}$ are the density and velocity of the plasma electrons, which can be evaluated from the Vlasov equation for the electron distribution function f_e,

$$\begin{aligned}\partial f_e/\partial t + \mathbf{v}\nabla f_e \\ -(e/m_e)(\mathbf{E} + [\mathbf{v}\times\mathbf{B}]/c)\partial f_e/\partial\mathbf{v} = 0.\end{aligned} \quad (3)$$

The assumption that the magnetic field, directed along the z-axis, is infinitely strong ($H_0 \longrightarrow \infty$) allows us to neglect electron motion across the magnetic field. Since we are seeking the solution describing a soliton that propagates with the velocity V_s and is steady-state in the comoving frame of reference, we can specify the dependence of f_e on time and coordinates in the form $z - V_s t$. In this case, equation (3) reduces to

$$-(V_s\partial_z)f_e + v_z\partial_z f_e + (e/m_e)(\partial_z\varphi)\partial f_e/\partial v_z = 0, \quad (4)$$

where $E_z = -\partial\varphi/\partial z$, so that the perturbed electron density $\delta n = n - n_0$ and the z-component of the electron current take the form

$$\begin{aligned}\delta n = -n_0(e\varphi/m_eV_s^2)(1 - 1.5e\varphi/m_eV_s^2), \\ j_z = -eV_s\delta n.\end{aligned} \quad (5)$$

We take into account (5) and keep the second-order terms in (2) to arrive at the nonlinear equation:

$$\begin{aligned}\varphi'' = [k_\perp^2 - (1 - V_s^2/c^2)(1 - 1.5e\varphi/m_eV_s^2) \\ \times\omega_p^2/V_s^2]\varphi/(1 - V_s^2/c^2),\end{aligned} \quad (6)$$

where the prime denotes the spatial derivative in the propagation direction of the soliton and $k_\perp$ is the trans-

1063-780X/00/2604-0369$20.00

verse component of the wave vector. Integrating (6) yields the following equation for $\phi = e\varphi/m_e V_s^2$:

$$(\phi')^2 = \phi^2\omega_p^2[k_\perp^2/\omega_p^2 + 1/c^2 - 1/V_s^2 + \phi(1/V_s^2 - 1/c^2)]/(1 - V_s^2/c^2). \quad (7)$$

Using the condition $\phi'|_{\phi = -\phi_0} = 0$, we find the velocity of a soliton propagating in the form of an electric-potential well:

$$V_c \approx c[1 + \phi_0 c^2 k_\perp^2/2(c^2k_\perp^2 + \omega_p^2)]/(1 + c^2k_\perp^2/\omega_p^2)^{1/2}. \quad (8)$$

We can see that the soliton is formed by the two modes described by the dispersion relations $\omega \approx \omega_p k/k_\perp$ and $\omega \approx ck$ and that the soliton velocity increases as its amplitude grows.

Defining the soliton width as $\Delta\xi = \phi_0/\phi'|_{\phi = -\phi_0/2}$, we approximately obtain

$$\Delta\xi = (2m_e/e\varphi_0)^{1/2}2c^2\omega_p/(c^2k_\perp^2 + \omega_p^2). \quad (9)$$

For $ck_\perp/\omega_p \ll 1$, we have $\Delta\xi \approx 2c^2(2m_e/e\varphi_0)^{1/2}/\omega_p$. The soliton width $\Delta\xi$ is seen to decrease as the soliton amplitude φ_0 grows. The properties of the soliton can be controlled by varying the two parameters $k_\perp$ and ω_p.

Using (8), we arrive at the following solution to equation (7):

$$\phi = -\phi_0/\cosh^2[\xi(\phi_0\eta)^{1/2}/2], \quad (10)$$

where ξ is the coordinate in the propagation direction of the soliton and $\eta = k_\perp^2 + \omega_p^2/c^2$.

Up to this point, we have described a steady-state soliton. Now we consider its interaction with a cold, low-density ($n_{b0} \ll n_0$) electron beam. Retaining the time derivative in the Vlasov equation (3) and using the methods of the perturbation theory allows us to obtain the following equation for the electron distribution function f_e:

$$\partial_t f_e^0 + (V - V_s)\partial_z f_e^{(1)} \approx 0, \quad (11)$$

where f_e^0 is a quasisteady electron distribution function, which satisfies equation (4), and $f_e^{(1)}$ is a correction introduced by the unsteady character of the potential $\phi(t)$. Integrating (11) over velocities, we can find the spatial derivative of the next-order correction to the electron density. The perturbed beam electron density can be evaluated from the electron hydrodynamic equations at $V_b \approx V_s$:

$$\partial_t^2 n_b = n_{b0}(e/m)\varphi''. \quad (12)$$

From (11), (12), and Poisson's equation, we have

$$\partial_t^3\varphi = -(n_{b0}/2n_0)V_s^3\varphi'''. \quad (13)$$

Using (6), (7), and (13), we can construct the equation

$$\partial_t^3\phi = -(n_{b0}/2n_0)\phi'(\phi_0 + 3\phi)\omega_p^2 V_s, \quad (14)$$

whose solution can be obtained using the formula

$$\phi = \phi_0(t)\mu\left[\xi - \int_{-\infty}^{t} d\tau\delta V_s(\phi_0(\tau))\right], \quad (15)$$

where $\mu(\xi) = 1/\cosh^2(\xi\sqrt{2}/\Delta\xi(\phi_0))$ by virtue of (9) and (10). In (15), we took into account the change δV_s in the velocity of the soliton due to its interaction with the beam electrons. From (14) and (15), we obtain the following expressions for δV_s and for the rate $\gamma = \partial\ln\phi_0/\partial t$ at which the amplitude ϕ_0 grows:

$$\delta V_s \approx -V_s(n_{b0}/n_0)^{1/3}, \quad \gamma \approx \omega_p(n_{b0}/n_0)^{1/3}(1.5e\varphi_0/m_eV_s^2)^{1/2}. \quad (16)$$

Note that both of these expressions contain the parameter $(n_{b0}/n_0)^{1/3}$, as in the case of a linear beam–plasma instability.

Hence, we have shown that the interaction between a cold electron beam and a soliton causes the soliton amplitude to grow. This conclusion agrees with the results obtained in [4–24] for soliton-like perturbations in a nonequilibrium plasma.

From (8), (9), and (16), we can see that a soliton in an unbounded plasma (i.e., at $k_\perp = 0$) possesses the following properties:

$$V_s \approx c, \Delta\xi = (2m_e/e\varphi_0)^{1/2}2c^2/\omega_p, \quad \gamma \approx (\omega_p/c)(n_{b0}/n_0)^{1/3}(1.5e\varphi_0/m_e)^{1/2}. \quad (17)$$

REFERENCES

1. S. V. Bulanov, T. Zh. Esirkepov, F. F. Kamenets, and N. M. Naumova, Fiz. Plazmy **21**, 584 (1995) [Plasma Phys. Rep. **21**, 550 (1995)].
2. R. W. Ziolkowski, Phys. Rev. A **44**, 3960 (1991).
3. B. I. Cohen, B. B. Afeyan, A. E. Chou, and N. C. Luhmann, Jr., Preprint No. UCRL-JC-117947 (Lawrence Livermore Nat. Lab., Livermore, CA, 1994).
4. H. Schamel, Phys. Rep. **140**, 163 (1986).
5. T. Sato and H. Okuda, Phys. Rev. Lett. **44**, 740 (1980).
6. K. Nishihara, H. Sakagami, T. Taniuti, and A. Hasegawa, Report No. 472 (Riso Nat. Lab., Riso, 1982), p. 41.
7. V. I. Maslov, Fiz. Plazmy **16**, 759 (1990) [Sov. J. Plasma Phys. **16**, 441 (1990)].
8. C. Barnes, M. K. Hudson, and W. Lotko, Phys. Fluids **28**, 1055 (1985).
9. M. Temerin, K. Cerny, W. Lotko, and F. S. Mozer, Phys. Rev. Lett. **48**, 1175 (1982).

10. C. Chan, M. H. Cho, N. Hershkowitz, and T. Intrator, Phys. Rev. Lett. **52**, 1782 (1984).
11. A. N. Sekar and Y. C. Saxena, Plasma Phys. Controlled Fusion **27**, 181 (1985).
12. A. Hasegawa and T. Sato, Phys. Fluids **25**, 632 (1982).
13. T. H. Dupree, Phys. Fluids **29**, 1820 (1986).
14. V. I. Maslov, in *Proceedings of 4th Symposium on Double Layers, Innsbruck, 1992*, p. 82.
15. S. M. Krivoruchko, Ya. B. Faĭnberg, V. D. Shapiro, and V. I. Shevchenko, Zh. Éksp. Teor. Fiz. **67**, 2092 (1974) [Sov. Phys. JETP **40**, 1039 (1974)].
16. J. P. Lynov, P. Michelsen, H. L. Pecseli, *et al.*, Phys. Scr. **20**, 328 (1979).
17. H. Ikezi, P. J. Barrett, R. B. White, and A. Y. Wong, Phys. Fluids **14**, 1997 (1971).
18. V. K. Sayal and S. R. Sharma, Phys. Lett. A **149**, 155 (1990).
19. V. I. Maslov, Phys. Lett. A **165**, 63 (1992).
20. M. A. Raadu, Phys. Rep. **178**, 25 (1989).
21. R. Bostrom, G. Gustafson, B. Holack, *et al.*, Phys. Rev. Lett. **61**, 82 (1989).
22. Y. Takeda and K. Yamagiwa, Phys. Fluids B **3**, 288 (1991).
23. J. E. Allen and H. S. Maciel, in *Proceedings of 4th Symposium on Double Layers, Innsbruck, 1992*, p. 3.
24. V. I. Maslov, Fiz. Plazmy **18**, 1310 (1992) [Sov. J. Plasma Phys. **18**, 676 (1992)].

Translated by O. E. Khadin

Plasma Physics Reports, Vol. 26, No. 4, 2000, pp. 372–373. Translated from Fizika Plazmy, Vol. 26, No. 4, 2000, pp. 399–400.

Semen Samoĭlovich Moiseev (In Honor of His 70th Birthday)

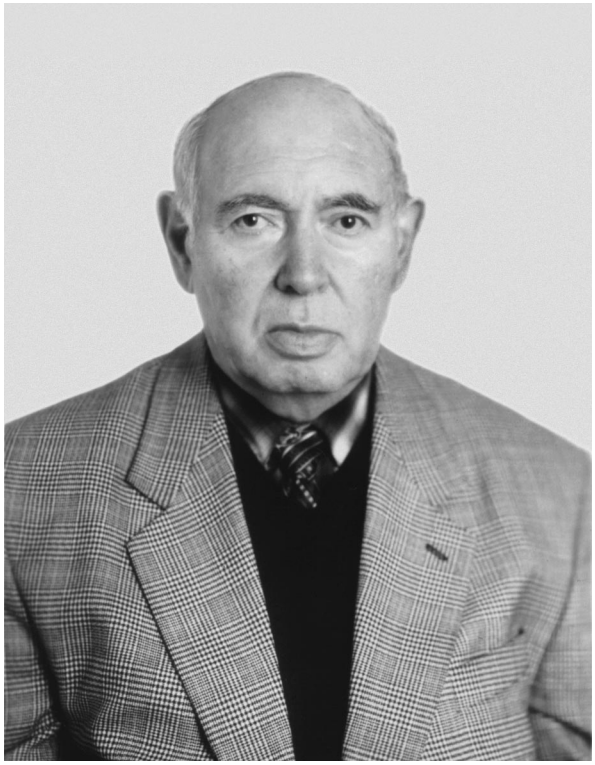

On November 23, 1999, we celebrated the 70th birthday of Semen Samoĭlovich Moiseev, a well-known theoretical physicist, professor, and principal researcher at the Institute of Space Research of the Russian Academy of Sciences.

Versatile scientific activity of S.S. Moiseev has been related to the development of a number of important directions in plasma physics, hydrodynamics, and nuclear energetics. His works, which were always in the vanguard of scientific research, have gained worldwide recognition in the scientific community.

After graduating with honors from Kharkov State University (KSU) in 1952, he worked as a teacher in Slavyansk and Poltava. However, his inquisitive intellect desired new knowledge, the more so since at that time a new, extremely important and complicated problem arose—the problem of creating a fundamentally new power source based on controlled nuclear fusion. Thus, in 1960, he radically changed his occupation and moved to Novosibirsk, where he began to work at the Institute of Nuclear Physics of the Siberian Division of the USSR Academy of Sciences. There, at the laboratory headed by Academician R.Z. Sagdeev, S.S. Moiseev, together with A.A. Galeev, V.E. Zakharov, V.N. Oraevskiĭ, G.M. Zaslavskiĭ, and other internationally known scientists, obtained pioneering results, which were reported at the largest international conferences and were the basis for his candidate's and doctoral theses. Among them, it is worth noting the solution to the problem of anomalous Bohm's diffusion in fusion devices, the studies on low-frequency instabilities in inhomogeneous plasmas and transformation of electromagnetic waves in nonsteady and inhomogeneous plasmas, and the development of principles of novel plasma diagnostics based on the generation of higher harmonics in plasma resonance layers.

In 1968, S.S. Moiseev moved to the Kharkov Institute for Physics and Technology (KIPT), the laboratory headed by Academician Ya.B. Faĭnberg. There, he further developed his earlier studies concerning plasma stability and plasma heating as applied to beam–plasma systems and proposed new, original ideas in other fields of plasma physics, among them, a model of the nonlocal transfer of electromagnetic signals in inhomogeneous plasmas (the effect of induced transparency of wave barriers), new mechanisms for the generation of electromagnetic radiation associated with the wave transformation due to plasma density gradients, focusing and channeling of radiation in a plasma, the resonant-cone effect in the excitation of electromagnetic waves by small-size sources, and the modulational instability. He developed new approaches to the theory of strong hydrodynamic turbulence and the formation of nonequilibrium power-law distributions of charged particles in collisional media. The results obtained were very important for practical applications, and S.S. Moiseev received a series of inventor's certificates. For their work on induced transparency of wave barriers in a plasma, S.S. Moiseev and his colleagues were awarded the 1979 Ukrainian SSR State Prize in Science and Technology.

In 1980, S.S. Moiseev began to work in Moscow at the Institute of Space Research of the USSR Academy of Sciences, where he was invited by Academician R.Z. Sagdeev. There, he developed new approaches to increasing the efficiency of absorption of high-power laser radiation in an inhomogeneous plasma via the channeling and self-focusing of laser beams. The results of his long-term studies on the mechanisms for the generation of electromagnetic radiation in a plasma were published in the monograph *Nonequilibrium and*

1063-780X/00/2604-0372$20.00 © 2000 MAIK "Nauka/Interperiodica"

Resonant Processes in Plasma Radiophysics (Nauka, Moscow, 1982) written together with A. A. Rukhadze, A.B. Shvartsburg, M.V. Kuzelev, and N.S. Erokhin. For his research in plasma physics, S.S. Moiseev was awarded the 1987 USSR State Prize in Science and Technology.

He also carried out investigations in hydrodynamics. An important result of these investigations was the discovery of a helical mechanism for the generation of large-scale tropical vortices (see the well-known paper by S.S. Moiseev, R.Z. Sagdeev, A.V. Tur, G.A. Khomenko, and A.M. Shukurov published in 1983 in Dokl. Akad. Nauk SSSR [Sov. Phys. Doklady]). This made it possible to develop a new approach to the important problem of typhoon formation and monitoring of cyclogenesis zones. Based on the results obtained, two expeditions to the Pacific Ocean were organized to carry out *in situ* measurements in the zones of intensive cyclogenesis. The theory of inverse helical cascade developed at the Institute of Space Research allowed S.S. Moiseev to elaborate the system of physical precursors and indicators of tropical cyclones. These studies laid the theoretical foundations of the contemporary methods for forecasting large-scale crisis processes in the atmosphere, such as typhoons and extratropical cyclones. The experimental data from the expeditions showed that these indicators may be abnormal fluctuations of background atmospheric parameters, such as infrasound activity, the dynamics of fractal parameters, and the helicity of atmospheric turbulence. Later, he investigated this field of research in more detail: he analyzed the formation of non-Kolmogorov spectra, examined the structural properties of hydrodynamic helical turbulence and the mechanisms for helicity generation, and studied the influence of turbulence helicity on particle and energy transport. In essence, he founded a new line of investigation—the helical dynamics of nonlinear media—which has various applications in hydrodynamics, plasma physics, biophysics, the physics of the Earth's liquid core, etc.

Along with these studies, S.S. Moiseev, together with V.I. Karas', V.I. Muratov, I.I. Zalyubovskiĭ, S.P. Kononenko, V.E. Novikov, and other colleagues from KIPT and KSU, investigated nonequilibrium power-law particle distributions in solid-state plasmas and developed the principles of their applications for direct and more efficient nuclear-to-electric energy conversion. In particular, based on theoretical and experimental results, they proposed a new secondary-emission radioisotope current source, which has obvious advantages in comparison with available nuclear batteries. The creation of a prototype of such a battery will stimulate the development of prospective future technologies of fabricating multilayer thin-metal-film structures.

In recent years, S.S. Moiseev has investigated very interesting chiral effects, which play an important role, e.g., in producing new materials with unusual electrodynamic characteristics. These studies are related to another promising area of investigation—the electrodynamics of bianizotropic media.

Due to Moiseev's talent for intuiting new, promising directions in physics, his works have stimulated a number of new lines of investigations. Many of his results have been confirmed experimentally and gained worldwide recognition. Although S.S. Moiseev is a theorist, he always tries to initiate experimental testing of the results obtained. He is justly recognized as a classic researcher in plasma physics. His style of work, kindness, sociability, and striking spiritual power make a deep impression on those around him. Owing to him, many of his pupils have achieved great success and gained wide recognition in the scientific community.

S.S. Moiseev spends a great deal of time and energy on the development of international collaboration. He has worked at various renowned science centers, such as the MHD Research Center of Ben-Gurion University (Israel) and the Nieuwegein Institute of Plasma Physics (Netherlands).

For a long time, S.S. Moiseev has been a convener of one of the sections of the General Assemblies of the European Geographic Society; he has been a member of the organizing committees of several large international conferences.

Friends, colleagues, and pupils of Semen Samoĭlovich Moiseev heartily congratulate him on his seventieth birthday and wish him robust health, happiness, and further success in his creative work.

R.Z. Sagdeev, A.A. Galeev, V.E. Zakharov, V.N. Oraevskiĭ, V.M. Balebanov, A.M. Dykhne, V.P. Silin, A.B. Mikhaĭlovskiĭ, A.A. Rukhadze, R.A. Kovrazhkin, E.A. Kuznetsov, L.M. Zelenyĭ, O.A. Pokhotelov, Yu.I. Gal'perin, M.B. Gokhberg, and N.S. Erokhin